Magnetic and Dielectric Properties of Ba Based M- and Y-type Hexaferrites

A Thesis Submitted

By

Pratap Behera

In Partial Fulfillment of the Requirements for the Award of the Degree of

Doctor of Philosophy in Physics

Department of Physics

Indian Institute of Technology Guwahati

Guwahati-781039, India

October, 2019

Statement

The work contained in the thesis entitled **"Magnetic and Dielectric Properties of Ba Based M- and Y-type Hexaferrites"** has been carried out by me under the supervision of Prof. S. Ravi, Department of Physics, Indian Institute of Technology Guwahati. This work has not been submitted elsewhere for the award of any degree.

October, 2019

(Pratap Behera)
Department of Physics
Indian Institute of Technology Guwahati
Guwahati-781039, India

Certificate

It is certified that the work contained in the thesis entitled **"Magnetic and Dielectric Properties of Ba Based M- and Y-type Hexaferrites"** by Mr. Pratap Behera, a Ph. D. student of the Department of Physics, Indian Institute of Technology Guwahati, for the award of the degree of *Doctor of Philosophy* has been carried out under my supervision. This work has not been submitted elsewhere for the award of any degree.

October, 2019

(S. Ravi)

Professor, Department of Physics

Indian Institute of Technology Guwahati

Guwahati-781039, India

Dedicated

To

My Family

Acknowledgments

"***Starting something can be easy; it's finishing is the highest hurdle***." The journey of doctoral study is one of the difficult and challenging tasks that I have come across. I am indebted to the direct and indirect support of numerous people, who made this whole journey successful and made this thesis possible. At the end of this journey, it is my pleasure to have the opportunity to thank those people whom I will be grateful forever.

First and foremost, I wish to express my sincere gratitude and respect to my research supervisor Prof. S. Ravi, Department of Physics, Indian Institute of Technology Guwahati for giving me the opportunity to carry out my doctoral research under his guidance. His resourceful guidance, encouragements, supports and belief on me during my Ph.D. tenure were the driving forces that motivated me to complete my research work and without him, this work would have never been completed. It's been a great journey of learning the beautiful area of Condensed Matter Physics especially magnetism and the related experimental techniques. Thank you very much sir, for our advice on my research as well as my carrier for which I shall remain grateful to you for rest my life.

I offer my sincere thanks to my Doctoral Committee (DC) members, Prof. S. Ghosh (Chairman), Dr. D. Pamu and Prof. G. Krishnamoorthy for their insightful suggestions and comments for the improvement of my research work from various perspective.

My sincere thanks to the current HoD, Department of Physics, Prof. Subhradip Ghosh and the former HoDs, Prof. P. Poulose and Prof. S. Basu for their prodigious support towards departmental facilities. I am also thankful to all the faculty members of Physics Department for helping me in various ways during my research period at IIT Guwahati.

I would like to express my sincere gratitude to Dr. Sidananda Sarma and other staff members of my department. I am also thankful to the former and present head of Central Instruments Facility (CIF), and all the scientific officers and technical officers of CIF, IIT Guwahati for providing me to access various sophisticated instruments to carry out my research work during my Ph.D. tenure.

It is my great pleasure to thank all my lab mates, whose presence has developed a pleasant working environment. So, I offer my sincere thanks, not in particular order, My seniors Dr. Tribedi Bora, Dr. Bipul Deka, Dr. Ranganadha Gopalarao, Dr. Junmoni Barman and Dr. Bibhuti Bhusan Dash. I offer my special thanks to my lab mates Aakansha, Dr.

Vishwajit Manohar Gaikwad, Mahananda Brahma, Ritupan Bora and K Puspanjali Patra for their kind help, support and cooperation.

My special thanks to my batch mates at IIT Guwahati for having good times spend together. I am also thankful to my department seniors and juniors, Dr. T. Santosh Kumar, Dr. Bhargab Deka, Dr. Bhagaban Kishan, Dr. Ranjan Bhuyan, Dr. P. Mahesh, Dr. Ravi Patta, Dr. Anabil Gayen, Omkar Tripathy, Gautam, Shyam, Sasmita, Aneeta, Dolly, Srinivas, Sushmita, Apurba, Prajna, Gajendra, Suchit, Pushpesh and all other research scholars of department of physics will always be remembered for their support and pleasant memories during my PhD life.

"A good friend is like a four-leaf clover, hard to find and lucky to have". I am fortunate enough to be surrounded by some amazing friends for their helping hands with beautiful hearts. I express my sincere thanks to some of my close friends and seniors, Sandeep Kumar, Sona Chandran, Uma Lavanya, Francis, Dr. Alekha Chandra Nayak, Arun Kumar Panda, Soumya Sahoo, Saroj Kr. Singh, Dr. Rashmi, Dr. Shibananda, Dr. Ananda, Dr. Ranjan, Dr. Ramesh, Dr. Sritam, Dr. Soumya, Saibal, Bidu Bhusan, Anil, Niranjan Mohanty and others. I am thankful to you all for their help and motivation during my Ph.D. life.

I am grateful to my family members and relatives for their love, blessings, care and constant support throughout my life. I offer my special sense of gratitude to my elder brother Mr. Pradeep Behera for always been inspiring, supporting and teaching me to understand the true value of human life.

Last but not the least, I am expressing my sincere thanks to the Ministry of Human Resource and Development (MHRD) and Indian Institute of Technology Guwahati for providing the financial assistantship during my Ph.D. tenure. Department of Science and Technology (DST), New Delhi is also acknowledged for providing financial supports for various experimental facilities.

At last, I thank the almighty God from the bottom of my heart for giving me the strength to face all the difficulties in life to pursue my dreams and move forward in the beautiful journey of life.

Pratap Behera

IIT Guwahati

Abstract

The condensed matter physicist and material scientists devote enormous effort to discover and develop new multiferroic materials possessing multiple functional properties that can be operated at room temperature. So far, only a few naturally occurring single-phase multiferroic materials have been discovered, such as $BiFeO_3$, $BiMnO_3$ and some rare earth based manganites, $RMnO_3$ (R = Y, Tb, Ho). Hexaferrites are one such class of materials that exhibit magnetoelectric properties near or above the room temperature for future applications. All the hexaferrite materials exhibit magnetocrystalline anisotropy and their magnetic properties are closely linked to their crystalline structures. Depending upon the preferred orientation of induced magnetizations within the crystal structure, hexaferrites are classified into two groups namely; (i) Uniaxial hexaferrite, where the magnetic moments are aligned along the easy axes of magnetization and (ii) Ferroxplana or Hexaplana ferrites, where the magnetic moments are aligned along the easy plane of magnetization. In order to carry forward the research in this area, our study is mainly focussed on the improvement in structural, dielectric and magnetic properties of these hexaferrites.

In general, ferrites are classified into three different categories based on their crystal structures such as spinel ferrites, garnets and hexaferrites. Ferrites with hexagonal structure (hexaferrites) are one of the important class of materials in the family of permanent magnets due to their excellent chemical stability, low cost, easy manufacturing, interesting dielectric and magnetic properties. Based on general chemical formula and crystal structure, hexaferrites are classified into six types such as; (i) M type – $AFe_{12}O_{19}$, (ii) Y type – $A_2B_2Fe_{12}O_{22}$, (iii) W type – $AB_2Fe_{16}O_{27}$, (iv) Z type – $A_3B_2Fe_{24}O_{41}$, (v) X type – $A_2B_2Fe_{28}O_{46}$, (vi) U type – $A_4B_2Fe_{36}O_{60}$. Where A represents Ba, Sr, Pb or Ca and B is the divalent cations of transition elements such as Co, Ni and Zn. As compared to the other five variants, M-type hexaferrites have relatively simple crystal structure and chemical formula and they can be prepared in single-phase form with ease. The presence of high uniaxial magnetic anisotropy, self-biasing nature, low eddy current loss, low microwave loss or narrow ferromagnetic resonance and magnetoelectric coupling make this compound as the natural choice for applications in magnetic recording, permanent magnet, microwave devices and multi-state memory devices. In order to enhance the saturation magnetization and coercivity, several researchers have carried out various attempts by substituting

different transition elements such as Cr, Mn, Co, Ni, Cu and Zn. If the down spin Fe^{3+} ions were replaced by the cationic substitutions, then the increase in net magnetization would be expected. In most of the cases, the dopant ions are in 2+ state and to maintain the charge neutrality, simultaneous substitution of tetravalent ions such as Ti, Sn, Zr, or Mo at Fe site or trivalent rare earth ions such as La at Ba site have been reported. Some of the above M-type hexaferrites show improvement in magnetic properties.

Y-type hexaferrite is another important class of materials with chemical formula $A_2B_2Fe_{12}O_{22}$, where A = Ba^{2+}, Sr^{2+} *etc*., and B = Co^{2+}, Ni^{2+}, Zn^{2+}, Mg^{2+} *etc*. The Y-type hexaferrite consists of same number of Fe ions as compared to M-type hexaferrite but with an additional A and two B atoms per formula unit. Y-type hexaferrites containing Co, Ni, Zn, Mg and combination of them exhibit ferrimagnetic transition temperature around 600 K to 700 K. These samples are found to exhibit magnetoelectric effect at relatively low magnetic field such as 30 mT in both $Ba_{0.5}Sr_{1.5}Zn_2Fe_{12}O_{22}$, and $Ba_2Mg_2Fe_{12}O_{22}$ and 1 mT in $Ba_{0.5}Sr_{1.5}Zn_2(Fe_{1-x}Al_x)_{12}O_{22}$. In addition to that, the dielectric constant is one of the key parameter of polycrystalline samples that depends on microstructure and heterogeneity such as grains and grain boundaries. Therefore, the analysis of impedance spectroscopy along with dielectric constant, electric modulus spectra will provide the detailed information about different electroactive regions in the multiferroic compounds. Even though Y-type hexaferrites are demonstrated as one of the key materials for magneto-electric applications, the systematic study on the substitution at Co or Fe site in $Ba_2Co_2Fe_{12}O_{22}$ compound is still lacking. Therefore, the main objective of the present thesis work is to improve these properties by suitable cationic substitutions.

In the present thesis work, the magnetic and dielectric properties of these M- and Y-type hexaferrites are extensively analyzed in terms of saturation magnetization, coercivity, anisotropy constant, impedance, conductivity and modulus studies. The following five series of M- and Y- type Barium Hexaferrites were prepared for the present thesis work.

1. M-type Barium Hexaferrite

(i) $BaFe_{12-y}Ni_yO_{19}$ (y = 0 – 0.5)

(ii) $BaFe_{12-y}Ti_yO_{19}$ (y = 0 – 0.8)

(iii) $Ba(Fe_{1-x}Al_x)_{12}O_{19}$ (x = 0 – 0.10)

2. Y-type Barium Hexaferrite

(iv) $Ba_2(Co_{1-x}Zn_x)_2Fe_{12}O_{22}$ (x = 0 – 1.0)

(v) $Ba_2(Co_{1-x}Mg_x)_2Fe_{12}O_{22}$ (x = 0 – 0.5)

The above samples were characterized by using the following instruments such as; X-ray diffractometer (XRD), Raman spectrometer, Field emission scanning electron microscope (FESEM), Vibrating sample magnetometer (VSM), Impedance analyzer and LCR meter. In order to determine the phase formation and crystal structure, the XRD patterns of all these samples were recorded at room temperature and these patterns were analyzed by Rietveld refinement technique using FULLPROF program. The microstructure and compositions of these samples were analyzed at room temperature by FESEM equipped with EDX facility. The temperature variations of magnetization measurements along with hysteresis loops were measured by Lakeshore make VSM. Impedance analyzer and LCR meter were used for the magnetic permeability and dielectric property measurements respectively.

The present thesis work on the above mentioned series of compounds contain seven chapters as follows.

1. Introduction
2. Experimental Techniques
3. $BaFe_{12-y}M_yO_{19}$ (M = Ni and Ti) Series
4. $Ba(Fe_{1-x}Al_x)_{12}O_{19}$ series
5. $Ba_2(Co_{1-x}Zn_x)_2Fe_{12}O_{22}$ series
6. $Ba_2(Co_{1-x}Mg_x)_2Fe_{12}O_{22}$ series
7. Conclusions

Chapter 1 describes the brief introduction about the structure of M- and Y-type barium hexaferrites and their importance in various physical properties. A brief introduction to the basics of magnetism, different types of magnetic interactions and the influence of magnetic anisotropy in magnetic properties are discussed. A brief introduction to impedance spectroscopy, dielectric data of ceramic materials including the methods followed by extracting and analyzing these data are presented. A short discussion about the multiferroic properties of the hexaferrite materials are also presented. Different mechanisms involved in the electrical conduction processes are discussed. Finally, a detailed review of earlier

reports on M- and Y-type hexaferrites with special emphasize on their structural, magnetic and dielectric properties are provided. A brief outline of the motivation of the present thesis work is also presented.

Chapter 2 provides the various experimental techniques used in the present thesis work. The method of sample preparation and the experimental techniques followed in characterizing the materials are discussed in detail. The structural, magnetic and dielectric properties of the prepared samples were studied by employing various sophisticated instruments such as X-ray diffractometer, Raman spectrometer, Field emission scanning electron microscope, Vibrating sample magnetometer, Impedance analyzer and LCR meter, *etc*. The working principles of these sophisticated instruments and details of their relevant central parameters used during the measurements are presented.

Chapter 3 discusses the detailed analysis of structural, magnetic and impedance spectroscopy data of Ni and Ti substituted $BaFe_{12}O_{19}$ (BaM) compounds.

Single-phase samples of $BaFe_{12-y}Ni_yO_{19}$ with $y = 0 – 0.5$ were prepared by using the standard sol-gel route. To determine the phase purity and crystal structure, XRD patterns are analyzed by Rietveld refinement technique. The samples are found to crystallize in hexagonal structure with $P6_3/mmc$ space group. The lattice parameters *a* and *c* are found to increase with increase in Ni concentration. Temperature variation of magnetization measurements reveal that the parent compound (BaM) exhibits ferrimagnetic transition at T_c = 720 K. The substitution of Ni^{2+} for Fe^{3+} ions is found to increase the ferrimagnetic transition from 720 K for $y = 0$ to 759 K for $y = 0.5$ due to strengthening of superexchange interaction. The frequency dispersion of dielectric permittivity along with its conductivity contributions are well explained based on Havriliak – Negami equation. The dielectric relaxation observed in these spectra signifies the contributions of grains and grain boundaries. The hopping of electrons between Fe^{2+} and Fe^{3+} ions and the hole transfer between Ni^{2+} and Ni^{3+} ions enhance the polarization mechanism. As a result, the dielectric constant is enhanced due to Ni substitution.

The $BaFe_{12-y}Ti_yO_{19}$ samples with $y = 0 – 0.8$ were prepared in single-phase form by standard solid state method and they crystallize in hexagonal structure with $P6_3/mmc$ space group. The lattice constant *c* is found to increase systematically with increase in Ti concentrations. The temperature variation of magnetization measurements show the reduction in ferrimagnetic T_c from 720 K for $y = 0$ to 608 K for $y = 0.8$. The impedance

spectroscopy and electrical conductivity were measured in the frequency range of $10^2 – 10^6$ Hz. The analysis of impedance spectra reveal that the relaxation process deviates from the ideal Debye type relaxation of charge carriers. The activation energy values estimated from the conductivity studies are found to decrease with Ti substitutions. As the temperature is increased, the diameter of semicircular arc of the Nyquist (Z'' vs Z') plots is also decreased. And it demonstrates the decrease in electrical resistance due to thermal activation of charge carriers.

Chapter 4 provides the detailed analysis of structural, magnetic and dielectric properties of $Ba(Fe_{1-x}Al_x)_{12}O_{19}$ samples with x = 0 – 0.10 prepared by solid state reaction route. Rietveld refinement of XRD patterns reveal the single-phase nature of the samples. Typical microstructural images of Al substituted samples show hexagonal shaped grains and the average grain size is found to be reduced with Al substitutions. The magnetic hysteresis loops measured at room temperature show that the saturation magnetization value is decreased with Al doping while the coercivity value is increased. In M-type hexaferrite, there are two formula units per unit cell. Therefore, 24 Fe^{3+} ions are distributed over five different crystallographic sites namely; three octahedral (12k, 2a, $4f_2$), one tetrahedral ($4f_2$) and one trigonal bi-pyramidal (2b) site. The decrease in saturation magnetization values can be attributed to the site occupation of Al^{3+} ions at spin up sub-lattices of Fe^{3+} ions. The complex dielectric permittivity and permeability along with dielectric and magnetic loss tangent were measured at room temperature. The real part of dielectric constant possesses maximum value at low frequency region and then starts decreasing with increase in frequency. The loss tangent also follows the similar trend as that of dielectric constant and its behavior can be well explained by Koop's theory. The real part of magnetic permeability and magnetic loss tangent were measured in the frequency range of 10 MHz to 1 GHz. The substitution of Al^{3+} for Fe^{3+} ions is found to decrease the permeability values and resonance peaks are observed for all the samples. The dissipation of magnetic energy can be determined from the magnetic loss tangent and it shows the decrease in loss tangent (< 2 %) with Al substitutions.

Chapter 5 presents the detailed analysis of structural, magnetic and dielectric properties of Zn substituted Y-type Barium hexaferrites. Samples of $Ba_2(Co_{1-x}Zn_x)_2Fe_{12}O_{22}$ with x = 0 – 1.0 were prepared in single-phase form by standard solid state method. XRD patterns of all these samples were analyzed by rhombohedral structure with R–3m space group. The lattice parameters *a* and *c* are found to increase with increase in Zn concentrations and this

can be understood due to the larger ionic radius of Zn^{2+} ion than that of Co^{2+} ions. The temperature variation of magnetization measurements reveal the decrease of ferrimagnetic T_c from 600 K to 380 K for $x = 0 – 1.0$. As the temperature is decreased, the samples exhibit helimagnetic spin -reorientation transitions and it decreases from 225 K to 66 K for $x = 0$ to 0.75 samples. The saturation magnetization value is found to be increase with increase in Zn concentration. The magnetic permeability of all the samples were measured at room temperature in a wide range of frequencies. The substitution of Zn^{2+} for Co^{2+} ions enhance the real part of magnetic permeability due to the reduction in domain wall stiffness caused by the decrease in magneto-crystalline anisotropy. However, the Zn substituted Y-type hexaferrite basically for $x = 0.5$ sample exhibits a high value of magnetic permeability with low magnetic loss compared to those of other samples and is suitable for radiofrequency and antenna applications in high frequency range. The complex impedance spectra, dielectric constant and ac electrical conductivity were analyzed in the frequency range of $10^2 – 10^6$ Hz. The high value of dielectric constant at low frequency is due to the interfacial polarization mechanism. In order to understand the distribution of relaxation time in impedance spectra are temperature dependent or not, the impedance spectra were plotted by normalizing them i.e. Z''/Z''_{max} versus $\log(f/f_{max})$. It reveals that the loss peaks of impedance spectra were merged into a single master curve and suggests the distribution of relaxation time is temperature independent.

Chapter 6 provides the structural, dielectric and magnetic properties of $Ba_2(Co_{1-x}Mg_x)_2Fe_{12}O_{22}$ ($x = 0 – 0.5$) samples synthesized by standard solid state reaction route. Rietveld refinement of the XRD patterns confirm that all the samples crystallize in rhombohedral structure with R–3m space group. The lattice parameter c is found to decrease from 43.51 Å to 43.47 Å for $x = 0 – 0.5$. The decrease in lattice parameter can be attributed to the lattice size mismatch between Mg^{2+} and Fe^{3+} ions. The FESEM micrographs show the hexagonal platelet like structure. The substitution of Mg^{2+} for Fe^{3+} ions dilute the superexchange interaction by resulting the decrease in ferrimagnetic T_c from 613 K to 581 K for $x = 0 – 0.5$. In addition to that, the samples exhibit helimagnetic spin-reorientation transitions at low temperatures and it decreases from 225 K to 182 K for $x = 0 – 0.5$ samples. The decrease in spin-reorientation transition temperature can be attributed to the decrease in magnetic anisotropy due to Mg substitutions. The complex impedance spectra, electric modulus spectra and ac conductivity spectra were measured at different temperatures in a wide frequency range. The impedance spectra measured at different

temperatures demonstrate the thermally activated relaxation process in the sample. The presence of two semi-circular arcs in the Nyquist (Z'' vs Z') plots indicate the contribution of both grains and grain boundaries towards the relaxation dynamics. Further, the depressed and asymmetric semi-circular arcs of Nyquist plots signify the presence of non-Debye type of dielectric relaxation and it corresponds to the short-range movement of oxygen vacancies. Electric modulus spectra were further analyzed to understand the detailed dielectric properties by modeling to an equivalent electric circuits to get more information about the grains and grain boundaries contributions in relaxation dynamics. The ac electrical conductivity data measured at different temperatures were analyzed by different theoretical models and they follow the small polaron tunneling model.

Chapter 7 describes the overall brief summary of the results obtained from the analysis of the above M- and Y-type based bulk samples. The substitution of Ni, Ti and Al have greatly influenced the magnetic and dielectric properties of the samples. With substitution of Ni^{2+}, Ti^{4+} and Al^{3+} for Fe^{3+} ions slightly decreases the saturation magnetization (M_s) values. The increase in coercivity (H_c) value can be attributed to the enhancement in magnetocrystalline anisotropy due to Al^{3+} ion substitutions. In Zn doped Y-type hexaferrites, the M_s value is found to increase up to x = 0.5 and then decreases, while in Mg doped hexaferrite, it is found to decrease systematically. Thus, the site occupation of different cations have large influence in tuning the magnetic properties. Complex impedance analysis of these M- and Y-type hexaferrites reveal the presence of non-Debye type of relaxation processes with contributions from both grains and grain boundaries. The future scope of research in these materials are also discussed briefly in this chapter.

List of Abbreviations used in this Thesis

AFM	Antiferromagnetic
BaM	$BaFe_{12}O_{19}$
BSE	Back-scattered electrons
CC	Cole – Cole
CD	Cole – Davidson
CCR	Closed Cycle Refrigerator
CO_2Y	$Ba_2Co_2Fe_{12}O_{22}$
CPE	Constant Phase Element
DE	Double Exchange
DM	Dzyaloshinskii – Moriya
EDX	Energy Dispersive X-ray Spectra
FC	Field Cooled
FIM	Ferrimagnetic
FM	Ferromagnetic
NN	Nearest neighbour
FESEM	Field Emission Scanning Electron Microscope
G	Grains
GB	Grain Boundaries
HN	Havriliak – Negami
JPL	Jonscher's Power Law
KWW	Kohlrausch – Williams – Watts
LAS	Law of Approach to Saturation
NTCR	Negative Temperature Co-efficient of Resistance

OLPT Overlapping of Large Polaron Tunneling

OV Oxygen Vacancy

PM Paramagnetic

QMT Quantum Mechanical Tunneling

RKKY Ruderman – Kittel – Kasuya – Yosida

SG Space group

SPT Small Polaron Tunneling

SR Spin reorientation

UDR Universal Dielectric Response

VSM Vibrating Sample Magnetometer

XRD X-ray Diffraction

ZFC Zero Field Cooled

Table of Contents

Contents **Page No.**

List of Figures

Chapter 1

Chapter 2

Chapter 3

Chapter 4

Chapter 5

Chapter 6

List of Tables

Chapter 1

Chapter 3

Chapter 4

Chapter 5

Chapter 6

Chapter 1

Introduction

Magnetic materials were first discovered in Neolithic age in the form of lodestone. Later on, their electrical and magnetic properties were understood and these materials have been put in use for various applications in automobiles, data processing, electronics, telecommunications, accelerators, household applications, *etc*. Since lodestone is an iron ore, it is also called ferrites. In general, ferrites are nonconductive ferrimagnetic material and derived from the hematite (Fe_2O_3) or magnetite (Fe_3O_4) or the other oxides of Fe. Based on the classification as per crystal structure, the magnetite is known as spinel ferrites having cubic structure; however, there are certain class of magnetic materials having hexagonal crystal structure known as hexaferrites.

Since their discovery, hexaferrites become one of the most prominent class of magnetic materials having multitudes of applications [1]. Due to the low cost, easy manufacturing, high value of intrinsic coercivity and large crystalline anisotropy, hexaferrites have attracted renewed research interest in the field of permanent magnet, high frequency and microwave devices, magnetic-recording media, magneto-optical devices, data storage materials, *etc*. [2, 3]. For example, the development of good permanent magnet reduces the size of motors in such a way that the rotational accuracy of stepping motor increases. Multiferroics and magnetoelectric effect are the other interesting phenomena that were observed in these materials. Multiferroicity is a phenomenon of materials undergoing more than one ferroic orderings such as (anti) ferromagnetic, ferroelectric and/or ferroelastic below the transition temperature [4, 5]. The coupling between magnetic and ferroelectric orderings provide the possibility of writing the data electrically and reading them magnetically. The presence of such magnetoelectric effect leads to more energy efficient devices for large storage capacity, electronic device miniaturization, applications in memory devices, sensors, transducers and spintronics devices *etc*. [6, 7]. Moreover, the mutual coupling of electric and magnetic properties adds one more degree of freedom in manipulating the properties of both electrical and magnetic materials [8]. Besides, such

fascinating multifunctional properties, hexaferrites have attracted more attention due to their distinct electric and magnetic properties like strong electric polarization and the high dielectric permittivity.

The hexagonal ferrites are all ferrimagnetic materials whose magnetic properties are intrinsically linked to their crystalline structure. It exhibits magnetocrystalline anisotropy (MCA) that means the induced magnetization has a preferred orientation within the crystal structure. If the material has easy axis of magnetization, it is called uniaxial hexaferrite, and on the other hand if they exhibit easy plane of magnetization, they are called ferroxplana or hexaplana ferrites. In addition to that, hexagonal ferrites have low crystal symmetry. As a result, these materials exhibit high crystalline anisotropy and high resonance frequency values. There are certain types of hexaferrites having *c*-plane anisotropy and soft magnetic properties. Therefore, they exhibit relatively large permeability values and considered as one of the promising materials for microwave absorbance applications. In the next section, we will discuss about the crystal structure of M- and Y- type hexaferrites in detail.

1.1 Crystal Structure

In general, the crystal structure of ferrites are considered as the interlocking reticulation of positively charged metal ions (Fe, Me) and negatively charged oxygen ions (O^{2-}), where Me = Mg, Co, Ni *etc*. The ordered arrangement of atoms or ions or crystal structure of ferrites give rise to magnetic interactions and hence its ferrimagnetic properties. The magnetic moment depends on the electronic configuration as well as the distribution of cations at different crystallographic sites. Therefore, based on the chemical formula and crystal structure, hexaferrites are classified into six different groups such as;

i. M – type ($AFe_{12}O_{19}$)
ii. Y – type ($A_2Me_2Fe_{12}O_{22}$)
iii. W – type ($AMe_2Fe_{16}O_{27}$)
iv. Z – type ($A_3Me_2Fe_{24}O_{41}$)
v. X – type ($A_2Me_2Fe_{28}O_{46}$)
vi. U – type ($A_4Me_2Fe_{36}O_{60}$)

where A corresponds to Ba, Sr, Ca or Pb and Me represents the divalent cations of transition elements like Co, Ni, Cu, Zn, Mg, *etc*. The chemical compositions of the above hexaferrites can be obtained from the ternary phase diagram of BaO – MeO – Fe_2O_3 system as shown

in Fig. 1.1. Besides that, the crystal structure of any type of hexaferrites can be constructed by the superposition of three basic building blocks such as *S*, *R* and *T*. The chemical compositions of all these hexaferrites along with the details constituting crystallographic blocks are given in Table 1.1. Here *S**, *R** and *T** represent the 180° rotation of *S*, *R*, and *T* blocks around the easy axis called *c*-axis.

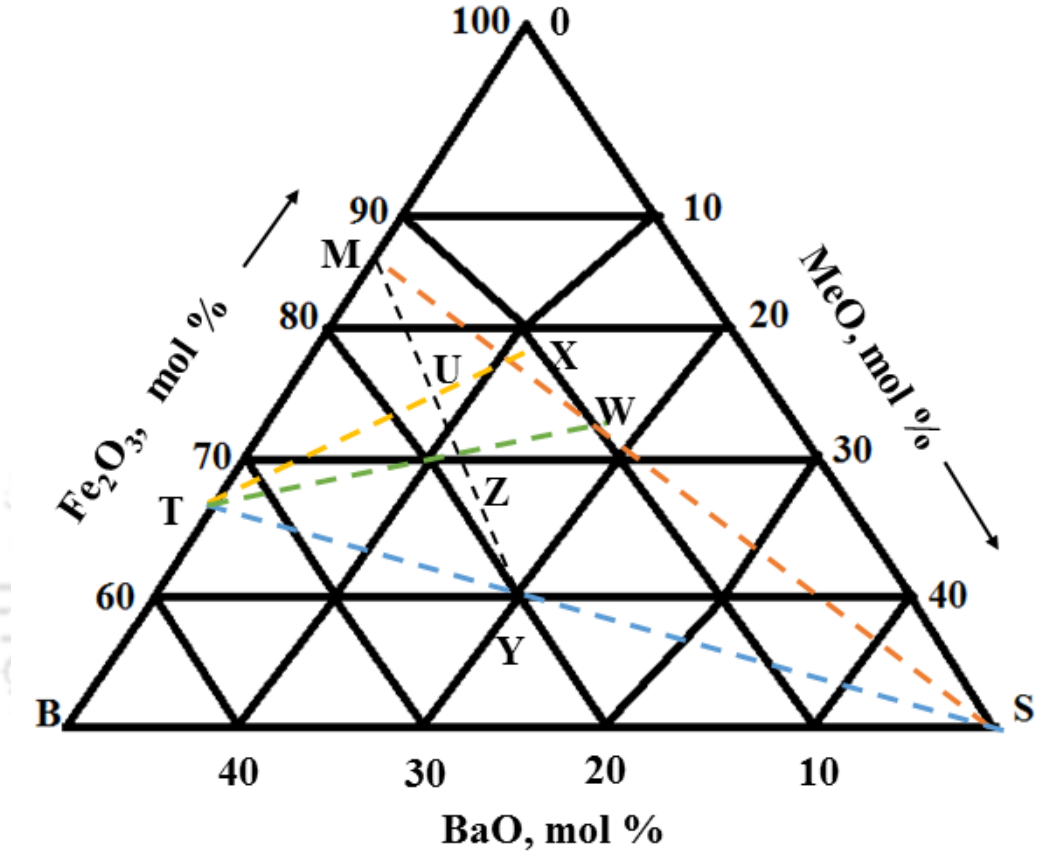

Figure 1.1: Compositional phase diagram of different hexagonal ferrites [2].

Table 1.1: Chemical compositions and crystallographic buildings of different Barium Hexaferrites.

Types	Chemical Compositions	Number of formula units per unit cell	Crystallographic building per unit cell
M	$BaFe_{12}O_{19}$	2	*R*S*RS*
Y	$Ba_2Me_2Fe_{12}O_{22}$	3	*STS′T′S′′T′′*
W	$BaMe_2Fe_{16}O_{27}$	2	*R*S*S*RSS*
Z	$Ba_3Me_2Fe_{24}O_{41}$	2	*R*S*T*S*RSTS*
X	$Ba_2Me_2Fe_{28}O_{46}$	3	*3(RSR*S*S*)*
U	$Ba_4Me_2Fe_{36}O_{60}$	1	*RSR*S*T*S**

The perspective representation of *S*, *R* and *T* blocks are shown separately in Fig. 1.2. In the barium hexaferrite family, one of the close-packed O^{2-} ion is replaced by Ba ion and the Fe^{3+} ions occupy the interstitial positions of the crystal lattice. The divalent cation (Me) is replaced by the Fe^{3+} ion in the interstitial sites. The *S* – block has the spinel structure with the unit formula of $Me_2Fe_4O_8$ and hence it has two tetrahedral and four octahedral sites. The *R* – block has the stoichiometry of $BaFe_6O_{11}$, where one of the centred O^{2-} ion is replaced by a Ba ion in three hexagonally packed layers of four oxygen atoms each. The presence of single Ba atom produces an asymmetry in some of the cations. Therefore, the *R* – block has five octahedral sites and one trigonal bipyramidal site. However, the *R* – block does not have any tetrahedral sites as it is pushed to octahedral sites by Ba atom. The *T* – block is made up of four oxygen layers where two Ba atoms replace two of the centred O_2 atoms. As a result, the *T* – block has become the stoichiometry of $Ba_2Fe_8O_{14}$ and has two tetrahedral and six octahedral sites. All these hexaferrites have multiples of these molecular ferrites. However, the combination of three important ferrite compounds S ($MeFe_2O_4$), M ($BaFe_{12}O_{19}$) and Y ($Ba_2Me_2Fe_{12}O_{22}$) can construct all other hexaferrites like W-type hexaferrite = M + 2S, Z-type hexaferrite = M + Y, X-type hexaferrite = W + M and U-type hexaferrite = 2M + Y. The crystal structure of these hexaferrites are very large due to its complex nature and the large size of the unit cell.

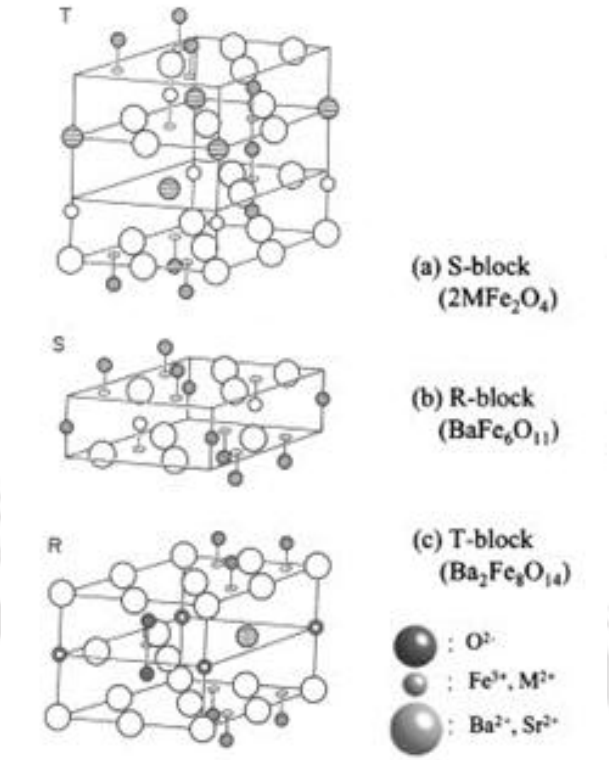

Figure 1.2: Perspective representation of *S*, *R* and *T* building blocks of hexagonal ferrites. The white sphere, stripped sphere and small sphere represent O^{2-}, Ba^{2+} and Fe^{3+} ions respectively [2].

1.1.1 M-type Hexaferrite

Among all hexaferrites, M-type hexaferrite has relatively simple crystal structure and it can be prepared in single-phase form with ease. The structure of M-type hexaferrite can be written as $AFe_{12}O_{19}$, where A may be Ba, Sr, Ca or Pb. The structure of barium hexaferrite $BaFe_{12}O_{19}$ (BaM) is same as natural mineral magnetoplumbite and it can be symbolically written as *R*S*RS* [2]. Where the * represents the 180° rotation of the respective blocks around the *c*-axis. In the unit cell of M-type hexaferrite, the *S* – block (spinel structure) consists of cubically close-packed O^{2-} ions and the Fe^{3+} ions, where the Fe^{3+} ions occupy in its tetrahedral and octahedral sites. Similarly, the *R* – block is made up of one Ba^{2+} and Fe^{3+} ions with hexagonally packed O^{2-} layers and the Fe^{3+} ions occupy the tetrahedral, octahedral and trigonal bipyramidal sites. In this case, the layer that contains Ba^{2+} ion is hexagonally packed with respect to two oxygen layers at each side and the four oxygen layers containing Ba^{2+} ion are cubically packed. A schematic representation of the

unit cell of BaM hexaferrite is demonstrated in Fig. 1.3. The crystal structure of BaM hexaferrite with $P6_3/mmc$ space group has two formula units per unit cell. There are five different crystallographic sites for Fe^{3+} ions, three octahedral (Fe_1, Fe_4 and Fe_5) with Wyckoff positions 12k, 2a, $4f_2$, one tetrahedral (Fe_3) with Wyckoff position $4f_1$ and one trigonal bi-pyramidal (Fe_2) site with Wyckoff position 2b. However, the Fe^{3+} ion at 2b site is surrounded by five oxygen ions. The distribution of spin up Fe^{3+} ions 12k (↑), 2a (↑) and 2b (↑) sites parallel to the crystallographic *c*-axis and the spin down $4f_1$ (↓) and $4f_2$ (↓) sites gives rise to net ferrimagnetic interaction. Thus, the net magnetic moment at a particular temperature (*T*) per unit cell of BaM hexaferrite can be enunciated as;

$$M\,(T) = 6M_{12k}\,(T) + 1M_{2a}\,(T) + 1M_{2b}\,(T) - 2M_{4f1}\,(T) - 2M_{4f2}\,(T) \qquad (1.1)$$

where *M* represents the magnetic moment of Fe^{3+} ions at different sublattices in BaM hexaferrite and the multiplication factors 6, 1, 1, 2, and 2 represent the number of Fe^{3+} ions in the respective site per formula unit. As the magnetic moment per Fe^{3+} ion is equal to 5 μ_B, then the pure BaM hexaferrite has the net magnetic moment of 20 μ_B per formula unit. The reported value of the lattice parameters *a* and *c* of BaM hexaferrites are 5.89 Å and 23.20 Å respectively [9].

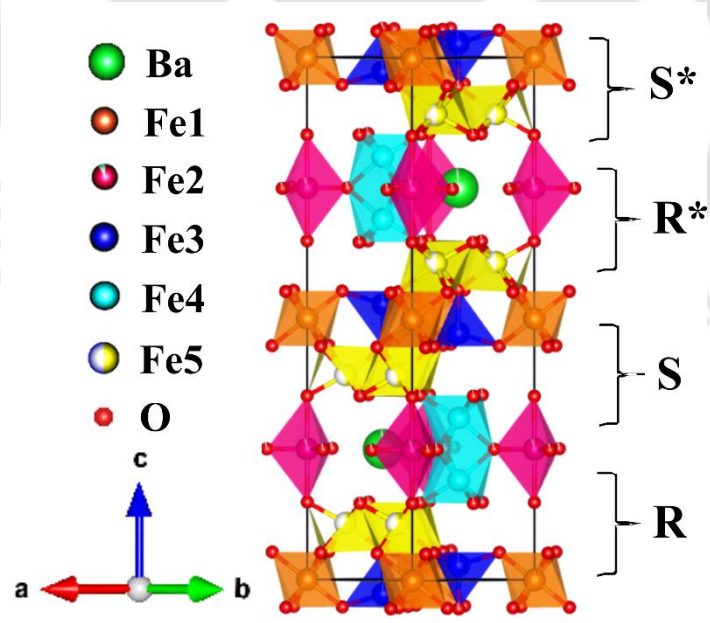

Figure 1.3: Schematic diagram of the unit cell of BaM hexaferrite.

1.1.2 Y-type Hexaferrite

Y-type hexaferrite is another important class of materials in the hexagonal family that exhibits interesting magnetic and magneto-dielectric properties. It is the first ferroxplana ferrites to be discovered where the easy plane of magnetization is perpendicular to the *c*-axis at room temperature. The typical chemical formula of Y-type barium hexaferrite is $Ba_2Me_2Fe_{12}O_{22}$, where Me represents a divalent cations (Co^{2+}, Ni^{2+}, Zn^{2+}, Mg^{2+} *etc*.) or combination of them. Among the Y-type hexaferrites, like $Ba_2Co_2Fe_{12}O_{22}$ (Co_2Y), $Ba_2Zn_2Fe_{12}O_{22}$ (Zn_2Y), $Ba_2Mg_2Fe_{12}O_{22}$ (Mg_2Y) *etc*., the Cobalt based Y-type ferrite (Co_2Y) possess higher Neel temperature and large magnetic anisotropy. The crystal structure of Y-type hexaferrite is such that it contains three formula units per unit cell with R-3m space group. Its layered structure is constructed by alternately stacking of *S* and *T* blocks in a sequence of *STS′T′S″T″*, where the prime represents the 120° rotation about the *c*-axis [10]. In Y-type hexaferrite, the 36 Fe^{3+} ions are distributed over six different crystallographic sites; four octahedral sites ($3a_{vi}$, $3b_{vi}$, $6c_{vi}$ and $18h_{vi}$) and two tetrahedral sites ($6c_{iv}$ and $6c_{iv*}$) [11, 12]. Here the asterisk mark denotes that although the sublattices having same crystal symmetry but it belongs to different blocks. The schematic diagram of the unit cell of Y-type hexaferrite is depicted in Fig. 1.4.

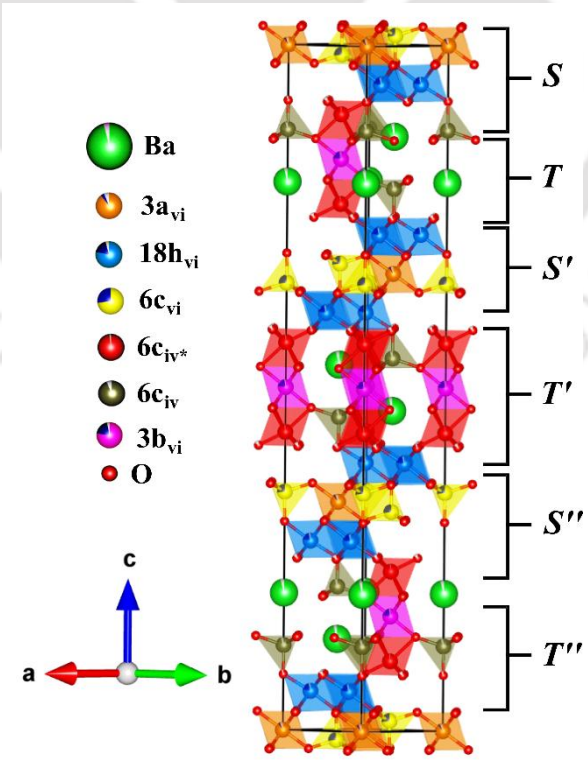

Figure 1.4: Schematic diagram of the unit cell of Y-type barium hexaferrite.

The study of electrical and magnetic properties of hexaferrites are crucial to explore their utility in various applications. An introduction to magnetism and dielectric properties is given in the following sections.

1.2 Magnetism and Exchange Interactions

The physical origin of magnetism in a material is developed due to the interaction of magnetic moments or magnetic dipoles of atoms or ions in a solid. In general, the magnetic moments in an atom arises due to the existence of two types of electrons motions. The first one corresponds to the rotation of electrons in atomic orbitals, which produces small magnetic field while the second one is due to the rotation of electrons (spins) in its own axis that produces a magnetic moment along the spin axis [13, 14]. Thus, the electrons motion in an atom can be considered as the principal origin of magnetic moment. However, the net magnetic moment of an atom is the consequence of collective effect of magnetic moments of spin and orbital motion of electrons. In addition to that, based on magnetic moments as well as their interactions with neighboring atoms or ions, the magnetic materials are broadly classified as; diamagnet, paramagnet, ferromagnet, antiferromagnet and ferrimagnet [13, 14].

The magnetic properties of ferromagnetic, ferrimagnetic and antiferromagnetic materials are governed by the various long-range interactions among the magnetic moments. In 1928, Heisenberg showed that the molecular field or exchange field is a quantum mechanical phenomenon responsible for the ordered magnetic states in these materials and is accountable for these long-range interactions [13]. Although, the exchange interactions are magnetic in nature but they are primarily originated from the electrostatics. The exchange interaction is related to Coulomb interaction and Pauli's exclusion principle based on the overlapping of electrons' wave functions. There are different types of distributions of wave functions in space such as symmetric and antisymmetric wave functions. If two interacting electrons spins are parallel with each other, the spatial part of the total wave function is called symmetric and if the spins are aligned in opposite directions it is called antisymmetric. The probability distribution of wave functions in space is different for both symmetric and antisymmetric wave functions and hence they have different electrostatic energy. When the interaction arises due to the wave functions of two or more electrons are being subjected to exchange symmetry i.e. remains in the symmetric or antisymmetric state by exchange of spins of electrons, such interaction is known as

exchange interaction and that depends upon the orientation of spins of electrons. However, at a particular temperature, the dominant thermal energy overcomes the exchange energy, leading to the disappearance of spontaneous magnetization and such temperature is called Neel temperature or Curie temperature. According to the Heisenberg model, if S_m and S_n are spins of two interacting electrons, then the exchange interaction can be defined as [13];

$$E_{exc} = - 2 \Sigma J_{mn} S_m . S_n \qquad (1.2)$$

where J_{mn} denotes the exchange integral due to overlapping of charge distribution of the atoms *m* and *n*. When $J_{mn} > 0$, the parallel alignment of spins are more favorable thus leading to lower energy value. Further if $J_{mn} < 0$, the antiparallel spin alignment is more favorable [14]. If the materials have antiferromagnetically coupled sublattices with unequal magnitudes of moment, then it is called ferrimagnetic material. Hexaferrites belong to such ferrimagnetic type with non-zero magnetic moment. There are different types of magnetic interactions and are discussed briefly in the following sub-sections.

1.2.1 Direct Exchange Interaction

The direct interaction between two neighboring magnetic atoms through the overlapping of their electronic wave functions without the aid of any intermediate molecules or ions are known as direct exchange interaction. The electrons having parallel spins keep away from each other due to Coulomb repulsion. Therefore, antiparallel spin configuration is mostly favored the direct exchange interaction. However, due to insufficient overlapping of neighboring magnetic orbitals, the direct exchange interaction is not an important mechanism to control the magnetic properties of most of the materials. Moreover, in hexaferrites, the cations (Fe and Me) are distributed over the interstitial positions of the oxygen lattice and as a result, the direct exchange interaction between the cations is not possible here.

1.2.2 Superexchange Interaction

In general, the orientation of magnetic moments of the cations in ferrite materials arises due to superexchange interaction. Superexchange interaction is an indirect exchange interaction where two non-neighboring magnetic ions interact with each other by means of a mediated non-magnetic ion between them and it is a long-range interaction. According to Kramers' model [15], the interaction between the cations having less than half-filled *d* – shells exhibit ferromagnetic interaction whereas such interaction between cations having

more than half-filled *d* – shells exhibit antiferromagnetic interactions. In addition to that, Goodenough and Loeb [16, 17] have also shown that the interaction among the cations having less than half-filled *d* – shells exhibit antiferromagnetic interactions.

To elucidate the mechanism of superexchange interaction, a suitable example was considered based on the interaction between two Mn – 3*d* orbitals. A schematic representation of superexchange interaction producing different magnetism such as ferromagnetism and anti-ferromagnetism are shown in Fig. 1.5(a) and (b) respectively. Fig. 1.5(a) depicts the antiferromagnetic interaction between two Mn^{3+} – 3*d* ions through an oxygen ion. Here the antiferromagnetism is facilitated due to strong Hund's coupling. The overlapping of both 3*d* and 2*p* orbitals assist the formation of covalent bond between the Mn^{3+} cations and the intermediate O^{2-} anions. In order to satisfy the Hund's rule, each of these two valence electrons of oxygen anions will point towards their respective sides of Mn^{3+} cations i.e. the up spin electron spends some time with the cation having up spin configuration and the down spin electron spends some time with the cation having down spin configuration. As a result, the cation – anion pair forms ferromagnetic (parallel) alignment of electrons while the net cation – cation interaction is antiferromagnetic as depicted in Fig. 1.5(a) for $Mn^{3+} – O^{2-} – Mn^{3+}$ networks.

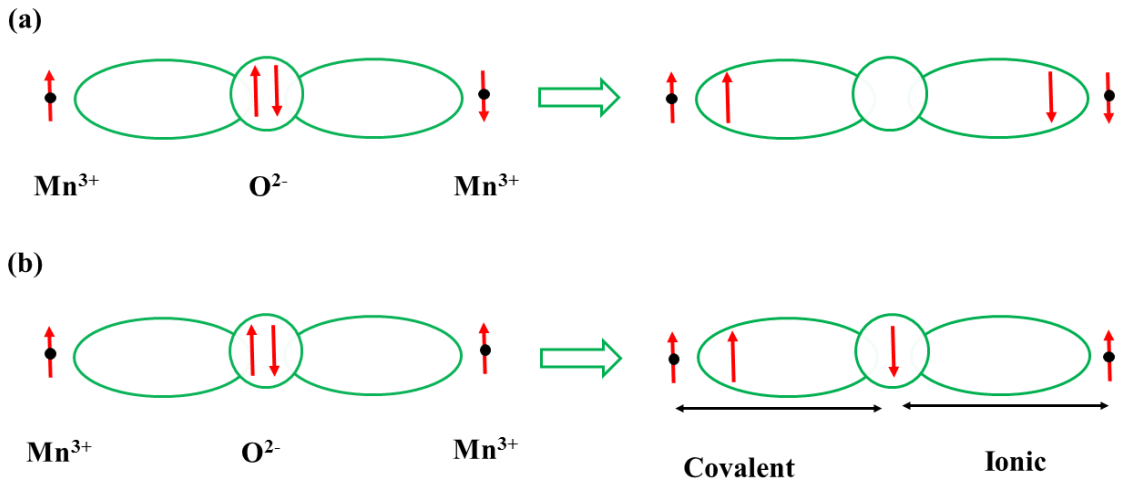

Figure 1.5: Schematic representation of spins and orbitals arrangement in (a) an antiferromagnetic and (b) a ferromagnetic superexchange interaction.

However, the above covalent bonding is not acceptable for the parallel alignment of magnetic moments of the core spins as shown in Fig. 1.5(b). According to Goodenough [16], when the cation – anion – cation interaction is asymmetric i.e. covalent bond at one

side and ionic bond at another side as shown in Fig. 1.5(b), ferromagnetism is preferred. Where the left side (Mn^{3+}) cation having spin up electron forms covalent bond with spin up electron of O^{2-} and the another spin down electron of O^{2-} forms ionic bond with right side Mn^{3+} cation. The direct exchange between oxygen and the right side cation is antiferromagnetic. Thus, the overall ferromagnetic interaction prevails between Mn^{3+} and Mn^{3+} ions.

1.2.3 RKKY Interaction

RKKY interaction is a special kind of indirect exchange interaction mostly observed in metals possessing localized magnetic moments where the conduction electron mediates the interaction. The localized magnetic moment of an ion spin polarizes the conduction electrons and this polarization couples to the neighboring localized magnetic moment at a distance *r* away [18-20]. This interaction does not couple directly and that appears in the form of an *r*-dependent exchange interaction J_{RKKY} (r) as [14];

$$J_{RKKY}(r) \; \alpha \; \frac{\cos(2k_F r)}{r^3} \qquad (1.3)$$

where k_F represents the radius of the spherical Fermi surface. It is a long-range interaction, anisotropic and exhibiting oscillatory behavior over the space. Thus, the RKKY interaction could be ferromagnetic or antiferromagnetic based on the distance between the magnetic ions.

1.2.4 Double Exchange Interaction

In 1951, Clarence Zener [21, 22] first introduced the concept of double exchange (DE) interaction by considering mixed valence compounds i.e. among magnetic ions having more than one oxidation states. This interaction is popularly known as Zener double exchange interaction. Zener have shown that such type of interaction gives rise to FM due to on-site strong Hund's coupling. Fig. 1.6(a) shows a typical example of DE interactions between Mn^{3+} and Mn^{4+} ions mediated through O^{2-} ions. In such cases, a spin up electron transfer from Mn^{3+} to O^{2-} followed by the transfer of spin up electron of O^{2-} to Mn^{4+} ion. Consequently, Mn^{3+} oxidizes to Mn^{4+} and Mn^{4+} reduces to Mn^{3+}. Due to the two-step process of exchange of electrons, this process is known as double exchange interaction. However, if the magnetic spins are not parallel, the electron transfer becomes more difficult due to strong onsite Hund's coupling as depicted in Fig. 1.6(b), where e_g and t_{2g} are two sub-orbitals of the *d* – orbitals. The electron transfer is also becoming more difficult if the

Mn – O – Mn bond is considerably bent away from 180°. Such deviation of bond angles affect the overlap of the manganese *d* – orbitals and oxygen 2*p* orbitals and hence the electron transfer. The movement of electron shown in Fig. 1.6 can be represented as $Mn^{3+}_{1\uparrow} O_{2\uparrow,3\downarrow} Mn^{4+} \rightarrow Mn^{4+} O_{1\uparrow,3\downarrow} Mn^{3+}_{2\uparrow}$, where the electron spins are labelled as 1, 2, 3. Anderson and Hasegawa [23] presented the DE mechanism in detail by visualizing a second order process in which the electron transfer takes place as follows $Mn^{3+}_{1\uparrow} O_{2\uparrow,3\downarrow} Mn^{4+} \rightarrow Mn^{3+}_{1\uparrow} O_{3\downarrow} Mn^{3+}_{2\uparrow} \rightarrow Mn^{4+} O_{1\uparrow,3\downarrow} Mn^{3+}_{2\uparrow}$.

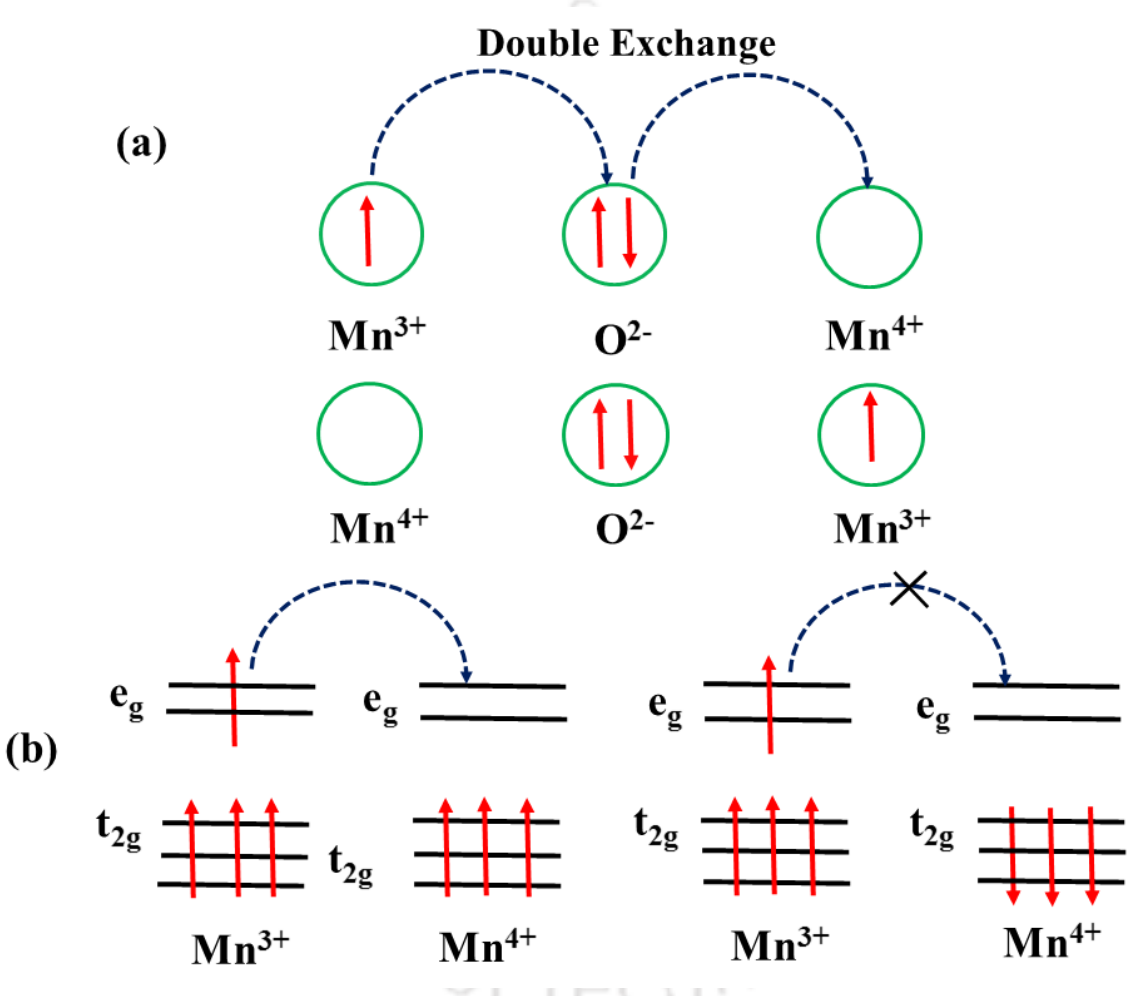

Figure 1.6: (a) Sketch of double exchange interaction between Mn ions and (b) Hopping of e_g electrons is allowed only when the localized spins are polarized and parallel to each other.

1.2.5 Dzyaloshinskii – Moriya Interaction

The Dzyaloshinskii – Moriya (DM) interaction is one type of anisotropic exchange interaction where the tilting of magnetic moments of antiparallel spins towards each other

gives rise to net magnetic moment [24, 25]. The DM exchange energy for this canted spin arrangement can be defined as;

$$H_{DM} = \vec{D}.(\overrightarrow{S_1} \times \overrightarrow{S_2}) \quad (1.4)$$

Here S_1 and S_2 are two neighboring magnetic spins and D is the DM constant. The constant D vanishes when the crystal field has inversion symmetry with respect to the middle point connecting the magnetic ions. Depending on the symmetry configuration, D lies either parallel or perpendicular to the line connecting two magnetic spins. The DM interaction tries to align both S_1 and S_2 vectors at right angle to each other in a plane perpendicular to D. Therefore, very often its effect is rotation spins by a small angle. The DM interaction is mostly observed in antiferromagnetic materials and such interaction gives rise to weak ferromagnetism. The antisymmetric exchange interaction is one of the most relevant factor for the understanding of magnetism induced electric polarization in multiferroic systems.

1.3 Magnetic Orderings

The materials having the spontaneous alignment of spins without the application of magnetic field is known as magnetically ordered materials. The diamagnetism and paramagnetism are two simple magnetic properties of the samples possessing isolated magnetic moments i.e. they do not interact with each other. However, in certain materials, the isolated magnetic moments interact with each other leading to a collective magnetism. Such collective magnetism gives rise to one of the following types of magnetism: ferromagnetism, antiferromagnetism, ferrimagnetism, spiral and spin glass behavior *etc*. Various magnetic orderings due to the above discussed magnetic interactions are briefly discussed below.

1.3.1 Diamagnetism

Diamagnetism is an inherent property of all the materials which is concealed within the other types of magnetism [26]. It possesses no net magnetic moment due to the absence of unpaired electrons. However, with the application of an external magnetic field, a magnetic moment is induced opposite to the direction of an applied field and such type of behavior can be understood by considering Lenz's law. Thus, the magnetic susceptibility of a diamagnetic material is always negative.

Langevin [27] elucidated the concept of susceptibility of a diamagnetic material. According to Langevin's equation, the susceptibility of a diamagnetic material having N number of atoms per unit volume and Z number of completely filled electrons per atom can be written as;

$$\chi = -\frac{\mu_0 N Z e^2}{6m}\bar{r}^2 \qquad (1.5)$$

where μ_0 denotes the permeability of free space, *e* and *m* correspond to charge and mass of an electron and $\bar{r}^2$ is the mean square radius of electron orbits. In general, the diamagnetic susceptibility is quite small and mostly independent of temperature. Superconductor is a special type of material possessing strong diamagnetism. Some of the examples of the diamagnetic materials are Si, Ge, Zn, Au, Ag *etc*., inert gases like He, Ne, Ar *etc*. and some organic materials.

1.3.2 Paramagnetism

Paramagnetism (PM) is the property of a material that possesses magnetic moment due to the application of magnetic field. In the absence of magnetic field, the magnetic moments are randomly oriented in such a way that the net magnetic moment is zero. Due to the application of magnetic field, the magnetic moments tend to align along the field direction. However, the thermal agitation disturbs their complete alignment along the field direction. Therefore, a partial alignment of moments along the field direction is possible and results in a small positive magnetization or susceptibility. The degree of alignment depends on both temperature (*T*) and applied magnetic field (*H*). By increasing, the applied field or decreasing the temperature, the degree of alignment can be increased and this leads to net increase in magnetic moment. Thus, the magnetization of PM material is directly proportional to *H/T*.

The PM susceptibility or Langevin paramagnetism as per the classical approach can be represented as;

$$\chi = \frac{\mu_0 N \mu^2}{3k_B T} \qquad (1.6)$$

where *N* denotes the number of magnetic dipoles (magnetic ions) per unit volume each having a magnetic moment of μ. The equation (1.6) signifies that the magnetic susceptibility is inversely proportional to the temperature and is known as Curie law [27].

Further, the quantum mechanical approach of PM susceptibility can be represented as;

$$\chi = \frac{N\mu_0 g^2 \mu_B^2 J(J+1)}{3k_B T} \tag{1.7}$$

where g is the Lande g factor and can be defined as;

$$g = \frac{3}{2} + \frac{S(S+1)-L(L+1)}{2J(J+1)} \tag{1.8}$$

Here L, S and J denote orbital, spin and total angular quantum number of the magnetic elements respectively. N is the number of dipoles per unit volume and μ_0 is the permeability of free space. The examples of paramagnetic materials are some salts and oxides of rare earth *etc*. [13, 26]. There is another class of paramagnetism known as Pauli's paramagnetism, where susceptibility is relatively small and temperature independent [13].

1.3.3 Ferromagnetism

Ferromagnetism (FM) is the basic mechanism of a material that exhibits a non-zero value of magnetic susceptibility even without the application of any magnetic field. According to Weiss molecular field theory [26], the presence of strong exchange force (molecular field) gives rise to the parallel alignment of magnetic moments in a region called magnetic domain and that exhibits spontaneous magnetization within the domain even in the absence of an external magnetic field. When the magnetic field is applied, all the domains align along the field direction and results in a large value of positive susceptibility. However, after the removal of magnetic field, such alignment persists up to certain extent inside the material and that gives rise to magnetic hysteresis [26].

In general, the FM behavior is observed below the transition temperature T_c. For $T > T_c$, they behave mostly like a paramagnet having susceptibility;

$$\chi = \frac{C}{T - \theta_c} \tag{1.9}$$

where C and θ_c are Curie constant and Curie temperature respectively. This equation is called the Curie-Weiss law. Here $C = \mu_0 N g^2 \mu_B^2 J(J+1)/3k_B$ or $\mu_0 N \mu^2/3k_B$, where μ is the magnetic moment of each dipole. Fe, Co, Ni are some of the known FM materials with typical θ_c values of 1043 K, 1394 K and 631 K respectively [27].

1.3.4 Antiferromagnetism

The Antiferromagnetism (AFM) corresponds to the antiparallel alignment of magnetic moments in such a way that the resultant magnetic moment is zero. The above behavior is observed below certain temperature called N*é*el temperature (T_N) and above that, mostly it behaves like a paramagnet. With the application of magnetic field, they tend to exhibit a small positive susceptibility. The magnetic susceptibility of AFM substance in the paramagnetic region ($T > T_N$) can be explained as;

$$\chi = \frac{C}{T + T_N} \tag{1.10}$$

Some of the examples of AFM materials are FeO, CoO, MnO, MnF_2, Cr_2O_3, α-Fe_2O_3 having N*é*el temperature of 116 K, 292 K, 116 K, 67 K, 307 K and 950 K [13].

1.3.5 Ferrimagnetism

Ferrimagnetism (FIM) is a special case of antiferromagnetism where the magnitude of magnetic moments differ in different sublattices and thereby lead to net non-zero magnetic moment even though they are antiparallel. In ferrimagnetic materials, the sublattices are crystallographically different and hence the molecular field is different at different sublattices. Some of the examples of FIM materials are garnets like $Y_3Fe_5O_{12}$, spinels like $NiCr_2O_4$, $CoFe_2O_4$ *etc*., and hexagonal ferrites such as $BaFe_{12}O_{19}$, $Ba_2Co_2Fe_{12}O_{22}$ *etc*.

1.4 Magnetic Anisotropy

The change in magnetic properties with respect to crystallographic directions, magnetic field directions with respect to macroscopic dimensions *etc*. is generally known as magnetic anisotropy. The domain magnetization present in the sample tends to align itself along a preferred crystallographic axis due to energetically favorable condition and such direction is known as easy axis. The magnitude and type of magnetic anisotropy have a large influence on the shape of magnetic hysteresis loop, remanent magnetization, coercivity, saturation magnetization *etc*. Some of the important types of anisotropies are discussed as follows;

i. Crystal anisotropy or Magnetocrystalline anisotropy
ii. Shape anisotropy

iii. Stress anisotropy

1.4.1 Magnetocrystalline Anisotropy

The tendency of magnetization to align itself along a particular crystallographic direction is known as magnetocrystalline anisotropy. In most of the magnetic materials, the magnetic properties are not isotropic with respect to crystallographic orientations. With the application of magnetic field along an easy direction, one can easily determine the complete saturation values. However, in certain materials, it is very difficult to saturate to the magnetization along a particular crystallographic direction and such direction is called hard axis. Magnetocrystalline anisotropy always keeps the magnetization in certain equivalent directions in a crystal. Materials having high anisotropy possess high value of coercivity i.e. hard to demagnetize and such materials are called hard materials. Similarly, materials having low magnetic anisotropy corresponds to low value of coercivity and they are called soft materials. The magnetocrystalline anisotropy energy is smaller as compared to that of exchange interaction. The energy associated in the crystal possessing magnetization orientation away from the easy axis is defined as [14, 28];

$$E_{ans} = K_0 + K_1(\alpha_1^2\alpha_2^2 + \alpha_2^2\alpha_3^2 + \alpha_3^2\alpha_1^2) + K_2(\alpha_1^2\alpha_2^2\alpha_3^2) + \cdots \quad (1.11)$$

where K_0, $K_1$and K_2 represent the constants for a particular crystal at particular temperatures and α_1, α_2 and α_3 are the respective direction cosines of the magnetization with respect to *a*, *b* and *c* crystallographic axes. If K_2 is zero, the sign of K_1will give rise to the direction of easy magnetization. If K_1 is positive, then $E_{100} < E_{110} < E_{111}$ and it corresponds to $< 100 >$ as the easy axis. This type of property is observed in iron, cubic ferrite containing cobalt *etc*. If K_1 is negative, then $E_{111} < E_{110} < E_{100}$ and the easy axis is $< 111 >$ as observed in nickel, cubic ferrite *etc*. if K_2 is not zero, then the direction of easy magnetization axis is determined by both K_1 and K_2 [14].

In certain cases, the anisotropy of the magnetic particle associated with the single crystallographic axis (easy axis) is known as uniaxial anisotropy. Such anisotropy energy then becomes the function of an angle θ, which is the angle between the magnetization vector and the *c*-axis. This anisotropy energy can be expressed as;

$$E_{ans} = K_0 + K_1 sin^2\theta + K_2 sin^4\theta + \cdots \quad (1.12)$$

Here E_{ans} will be minimum for $\theta = 0$ only when K_1 and K_2 have positive values that means the magnetization is lying along the easy axis and the *c*-axis is the easy axis of magnetization. Some of the examples belong to these categories are barium hexaferrites, cobalt and many rare earth metallic and intermetallic compounds. Further, if both K_1 and K_2 have negative values, then the E_{ans} will be minimum for $\theta = 90°$. Such situation leads to an easy plane of magnetization and such easy plane in the hexagonal materials is the basal plane lying perpendicular to the *c*-axis. The anisotropy energy is larger for low symmetry crystals. Some of the examples like cubic Fe and Ni have $K_1 = 4.8\times10^4$ Jm^{-3} and -5.7×10^3 Jm^{-3} respectively while hexagonal Co has $K_1 = 5\times10^5$ Jm^{-3} [14]. As the temperature is increased, the magnitude of crystal anisotropy decreases sharply and it vanishes at Curie temperature. The magnetic anisotropy provides the enhanced coercive field [13]. The ferrites having hexagonal structure exhibit two types of anisotropy such as *c*-axis and *c*-plane anisotropy. In the hexagonal family, only the Y-type hexaferrites have *c*-plane anisotropy and others have *c*-axis anisotropy.

The physical origin of magnetocrystalline anisotropy in a magnetic material arises due to the spin – orbit coupling of electrons [28]. Electrons in a crystal undergoes four different types of couplings namely; spin – spin coupling, spin – lattice coupling, orbit – lattice coupling and spin – orbit coupling. The spin – spin coupling is very strong, which forces the neighboring spins to be either parallel or antiparallel to each other. The interaction energy associated with this is isotropic which depends upon the angle between the spins rather than crystallographic orientations. The orbital magnetic moments of electrons in FM materials are mostly quenched and thus the orientations of the orbits are fixed with the crystal lattice. As a result, the orbit – lattice coupling is very strong and these couplings can't be changed by the application of large magnetic field. The spin – orbit coupling is relatively weak. When an external magnetic field is applied, the spin and orbital moments of an electron try to align along the field direction. However, due to strong coupling of orbits with the lattice, it resists the spin axis to rotate. The spin – orbit coupling in most of the materials is very weak compared to the exchange interaction and it is quite strong in rare-earth systems [28].

1.4.2 Shape Anisotropy

The shape of polycrystalline magnetic samples can produce magnetic anisotropy. If the sample is spherical in shape, the magnetization produced by an external magnetic field

is uniform in all directions. However, if the sample is not spherical in shape, it will be easier to magnetize the sample along the longer axis due to the small demagnetization factor compared to the shorter axis. This shape dependent mechanism is known as shape anisotropy. A magnetized material can itself create a magnetic field and is known as demagnetization field H_d. The H_d is related to the magnetization of the material as well as the shape and dimension dependent parameter known as demagnetization factor N_d as;

$$\overrightarrow{H_d} = -N_d\vec{M} \tag{1.13}$$

The addition of the demagnetization factors along three orthogonal axes of an ellipsoid is a constant as;

$$N_a + N_b + N_c = 1 \text{ (SI) } or\ 4\pi \text{ (cgs)} \tag{1.14}$$

All the three demagnetization factors are equal for the spherical samples and thus $N_{sphere} = 4\pi/3$ (cgs) or 1/3 (SI). The energy associated with demagnetization field is known as magnetostatic energy (E_{ms}) and can be expressed in the unit of J/m^3 as;

$$E_{ms} = \frac{1}{2}\mu_0 N_d M^2 \tag{1.15}$$

1.4.3 Stress Anisotropy

The domain structure of a material can be changed due to stress by creating one or more easy axis of magnetization. Thus, if stress is present, the stress anisotropy must be considered along with other anisotropies. It is known as uniaxial anisotropy and the stress anisotropy or magnetoelastic energy can be defined as;

$$E_\sigma = K_\sigma sin^2\theta \tag{1.16}$$

Here K_σ is the stress anisotropy constant and θ represents the angle between magnetization and axis of stress. If K_σ is positive, the axis of stress behaves like easy axis while if K_σ is negative, it behaves like hard axis [13, 28].

1.5 Magnetic Permeability

Magnetic permeability is defined as the degree of magnetization achieved by a material obtained in response to an applied magnetic field. In general, the complex permeability ($\mu_r = \mu' + \mu''$) represents the dynamic magnetic properties of the material. The real part of complex permeability (μ') represents the magnetic energy storage

capability of material while the imaginary part (μ'') denotes the loss of magnetic energy of a material. For polycrystalline ferrites, the permeability spectra arises due to two different magnetization mechanisms such as; spin rotation and domain wall motion. The effect of spin rotational magnetization is determined from the density of the material and the domain wall motion is determined from the grain size [29]. If a material exhibits smaller grains with more grain boundaries then the movement of domain wall motion will be difficult and resulting to low value of permeability. Thus, the control of grain size, microstructure and sintering process are important parameters for obtaining a low loss material for various applications. Due to high magnetocrystalline anisotropy, hexaferrites are suitable candidates for very high frequency antenna applications [30]. Lee *et al* [30]; have shown that Co – Ti substituted BaM hexaferrite possesses high value of magnetic permeability with low magnetic loss and materials become magnetically soft with impurity substitution. Therefore, these are excellent magneto-dielectric materials for high frequency miniature antenna applications. Permeability is one of the most significant property of the material for high frequency applications.

1.6 Dielectric Properties

The dielectrics is a class of electrical insulators having lack of free charges but contain bound charges. With the application of the electric field, the bound charges form electric dipoles by slightly moving from their equilibrium positions and the following dipole moment can be determined in terms of dielectric polarization. For a linear, isotropic and uniform dielectric material, the polarization *P* depends on the strength of the electric field *E* as,

$$P = \varepsilon_0 \chi_e E \qquad (1.17)$$

where χ_e is the dielectric susceptibility that depends upon all polarization mechanisms as well as the frequency of applied electric field and ε_0 is the permittivity of free space. For linear dielectrics, the relation between susceptibility and relative permittivity can be written as;

$$\chi_e = \varepsilon_r - 1 \qquad (1.18)$$

The relative permittivity (ε_r) is defined as the ratio of permittivity of the dielectric material to the permittivity of free space (ε_0). It is the measure of storage capacity of a dielectric material under the application of an electric field.

In general, the polarization is classified into four categories such as (a) Electronic polarization, (b) Ionic polarization, (c) Orientation polarization and (d) Interfacial polarization. The displacement of an electron cloud from the positively charged nucleus in an atom due to the application of an electric field is known as electronic polarization. The relative displacement of cations and anions in opposite directions in an ionic material by the application of an electric field gives rise to ionic polarization. Generally, in the absence of an electric field, the dipoles are randomly oriented in dielectric materials. Under the application of an electric field, the dipoles tend to orient or align along the field direction and the polarization arising out of such type of dipoles is known as orientation/dipolar polarization, which dependents on temperature. Interfacial or space charge polarization occurs due to the interface of two phases within the material having different conductivity and permittivity. The different conductivity and permittivity value cause the accumulation of space charges at their interfaces due to the electric field and it gives rise to polarization called interfacial polarization.

Depending on these polarization mechanisms, the dielectric properties of the materials are quantified in terms of few complex parameters and are discussed briefly in the following sections.

1.6.1 Complex Electric Impedance

In 1886, Oliver Heaviside first coined the concept of complex electric impedance (Z^*) and later it was developed by Kennelly and Steinmetz [31]. The resistance offered to the AC current in a system is termed as Electric impedance and it is defined in terms of Ohm's law:

$$Z^*(\omega) = Z' - jZ'' = \frac{V^*(\omega)}{I^*(\omega)} \qquad (1.19)$$

where Z' and Z'' represent the real and imaginary part of complex impedance respectively. $V^*(\omega)$ and $I^*(\omega)$ are the voltage and current through the dielectric material. For an ideal dielectric, Z' = 0. Thus the net impedance is capacitive and is defined as $Z^*(\omega) = j/\omega C$, where ω is the angular frequency and C is the capacitance.

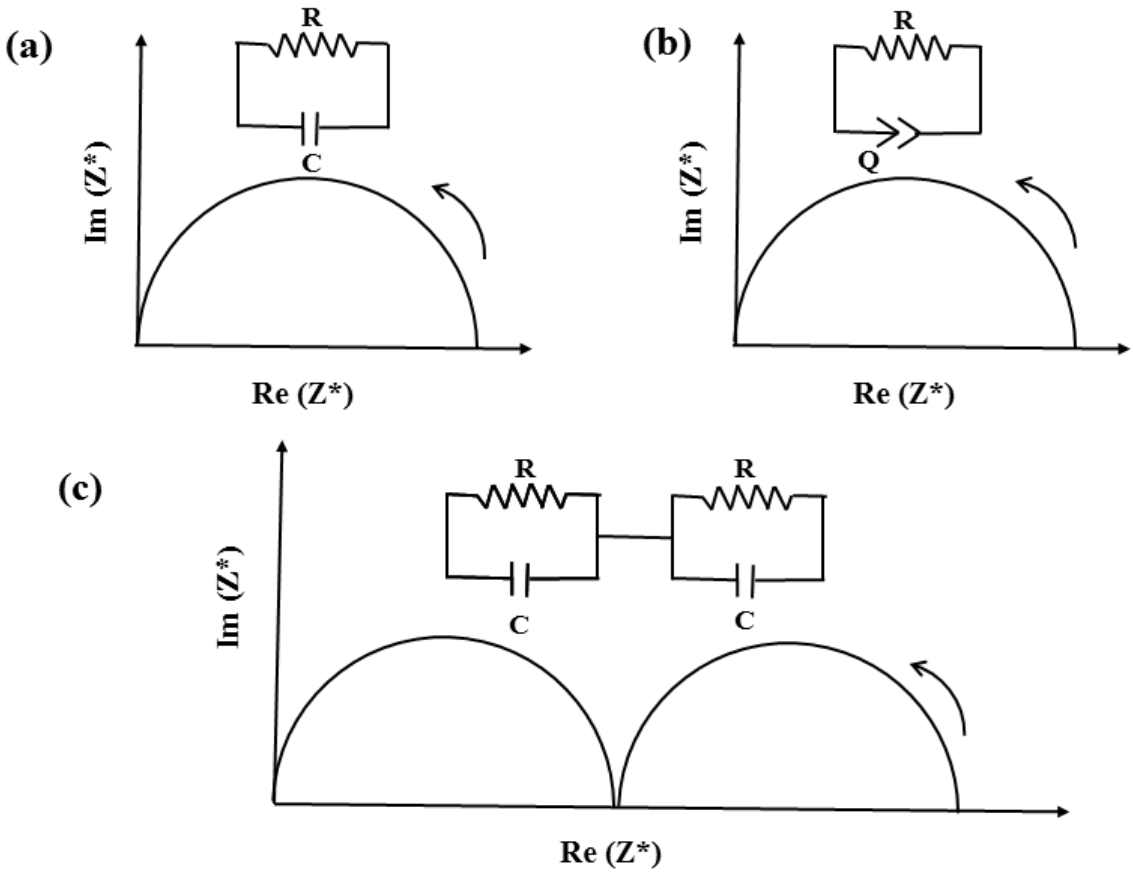

Figure 1.7: Nyquist (Im(Z^*) vs Re(Z^*)) plots for various electrical circuits.

The complex impedance plane (Z^*) i.e. Im(Z^*) versus Re(Z^*) plots is known as Nyquist plot [31]. For example, the parallel combination of *R* and *C* components of a sample in the Nyquist plot always gives rise to a semicircular arc with its centre lying on the Z' axis as shown in Fig. 1.7. From the above plot, the diameter of the semicircular arc provides the resistance value. A perfect semicircle i.e. no distortion/ depression in the arc can be expected only for an ideal *R* and *C* elements. However, such ideal *R* and *C* elements is not observed in reality. As a result, a depressed semicircle having distorted shape is observed where its centre lies below the Z' axis as shown in Fig. 1.7(b). The polycrystalline samples are generally composed of grains separated by thin grain boundaries. As compared to grain boundaries, grains are more conductive and less capacitive. Therefore, if the grains and grain boundaries have large difference in time constants ($\tau = 1/RC$) then the polycrystalline sample will exhibit two distinct semicircles in the Nyquist plots as shown in Fig. 1.7(c). In Nyquist plots, the semicircle in the low frequency region (higher Z') is due to the grain boundaries contributions whereas the semicircle at high frequency region (low Z') is due to the grains contributions. One can easily estimate the resistance of grains

and grain boundaries from the diameter of the respective semicircles. The depressed and/or distorted nature of the semicircle signifies the departure of relaxation process from the ideal Debye like behavior. The departure from the ideal behaviour leads to the departure of certain elements from its original behaviour and that is represented by a factor known as Constant Phase Element (*CPE*, denoted by *Q*). The impedance of such *CPE* can be expressed as;

$$Z_{CPE} = 1/A(j\omega)^n \tag{1.20}$$

where A is a constant and n is the relaxation time distribution factor such that $0 \leq n \leq 1$. When n = 1, the *CPE* behaves like an ideal capacitor and for n = 0, it behaves like an ideal resistor.

1.6.2 Complex Dielectric Constant

The complex dielectric constant (ε^*) of a material is defined as;

$$\varepsilon^* = \varepsilon' - \varepsilon'' = \frac{1}{j\omega C_0 Z^*} \tag{1.21}$$

$$\varepsilon' = -\frac{Z''}{\omega C_0 (Z'^2 + Z''^2)} \tag{1.22}$$

$$\varepsilon'' = \frac{Z'}{\omega C_0 (Z'^2 + Z''^2)} \tag{1.23}$$

where ε' and ε'' denote the real and imaginary parts of complex permittivity, ω is the angular frequency and C_0 is the geometrical capacitance.

When a dielectric material is placed in an AC electric field, the dipoles do not respond to the electric field immediately. Thus, the polarization takes certain time to reach its equilibrium and this is known as dielectric relaxation. The relaxation mechanism inside the dielectric materials are derived in terms of generalized Havriliak – Negami equation as [32];

$$\varepsilon^* = \varepsilon' - j\varepsilon'' = \varepsilon_\infty + \frac{\varepsilon_s - \varepsilon_\infty}{[1+(j\omega\tau)^{1-\alpha}]^\beta} \tag{1.24}$$

where ε_∞ denotes the permittivity at high frequency, ε_s is the static, low frequency permittivity and τ is the most probable relaxation time. The difference between ε_s and ε_∞ i.e. $\varepsilon_s - \varepsilon_\infty$ provides the dielectric strength. The parameters α ($0 \leq \alpha \leq 1$) and β ($0 \leq \beta \leq 1$) determine the broadness and asymmetry of the corresponding spectra respectively.

If $\alpha = 0$, $\beta = 1$, then it corresponds to the ideal Debye like relaxation behavior having single relaxation time. Any deviation from these values, the relaxation will be broader with distribution of relaxation time. If $\alpha = 0$ and $0 \leq \beta \leq 1$, then it represents Cole – Davidson (CD) relaxation model while for $0 \leq \alpha \leq 1$, the relaxation mechanism can be understood by using Cole – Cole (CC) model. The relation between relaxation time τ and the time (τ_{max}) corresponding to maximum value of ε'' can be written as [33];

$$\tau_{max} = \tau \left[\frac{sin\frac{\pi(1-\alpha)\beta}{2(1+\beta)}}{sin\frac{\pi(1-\alpha)}{2(1+\beta)}} \right]^{\frac{1}{1-\alpha}} \quad (1.25)$$

1.6.3 Complex Electric Modulus

Complex electric modulus is another class of parameter used for the understanding of dielectric properties of the materials in detail. The concept of electric modulus arises, when the reciprocal of complex dielectric permittivity is thought to be analogous to that of mechanical shear modulus [34]. Electric modulus is an important parameter for the dielectric materials having mobile charges and it can be defined as;

$$M^* = M' + jM'' = \frac{1}{\varepsilon^*} = \frac{\varepsilon'}{\varepsilon'^2 + \varepsilon''^2} + j\frac{\varepsilon''}{\varepsilon'^2 + \varepsilon''^2} \quad (1.26)$$

The electric modulus provides the relaxation of the electric field in the material having constant electric displacement [35]. In addition to that, the dynamical process of electron transport phenomena can be understood from the complex electric modulus as it surpasses the electrode polarization and apparent conductivity [36]. Mathematically, M^* can be derived from the relaxation of Kohlrausch – Williams – Watts (KWW) decay function $\varphi\ (t)$ as [37, 38];

$$M^*(\omega) = M_\infty \left[1 - \int_0^\infty e^{-j\omega t} \frac{d\varphi(t)}{dt} dt \right] \quad (1.27)$$

The KWW function is defined as [39, 40];

$$\varphi(t) = exp\left[-(t/\tau)^{\beta_{KWW}} \right],\ 0 \leq \beta_{KWW} \leq 1 \quad (1.28)$$

where τ is the relaxation time and β_{KWW} is the stretching parameter. The above two equations (1.27) and (1.28) are in time domain. In the frequency domain, the M'' data as a function of frequency can be derived in terms of the four-parameter formula for generalized susceptibility χ'' (where χ'' can be replaced with M'', ε'' or Z'') by Bergman as [41];

$$\chi''(\omega) = \frac{\chi''_{max}(\omega)}{\left(\frac{1-|q-p|}{q+p}\right)\left[p\left(\frac{\omega}{\omega_{max}}\right)^{-q}+q\left(\frac{\omega}{\omega_{max}}\right)^{p}\right]+(|q-p|)} \quad (1.29)$$

where χ''_{max} represents the imaginary part of complex susceptibility (χ'') at peak maxima and ω_{max} is the respective peak frequency. The parameters p ($0 < p < 1$) and q ($0 < q < 1$) are the stretching parameters at low (below maximum peak) and high (above maximum peak) frequency regions respectively.

1.6.4 Complex AC Conductivity

The AC conductivity (σ^*) of a material can be expressed as [31];

$$\sigma^*(\omega) = \sigma' + j\sigma'' = j\omega\varepsilon_0\varepsilon^* \quad (1.30)$$

The real and imaginary parts of the conductivity can be derived from the above equation as;

$$\sigma'(\omega) = \omega\varepsilon_0\varepsilon'' \quad (1.31)$$

$$\sigma''(\omega) = \omega\varepsilon_0\varepsilon' \quad (1.32)$$

The frequency variation of $\sigma'(\omega)$ can be expressed in terms of Jonscher's power law as [42];

$$\sigma'(\omega) = \sigma(0) + A\omega^n \quad (1.33)$$

where $\sigma(0)$ denotes the limiting zero frequency conductivity, A is the pre-exponential factor and n ($0 \leq n \leq 1$) is the frequency exponent term. As per equations (1.31) and (1.33);

$$\varepsilon'' \propto \omega^{n-1} \quad (1.34)$$

This behavior is commonly known as universal dielectric response (UDR) [42].

1.7 Literature Review on Hexaferrites

Hexaferrites having magnetoplumbite structure was first discovered in Philips Laboratory in 1950s. These hexaferrites continue to be amazing materials with very interesting magnetic and dielectric properties. As discussed in the above section 1.1, the *S* – block is composed of two layers of four oxygen atoms with three cations between each layer in octahedral and tetrahedral sites having opposite magnetic spins. In *S* – block, there are four octahedral sites and two tetrahedral sites. The four magnetic cations having spin

up (↑) moments occupy at octahedral sites, while two magnetic cations having spin down (↓) moments occupy at tetrahedral sites. The two spin up magnetic moments of cations at octahedral sites are compensated with two spin down moments of cations at tetrahedral sites. As a result, the net magnetic moment in *S* – block arises due to the presence of two spin up magnetic cations at octahedral sites. Further, the *R* – block consists of six spin up cations out of which five spin up cations occupy at octahedral sites and a spin up cation at trigonal bi-pyramidal site. However, in barium based hexaferrites, the presence of large size Ba^{2+} ion creates an asymmetry among the cations in *R* – block and that leads to distorting two spin up cations to spin down state at octahedral sites which oppose the remaining three spin up magnetic cations. Therefore, the net magnetic moment in *R* – block is due to the presence of one spin up cation at octahedral site and one spin up cation at trigonal bipyramedal site. Similarly, the *T* – block consists of six octahedral and two tetrahedral sites. The six octahedral sites are occupied by four spin up cations and two spin down cations, whereas the two tetrahedral sites are occupied by two spin down cations. Therefore, the cations occupying in *T* – blocks are compensated with each other and they possess net zero magnetic moment. The brief representation of net moments along with their different crystallographic sites of magnetic cations at different blocks of hexaferrites are given below.

S – block = 4 ↑ octahedral + 2 ↓ tetrahedral = 2 ↑

R – block = 3 ↑ 2 ↓ octahedral + 1 ↑ trigonal bi-pyramidal = 2 ↑

T – block = 4 ↑ 2 ↓ octahedral + 2 ↓ tetrahedral = 0

In the M-type barium hexaferrite, the magnetic moment of Fe^{3+} ions in 12k, 2a and 2b sites are aligned parallel to the crystallographic *c*-axis while those at $4f_1$ and $4f_2$ sites are aligned in opposite directions. By considering the magnetic moment of 5 μ_B per Fe^{3+} ion at 0 K, the net magnetic moment of BaM is found to be 20 μ_B per formula unit as derived from equation 1.1. Similarly, the net magnetic moment in Y-type BaM hexaferrite can be estimated by using the following concept. However, there are certain essential factors like composition and temperature that can affect the net magnetic moment of a material. Since the opposing spins of *T* block are antiferromagnetic, the Y-type ferrites generally exhibit lower saturation magnetization due to the antiparallel arrangement of *T* – block.

M-type = 1 ↑ trigonal bi-pyramidal + 7 ↑ 2 ↓ octahedral + 2 ↓ tetrahedral

Y-type = 8 ↑ 2 ↓ octahedral + 4 ↓ tetrahedral

Further, magnetic ordering temperature, saturation magnetization, coercivity, and permeability are the important magnetic properties of a material. In order to understand the importance of M- and Y- type hexaferrites along with their various magnetic and physical properties, some of the earlier works based on these hexaferrites are reviewed in this section.

1.7.1 Review on M-type Hexaferrite

BaM hexaferrite is a hard magnetic material with the coercivity value of 2000 – 3200 Oe. It is one of the cheapest material with high value of electrical resistivity in the order of 10^8 Ω cm. The high electrical resistivity and low magnetic loss in these materials play a major role in applications such as circulators, isolators, inductors, filters and phase shifters [43]. The presence of high uniaxial magnetic anisotropy, high coercivity value, excellent chemical stability, self-biasing nature, low eddy current loss, low microwave losses and magnetoelectric coupling in BaM hexaferrites make these compounds a natural choice for the applications in permanent magnet, magnetic recordings and multi-state memory devices [9, 44-47]. The materials exhibiting magneto-dielectric properties can be used for magneto-optical and microwave devices applications. However, the substitution of suitable cations may modify the electrical and magneto-dielectric properties and that stipulate their applications in various devices. As compared to spinel ferrites, the BaM hexaferrite along with certain doped materials have large permeability and high resonance frequency. As a result, these materials can be used as chip inductors and microwave absorbers in the GHz range. Thus, to make use of these materials for specific applications, suitable cationic substitution is the most relevant way to enhance their functional properties.

To improve the fundamental magnetic and dielectric properties of BaM hexaferrites, many researches have been carried out on various cationic substitutions. Since the dielectric behavior of a material gives rise to valuable information regarding the localized charge carriers and conduction mechanism, thus the electrical properties of hexaferrites depend on the type of cationic substitutions. Substitution of Ba by using other elements such as Sr, Ca, Pb, La has been reported [44, 46-48]. An increase in saturation magnetization is reported upon La substitution at Fe site [46]. An unusual mechanism of electric polarization based on the displacement of Fe ion is reported in Sr substituted BaM [48]. Several authors have carried out the substitution at Fe^{3+} site by using either transition elements such as Cr, Mn, Co, *etc.* [49-51], or the co-substitution of various cations such as

Co – Ti [9], Co – Zr [52], Ni – Zr [53], Ni – Ti [54], and Cu – Zr [47], *etc*. The lower saturation magnetization (M_s) and increased coercivity (H_c) values are reported in the Cr and Mn substituted BaM hexaferrites [49, 51]. However, the Ni – Ti substituted BaM hexaferrite exhibits reverse behavior i.e. the M_s value increases with decrease in H_c values and such type of material can be useful for applications in the perpendicular magnetic recording media [54]. Further, the substitution of Ni^{2+} and Zr^{4+} in M-type hexaferrite causes the expansion of crystal lattice along the *c*-axis [53]. With increase in Ni and Zr concentration, the H_c value decreases while M_s value increases. The dielectric constant and the loss tangent values decrease with increase in Ni – Zr concentrations suggesting that they are suitable for microwave applications [53]. The $BaFe_{12-2x}(CoTi)_xO_{19}$ samples sintered at 1100 – 1200 ℃ show a significant dispersion in complex permittivity and permeability values [55]. Moreover, the Co – Ti substituted nanoparticles show irreversibility between zero field cooled and field cooled magnetization curves below the room temperature and it disappears above the room temperature [9]. Guan *et al*., [56] have reported that $BaCo_xTi_xFe_{12-2x}O_{19}$ is a suitable candidate for room temperature magnetoelectric material. The doping of Co – Ti in BaM hexaferrite induces the complicated cycloidal spin ordering and significantly increases the resistivity values. Further, the M_s and H_c values are reported to be decreased with doping of both non-magnetic Mg – Ti ions at Fe sites in BaM hexaferrite [3]. The Curie temperature is found to decrease with increase in Mg – Ti concentration due to the decrease in inter sublattice exchange interactions. The dielectric properties of these doped samples were analyzed based on the hopping mechanism between Fe^{2+} and Fe^{3+} ions. Wang *et al*., [57] have prepared the Al substituted BaM hexaferrite ($BaFe_{10}Al_2O_{19}$) by mechanical alloying process with subsequent heat treatment. It is found that the coercivity value (H_c) increases significantly to 9.3 kOe while its saturation magnetization decreases drastically. The substitution of Al^{3+} for Fe^{3+} ion has a large influence on its complex permittivity and permeability values. As the Al^{3+} concentration increases, the real part of complex permittivity increases while the peaks in the complex permeability shifts towards the higher frequency range [58]. This behaviour indicates that the preferential site occupation of Al^{3+} ion modifies the magnetocrystalline anisotropy of BaM hexaferrites.

1.7.2 Review on Y-type Hexaferrite

The Y-type hexaferrites are the most relevant materials used for various applications for many years. The Y-type hexaferrite possesses high dielectric constants,

low AC electrical conductivity and low dielectric loss that make them suitable for microwave applications and chip components. It is worth noting that most of the hexaferrites are hard magnetic materials; however, the presence of low coercivity and high permeability values make these Y-type hexaferrites soft ferrimagnetic in nature. Further, these ferrites provide high saturation magnetization and the cut-off frequency are very much higher than that of spinel ferrites and garnets. Therefore, these materials are the natural choice for high frequency and ultra-high frequency applications.

Recently, the hexaferrites with helical spin order is one of the exciting material for high temperature multiferroics [59]. In 2005, the magnetoelectric (ME) effect was first investigated in Y-type hexaferrites [60]. After that, the hexaferrites have attracted an enormous research interest due to their high temperature ME effect. There are certain Y-type hexaferrites like; $Ba_2Mg_2Fe_{12}O_{22}$ and $(Ba, Sr)_2Ni_2Fe_{12}O_{22}$, whose spiral magnetic structures can be modified by the application of magnetic field and it results pronounced ME effect along with magnetically induced ferroelectricity. The ME effect can also be modified by magnetic or non-magnetic cationic substitutions. Kimura *et al*., have shown that, although the ferrimagnetic transition in Y-type hexaferrite ($Ba_{0.5}Sr_{1.5}Zn_2Fe_{12}O_{22}$) occurs above the room temperature, the magnetically induced polarization can be observed at low temperature around 130 K [60]. Ishiwata *et al*., have shown that the Mg doped Y-type hexaferrite ($Ba_2Mg_2Fe_{12}O_{22}$) exhibits ME effect below 195 K [61]. The microscopic origin of magnetic field induced electric polarization has also observed in $Ba_2(Mg_{1-x}Zn_x)_2Fe_{12}O_{22}$ [62]. The substitution of Zn in $Ba_2Mg_2Fe_{12}O_{22}$ destabilizes the longitudinal conical spin state of the system. Subsequently, the magnetically induced polarization decreases due to change in magnetic-easy surface from conical to planar. With the application of magnetic field, the spin structure is transformed into transverse conical magnetic structure. Consequently, the electric polarization can be produced in the material based on the inverse Dzyaloshinskii – Moriya mechanism or spin current model [63, 64]. Thus, magnetic field induced ferroelectricity can be expected at room temperature in Y-type hexaferrites. In $Ba_{2-x}Sr_xCo_{2-y}Zn_yFe_{12}O_{22}$, the Zn^{2+} ion prefers to occupy at tetrahedral sites and it reduces the Neel temperature [65]. The substitution of Zn^{2+} and Sr^{2+} increases the M_s and H_c values. Haijun *et al*., [66] have reported that the ferroxplana Co_2Y and Zn_2Y hexaferrites are ideal materials for use at GHz frequency range and the substitution of Zn in $Ba_2Co_{2-z}Zn_zFe_{12}O_{22}$ modifies its microwave properties. The DC electrical conductivity, drift mobility and carrier concentration are found to be enhanced upon Zn substitution in

$Ba_2Ni_{2-x}Zn_xFe_{12}O_{22}$ [67]. Further, the Zn – Cu substitution leads to the lowering of sintering temperature of pure Co_2Y hexaferrites by providing high permeability and high cut-off frequency values [68]. Ali *et al*., have shown that the substitution of Eu – Ni in Y-type hexaferrite leads to significant enhancement in grain boundary resistance as compared to grain resistance with appreciable improved value of quality factors [69]. The substitution of Mg and Ni at Co site reduces the saturation magnetization and remnant magnetization of Y-type hexaferrite [70]. In addition, the particle size is decreased upon Mg and Ni substitution and results in increase in H_c values. Elahi *et al*., [71] have shown that, in $Sr_2Ni_{2-x}Mg_xFe_{12}O_{22}$, the Mg substitution provides homogenous microstructure, high value of electrical resistivity with low coercivity values and that can be useful for various multilayer chip inductor and multilayer chip beads applications.

1.8 Motivations of Present Thesis Work

As per the literature summary, it was found that the M- and Y- type hexaferrites are the multiferroic materials possessing interesting magnetic and dielectric properties. Among the Hexagonal family, M-type barium hexaferrites have the uniaxial anisotropy and are magnetically hard materials. However, the Y-type hexaferrites are the ferroxplana ferrites having high value of magnetic permeability and these are magnetically soft materials useful for electrical device applications. Since these are multiferroic materials, any improvement on magnetic, dielectric and electrical properties will provide a huge advantages for various applications. Although, there are various reports on doping of cations at Fe site in M-type hexaferrites, but systematic study of dielectric, electrical and magnetic properties of Ni, Ti and Al doped M-type hexaferrites are still lacking. The substitution of both magnetic and non-magnetic cations with different oxidation states (Ni^{2+}, Al^{3+}, and Ti^{4+}) at Fe site are found to have large influence on its magnetic and dielectric properties. As reviewed in the previous sections, several reports are available on magnetic and dielectric properties of Y-type hexaferrite; however, the systematic analysis of the effect of substitution at Co site in Y-type hexaferrites are still limited. The substitution of these cations are found to modify the magnetic and electrical properties such as the saturation magnetization, magnetocrystalline anisotropy, magnetic ordering temperature, permittivity and permeability of the materials for specific applications. Won *et al*., [72] have reported that the magnetic ordering temperature has a large importance in understanding the magnetoelectric characteristics of the Y-type hexaferrites. The systematic investigation of

dielectric relaxation in terms of different microstructural effect in M- and Y- type hexaferrites along with appropriate doping is still lacking. In order to understand the different dielectric relaxation dynamics and appropriate doping driven magnetic properties of M- and Y- type hexaferrites, the following series of samples are chosen for the present thesis work:

1. M-type Barium Hexaferrite

i. $BaFe_{12-y}Ni_yO_{19}$ (y = 0 to 0.5)

ii. $BaFe_{12-y}Ti_yO_{19}$ (y = 0 to 0.8)

iii. $Ba(Fe_{1-x}Al_x)_{12}O_{19}$ (x = 0 to 0.10)

2. Y-type Barium Hexaferrite

i. $Ba_2(Co_{1-x}Zn_x)_2Fe_{12}O_{22}$ (x = 0 to 1.0)

ii. $Ba_2(Co_{1-x}Mg_x)_2Fe_{12}O_{22}$ (x = 0 to 0.5)

The above mentioned samples were characterized by using the following sophisticated instruments such as X-ray diffractometer (XRD), Raman Spectrometer, Field emission scanning electron microscope (FESEM), Energy dispersive X-ray spectrometer, Vibrating sample magnetometer (VSM), Impedance analyzer and LCR meter. In order to understand the crystal structure, XRD patterns of all these samples were recorded at room temperature by Rigaku make TTRAX III diffractometer. The morphological and compositional analysis were characterized by recording micrographs using FESEM equipped with EDX. To understand the magnetic properties of these samples, the temperature and field variation of dc magnetization were studied by using Lakeshore make VSM of model no. 7410. The permeability and dielectric data of these samples were obtained by using Impedance analyzer and LCR meter respectively. The method of preparation of the above samples and the working principles of these sophisticated instruments are briefly discussed in Chapter 2.

Chapter 2

Experimental Techniques

In order to understand various physical as well as functional properties of hexaferrite materials, various experimental facilities are required to extract the information about their crystal structure, microstructure, magnetic and dielectric properties. The analysis of such experimental data will provide a complete idea to construct high quality materials for numerous applications. The preparation of materials followed by different experimental techniques used in various physical measurements are briefly discussed in this chapter.

In the present thesis work, the samples were prepared by standard solid state route and the sol-gel method. To achieve the required single-phase material with high density, the starting compounds were synthesized by using various furnaces. In this chapter, the technical details and the operating condition of furnaces are discussed. The phase purity and the crystal structure of the prepared samples were characterized by recording diffraction patterns using X-ray diffractometer (XRD). The effect of doping on crystal structure and its lattice parameters were obtained from the analysis of XRD patterns as per Rietveld refinement technique using the FULLPROF program. The presence of disorders in the crystal structure of the samples were analyzed at room temperature by recording Raman spectra using micro-Raman spectrometer. The microstructure and the compositional analysis of the samples were studied by using field emission scanning electron microscope (FESEM) equipped with energy dispersive X-ray spectrometer (EDX). Temperature and field variations of magnetization measurements were carried out by using vibrating sample magnetometer (VSM). The fundamental working principles of VSM is also discussed in this chapter. The complex permeability spectra were measured at room temperature by using RF Impedance/Material analyzer. The frequency variations of complex impedance data were recorded at different temperatures by using an LCR meter.

2.1 Sample Preparation

The polycrystalline oxide samples were prepared by most widely used standard solid state reaction route and sol-gel methods. Although the desired phase formation is thermodynamically favored, due to the lack of diffusion of constituent elements, the solids do not react together at ambient temperature over laboratory time scales and hence heat treatment at higher temperature is required to overcome the kinetic barriers. Initially, the powders of stoichiometric ratio of constituent oxides and/or carbonates are often pressed into cylindrical pellets followed by heating at high temperature to increase the good contact between the particles. Since the reaction time for the formation of the samples are usually several days thus, it is necessary to repeat the above process to get good homogeneity. The starting materials are generally single cation oxides, carbonates, nitrates or hydroxides, which decompose to form the oxides under heat treatment. The initial stage of heat treatment i.e. presintering of carbonates or oxide mixtures produce carbon dioxides and it escapes from the solid. Therefore, an additional heat treatment is required to produce the dense materials.

Sol-gel is another chemical reaction process where the molecular scale mixing of reactants can be obtained at relatively low temperatures. In such process, the nitrates or acetates of cationic materials are dispersed in a solvent and then the solvents are converted into gel form through the hydrolysis polymerization reaction process. The heat treatment of gel leads to combustion reaction and results in the fine dry powders in nano-metric scale. The sol-gel process has certain advantages over the solid state route as: (i) the mixing of the starting compounds at molecular level is possible in sol-gel process due to the dispersion of the constituent materials in a solvent, (ii) the homogeneous mixture of the doping materials can be achieved by incorporating the dopant at molecular level and (iii) the annealing temperature of the required samples is relatively small in sol-gel process compared to that of solid state route.

The samples were prepared by using the following compounds such as; barium carbonate (Ba_2CO_3), ferric oxide (Fe_2O_3), aluminium oxide (Al_2O_3), titanium oxide (TiO_2), cobalt oxide (Co_3O_4), zinc oxide (ZnO), magnesium oxide (MgO), barium nitrate $(BaNO_3)_2$, ferric nitrate $(Fe(NO_3)_3.9H_2O)$, nickel nitrate $(Ni(NO_3)_2.6H_2O)$ and ethylene glycol ($C_2H_6O_2$) with high purity (> 99%).

2.1.1 Solid State Reaction Route

The stoichiometric ratio of required compounds and/or materials were weighed using an electronic balance supplied by Mettler Toledo Model no: AG135 with an accuracy of $\pm$ 0.01 mg. The weighed compounds were ground thoroughly under the acetone medium using an agate mortar and pestle. The homogeneous mixture of these compounds was then transferred to the alumina crucible and calcined at different temperatures ranging from 400 ℃ to 800 ℃ for 12 h, followed by furnace cooling to room temperature. To get the homogeneous mixture, the calcined powder was ground repeatedly and then the homogeneous mixture of the calcined powder was pressed into cylindrical shape pellets using a 13 mm dia with a hydraulic press supplied by Techno Search Instruments, Thane, India with a maximum load of 2.94×10^8 N/m^2. With repeated intermediate grinding and repelletizing, the final sintering was carried out in pellet form in air with a step by step processes at different temperatures. Depending upon the nature of compositions, the final sintering was carried out at different temperatures and the details about the respective series of materials are discussed in chapters 3, 4, and 5 respectively.

2.1.2 Sol-gel Technique

In this process, the stoichiometric ratio of the starting compounds and/or elements are dissolved in either nitric acid or distilled water and then mixed together. In most of the cases, nitrates were used to prepare the solutions due to their solubility in water. The uniform mixture of the above solution was obtained by using magnetic stirrer with hot plate in the temperature range of 80 ℃ to 100 °C. Since citric acid is a chelating agent which can bind up metal ions and remove the non-metallic ions, therefore an excess amount of citric acid was added to the solution to convert them into citrates and proper amount of an ethylene glycol was added to the solution to convert into dense gel form. In order to ensure the good homogeneity, the resultant solution was stirred continuously for 4 – 6 hours and kept in the hot plate for several hours at constant temperature for complete evaporation of water and acid. Finally, a polymeric metal citrate gel was formed. To induce self-combustion, the product was then heated to 400 °C to decompose the remaining volatile components trapped inside the pores of the gel, organic reagents, *etc*., and thus precursor powder is obtained in a fine powder form. Depending on the nature of the material, the obtained precursor powder was presintered at 600 ℃ to 800 ℃ for 12 h with repeated grinding followed by final sintering in pellet form.

2.2 High Temperature Furnace

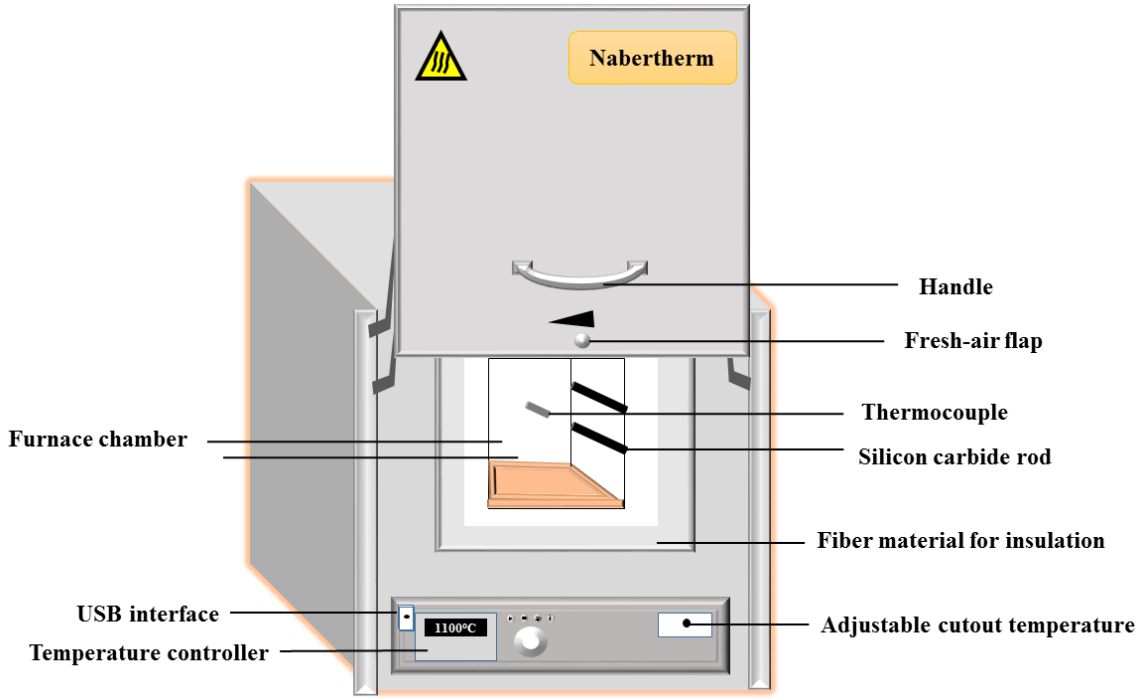

Figure 2.1: Overview of high temperature furnace with lift door (model no. HTCT 03/15).

The synthesis of the samples presented in this thesis work were carried out by using Nabertherm make commercial high temperature furnace with a maximum operating temperature of 1500 ℃. Fig. 2.1 illustrates the photograph of the commercial furnace. It is designed in lift door system (tabletop model) with model no. HTCT 03/15. The high temperature furnace is powered by a thyristor unit with a rating of 20.7 A. The furnace chamber was fabricated with the insulation from high quality non-classified fiber material having the inner dimensions of 12×12×21 cm^3. In addition, dual shell housing type chamber was modeled for low external temperatures and high stability with an adjustable air inlet to control the fresh air. The German made PID programmable temperature controller with model no. C440/C450 having 10 programs with 20 segments facility was used to control the temperature of the furnace. The Platinum based thermocouple was used as temperature sensor and four Silicon carbide (SiC) rods are used as heating elements inside the furnace. The temperature of the high temperature furnace can be controlled with an accuracy of ± 1 ℃.

2.3 X-Ray Diffraction

X-ray diffraction pattern is one of the important techniques used to understand the phase purity and crystal structure of the sample. In this technique, X-ray beam is incident on the powder sample, which contains the lattice planes separated by a distance of a few Angstroms unit and that is comparable to that of the wavelength of the monochromatic X-ray. Depending on the interplanar spacing and the inclination angle (θ), the scattered X-ray from the surfaces of several parallel lattice planes undergo constructive interference and they follow the Bragg's diffraction law as;

$$2d\ sin\theta = n\lambda \qquad (2.1)$$

Here d stands for the lattice spacing between two consecutive planes corresponding to particular miller indices (h, k, l), n is the order of the diffraction spectrum, θ is the glancing angle and λ represents the wavelength of incident X-ray beam [13]. When θ is changed, the maximum intensity peaks are observed due to exposer of different planes otherwise no peak is observed. The diffracted X-rays are detected by a detector. Thus, in this process, XRD patterns are obtained as a function of 2θ for all the possible (h, k, l) planes in the crystal. The Schematic ray diagram of Bragg's X-ray diffraction is shown in Fig. 2.2.

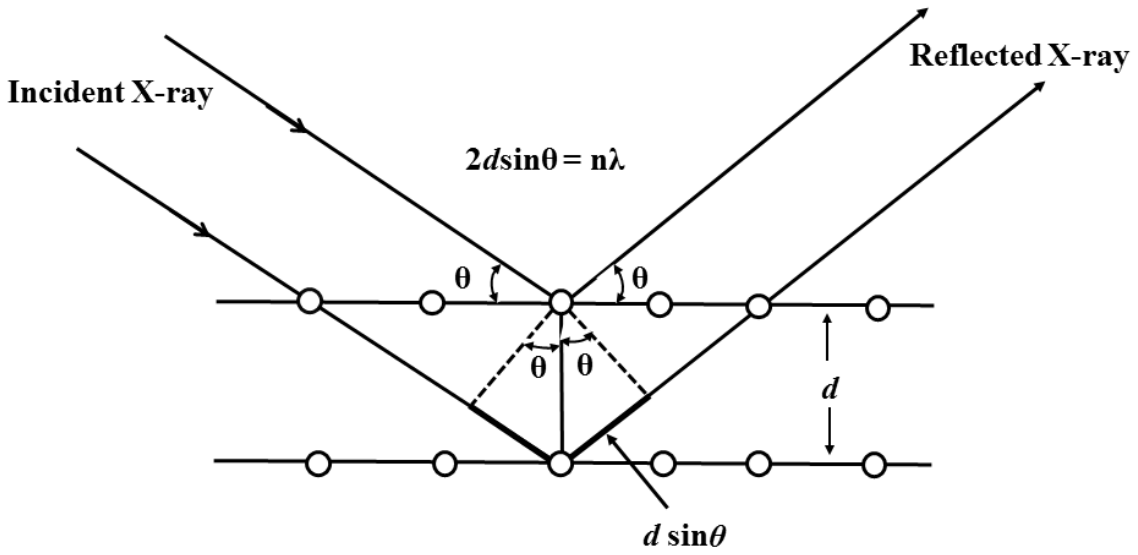

Figure 2.2: Schematic diagram of Bragg's X-ray diffraction.

The XRD patterns of the powder samples were recorded at room temperature with the help of Rigaku make TTRAX III (*Theta – Theta Rotating Anode X – Ray*) power diffractometer by employing CuK $_\alpha$ radiation of wavelength $\lambda = 1.5406$ Å. In the present

thesis work, the XRD patterns of all the samples were collected with a setting of 50 kV voltage and 180 mA tube current of X-ray generator. The ray diagram of the instrument which is based on Bragg – Brentano geometry are shown in Fig. 2.3. In this geometry, the X-ray source (F1) to sample distance and sample to detector (F2) distance are kept equal. So, the X-ray produced from the source and diffracted from any point on the sample by an angle 2θ will arrive exactly at the same point F2. In other words, the focusing is perfect in such geometry that the X-ray source, sample and detector remain in the plane of the circle. This circle is known as the focusing circle. The scanning was carried out from 20° to 80° in an usual $\theta - \theta$ scan during the data collection with a scan speed of 3 °/minute and a step size of 0.02°.

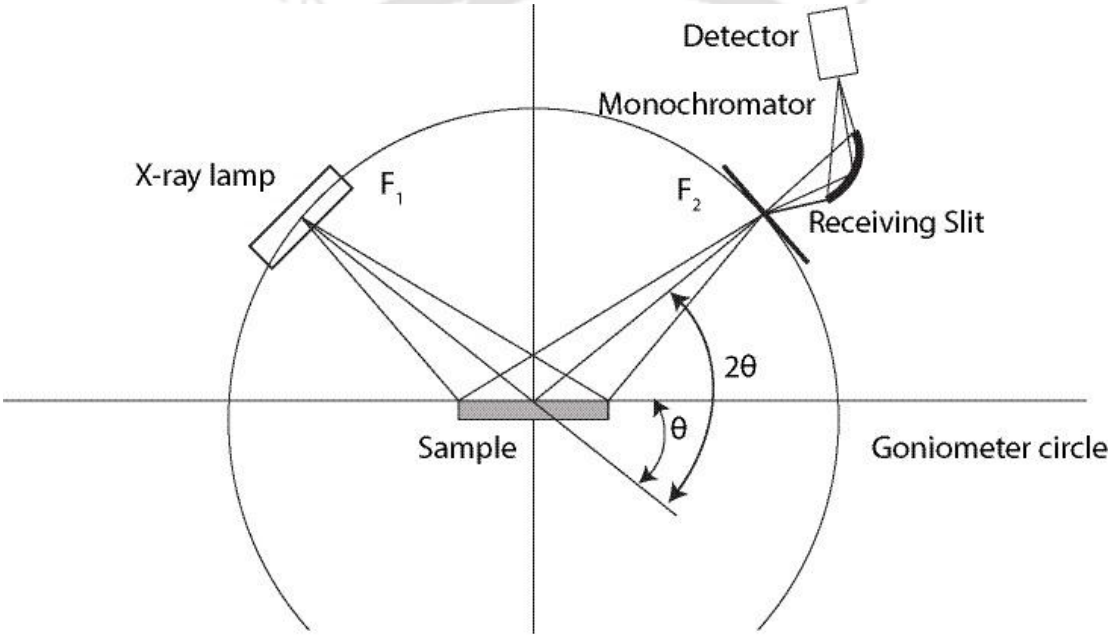

Figure 2.3: Ray diagram of X-ray diffractometer.

The XRD patterns of the samples were analyzed by the Rietveld refinement technique with the help of FullProf suite program [73]. The background was refined by selecting a polynomial function and the peak shape was fitted by considering the Pseudo-Voigt function. The global parameters, such as coefficients of background polynomial, scaling factor, half width parameters (*u*, *v*, *w*) and lattice parameters (*a*, *b*, *c*) were mainly varied during refinement. In addition to that nuclear structure variables such as fractional atomic coordinates (*x*, *y*, *z*), isotropic displacement parameters and occupancy values were

varied. Here, occupancy is the chemical occupancy normalized to the multiplicity of the general positions of the group. The occupancy of oxygen was taken as 1 (100%) for all the refined parameters and it was not varied during the refinement. The quality of the refinements are known based on the values of reliability factors such as R_p, R_{wp}, R_{exp}, R_{Bragg}, R_F and χ^2 and they are defined as follows [73];

$$\text{Profile factor, } R_p = \frac{\sum_{i=1,n}|y_i - y_{c,i}|}{\sum_{i=1,n} y_i} \times 100 \qquad (2.2)$$

Here, y_i is the observed data (experimental) and $y_{c,i}$ is the calculated data and n represents the number of data points.

$$\text{Weighted profile factor, } R_{wp} = \left[\frac{\sum_{i=1,n}\omega_i|y_i - y_{c,i}|^2}{\sum_{i=1,n}\omega_i y_i^2}\right]^{\frac{1}{2}} \times 100 \qquad (2.3)$$

where $\omega_i = \frac{1}{\sigma_i^2}$, σ_i^2 is the variance of y_i.

$$\text{Expected weight factor, } R_{exp} = \left[\frac{|n-p|}{\sum_{i=1,n}\omega_i y_i^2}\right]^{\frac{1}{2}} \times 100 \qquad (2.4)$$

Here, (n–p) is the number of degree of freedom, n is the total number of experimental data points and p is the number of refined parameters.

$$\text{Reduced chi-square, } \chi^2 = \left[\frac{R_{wp}}{R_{exp}}\right]^2 \qquad (2.5)$$

$$\text{Bragg factor, } R_B = \frac{\sum_h |I_{obs,h} - I_{calc,h}|}{\sum_h I_{obs,h}} \times 100 \qquad (2.6)$$

Here h is the vector that levels the Bragg reflections. The $I_{obs,h}$ is the observed integrated intensities and $I_{calc,h}$ is the calculated intensities.

$$\text{Crystallographic } R_F \text{ factor, } R_F = \frac{\sum_h |F_{obs,h} - F_{calc,h}|}{\sum_h F_{obs,h}} \times 100 \qquad (2.7)$$

Here $F_{obs,h}$ is the observed structural factor and $F_{calc,h}$ is the calculated structural factor.

2.4 Raman Spectroscopy

Raman spectroscopy is a vibrational spectroscopy used to study the crystal structure related parameters such as their bonding information, crystalline phase, defects, strain, *etc.* in a system. It is mainly a light scattering phenomenon where both photon and phonon interacts with each other based on the famous Raman Effect [74]. In general, the infrared

bands arise from the interaction of light with the molecule due to change in the dipole moment while the Raman bands originate from the same interaction with change in the polarizability of the molecule. This means that the specific molecular vibration is responsible for these observed bands (corresponding to specific energy transitions). They can be used to identify the molecule as they provide a fingerprint of the molecule being observed. The Raman spectrum provides the detailed information about various frequency at which the radiation is absorbed by the molecule for transition into higher vibrational energy states. Since the discovery of the Raman effect in 1928 by Sir. C.V. Raman, for which he got the Nobel Prize in 1930, Raman spectroscopy has become an established as well as a practical method of chemical analysis and this method is applicable to many different chemical species. Raman spectroscopy can be used to characterize the samples in the form of solids (particles, pellets, powders, film, and fibers), liquids (gels, pastes), and gases.

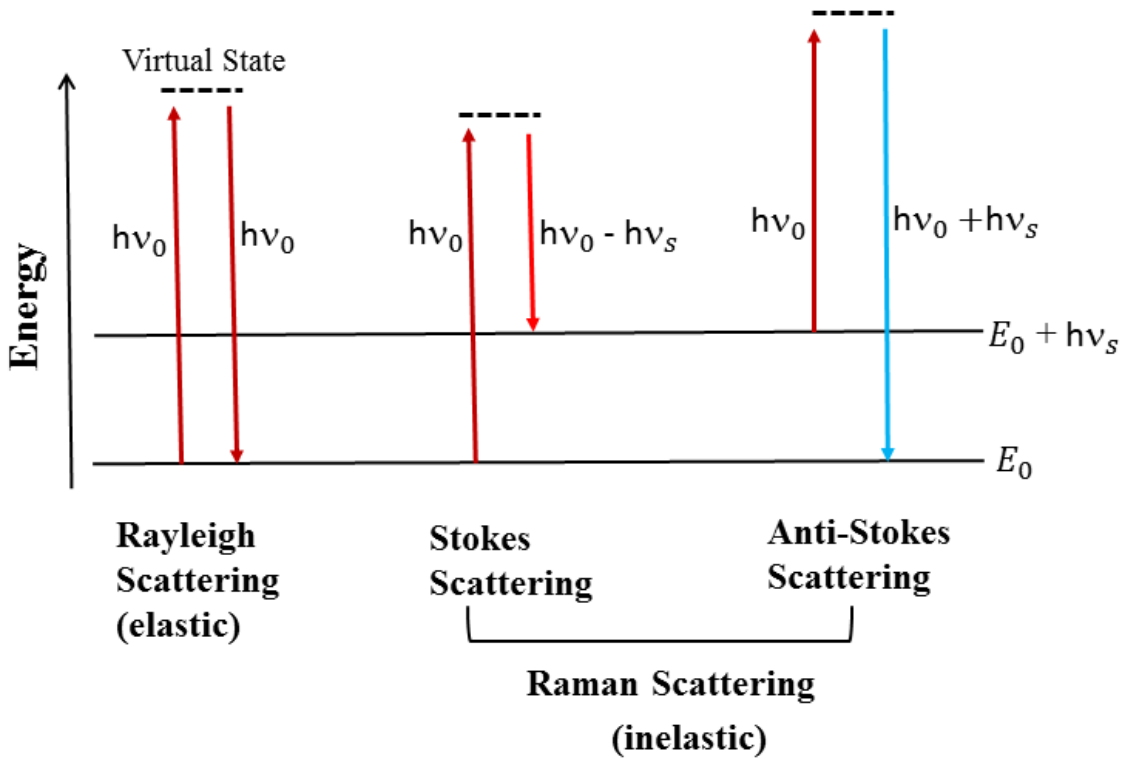

Figure 2.4: Schematic representation of Rayleigh and Raman scattering process.

In Raman spectroscopy, a monochromatic laser beam is incident on the sample and it interacts with the molecular vibration and gets scattered. When a sample is irradiated with intense monochromatic light (energy $h\nu_0$), great majority of the scattering takes place with no loss of energy and hence no frequency change. This phenomanon is known as

elastic or Rayleigh scattering (Fig. 2.4). However, the Raman spectrum arises from a very small fraction of scattered beams whose wavelengths are different from the incident wavelength of the spectrum. Therefore, there is a change in energy and the frequency of scattered light. This inelastic scattering is known as Raman scattering. If the frequency of scattered radiation is shorter than the frequency of incident radiation, then the scattered lines are called Stoke lines, whereas if the frequency of scattered radiation is higher than that of the frequency of incident radiation, then the antiStokes lines are formed in the Raman spectrum. These Stokes and anti–Stokes scattering are shown in Fig. 2.4. Let ν_0 is the frequency of incident radiation and ν_s is the frequency of scattered radiation, then the Raman shift can be defined as $\Delta\nu = \nu_0 - \nu_s$. When the frequency of incident photon is decreased after interacting with sample, then it is scattered with a red-shifted frequency called Stokes shift ($\nu_s < \nu_0$). If initially the molecule is in excited energy state and provides energy to the scattered photon, then that yields a blue-shifted frequency called anti–Stokes shift ($\nu_s > \nu_0$) (Fig. 2.4). In general, the vibrational ground state is more populated as compared to that of excited states and resulting in higher Stokes scattering intensity than the anti-Stokes scattering. Therefore, the Raman scattering photons observed for the analysis are Stokes photons called Stokes lines. But in general, it is the polarizability of molecular vibrations which decides whether the Raman spectra will occur or not. When Raman spectra occur, the molecules should be polarizable to different extents in different directions. Further, the Raman spectra and the infrared data provides the useful information on shape (linear or bent) and symmetry of the molecules [74]. If a molecule having centre of symmetry, the frequencies observed in the infrared spectra are not observed in the Raman spectra and vice-versa. If the infrared bands coincide with the Raman bands, then the molecules do not have centre of symmetry. Hence this study enables us to provide the structure of molecules.

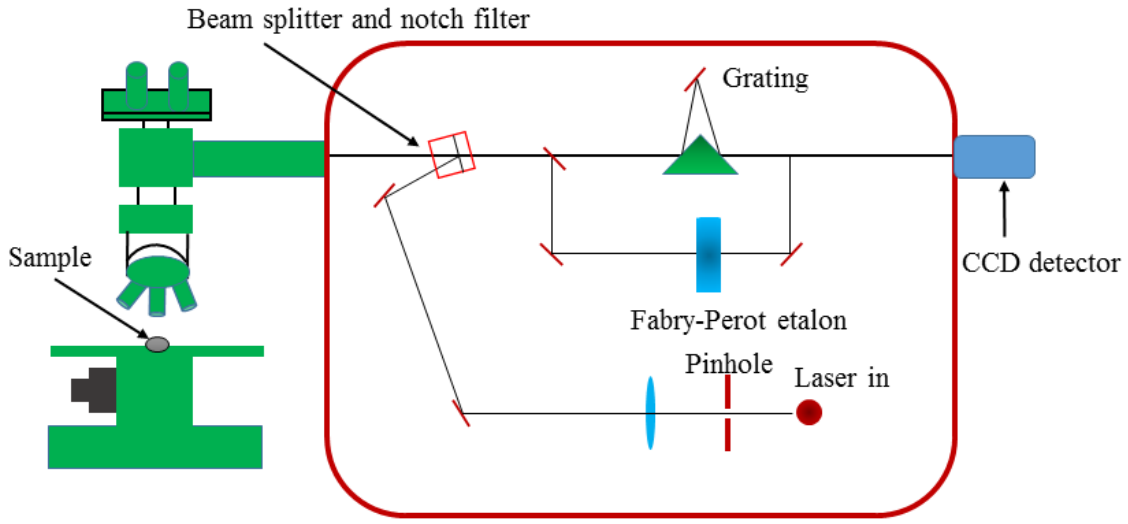

Figure 2.5: Schematic representation of Raman spectrometer.

In the present thesis work, the Raman spectra were recorded at room temperature by using micro-Raman spectrometer (LabRam HR800, Horiba Jobin Yvon) in the wavenumber range of 100 – 800 cm^{-1} with an excitation wavelength of 488 nm. There are two types of Raman spectrometers such as dispersive and non-dispersive. In the dispersive spectrometer, grating or prism is used whereas interferometer like Michaelson interferometer is used in non-dispersive spectrometer. The basic building block of the dispersive micro-Raman spectrometer used for the sample characterization is shown in Fig. 2.5. Here the sample is placed under the intense laser beam through a microscope with a spot size of few microns. The microscope equipped with two switchable gratings is coupled confocally to a spectrometer of 800 mm focal length. Two laser sources such as He – Ne laser (wavelength 632.8 nm) or Argon laser (488 or 514 nm) can be used for excitation of photons. The laser beam coming from the source is reflected by the beam splitter, which splits the beam into two parts having same wavelengths. The beam was allowed to fall on the sample in such a way that both Rayleigh and Raman scattering can take place. The notch filter shown in the above figure permits only the Raman scattered wavelength while it blocks the incident wavelength. The grating was used to allow the inelastically scattered light while etalon resolves the weak inelastically scattered wavelength coming from the sample more efficiently. In addition to that, the beam was allowed to enter into the charge coupled device (CCD) where it detects the change in polarizability of the sample from the change in wavelength and converts into the intensity. The intensity versus wavenumber

graph can be seen on the computer screen. For a given series of samples, all the measurements are done with the same spectrometer under the same condition.

2.5 Field Emission Scanning Electron Microscope (FESEM)

Field emission scanning electron microscope (FESEM) is a scanning electron microscope (SEM) based technique used in various fields of research areas such as biology, chemistry and physics to visualize the topographical details like surface morphology, fractured components, foreign particles residues, *etc*. on a very fine scale. The surface morphology and compositional analysis of the samples in the present work have been carried out by ZESIS make FESEM (ΣIGMA) equipped with Oxford energy dispersive spectrometer (EDS). The resolution of this FESEM is 1.3 nm at 50 kV and 2.8 nm at 1 kV. Two types of electron emission sources can be used for the scanning of the materials such as thermionic emitter and field emitter. The SEM and FESEM can be differentiated easily based on their electron emitter source. Thermionic emitters heat up a filament by using electrical current. When the heat is very high to overcome the work function of the filament material, the electrons can escape from the material. Thermionic sources possess relatively low brightness, evaporation of cathode material and thermal drift during operation. Thermionic emitters are mostly used in SEM. However, field emission (FE) sources called cold cathode field emitter is used in FESEM and hence the name field emission SEM is adopted. It does not heat the filament but it requires a huge electrical potential gradient to reach the electron emission for operation. Therefore, the thermionic emitter problem is avoided in FESEM while generating electrons.

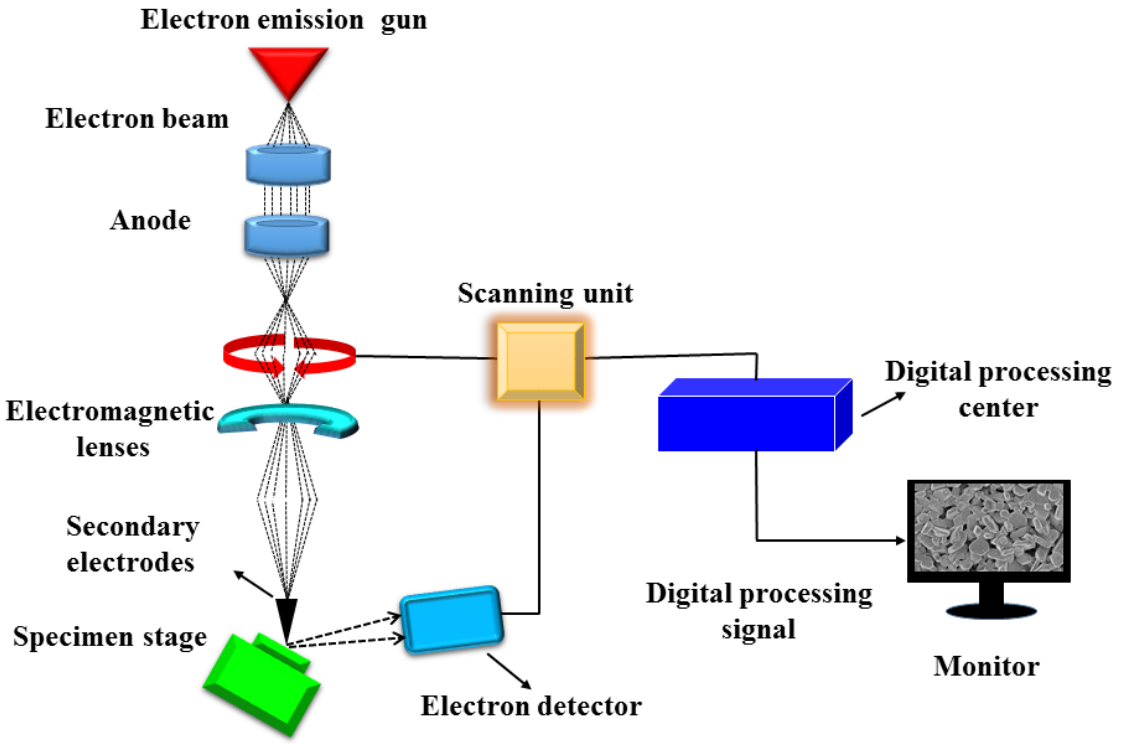

Figure 2.6: Schematic view of the field emission scanning electron microscope.

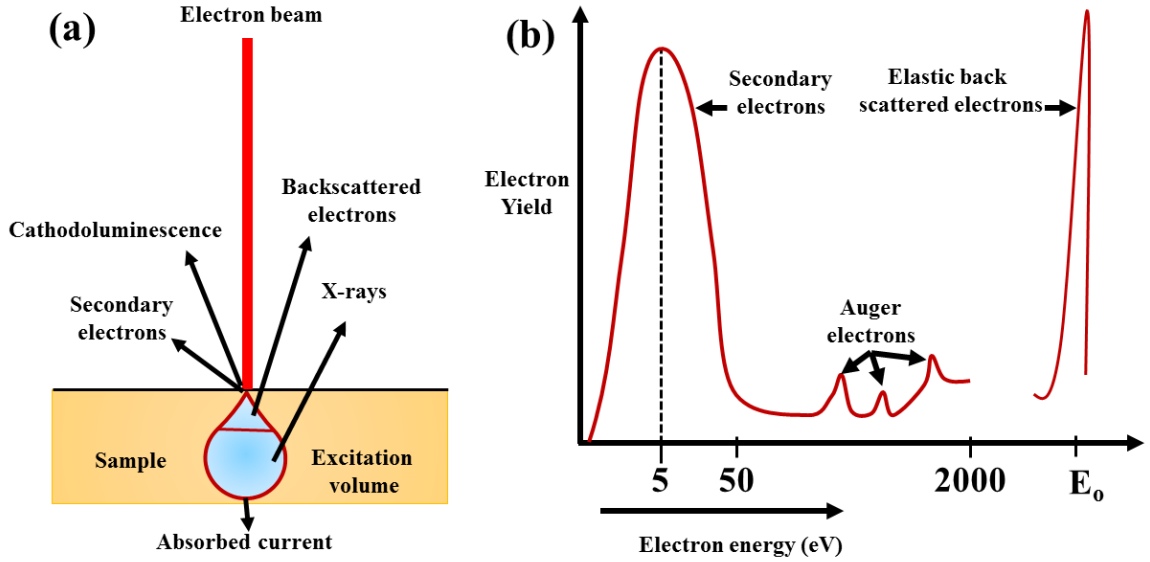

Figure 2.7: (a) Electrons and photons emanating from tear-shaped interaction volume during electron beam imprignment on specimen surface and (b) Energy spectrum of electrons emitted from the specimen surface.

The fundamental principles of FESEM analysis are discussed briefly as follows. The emission of electrons from the valence band to conduction band of semiconductors

induced by external electromagnetic field is called field emission (FE). There is an another effect called cold electronic emission where the emission of electrons occur in strong static (or quasi-static) electric fields. The electron gun used in this system is basically a zirconium oxide coated tungsten (ZrO_2/W) emitter. This gun operates in a thermally assisted Schottky emission mode, which provides narrower probing beams as well as high electron energy. As a result both improved spatial resolution and minimized sample charging and damage. The electrons are emitted from a field emission source called primary electrons under extreme vacuum and accelerated in a high electric field gradient. The presence of high vacuum provides the movement to electrons along a column without scattering which encourages to prevent discharge inside the instrument. These primary electrons inside the high vacuum column are focussed and deflected by the electromagnetic (Fig. 2.6) lenses to produce a narrow scan beam that bombards the object. As a result, the secondary electrons are emitted from each spot on the object as shown in Fig. 2.7. Depending upon the surface structure of the object, these secondary electrons will change their angle and velocity. These secondary electrons were captured by a high efficient annular in-lens ac detector and produces an electronic signal. This process results in image construction and the image is displayed on a monitor. One more detector i.e. solid state backscattered detector is used to detect the backscattered electrons. The FESEM has a lot of advantages over SEM such as; (1) FESEM produces clearer and less electrostatically distorted images with a spatial resolution of 1 nm which is 3 to 6 times better resolution images than conventional SEM, (2) Small area contamination spots can be determined at electron accelerating voltages equipped with Energy Dispersive X-ray Spectrometer, (3) High quality, low voltage (accelerating voltage range from 0.5 to 30 kV) images are obtained with negligible electrical charging of samples.

In order to analyze the FESEM micrographs of an object, the sample must be electrically conducting. Thus, the thin solid sample was mounted on a carbon coated tape with an extremely thin layer (1.5 – 3.0 nm) of gold or carbon by using respective coater. For the conducting sample, the FESEM measurement can be done without any metal coating. In the present thesis work, the samples are semiconducting and hence to make electrically conducting, the samples are coated with thin layer of gold as an electrode.

2.6 Energy Dispersive X-ray Spectroscopy

Energy dispersive X-ray spectroscopy (EDX or EDS) is an analytical technique used for the elemental analysis or chemical characterization of a sample. Since each element has a unique atomic structure, it emits its characteristic X-ray upon excitation. In order to stimulate the emission of the characteristic X-rays from a specimen, a high energy beam of charged particles such as electrons or protons or a beam of X-rays is focussed into the sample. At rest, the ground state electrons of an atom within the sample exhibit discrete energy levels or electron shells bound to the nucleus. The incident beam may excite and eject an electron from an inner shell and it results in a hole or electron vacancy in the shell. The hole is then filled by an electron from the outer energy shell and the difference in energy between the higher and the lower energy shells are released in the form of X-rays. The atoms of each element releases X-ray with unique amount of energy during the above process. Thus, by measuring the energy of X-rays released by the specimen during electron beam bombardment, the identity of the atoms present in the specimen can be established. As a result, the EDX spectrum gives the frequency dependence of emitted X-ray. The peak observed corresponding to a particular frequency or energy corresponds to a single element. The intensity of peaks depend upon the concentration of elements present in the specimen. In the present thesis, EDX spectra of all the samples were recorded by ZEISS make FESEM (ΣIGMA) equipped with EDX facility.

2.7 Magnetic Properties

2.7.1 Vibrating Sample Magnetometer

Vibrating sample magnetometer (VSM) is one of the most widely used instrument that provides the information about the magnetic properties of a large variety of magnetic samples with high precision. The VSM developed originally by Foner [75] has now become the most successful instrument for low/high temperatures and high magnetic field studies of the corelated electron system. The combination of flexible designing with high sensitivity makes this instrument more handy for sample mounting and exchange. Samples can be changed rapidly at any operating temperature. One can easily measure the dc magnetic moment as a function of temperature, magnetic field and time by using VSM. Therefore, susceptibility and magnetization studies can be performed by this system. Magnetic moment down to the order of 5×10^{-5} emu can be measured by VSM [75].

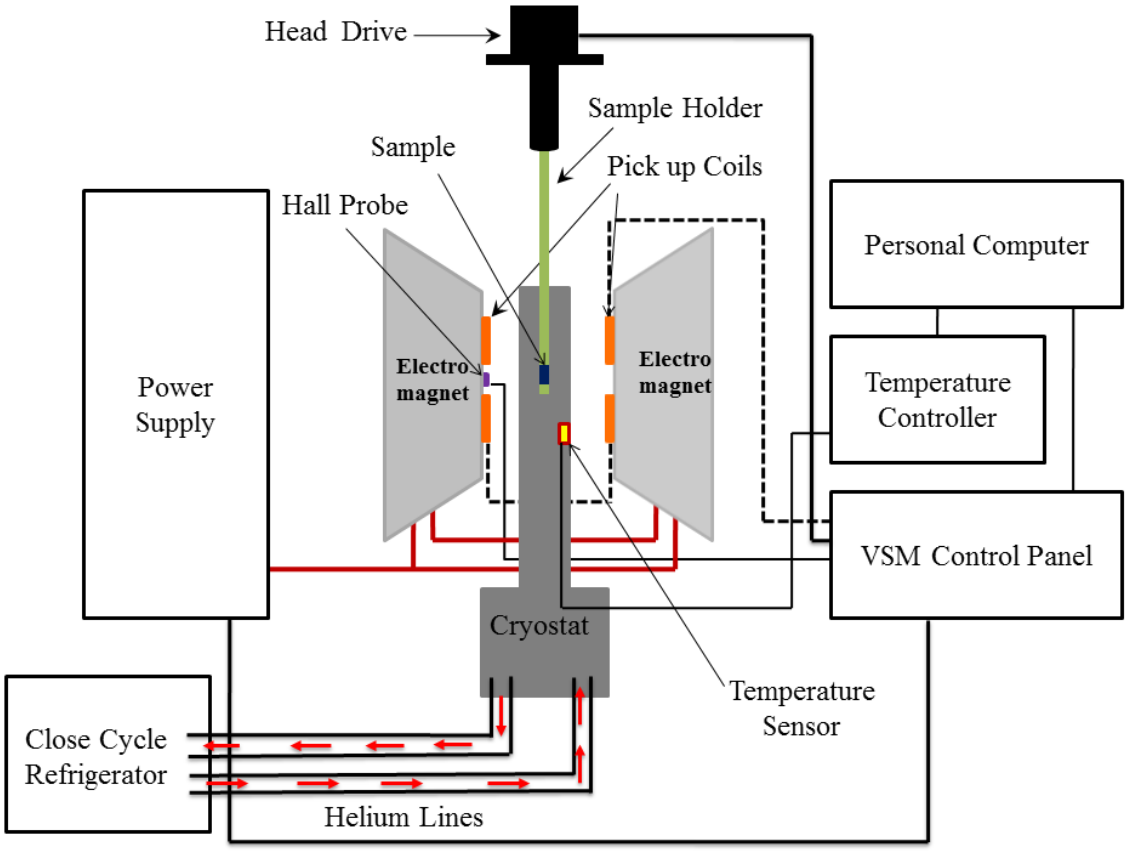

Figure 2.8: Block diagram of vibrating sample magnetometer (VSM).

The fundamental working principles of VSM is based upon Faraday's law, according to which an emf is induced in a coil by changing the flux through the coil. Initially, a magnetic sample is mounted on a long quartz rod in such a way that the sample is located between the pole pieces of an electromagnet producing an uniform magnetic field. Thus, a dipole moment will be induced. If a sinusoidal i.e. up and down motion is produced in the sample by a mechanical vibrator, then the vibration of sample generates an electrical signal by changing the magnetic flux. This flux change will induce a voltage in the pick-up coils mounted on the pole pieces of the electromagnet and the voltage is proportional to the magnetic moment of the sample. Lock-in-amplifier and feedback techniques are used to measure these signal and convert it into the unit of magnetic moment. A suitable VSM signal detector is used to detect the voltage, V(t) produced in the system with high resolution and accuracy. The basic block diagram of a VSM equipped with the low temperature measurement attachments is shown in Fig. 2.8 and its important parts along with their working principles are discussed below.

(i) Water cooled electromagnet and Power supply:

A variable bipolar power supply offers power to the electromagnets. In order to magnetize the sample, the electromagnet along with the power supply is used to generate the constant external applied magnetic field. Both the electromagnet coil and the power supply circuits are cooled by circulating cold water with the help of a water chiller to avoid overheating.

(ii) Mechanical vibrator (Head Drive) and Sample holder:

A long quartz rod is connected to a mechanical vibrator and the sample is mounted at the other end of the rod. The sample moves up and down at a set frequency and amplitude with the help of vibrating head drive. The sample rod can be rotated to achieve the desired orientation of the sample to the constant magnetic field. The x, y, z positions of the sample can be controlled by rotating three knobs attached in the head drive. For high temperature measurements i.e. above room temperature, high temperature oven assembly with a ceramic sample holder is used. A ceramic putty is used to attach the sample in the sample holder (rod) for high temperature measurement.

(iii) Pick–up Coils:

A pair of coils is mounted on the pole pieces of the magnets and it picks up the induced emf generated by the change in magnetic flux due to sample vibration. The induced emf in the pick-up coils is proportional to the magnetic moment of the sample.

(iv) Hall Probe:

A Gauss – meter is used to measure the magnetic field with analog output capabilities. The Hall probe is mounted between the magnetic pole pieces close to the sample position.

(v) Lock–in–amplifier:

The emf induced in the pick-up coils is detected accurately by means of a lock-in-amplifier. It gives dc output which is proportional to the magnetic moment. This lock-in-amplifier eliminates noise from the environment and picks up the signal of desired frequency.

(vi) Computer Interface:

A personal computer is used to interface the various components of the instrument such that they can be controlled easily by the software. The standard IDEAVSM software supplied by Lakeshore is used for interfacing, controlling the parameters and collecting the data.

(vii) Temperature Controller:

The variation of temperature i.e. below and above the room temperature during the magnetization measurement is controlled by a suitable temperature controller. A proportional, integral and derivative (PID) temperature controller facilitates temperature control over the range of 25 K < T < 300 K and 300 K < T < 1000 K. The temperature sensor gives the input to the temperature controller and the output is connected to a control element (heater). A closed-cycle Helium refrigerator cryostat is used for the cooling process.

(viii) Closed Cycle Helium Refrigerator:

A closed-cycle Helium refrigerator along with a temperature controller is used to cool the sample down to 25 K. The sample chamber is connected thermally to the cold head motor and the cold head motor is attached to the Helium compressor. For the sake of good thermal contact and uniformity in temperature over the sample, dry helium gas is allowed to flow continuously into the sample chamber. A heater wire is connected to the temperature controller for the temperature variation measurement. A cernox sensor is used to measure the temperature.

(ix) High Temperature Oven:

To measure the magnetic properties of the samples at high temperature, the cryostat is replaced by a high temperature oven in the VSM set up with model no. 74034. Fig. 2.9 shows the photograph of high temperature oven assembly. The temperature is controlled by means of temperature controller in the VSM control panel and a heater attached inside the oven. To avoid oxidation of the samples at high temperature, overheating of the flanges and for uniform temperature in the entire sample region, the oven is continuously purged by Nitrogen/Argon gas throughout the measurements. A type K thermocouple is attached to the oven for the temperature measurement.

Figure 2.9: High Temperature Oven.

2.8 R.F. Impedance/Material Analyzer

RF Impedance/Material analyzer is a widely used equipment for high frequency measurements. With the help of this equipment, one can measure various electrical parameters of a material like impedance values, dielectric permittivity and magnetic permeability. In the present work, the complex permeability of the samples was measured at room temperature in the high frequency range of around 10 MHz to 2 GHz by using RF impedance analyzer. Fig. 2.10(a) shows the photograph of Novocontrol make (model no. BDS 2300) RF Impedance analyzer. To determine the magnetic permeability, a toroidal core (DUT) sample was used as shown in Fig. 2.10(b), where 'h' represents the thickness of the sample, 'b' and 'c' symbolize the inner and outer diameter of the toroidal core (sample). Initially, to get the high accuracy in the permeability measurement, a four-step calibration process such as a conventional one-port calibration (low – loss phase), open, short, and 50 Ω load standards are used step by step for the measurements. Before starting the measurement, the inner and outer diameter and the thickness of the samples were measured by vernier caliper and screw gauge. The sample was mounted inside the magnetic test fixture (16454A) as shown in Fig. 2.10 (c). The magnetic test fixture is then connected to the impedance analyzer. The impedance analyzer is connected to a personal computer, where the WINDATA software is installed for the measurement. Before running the WINDATA software, the sample specifications such as; thickness, inner and outer diameter

were provided accurately. The permeability data were collected by running the WINDATA software provided by the Novocontrol and simultaneously, it displays on the computer screen.

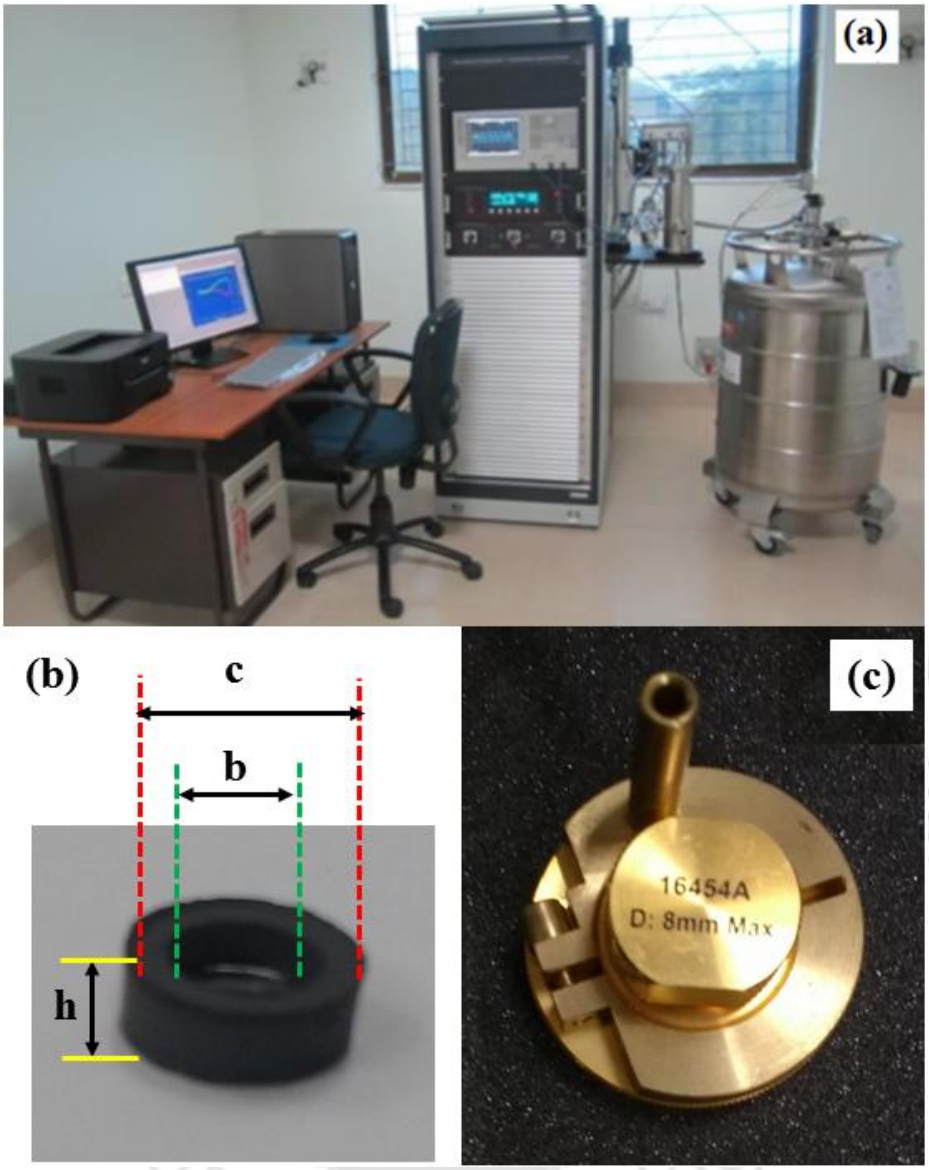

Figure 2.10: (a) RF Impedance/Material Analyzer, (b) Toroidal core sample with thickness 'h', inner and outer diameters 'b' and 'c' respectively and (c) Magnetic Test Fixture (16454A).

In general, the inductance measurement method is employed for the complex permeability measurement in impedance analyzer i.e. the permeability value is calculated from the inductance (L) values. It is known that the magnetic flux density (B) induced by current flowing in an infinitely long straight wire is

$$B = \frac{\mu_0 I}{2\pi r} \qquad (2.8)$$

The magnetic flux (Φ) induced by current (I) in the closed loop is

$$\Phi = LI \tag{2.9}$$

Moreover, the magnetic flux can also be determined from the magnetic flux density as;

$$\Phi = \int B\, ds \tag{2.10}$$

When a toroidal core is mounted in the 16454A, the self-inductance of the measurement circuit can be derived from the above equations (2.8), (2.9) and (2.10) as;

$$L = \frac{1}{I} \int B\, ds = \iint \frac{\mu}{2\pi r}\, dr\, dz \tag{2.11}$$

When the toroidal core is not mounted in the magnetic test fixture, then the self-inductance is

$$L_{ss} = \frac{\mu_0}{2\pi}\, h_0 ln \frac{e}{a} \tag{2.12}$$

where μ_0 is the permeability of free space. If μ_r is the relative permeability of the toroidal core, then the self-inductance from equations (2.11) and (2.12) is

$$L_{ss} = \frac{\mu_0}{2\pi} \left\{ (\mu_r - 1) h ln \frac{c}{b} + h_0 ln \frac{e}{a} \right\} \tag{2.13}$$

From the equation (2.13) the relative permeability of the toroidal core can be written as;

$$\mu_r = \frac{2\pi (L - L_{ss})}{\mu_0 h ln \frac{c}{b}} + 1 \tag{2.14}$$

2.9 Dielectric Measurements

The dielectric measurements for various samples in the present thesis work were carried out by using Wayne Kerr make LCR meter (Model no. 1J4300R/43100R) in the frequency range of 10^2 – 10^6 Hz with an AC voltage of 1.0 V_{rms}. The data were collected by WAYNE KERR LCR METER software provided by WayneKerr, where the LCR meter is connected to personal computer through RS232 interface. The frequency variation of dielectric measurements at different temperatures were carried out by using a high temperature oven. During the data collection, the temperature measurement and its controlling were carried out by Chromel – Alumel (Cr – Al) thermocouple and a Eurotherm make temperature controller (model no. 3216). For electrical measurements, the samples were prepared in cylindrical pellet form with a typical thickness of around 1 – 1.5 mm and diameter 8 – 10 mm. A screw gauge and a digital vernier caliper were used for the

measurement of the thickness and the diameter of the samples accurately. The electrical contacts were fabricated by painting silver pastes (McMillan) on both sides of the pellets followed by drying it continuously for 4 h in hot air oven. Before carrying out the measurements, the samples were cool down to room temperature.

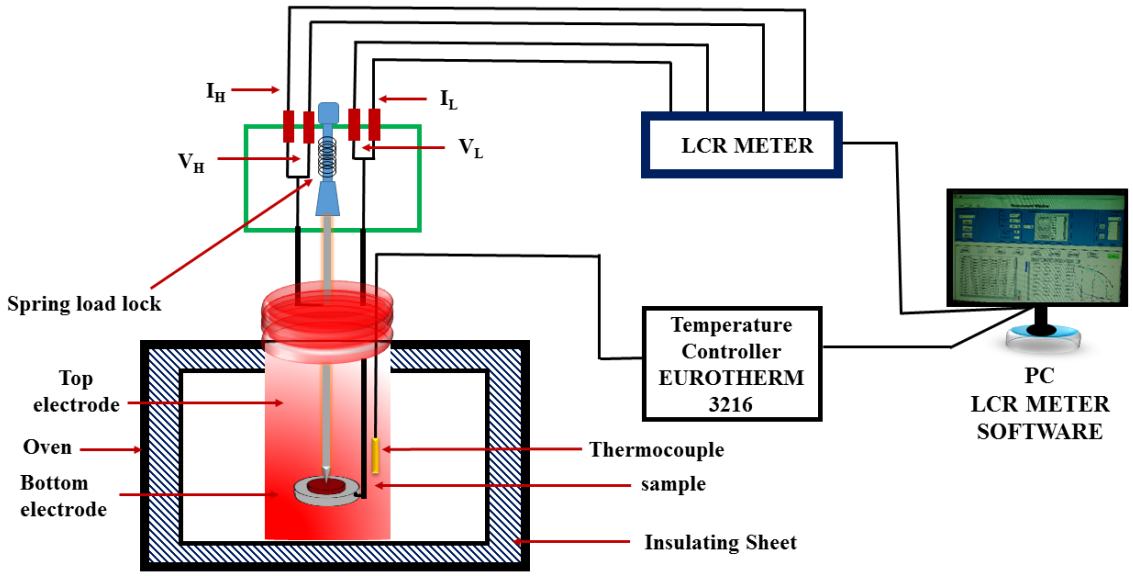

Figure 2.11: Schematic block diagram of Dielectric measurement system.

The schematic block diagram of dielectric measurement set up is shown in Fig. 2.11. The set up consists of a sample holder and a LCR meter and these two are connected through four BNC connectors. In the dielectric measurements, the four terminals of the BNC cables were used as parallel plate capacitors. The sample holder is made up of stainless steel. The top electrode is spring loaded to make the possible adjustments depending on the sample dimensions. The bottom electrode is connected to the VL and IL while the top electrode is connected to the VH and IH terminals. The VH/VL pair is used for voltage measurements while the IH/IL pair is connected to signal generator to pass the current through the sample. The LCR meter measures the voltage across the device under test (DUT) by sending current of certain frequency (ω) and calculates the impedance of DUT using the relation;

$$Z^*(\omega) = V^*(\omega)/I^*(\omega) \qquad (2.15)$$

Here Z^*, V^* and I^* are the complex. The LCR meter used in this work internally calculates and displays the real (Z') and imaginary (Z'') parts of impedance Z^* and capacitance. The Z' and Z'' datas were measured in the frequency range of 10^2 – 10^6 Hz. The impedance

data in the present thesis work were analyzed based on commercially available ZSimp Win software (version: 3.21). The related parameters such as real and imaginary part of dielectric constant, loss tangent, electric modulus and conductivity were determined by employing the relation as;

$$\varepsilon' = -\frac{Z''}{\omega C_0(Z'^2 + Z''^2)} \tag{2.16}$$

$$\varepsilon'' = \frac{Z'}{\omega C_0(Z'^2 + Z''^2)} \tag{2.17}$$

$$\mathrm{M}' = \frac{\varepsilon'}{(\varepsilon'^2 + \varepsilon''^2)} \tag{2.18}$$

$$\mathrm{M}'' = \frac{\varepsilon''}{(\varepsilon'^2 + \varepsilon''^2)} \tag{2.19}$$

$$tan\delta = \frac{\varepsilon''}{\varepsilon'} \tag{2.20}$$

$$\sigma' = \omega\varepsilon_0\varepsilon'' \tag{2.21}$$

The geometrical capacitance, C_0 of the DUT having thickness t and area A can be expressed as;

$$C_0 = \frac{\varepsilon_0 A}{t} \tag{2.22}$$

Thus, a brief overview of the experimental techniques used in the sample preparations, characterizations and the relevant physical measurements to study their electric and magnetic properties are discussed in this chapter.

Chapter 3

$BaFe_{12-y}M_yO_{19}$ (M = Ni and Ti) Series

As discussed in the first chapter, M-type barium hexaferrite (BaM) continues to draw the research interest due to its interesting physical/chemical properties and its technological applications [76]. The BaM hexaferrite crystallizes in hexagonal structure with $P6_3/mmc$ (No 194) space group and it undergoes ferrimagnetic transition (T_c) at 725 K [50, 77]. To improve the performance of BaM hexaferrite, several cationic substitutions including co-substitution of cations at Fe sites have been carried out such that its microstructure, magnetic and electrical properties are tuned. High value of dielectric constant, permeability and resonance frequencies in the order of several tens of gigahertz range have been observed in hexaferrite materials [78]. Large spontaneous polarization, magnetoelectric effect and multiferroic properties have been observed at room temperature in diamagnetic elements substituted BaM hexaferrite [79, 80]. The substitution of Er^{3+} and Ni^{2+} in strontium hexaferrite gives rise to decrease in dielectric constant and dielectric loss and increase in saturation magnetization and remanence magnetization values [81]. The substitution of trivalent metal cations such as Al^{3+}, Cr^{3+} and Ga^{3+} at Fe site gives rise to an increase in coercivity; whereas a significant drop in coercivity values are observed upon Mn, Co or Ni substitutions [51, 82-86]. In addition, magnetocrystalline anisotropy of BaM hexaferrite can be switched from uniaxial to planar by substituting Co^{2+} – Ti^{4+} ions at Fe sites [87]. The Co^{2+} – Ti^{4+} substitution has produced excellent magnetic properties with higher permeability values at very high frequency regions. Similarly, the dielectric properties of BaM hexaferrites were modified significantly by Mg^{2+} and Ti^{4+} substitutions [3]. The Ti^{4+} substitution in ferrites enhance the grains and grain boundaries resistances [88]. Baniasadi *et al*., have reported that the saturation magnetization and coercivity values decrease along with appropriate reflection losses and bandwidths upon doping of Zn – Ti ions in M-type hexaferrites [89]. Although the substitution of Ni and Ti ions have been studied in the literatures, a systematic study of structural properties and their correlation with magnetic and dielectric properties of the doped BaM hexaferrite are still lacking.

However, the lack of study on structural, dielectric and magnetic properties of Ni and Ti substituted BaM hexaferrite motivated us to characterize them. With this motivation, the effect of Ni and Ti substitution on structural, dielectric and magnetic properties of BaM hexaferrites are systematically discussed in this chapter.

3.1 Ni Substituted $BaFe_{12}O_{19}$ Series

The following section presents the preparation of Ni substituted $BaFe_{12}O_{19}$ samples. The effect of Ni substitution at Fe site along with its structural, dielectric and magnetic properties are discussed in detail in this chapter.

3.1.1 Sample Preparation and Characterization

There are several methods along with certain new synthesis techniques have been used to prepare the M-type hexaferrite [90, 91]. However, in this case the conventional sol-gel method is used for the preparation of M-type hexaferrite. The Ni substituted M-type barium hexaferrite i.e. $BaFe_{12-y}Ni_yO_{19}$ (y = 0, 0.1, 0.2, 0.3, 0.4, 0.5) samples were prepared by sol–gel method. Stoichiometric ratio of high purity $Ba(NO_3)_2$ (Loba, 99%), $Ni(NO_3)_2{\cdot}6H_2O$ (Loba, 99%), and $Fe(NO_3)_3.9H_2O$ (Sigma-Aldrich, 99%) were weighed and dissolved in distilled water and mixed in a beaker. To convert them into citrates, an appropriate amount of citric acid was added to the solution and stirred for 1 h at room temperature. Finally, ethylene glycol was mixed to the uniform solution with a slow heating rate to form a highly viscous gel and with further heating at 250 °C, the gel was converted into a fine precursor powder. The precursor powder was ground and calcined at 600 °C and 800 °C for 12 h each. These powders were pressed into cylindrical pellets of approximately ~10 mm diameter by using a hydraulic press with a maximum pressure of 2.94×10^8 N/m^2. The final sintering was carried out in pellet form at 1150 °C for 12 h. X-ray powder diffraction patterns at room temperature were recorded using Rigaku make TTRAX III X-ray diffractometer with CuK_α (1.54056 Å) radiation. Microstructure analysis was performed using ZEISS make field emission scanning electron microscope (FESEM, ΣIGMA) equipped with energy dispersive X-ray (EDX) facility. Magnetization measurements were carried out using Lakeshore (model no. 7410) Vibrating Sample Magnetometer (VSM). The frequency variation of dielectric constant was measured at selected temperatures with an applied ac voltage of 1.0 V_{rms} by using LCR meter (Wayne Kerr Electronics *Pvt. Ltd.*, 1J43100) in the frequency range of 10^2 – 10^6 Hz and the impedance spectra were analyzed by ZSimpWin software (version 3.2). Here, the electrical

contacts were made by painting silver paste on both sides of the pellets of a typical thickness of ~1 – 1.5 mm.

3.1.2 Structural Properties

Fig. 3.1 shows the typical XRD patterns of $BaFe_{12-y}Ni_yO_{19}$ (BFNO) hexaferrites recorded at room temperature for y = 0, 0.1, 0.2, 0.3, 0.4 and 0.5. As per the XRD patterns, the parent compound $BaFe_{12}O_{19}$ (y = 0) along with Ni substituted samples are found to be in single-phase form. Furthermore, the formation of single-phase hexaferrite in Ni doped samples is confirmed by comparing XRD patterns with the standard JCPDS: 84 – 0757 pattern as shown in Fig. 3.1. It is observed that the diffraction peaks are shifting towards the lower 2θ value with increase in Ni concentration. The enlarged view of high intense [114] and [107] peaks of these XRD patterns are shown in the inset of Fig. 3.1. The shifting of [114] and [107] peaks towards lower 2θ value signifies the increase in lattice constants as the Ni concentration is increased. The analysis of these XRD patterns was carried out by the Rietveld refinement technique with the help of FULLPROF software [92]. The best refinement of these XRD patterns were obtained by choosing $P6_3/mmc$ space group with hexagonal structure. No extra peak is observed in these samples i.e. all the samples are found to be in single-phase form. The typical XRD patterns for y = 0, and 0.1 samples along with Rietveld refinement data are shown in Fig. 3.2 and the patterns for y = 0.3 and 0.5 samples are shown in Fig. 3.3. The lattice parameters, volume of the unit cell and various reliability factors such as χ^2, R_p, R_{exp} and R_{Bragg} obtained from the refinement are given in Table 3.1. It can be seen that for y = 0 sample, the lattice parameters a and c are found to be 5.8909 Å and 23.2081 Å respectively. The lattice parameters a and c obtained from the Rietveld refinement are found to increase with increase in Ni concentration. This increase in lattice parameters could be attributed to the larger ionic radius of divalent Ni^{2+} (0.69 Å) compared to that of trivalent Fe^{3+} (0.645 Å) ion.

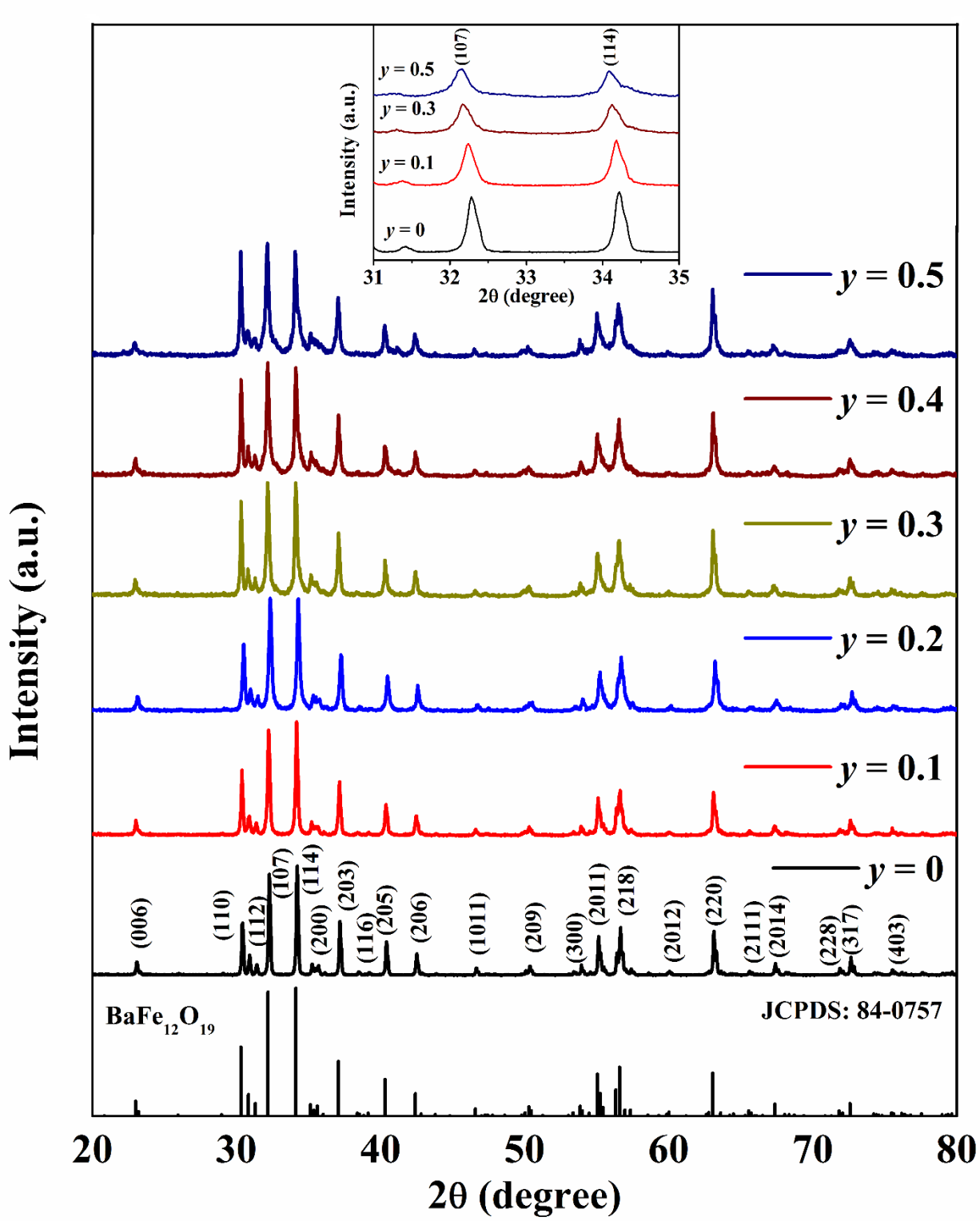

Figure 3.1: XRD patterns of BFNO samples for $y = 0 – 0.5$ recorded at room temperature.

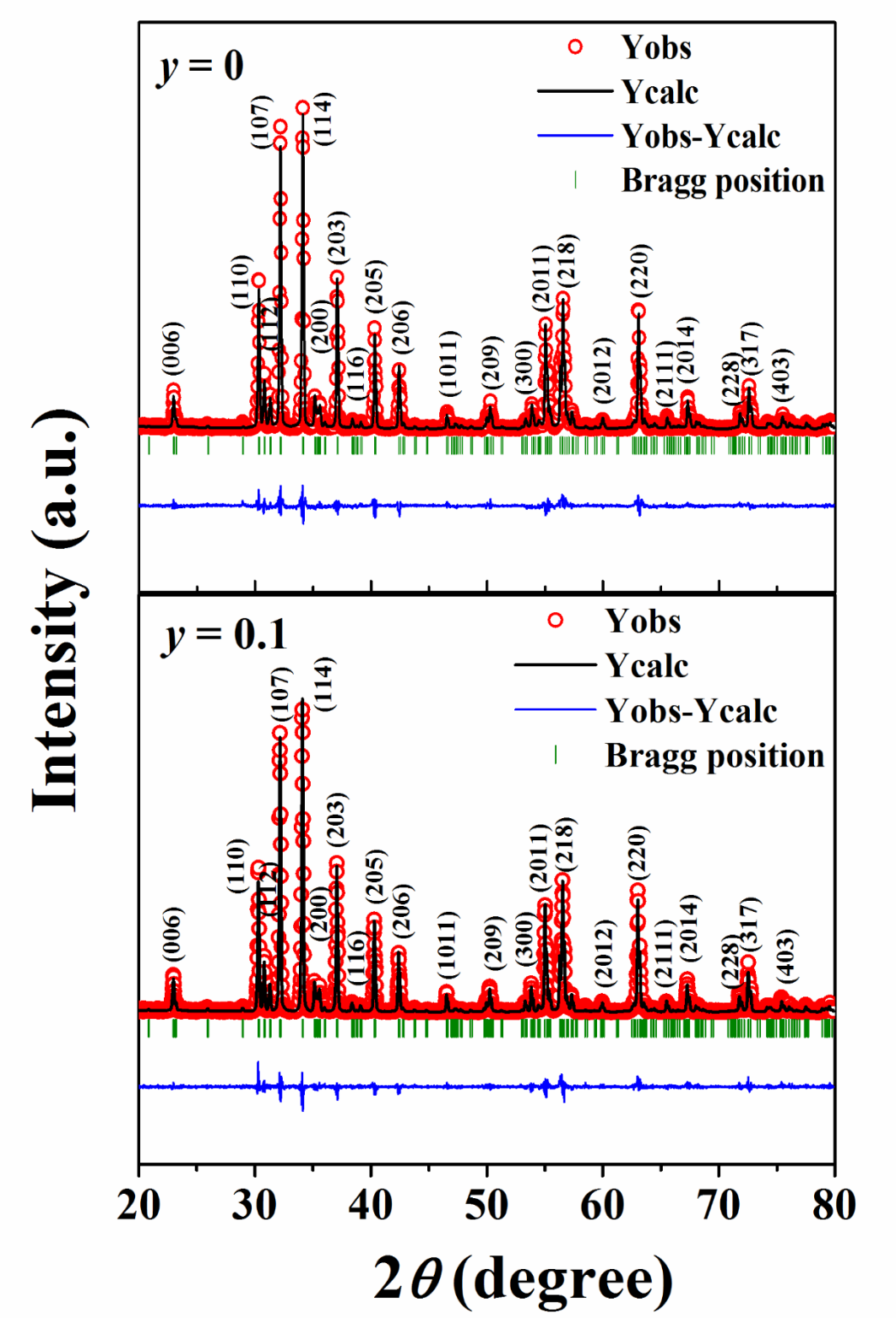

Figure 3.2: Rietveld refinement of XRD patterns of BFNO samples with y = 0 and 0.1. The red open circles represent the experimental data and the black solid lines are the fitted data. The bottom line represents the difference between experimental and refined data.

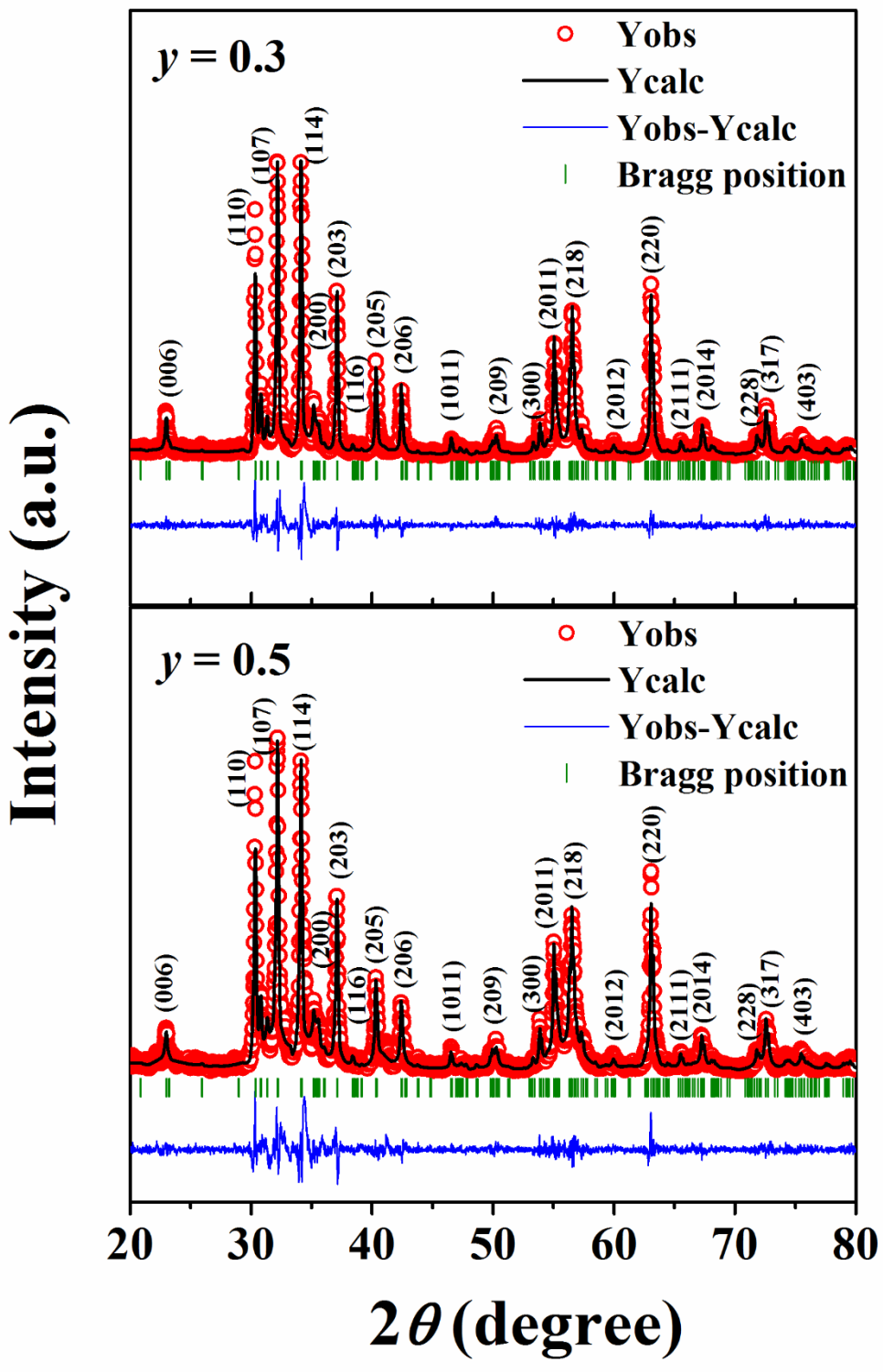

Figure 3.3: Rietveld refinement of XRD patterns of BFNO samples with y = 0.3 and 0.5. The red open circles represent the experimental data and the black solid lines are the fitted data. The bottom line represents the difference between experimental and refined data.

Table 3.1: Parameters obtained from the Rietveld analysis of XRD patterns for the samples $BaFe_{12-y}Ni_yO_{19}$ (y = 0 – 0.5). R_F, R_{Bragg}, R_P and χ^2 are the reliability factors.

Sample/ Parameters	***y* = 0**	***y* = 0.1**	***y* = 0.2**	***y* = 0.3**	***y* = 0.4**	***y* = 0.5**
Space group	*$P6_3/mmc$*	*$P6_3/mmc$*	*$P6_3/mmc$*	*$P6_3/mmc$*	*$P6_3/mmc$*	*$P6_3/mmc$*
***a* (Å)**	5.8909 (2)	5.8918 (3)	5.8923 (5)	5.8937 (5)	5.8941 (5)	5.8955 (6)
***c* (Å)**	23.2081 (5)	23.2119 (4)	23.2151 (2)	23.2180 (1)	23.2246 (3)	23.2261 (8)
***Volume* ($Å^3$)**	698.31 (4)	697.95 (6)	699.11 (1)	697.76 (1)	697.78 (1)	698.20 (3)
R_F (%)	4.53	4.65	5.72	4.62	5.09	5.05
R_{Bragg} (%)	4.02	5.41	6.30	5.83	6.89	7.00
R_P (%)	12.5	17.4	18.6	20.4	22.9	23.6
R_{exp} (%)	10.72	12.19	12.94	13.02	12.90	13.06
χ^2	3.13	3.71	3.57	3.96	4.71	4.86

To characterize the surface morphology, the microstructural images were recorded for all the samples. The typical FESEM micrographs of BFNO for y = 0, 0.1, 0.3 and 0.5 samples are shown in Fig. 3.4. The mixture of smaller and larger hexagonal shaped grains are distributed over a wide range with random orientations. This behavior can be easily understood from the grain size distribution histograms as shown in the right column of the Fig. 3.4. The average grain size of each sample can be calculated from the above size distribution histogram plots by fitting the log-normal distribution function; which can be expressed as [93];

$$f(d, \mu, \sigma) = \frac{1}{d\sigma\sqrt{2\pi}} \exp \frac{-(lnd - \mu)^2}{2\sigma^2} \qquad (3.1)$$

Here *d* represents the cross-sectional length of the particle, σ is the standard deviation and μ is the logarithmic mean. The average grain size value for $y = 0$ sample is 0.246 μm with the appearance of small pores. With increase in Ni concentration, the average grain size increases and the porosity reduces. The increase in grain size leads to the decrease in number of grain boundaries. The average grain size value for $y = 0.5$ sample is found to be 0.930 μm. Since the samples are sintered at high temperature for 12 h, there is a possibility of creation of oxygen vacancies and such vacancies are expected to inhibit the grain growth thereby reducing the average grain size [94]. However, upon Ni substitution, the grain size is found to increase due to possible reduction in oxygen vacancies. The chemical compositions were investigated by recording the EDX spectra at room temperature as shown in Fig. 3.5. The chemical composition of each element obtained from the analysis of EDX spectra is comparable to that of nominal starting compositions. The cationic ratio for $y = 0$, 0.1, 0.2, 0.3, 0.4 and 0.5 samples are tabulated in Table 3.2.

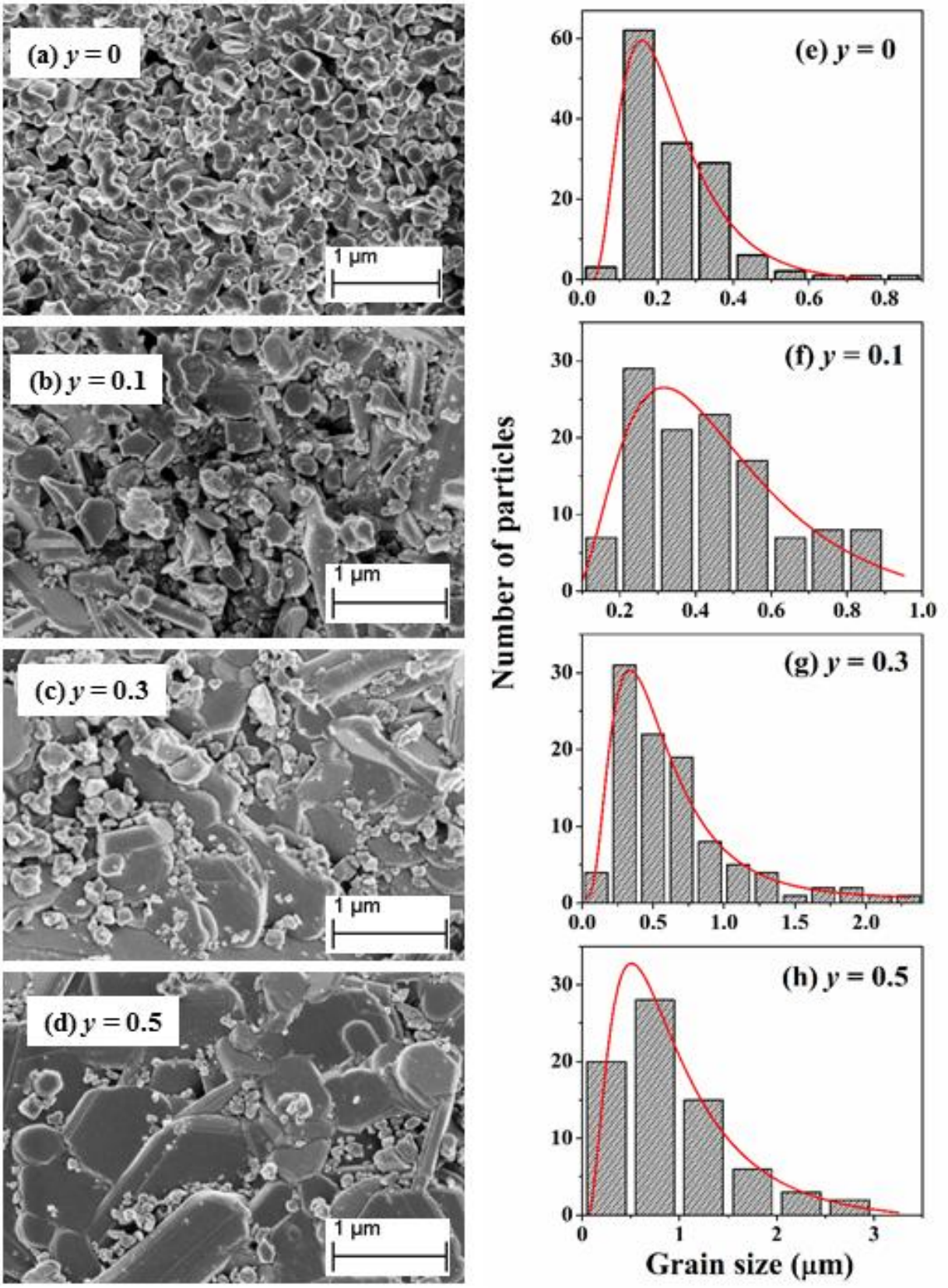

Figure 3.4: FESEM micrographs of BFNO (y = 0, 0.1, 0.3 and 0.5) samples (a-d) and their particle size distributions (e-h).

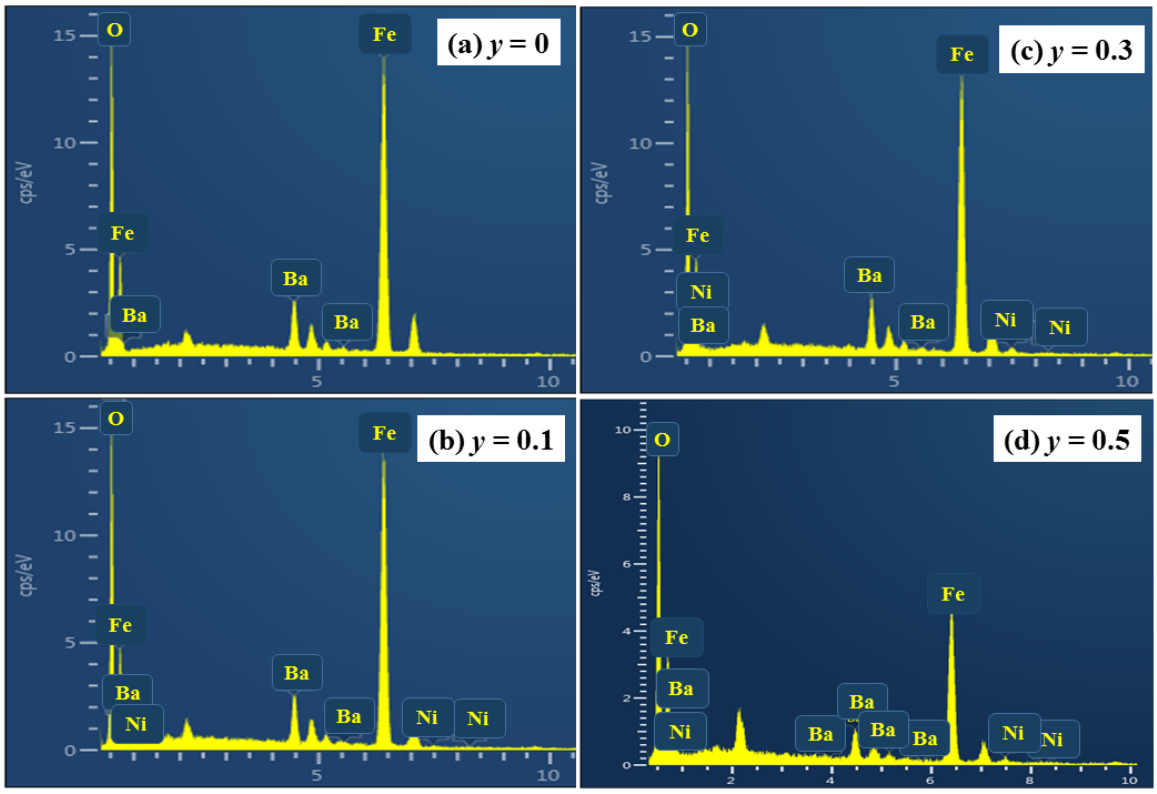

Figure 3.5: EDX spectra of BFNO samples with y = 0, 0.1, 0.3 and 0.5 (a-d).

Table 3.2: The cationic ratio calculated from EDX analysis for y = 0 to 0.5 samples.

Samples	Calculated Cationic Ratio from EDX Analysis		
	Ba	**Fe**	**Ni**
***y* = 0**	1.04	11.96	0.00
***y* = 0.1**	1.04	11.81	0.13
***y* = 0.2**	1.07	11.79	0.20
***y* = 0.3**	1.00	11.64	0.35
***y* = 0.4**	1.00	11.59	0.40
***y* = 0.5**	0.96	11.52	0.48

3.1.3 Complex Impedance Spectroscopy Analysis

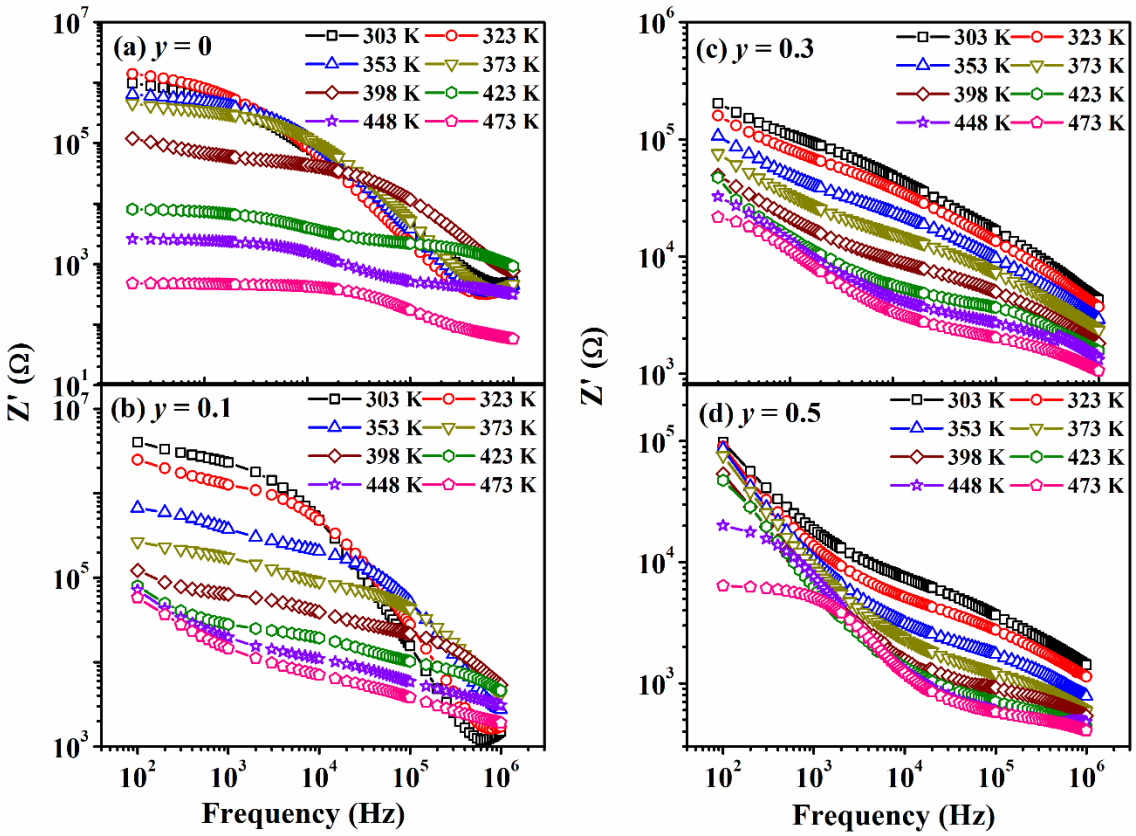

Figure 3.6: (a-d) Frequency variation of the real part of impedance (Z') of BFNO for y = 0, 0.1, 0.3 and 0.5 samples measured at different temperatures in the range of 303 K to 473 K.

In order to understand the dielectric and electrical properties of the polycrystalline samples, the complex impedance spectroscopy was studied at different temperatures from 303 K to 473 K in the frequency range of 100 Hz to 1 MHz. Fig. 3.6 shows the typical plots of the real part (Z') of the complex impedance (Z^*) as a function of frequency for BFNO samples with y = 0, 0.1, 0.3 and 0.5 at different temperatures. At a particular temperature, the Z' value is found to decrease gradually with increase in frequency followed by a rather sharp fall at higher frequencies (> 10^5 Hz). The decrease in Z' value with increase in frequency corresponds to the release of space charges and the sharp fall of Z' at higher frequencies signify the relaxation process in the sample. Furthermore, for a particular composition, the Z' value is found to decrease with increase in temperature and such type of behavior is observed for all the samples. It suggests that the conductivity of the sample is increased with increase in temperature. This can be attributed that the material has

negative temperature coefficient of resistance [95]. With increase in Ni concentration, the magnitude of Z' is found to decrease systematically at a given frequency and it suggests the increase in electrical conductivity of the samples.

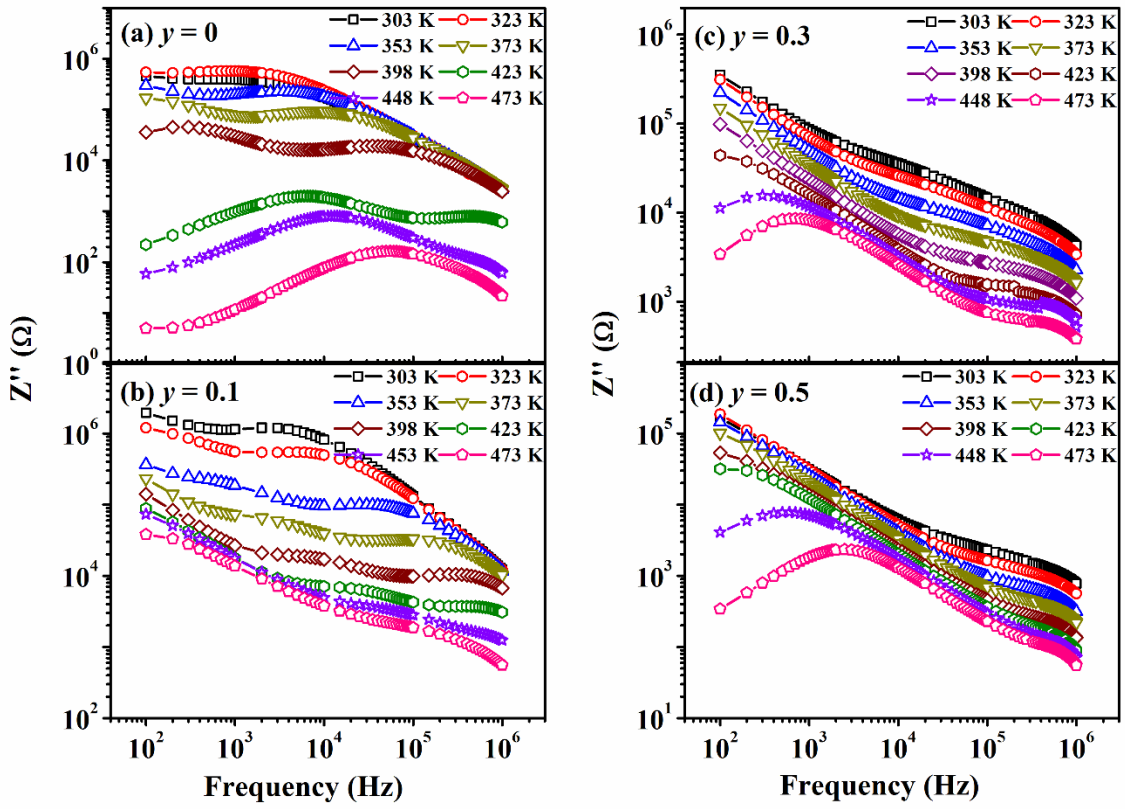

Figure 3.7: (a-d) Frequency variation of imaginary part of impedance (Z'') of BFNO for y = 0, 0.1, 0.3 and 0.5 samples measured at different temperatures in the range of 303 K to 473 K.

Further, to elucidate the dielectric relaxation behavior of BFNO samples, the imaginary part of the impedance data were measured at different temperatures ranging from 303 K to 473 K. The imaginary part of the impedance (Z'') vs frequency (f) plots for y = 0, 0.1, 0.3 and 0.5 samples at different temperatures are shown in Fig. 3.7. The most interesting feature observed in Z''spectra is the relaxation peak, which shifts towards the high frequency with increase in temperature (T) followed by decrease in the magnitude of Z''spectra. For y = 0 sample, two broad relaxation peaks are observed at a particular temperature for $T >$ 373 K and below this temperature ($T \leq$ 373 K) only one relaxation peak is observed as shown in Fig. 3.7(a). For example, at T = 398 K, the y = 0 sample exhibits two different peaks at the characteristic frequencies of 300 Hz and 35 kHz respectively. The relaxation peak observed at lower frequency region corresponds to the

relaxation across the grain boundaries and the relaxation peak at higher frequency is due to the grains. As the temperature is increased, the peaks shift towards the higher frequency region and move out of the measured frequency range. The peak shifting towards the higher frequency with increase in temperature signifies the presence of thermal activation of relaxation process. Similarly, all other samples exhibit two peaks corresponding to relaxation at grains and grain boundaries.

The Nyquist plot i.e. Z''vs Z', is one of the important technique that provides the distinguished information regarding the grains and grain boundaries contribution towards the relaxation behavior in dielectric materials. The Nyquist plots of BFNO for y = 0, 0.1 and 0.3 samples along with their fitted data (solid lines) at different temperatures are shown in Fig. 3.8. Fig. 3.8(a) shows the Nyquist plot for y = 0 sample at different temperatures ranging from 323 K to 373 K. As the temperature is increased, the arcs start bending towards the Z' axis to form a semicircle with decreased diameter and the width of the semicircle represents the resistance of the sample. This decrease in diameter with increase in temperature is a signature of decrease in resistance of the samples and it corresponds to the thermal activation of conduction process. In general, the semicircular arcs in the impedance spectra of polycrystalline materials are assigned to the grains and grain boundaries contributions. The observed single semicircular arc for y = 0 sample from 323 K to 373 K is due to the grains contribution. As the temperature is increased (Fig. 3.8(d)), another semicircular arc is observed in the low frequency range and these peaks are assigned to the grain boundaries contributions. However, with increase in Ni concentration, two semicircular arcs are observed in the measured frequency range of 100 Hz to 1 MHz. Fig. 3.8(b-f) show two semicircular arcs in the Nyquist plots that arise due to grains and grain boundaries contributions. The semicircular arcs observed at high (lower Z') and low (higher Z') frequency regions are attributed to the grains (marked as G) and grain boundaries (marked as GB) contributions respectively. As the Ni concentration is increased, the grains and grain boundaries contribution towards the relaxation behavior are clearly distinguished. It is well known that the Nyquist plots possess the depressed and distorted nature of semicircles such that their centres lie below the Z' axis. The depressed nature of semicircles mostly signifies the statistical distributions of relaxation times. A single relaxation time can be obtained, if there exists a perfect semicircle with its centre on the Z' axis and such type of mechanism is popularly known as ideal Debye behavior. However, the distortion mainly occurs if there is more than one relaxation process. This

can be attributed to the non-uniformity of the microstructures and the electromagnetic diffusions in intra grain/inter grain regions. The asymmetric and depressed semicircular arcs in the Nyquist plots signify the non-Debye like relaxation behavior. The deviation from Debye behavior in impedance spectra can be explained by using a constant phase element (*CPE*, Q) with impedance $Z_{CPE} = \frac{1}{A}(j\omega)^{-s}$. Here A is a constant, s is the relaxation time distribution and lies in the range of 0 to 1. The observed semicircular arcs can be understood by considering an equivalent circuit comprising of resistance (*R*), capacitance (*C*) and the constant phase element (*CPE*, *Q*) as shown in Fig. 3.8(g-h). The single semicircular arc due to grains follow the equivalent electrical circuit as shown in Fig. 3.8(g), where the parallel combination of R_g, C_g and Q_g are connected in series with an inductance (*L*) arising out of measuring leads. Whereas the presence of two semicircles due to grains and grain boundaries follow two parallel circuits (R_gQ_g) and ($R_{gb}Q_{gb}$) connected in series and the fitted data for all the samples are shown as solid lines in Fig. 3.8. Here R_g and R_{gb} represent the grains and grain boundaries resistance, C_g is the capacitance due to grains, Q_g and Q_{gb} are *CPE* of grains and grain boundaries respectively. From this electrical circuit, it can also be confirmed that below 373 K, grains contribution is dominant for $y = 0$ sample, whereas both grains and grain boundaries contributions are significant for Ni doped samples. The plots show that the experimental data closely follow the fitted data. The grains and grain boundaries resistances are found to decrease with increase in temperature suggesting the negative temperature coefficient of resistance.

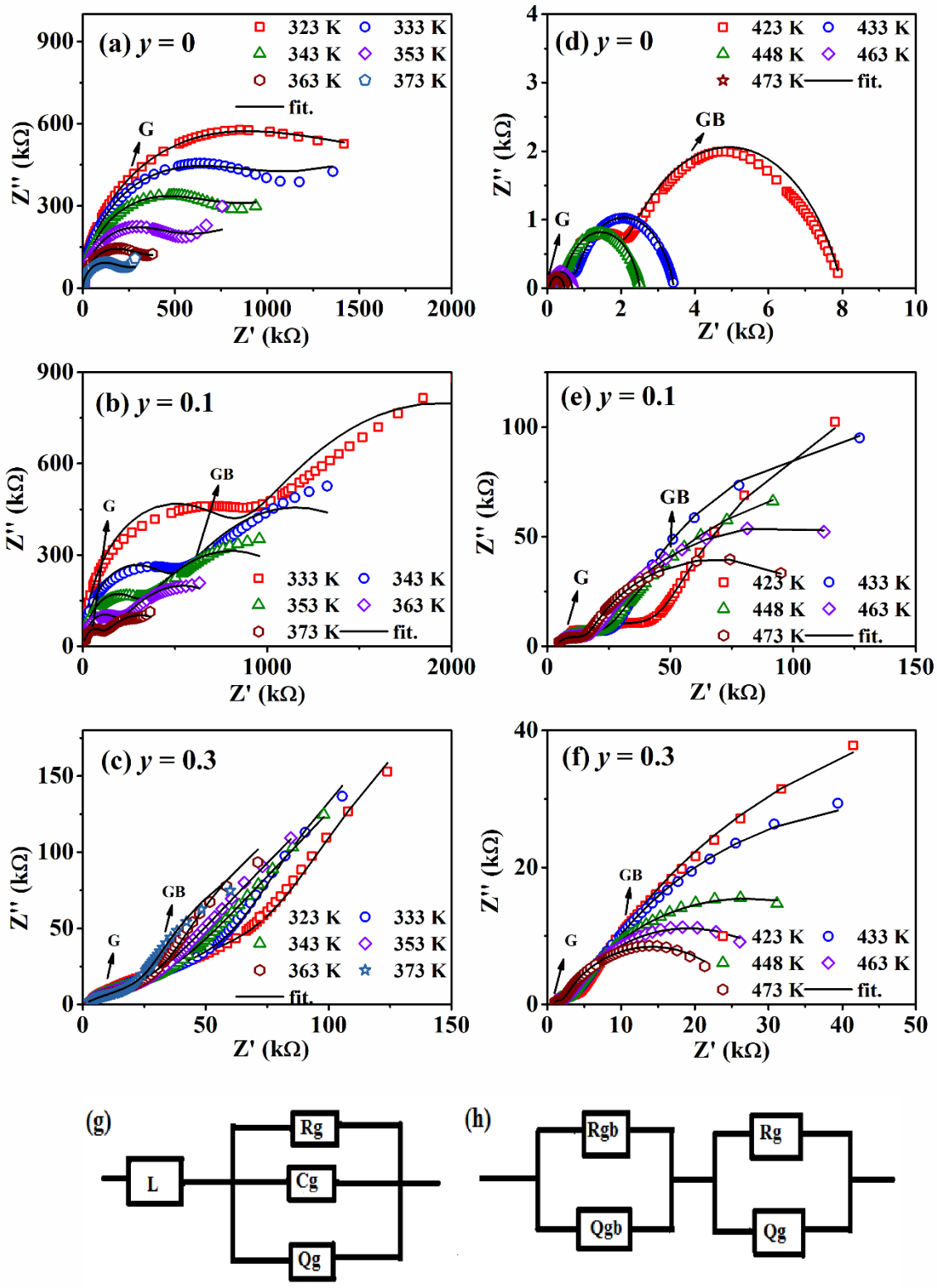

Figure 3.8: Nyquist plots (Z'' vs Z') of BFNO for (a-f) y = 0, 0.1 and 0.3 samples at different temperatures and along with their equivalent circuits (g-h).

3.1.4 Complex Dielectric Permittivity Analysis

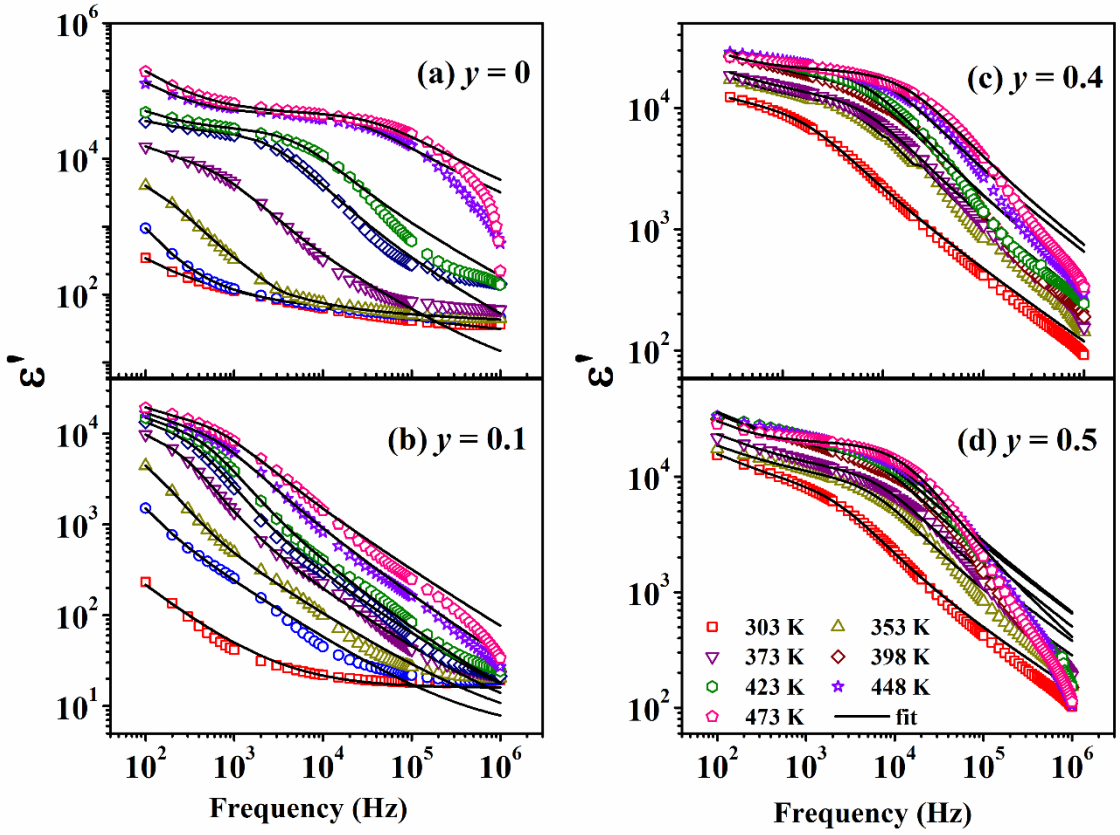

Figure 3.9: Frequency dispersion behavior of ε' of BFNO in logarithmic scale for (a-d) y = 0, 0.1, 0.4 and 0.5 samples at different temperatures. The solid line represents the fitted data using equations (3.6) and (3.7) respectively.

The real (ε') and imaginary (ε'') parts of the complex relative dielectric permittivity (ε^*) were determined from the complex impedance by employing the following relations as;

$$\varepsilon' = -\frac{Z''}{\omega C_0 (Z'^2 + Z''^2)} \quad (3.2)$$

$$\varepsilon'' = \frac{Z'}{\omega C_0 (Z'^2 + Z''^2)} \quad (3.3)$$

where ω is the angular frequency, C_0 is the geometric capacitance, Z' and Z'' represent the real and imaginary parts of the complex impedance (Z^*) respectively. The frequency variations of real (ε') and imaginary (ε'') parts of the complex dielectric permittivity (ε^*) measured at different temperatures for BFNO samples with y = 0, 0.1, 0.4 and 0.5 are shown in Fig. 3.9 and Fig. 3.10 respectively. The ε' plots exhibit a relaxation behavior in the mid-

frequency region accompanied by relaxation peak in ε'' plots. With increase in temperature, the relaxation peak is found to shift towards the higher frequency along with plateau like behavior in the mid-frequency region. At low frequency (< 1 kHz), the ε' value is found to decrease quite sharply with increase in frequency due to space charge polarization. However, in diamagnetic ions substituted M-type hexaferrites such decrease in ε' is quite slow [96]. As the temperature is increased, the drift mobility of the charge carriers contributing towards the space charge polarization is increased and hence ε' increases. The decrease in ε' at higher frequency can be attributed to the considerable lagging of electric dipoles with respect to the applied electric field. With increase in temperature, the relaxation peaks are found to shift towards the higher frequency range and it could be assigned to the thermal activation of charge carriers.

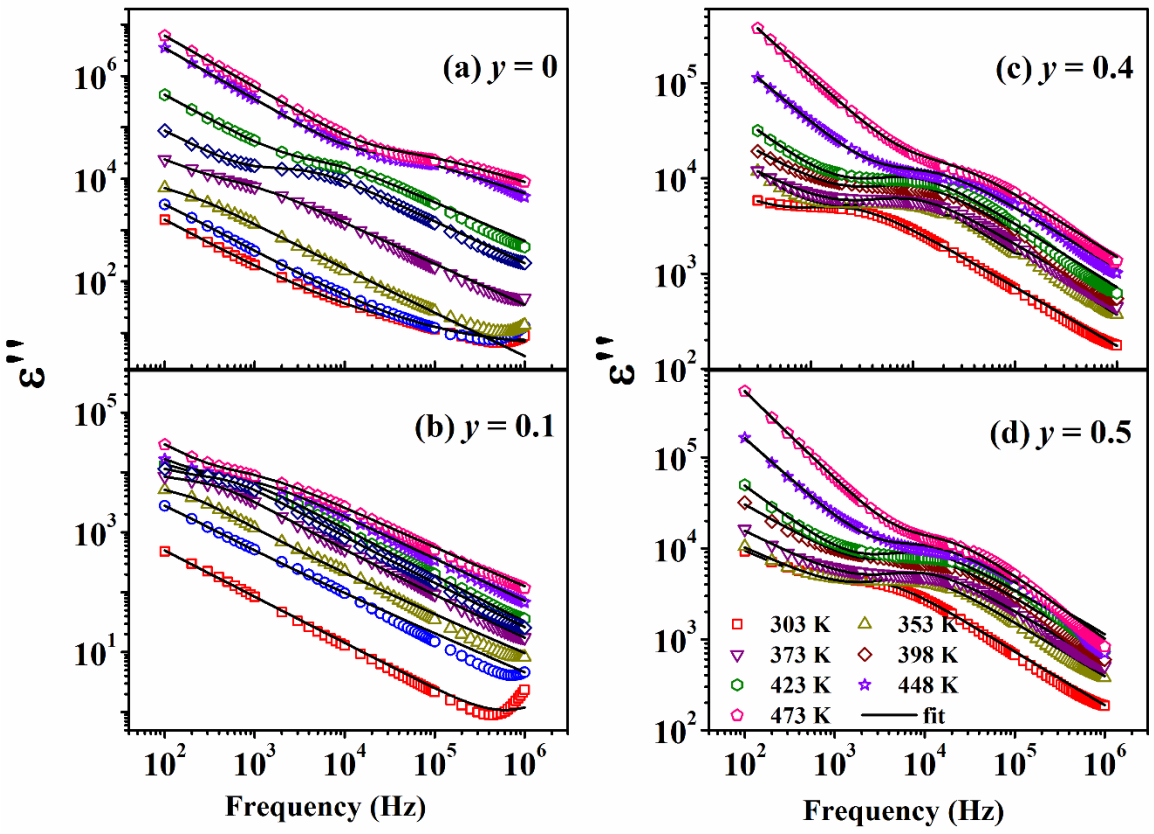

Figure 3.10: Frequency dispersion behavior of ε'' of BFNO in logarithmic scale for (a-d) y = 0, 0.1, 0.4 and 0.5 samples at different temperatures. The solid line represents the fitted data using equations (3.6) and (3.7) respectively.

In general, the frequency dispersion behavior of ε' and ε'' can be understood from the Havriliak – Negami (HN) equation [32];

$$\varepsilon^* = \varepsilon' - j\,\varepsilon'' = \varepsilon_\infty + \frac{\varepsilon_s - \varepsilon_\infty}{(1+(j\omega\tau)^{1-\alpha})^\beta} \quad (3.4)$$

where ε_s and ε_∞ represent the static low frequency permittivity and the permittivity at higher frequency limits respectively and τ is the most probable relaxation time. The difference between ε_s and ε_∞ (i.e. $\varepsilon_s - \varepsilon_\infty = \Delta\varepsilon$) provides the dielectric strength. The exponents α ($0 < \alpha < 1$) and β ($0 < \beta < 1$) describe the broadness and asymmetry of corresponding spectra respectively. If $\alpha = 0$ and $\beta = 1$, then it is an ideal Debye type relaxation with a single relaxation time and any deviation from these values give rise to broader relaxation with distribution of relaxation time. If $\alpha = 0$ and $\beta < 1$, then it defines the Cole – Davidson relaxation model while $\alpha < 1$ and $\beta = 1$ signifies the Cole – Cole model. Fig. 3.9 and Fig. 3.10 demonstrate an apparent increase in ε' and ε'' at low frequency and high temperature due to the presence of space charge (localized charge) and mobile charge carriers and these are closely related to conductivity of the samples. Therefore, an additional term contributed by electrical conductivity is required in equation (3.4).

The modified HN equation can be written as [97];

$$\varepsilon^* = \varepsilon_\infty + \frac{\Delta\varepsilon}{(1+(j\omega\tau)^{1-\alpha})^\beta} - j\frac{\sigma^*}{\varepsilon_0\omega^s} \quad (3.5)$$

where σ^* ($\sigma^* = \sigma' + j\sigma''$) is the complex conductivity, σ' and σ'' represent the conductivity due to free charge carriers (dc conductivity) and the space charges (localized charges) respectively. The dimensionless exponent term s ($0 < s < 1$) represents the distribution in polarization mechanism. The ε' and ε'' can be derived from the equation (3.5) as [97];

$$\varepsilon' = \varepsilon_\infty + \frac{\Delta\varepsilon\cos(\beta\varphi)}{\left(1+2(\omega\tau)^{1-\alpha}\sin\left(\frac{\alpha\pi}{2}\right)+(\omega\tau)^{2-2\alpha}\right)^{\beta/2}} + \frac{\sigma''}{\varepsilon_0\omega^s} \quad (3.6)$$

and

$$\varepsilon'' = \frac{\Delta\varepsilon\sin(\beta\varphi)}{\left(1+2(\omega\tau)^{1-\alpha}\sin\left(\frac{\alpha\pi}{2}\right)+(\omega\tau)^{2-2\alpha}\right)^{\beta/2}} + \frac{\sigma'}{\varepsilon_0\omega^s} \quad (3.7)$$

where $\varphi = tan^{-1}\left(\frac{(\omega\tau)^{1-\alpha}\cos(\alpha\pi/2)}{1+(\omega\tau)^{1-\alpha}\sin(\alpha\pi/2)}\right)$

The first term of equation (3.7) provides the information about the loss associated with the relaxation of dipoles without involvement of long-range movement of mobile charge

carriers, whereas the second term represents the losses associated due to long-range motion of the charge carriers. The equation (3.6) reveals that the localization of charge carriers at defect sites and interfaces lead to higher σ'' and hence larger ε'. According to equation (3.7), the free charge carriers give rise to larger σ' and hence ε'' also increases. As the temperature is increased, the conductivity contribution towards permittivity is more prominent. The experimental data of ε' and ε'' were analyzed by fitting the data using the equations (3.6) and (3.7). The solid lines in Fig. 3.9 represents the fitted data and they closely follow the experimental data (symbols) within the measured frequency range. From the above analysis, the ε_∞ value is found to increase from 35 for y = 0 to 102 for y = 0.5 at characteristic frequency of 1 MHz. The $\Delta\varepsilon$, σ' and σ'' values are found to increase with increase in temperature as well as the Ni concentration. The value of α does not show much variation at 353 K, but it varies from 0.29 – 0.08 for x = 0 – 0.5 samples at high temperature (473 K). The value of β is found to decrease systematically with Ni concentration, i.e. from 1 for y = 0 to 0.68 for y = 0.5 sample at 353 K. However, at high temperatures (473 K), the value of β increases towards 1 with Ni doping. The substitution of Ni is found to increase the conductivity values. Since the samples are sintered at higher temperature for long duration, there is a possibility of creation of oxygen vacancies and further, due to the reduction tendency of Ni, the Ni^{2+} ion can easily transfer to Ni^{3+} state [98]. To maintain the charge neutrality, some of the Fe^{3+} may transferred to Fe^{2+} state by the following relation as; $Fe^{3+} + Ni^{2+} \leftrightarrow Fe^{2+} + Ni^{3+}$. As the conductivity in ferrites occur due to hopping mechanism between Fe^{2+} and Fe^{3+} ions at octahedral sites, the increase in conductivity can be attributed to the possible electron transfer between Fe^{2+} and Fe^{3+} ions and the hole transfer between Ni^{2+} and Ni^{3+} ions [99]. Further, since the conductivity is directly related to the dielectric constant and dielectric loss as per the equations (3.6) and (3.7) and the dielectric constant also increases upon Ni substitution. All the fitted parameters such as $\Delta\varepsilon$, α, β, σ' and σ'' at 353 K and 473 K are given in Table 3.3.

Table 3.3: The fitted parameters such as Δε, α, β, σ' and σ'' of BFNO samples as per the analysis using equations (3.6) and (3.7).

y	$\Delta\varepsilon$ (10^3 K)		α		β		σ'(10^{-6} s/m)		σ''(10^{-6} s/m)	
	(353K)	(473K)	(353K)	(473K)	(353K)	(473K)	(353K)	(473K)	(353K)	(473K)
0	0.11	15.67	0	0.29	1	0.64	0.10	0.39	2.9	0.25
0.1	3.70	12.47	0	0.05	1	0.66	0.79	46.40	0.51	12.70
0.2	4.23	11.51	0	0.05	1	0.63	1.39	133.91	0.78	16.61
0.3	4.05	15.92	0	0.06	0.71	0.61	2.31	624.53	2.01	30.22
0.4	7.50	19.43	0.09	0.10	0.73	0.76	1.70	2381.9	1.87	48.76
0.5	10.24	20.18	0.03	0.08	0.68	0.70	6.75	5141.7	4.63	92.17

Fig. 3.11 depicts the dielectric loss tangent ($\tan\delta = \varepsilon''/\varepsilon'$) as a function of frequency for y = 0, 0.1, 0.3 and 0.5 samples at different temperatures from 303 K to 473 K. A dielectric relaxation peak is observed for all the samples for measurements carried out at different temperatures. However, for y = 0 sample, the peak is observed for $T >$ 353 K and this can be understood in terms of peak shifting below the measured frequency limit of the setup. The relaxation peak occurs when the hopping frequency of charges match with the frequency of applied ac electric field and the presence of the peak in $\tan\delta$ could be due to the relaxation of active dipoles. As the temperature is increased, the peaks are found to shift towards the higher frequency range with slight increase in peak intensity. This shifting of peak can be attributed to the increase in hopping frequency with increase in temperature. In the low frequency region, the $\tan\delta$ values are found to decrease with increase in Ni concentration. At higher frequency range, an increasing trend of $\tan\delta$ is noticed and this

can be attributed to the occurrence of onset of another loss peak at high frequency regime. The tanδ value for y = 0 sample is found to be 4.68 and it decreases drastically to 0.54 for y = 0.5 in the measuring frequency of 100 Hz at 303 K. With increase in Ni concentration for $y \geq 0.3$, the tanδ spectra exhibit a valley like behavior i.e. tanδ has high value at low and high frequency region followed by a minimum at intermediate frequency range. The relatively large tanδ values observed in the low frequency region can be attributed to grain boundaries contributions having large resistance. This can be understood due to the large time scale (low frequency) of applied electric field and the charge carriers are transported in long-range covering grain boundaries. However, in the mid-frequency region, the small time scale of electric field gives rise to predominant grains contributions having small resistance in short-range scale. Further, the tanδ is found to decrease with increase in Ni concentrations. This can be attributed to the decrease in number of grain boundaries due to increase in grain sizes.

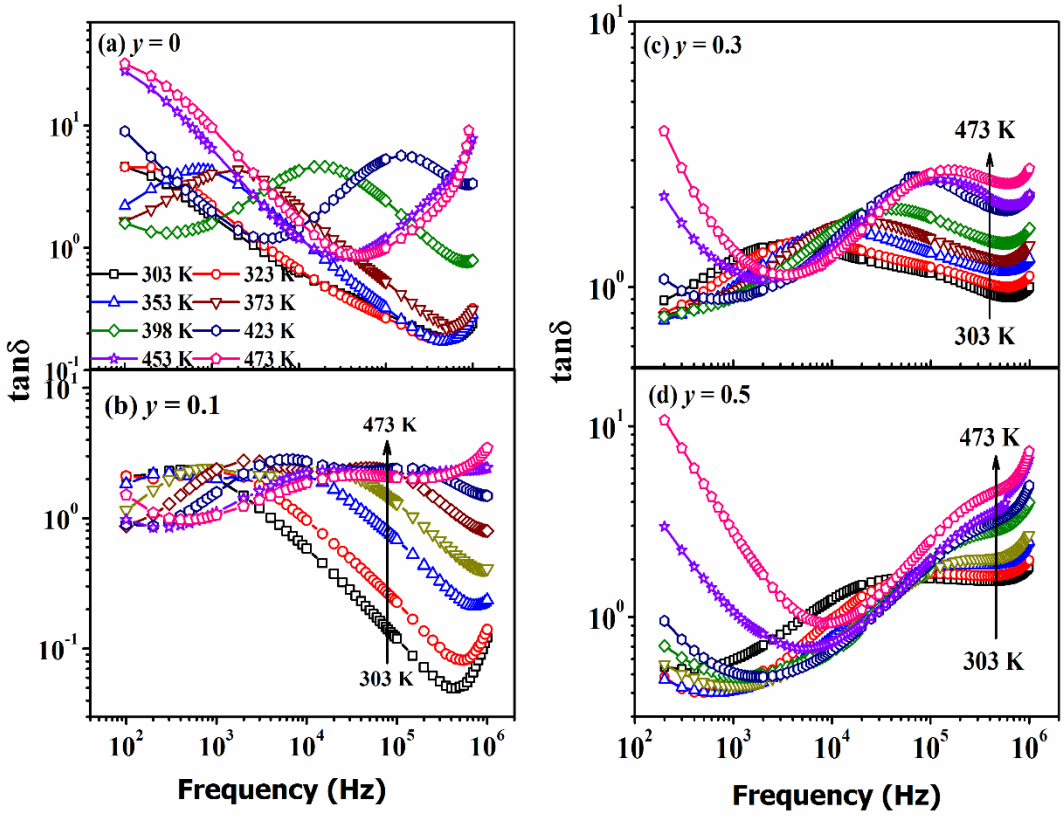

Figure 3.11: Frequency variation of tanδ for BFNO samples with y = 0, 0.1, 0.3 and 0.5 (a-d) at selected temperatures in the range of 303 K to 473 K.

3.1.5 Magnetic Properties

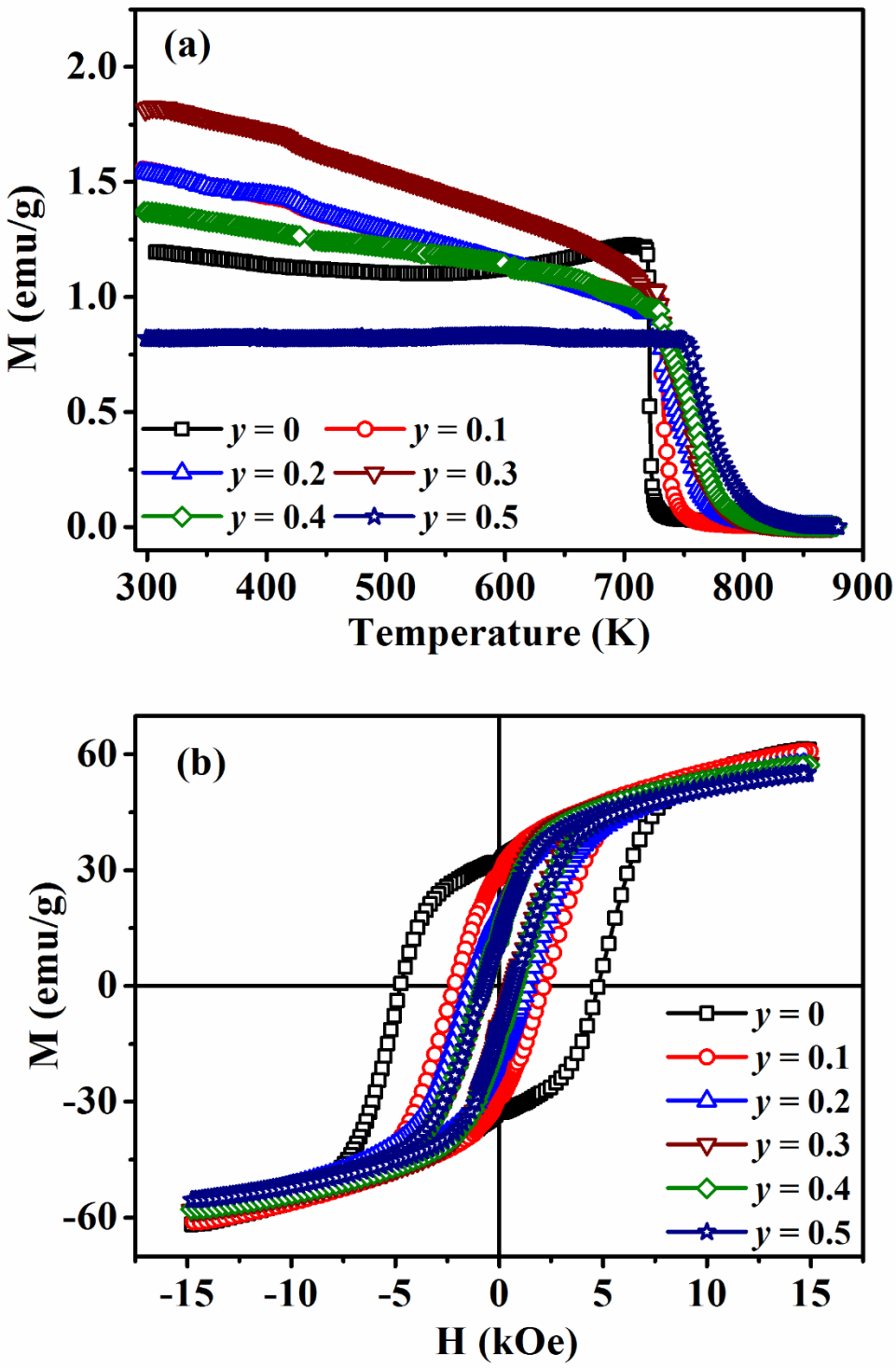

Figure 3.12: (a) Temperature dependence of magnetization from 300 K to 873 K and (b) Room temperature *M* – *H* loops of BFNO (*y* = 0, 0.1, 0.2, 0.3, 0.4 and 0.5) samples.

The temperature dependence of magnetization measurements of BFNO samples were carried out under zero field cooled (ZFC) mode with the applied field of 100 Oe. Fig. 3.12(a) shows the magnetization versus temperature ($M - T$) plots for y = 0, 0.1, 0.2, 0.3, 0.4 and 0.5 samples. All the samples are found to exhibit the ferrimagnetic behavior and the ferrimagnetic transition (T_c) is observed in the measured temperature range of 300 K to 873 K. The T_c values were determined from the minima of dM/dT versus temperature plots. The T_c value for y = 0 sample is found to be 720 K and is comparable with the earlier literatures [50, 100]. However, the T_c value is found to increase with increase in Ni concentrations from 720 K for y = 0 to 759 K for y = 0.5 due to enhancement in superexchange interaction [72]. In other words, the increase in T_c due to the substitution of Ni at Fe site in BaM hexaferrite suggests the strengthening of superexchange interaction among the magnetic sublattices. Furthermore, the magnetic properties are intricately related to oxygen off-stoichiometry or vacancy and such vacancies are expected to reduce the superexchange interaction [101]. Here the improvement in T_c can be attributed to reduction in oxygen vacancies.

Further, to get more understanding on the magnetic properties of these materials, the magnetic hysteresis ($M - H$) loops of BFNO samples were recorded at room temperature. Fig. 3.12(b) shows the $M - H$ loops of BFNO samples with y = 0, 0.1, 0.2, 0.3, 0.4 and 0.5. The saturation magnetization (M_s) and coercivity (H_c) values are found to decrease with increase in Ni concentrations. There are five different crystallographic sites for Fe^{3+} ions in BaM hexaferrites such as; three octahedral (Fe_1 – 2a, Fe_4 – $4f_2$, Fe_5 – 12k), one tetrahedral (Fe_3 – $4f_1$) and one trigonal bi-pyramidal site (Fe_2 – 2b) [102, 103]. In the earlier reports, researchers have shown that the magnetic moment per Fe^{3+} ion at different crystallographic sites are different [104, 105]. From neutron diffraction study, the magnetic moment per Fe^{3+} ions at different sites are reported to be Fe_1 = 3.42 μ_B , Fe_2 = 3.42 μ_B, Fe_3 = 3.90 μ_B, Fe_4 = 3.17 μ_B and Fe_5 = 3.59 μ_B respectively [105]. Thus the preferred site occupation of Ni ion decides the magnetic moment of the respective sublattices and the net magnetic moment. As per the earlier reports on hexaferrite, Ni^{2+} ions occupy the $4f_2$ and 12k sites for the low level of substitution and 12k site for higher substitutions [77]. Such substitutions at spin up site is expected to reduce the overall magnetization in Ni doped system. Therefore, the substitution of Fe^{3+} by Ni^{2+} ions reduce the net magnetic moment. The experimental M_s values were determined by using the law of approach to saturation (LAS) model [106];

$$M = M_s \left(1 - \frac{A}{H} - \frac{B}{H^2}\right) + \chi_d H \qquad (3.8)$$

where M_s is the saturation magnetization, the term A arises due to sample inhomogeneity and structural defects, and the term B represents the magnetocrystalline anisotropy contribution. The term $\chi_d H$ is related to field induced increase in the spontaneous magnetization of the domains and it is active for high temperature analysis. However, the A value is assumed to be zero due to its low value in this field range. Thus the 2nd (A/H) and 4th ($\chi_d H$) terms in equation (3.8) can be neglected [107]. The fitting of the LAS model to the initial magnetization curve provides the exact saturation magnetization value of the samples excluding the linear forced magnetization part. In the present case, the initial magnetization curves were fitted by using the above expression (3.8) by neglecting the 2nd and 4th terms. The experimental magnetization (M) data were plotted against the inverse square of applied magnetic field ($1/H^2$) and a straight line is obtained in the field range of 12 kOe to 15 kOe. By using modified LAS model, these straight lines were analyzed for all the samples and are shown in Fig. 3.13. The symbols denote the experimental data while the fitted data are shown as solid lines. It is known that magnetic anisotropy is one of the important parameter for magnetic materials. The constant B in the above mentioned equation (3.8) is related to the effective magnetic anisotropy. Thus, the experimental saturation magnetization (M_s) and the constant B values were obtained by fitting the data to the above equation (3.8). The anisotropy field (H_a) can be estimated by employing the relation [9];

$$B = \frac{H_a^2}{15} \qquad (3.9)$$

The effective magnetic anisotropy constant (K_1) was calculated by using the following relation;

$$H_a = \frac{2K_1}{M_s} \qquad (3.10)$$

The H_a and K_1 values were determined from equations (3.9) and (3.10). The anisotropy constant K_1, M_s and H_c values are found to decrease with increase in Ni concentrations. The reduction in M_s value may cause the reduction in K_1 values in the doped samples. For $y = 0$ sample, the M_s value is 68.16 emu/g and is decreased to 58.99 emu/g for $y = 0.5$ sample. The decrease in M_s values can be attributed to the smaller magnetic moment of Ni^{2+} (2 μ_B)

ions as compared to that of Fe^{3+} (5 μ_B) ions. Further, the coercivity (H_c) of the samples were determined by employing the following relation as;

$$H_c = (H_+ - H_-)/2 \qquad (3.11)$$

where H_+ and H_- are two magnetic field values of the ascending and descending branch of $M - H$ loop corresponding to $M_s = 0$. The parent compound i.e. $y = 0$ sample exhibits high coercivity value and can be ascribed due to the uniaxial magnetocrystalline anisotropy along the *c*-axis. It is known that in ferrite materials, the magnetocrystalline anisotropy and particle sizes are responsible for the change in H_c values. The increase in particle size with Ni substitution may cause the decrease in coercivity. Thus, the decrease in H_c values with Ni substitution can be attributed to the increase in particle size and the reduction in magnetocrystalline anisotropy. The values of magnetic parameters such as M_s, H_c, H_a and K_1 are given in Table. 3.4. Similar results have been reported in Zn substituted barium hexaferrite [107].

Table 3.4: The values of M_s, H_c, H_a and K_1 at room temperature for different Ni concentrations.

y	***M_s* (emu/g)**	***H_c* (Oe)**	***H_a* (10^4 Oe)**	***K_1* (10^6 erg/cc)**
0	68.16	4731	15.26	5.20
0.1	66.55	2153	14.09	4.68
0.2	63.09	1406	13.82	4.36
0.3	62.58	660	12.81	4.01
0.4	61.48	758	12.09	3.71
0.5	58.99	683	11.49	3.39

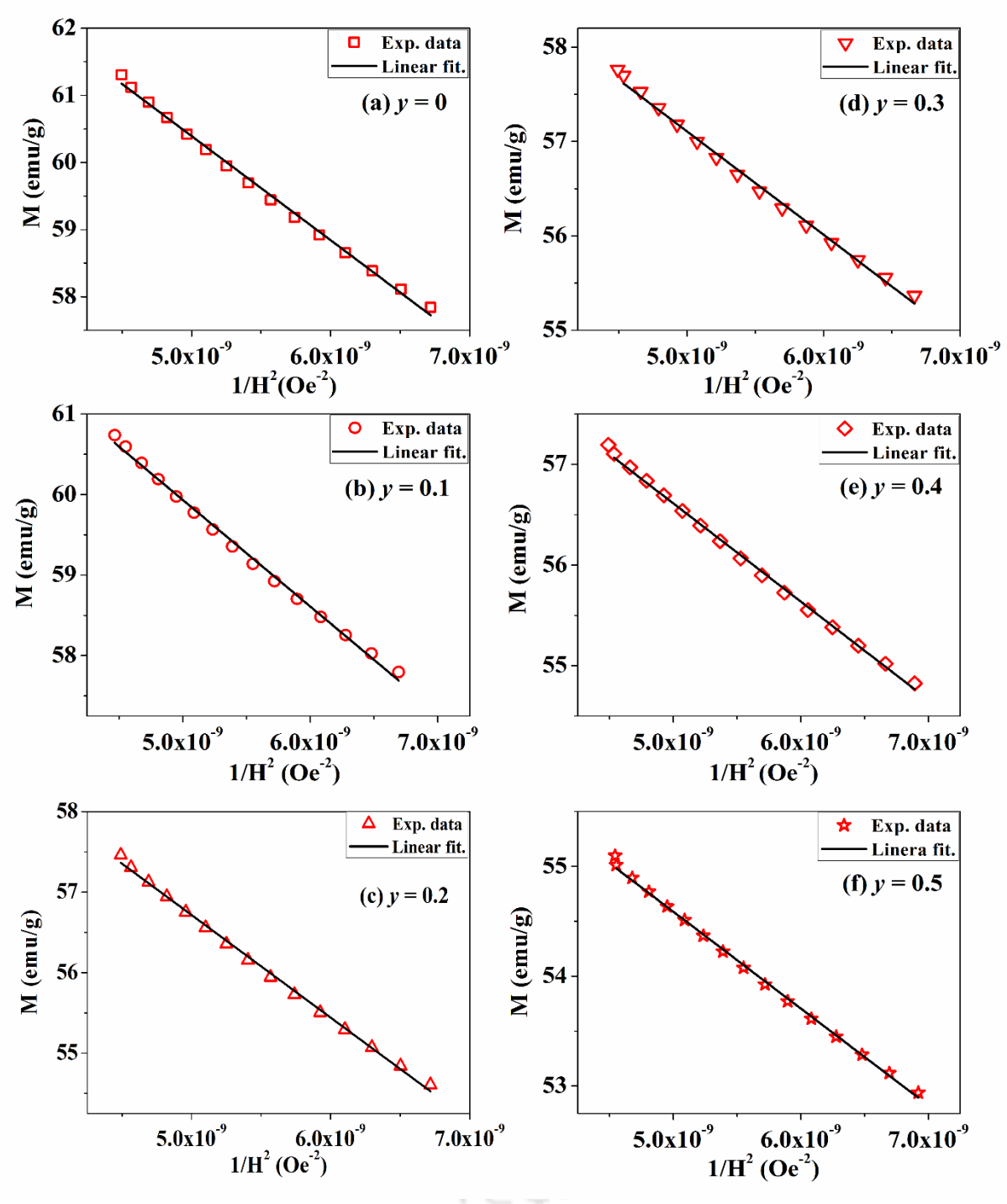

Figure 3.13: Room temperature magnetization (*M*) vs $1/H^2$ plots analysed by LAS (equation (3.8)) for BFNO samples with y = 0, 0.1, 0.2, 0.3, 0.4 and 0.5. Where the red symbols represent the experimental data and the solid line represents the fitted data

3.2 Ti Substituted $BaFe_{12}O_{19}$ Series

The following section deals with the influence of Ti substitution at the Fe site of $BaFe_{12}O_{19}$. The preparation of $BaFe_{12-y}Ti_yO_{19}$ (y = 0 – 0.8) samples along with their structural, dielectric and magnetic properties are presented in detail.

3.2.1 Sample Preparation and Characterization

Polycrystalline samples of $BaFe_{12-y}Ti_yO_{19}$ with y = 0, 0.2, 0.4, 0.6 and 0.8 were prepared via solid state reaction method. Stoichiometric amount of high purity (> 99.9%) constituent oxides/carbonates such as $BaCO_3$, Fe_2O_3 and TiO_2 were initially mixed and ground together using agate mortar and pestle. The obtained powders were calcined subsequently at 600 ℃ and 800 ℃ for 12 h. For better homogeneity, the calcined powders were ground and pressed into cylindrical pellets of diameter ~13 mm using a hydraulic press. These pellets were finally sintered at 1150 ℃ for 12 h in air. X-ray powder diffraction patterns of these samples were recorded at room temperature using Rigaku make TTRAX III X-ray diffractometer with CuK_α radiation. Microstructure and compositional analyses were performed using ZEISS make field emission scanning electron microscope (Model. ΣIGMA) equipped with an energy dispersive X-ray spectrometer (EDX). Magnetization measurements were performed by varying temperatures from 30 K to 773 K and the room temperature magnetic hysteresis loop measurements were carried out using Lakeshore make vibrating sample magnetometer (VSM, model no.7410). The impedance spectra and electrical conductivity were measured at different temperatures from 303 K to 473 K in the frequency range from 100 Hz to 1 MHz using Wayne Kerr LCR meter of model no. 4300. The electrical contacts were made by applying the silver paste on both sides of the pellets of thickness around ~ 1 – 1.5 mm and diameter ~ 10 mm followed by drying for 4 h in a hot air oven.

3.2.2 Structural Analysis

The XRD patterns of $BaFe_{12-y}Ti_yO_{19}$ (BFTO) samples for y = 0 – 0.8 are shown in Fig. 3.14. Similar to Ni doped samples, no signature of structural transition is observed in these Ti doped samples. These XRD patterns were analyzed based on the Rietveld refinement technique using the FULLPROF program [92]. The XRD patterns were refined based on hexagonal structure (Space group: $P6_3/mmc$) [Goodness of fit (GOF) χ^2 of BaM ~ 1.94], and the analysis confirms the single-phase nature of the samples. Furthermore, the

formation of single-phase hexaferrite in Ti doped samples is confirmed by comparing XRD patterns with the standard JCPDS: 84 – 0757 pattern as shown in Fig. 3.14. The typical XRD patterns for y = 0, and 0.2 samples along with Rietveld refined data are shown in Fig. 3.15 and the patterns for y = 0.4 and 0.8 samples are shown in Fig. 3.16. The lattice constant a is almost constant while c is found to increase with increase in Ti concentration (23.206 Å for y = 0 to 23.260 Å for y = 0.8) and they are comparable to the literatures [9, 108]. The systematic increase in lattice constant c can be understood due to the incorporation of larger Ti^{4+} (0.68 Å) ions at Fe^{3+} (0.645 Å) site [109]. The variation of lattice parameters with Ti substitution and the reliability factors of Rietveld refinement are given in Table 3.5.

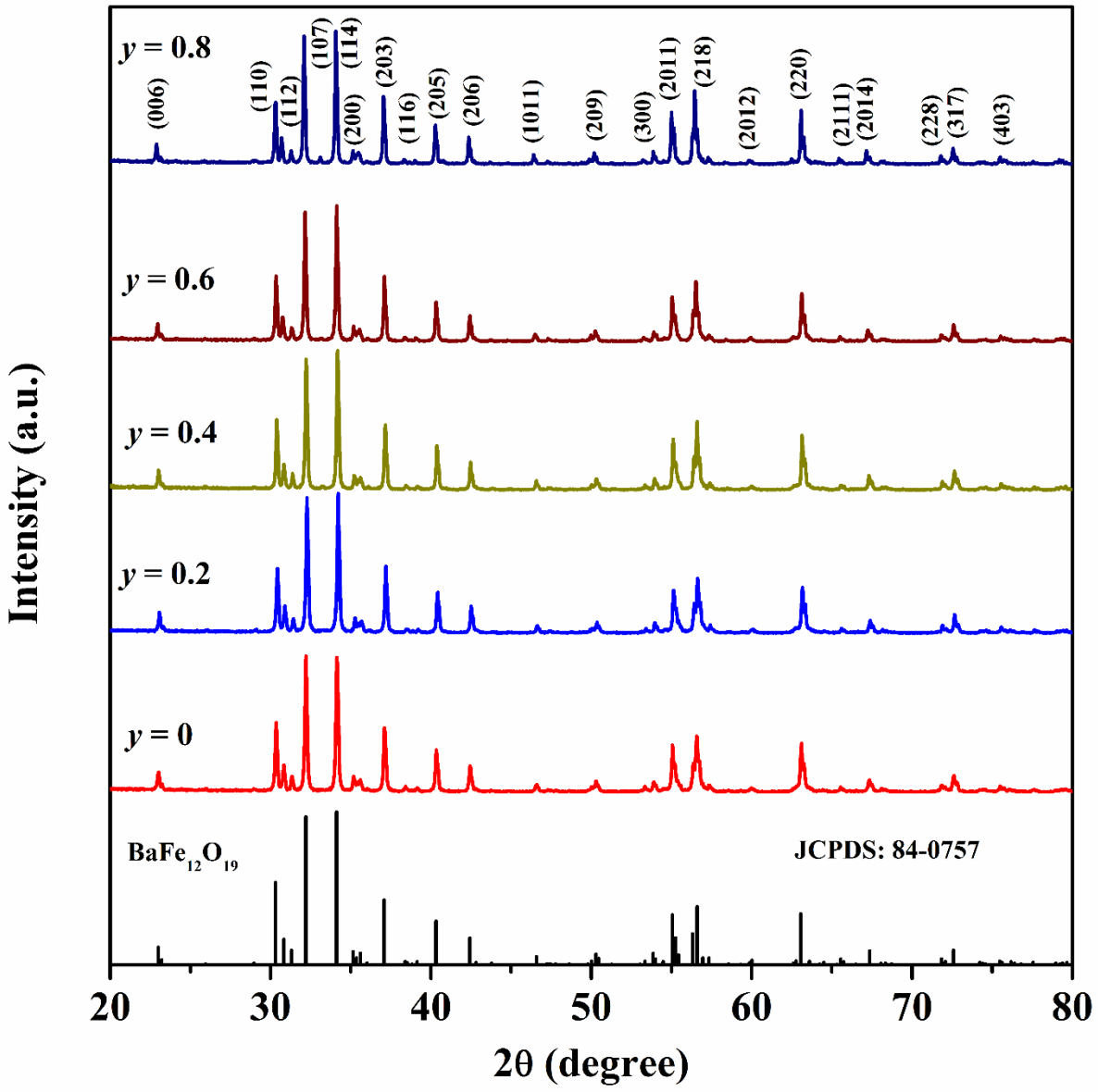

Figure 3.14: XRD patterns of BFTO samples for y = 0 – 0.8 recorded at room temperature.

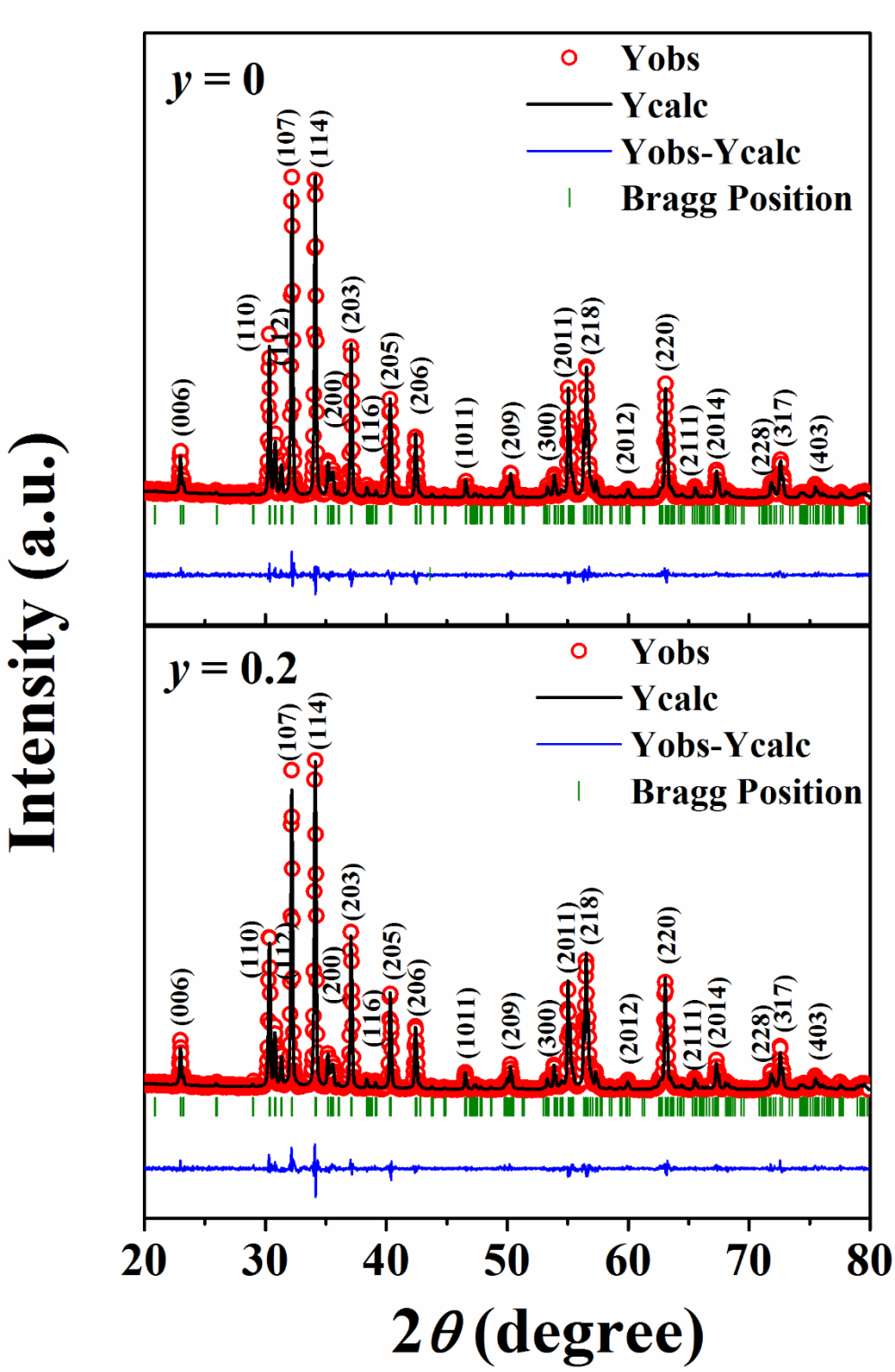

Figure 3.15: Rietveld refined XRD patterns of BFTO samples with y = 0 and 0.2. The red open circles represent the experimental data and the black solid lines are the fitted data. The bottom line represents the difference between experimental and refined data.

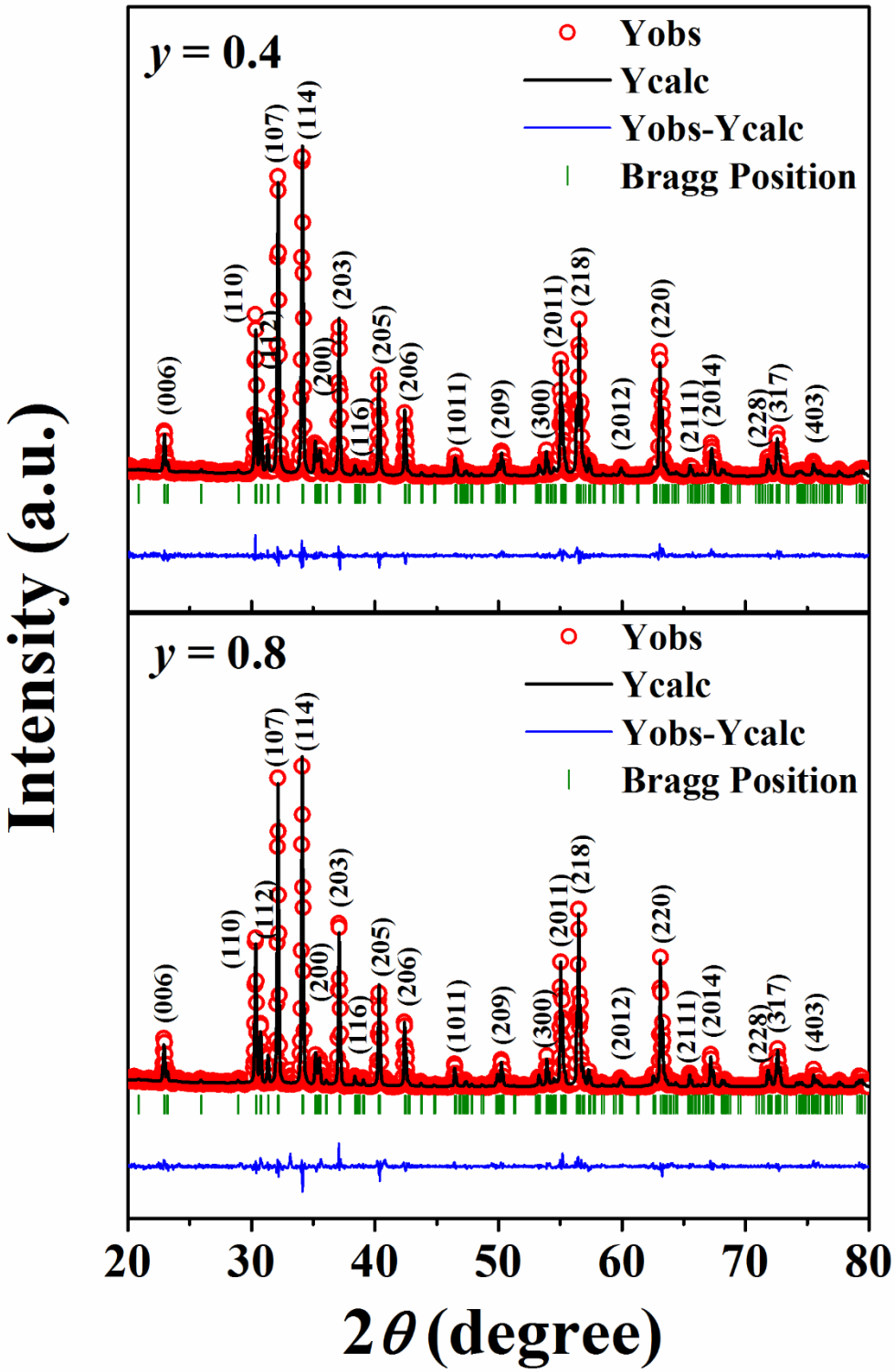

Figure 3.16: Rietveld refined XRD patterns of BFTO samples with y = 0.4 and 0.8. The red open circles represent the experimental data and the black solid lines are the fitted data. The bottom line represents the difference between experimental and refined data.

Table 3.5: Parameters obtained from the Rietveld analysis of XRD patterns for the samples $BaFe_{12-y}Ti_yO_{19}$ (y = 0 – 0.8). R_F, R_{Bragg}, R_P and χ^2 are the reliability factors.

Sample/ Parameters	***y* = 0**	***y* = 0.2**	***y* = 0.4**	***y* = 0.6**	***y* = 0.8**
Space group	*$P6_3/mmc$*	*$P6_3/mmc$*	*$P6_3/mmc$*	*$P6_3/mmc$*	*$P6_3/mmc$*
***a* (Å)**	5.8893(1)	5.8906(1)	5.8878(1)	5.8862(1)	5.8873(1)
***c* (Å)**	23.206(7)	23.2157(7)	23.2233(7)	23.2376(7)	23.2601(7)
***Volume* (Å^3)**	696.97(3)	697.66(2)	697.21(1)	697.25(2)	698.18(1)
R_F (%)	2.37	2.85	2.97	2.85	4.83
R_{Bragg} (%)	2.32	2.64	2.95	2.89	4.57
R_P (%)	10.9	11.9	12.4	12.3	15.2
R_{exp} (%)	10.56	10.88	11.48	10.88	11.79
χ^2	1.94	2.03	2.11	2.22	2.73

Fig. 3.17(a-c) show the FESEM micrographs of Ti doped BaM hexaferrites for y = 0, 0.4 and 0.8 samples. Hexagonal shaped grains of different sizes are visible in both parent and doped M-type hexaferrites. The grains of different sizes are found to be distributed over a wide range as depicted in Fig. 3.17(d-f). From the distribution histograms, the average grain sizes were determined by fitting log-normal distribution function as discussed in equation (3.1). The average grain size value is found to increase with Ti concentration i.e. from 0.63 µm for y = 0 to 1 µm for y = 0.8 sample. Further, it is known that the grain size is one of the most important parameter that affects the magnetic properties of the materials. Larger the grain size, smaller will be the grain boundaries volume and it effectively suppresses the coercivity values due to the lack of pinning of magnetic moments at the grain boundaries. Further to verify the elemental ratio of the samples, the EDX

spectra were recorded at room temperature for y = 0 and 0.8 samples as shown in Fig. 3.18. The presence of Ba and Fe (y = 0) along with Ti (y = 0.8) is confirmed from the EDX spectra. The analysis of EDX spectra reveals that the cationic ratios of Ba: Fe: Ti for y = 0 and 0.8 samples are found to be 1.07: 11.91: 0.00 and 0.92: 11.35: 0.71 respectively and are comparable with the nominal starting compositions.

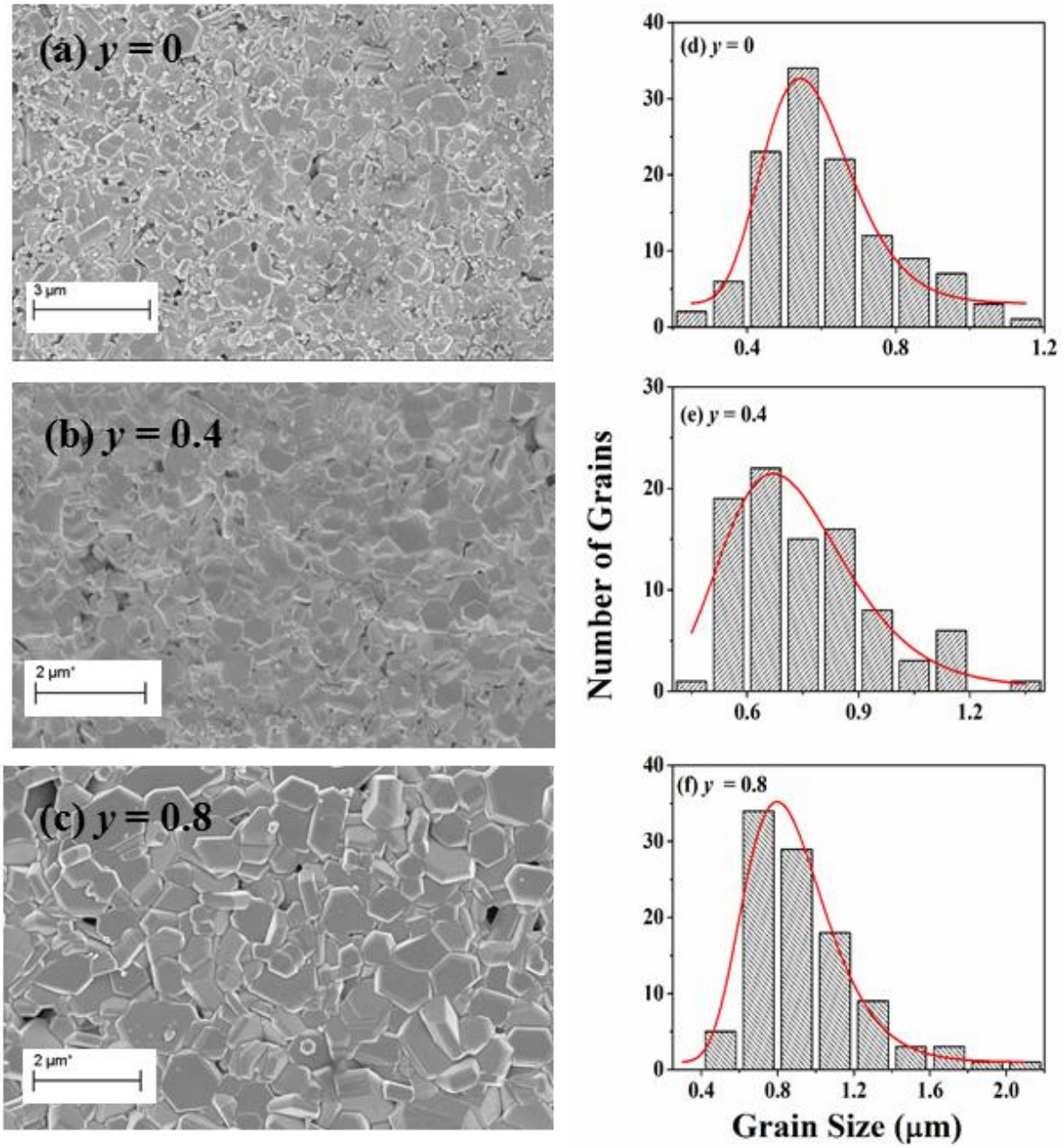

Figure 3.17: (a-c) FESEM micrographs of Ti doped BaM samples for y = 0, 0.4 and 0.8 along with their grain size distributions (d-f).

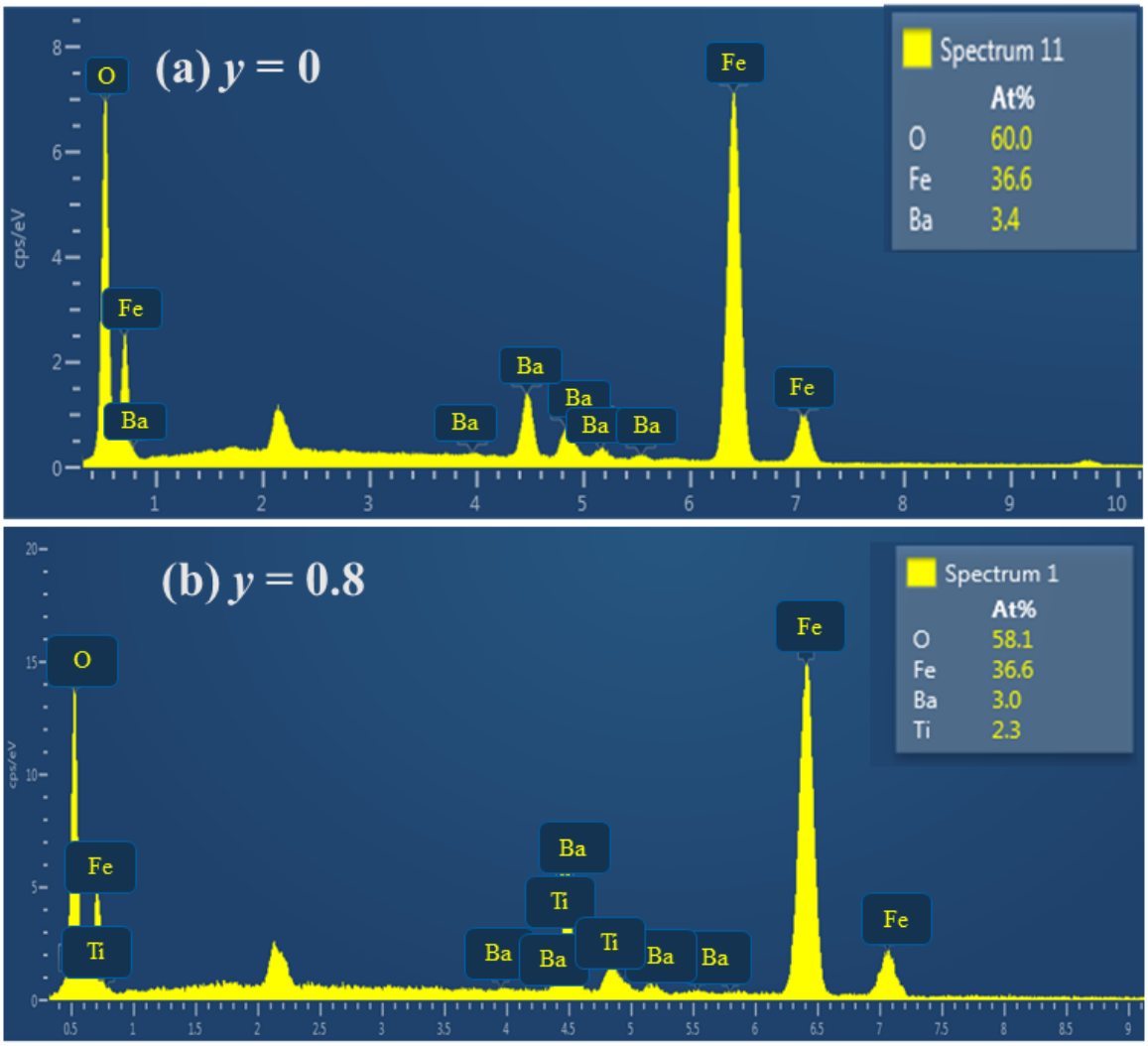

Figure 3.18: EDX spectra of BFTO hexaferrite for (a) y = 0 and (b) y = 0.8 samples.

3.2.3 Complex Impedance Spectroscopy Analysis

As discussed in the earlier section that the Impedance spectroscopy is one of the important techniques used to understand the electrical transport behavior of the polycrystalline samples. The electrical properties of the materials are due to different contributions such as grains, grain boundaries and electrode interfaces. The impedance spectra of Ti doped BaM hexaferrites were measured as a function of frequency in the range of 100 Hz to 1 MHz. Fig. 3.19 shows the variation of the real part of impedance (Z') as a function of frequency for y = 0, 0.2, 0.4 and 0.8 samples in the temperatures range of 323 K to 473 K. At a particular temperature, the Z' value is found to decrease with increase in frequency. Further, the magnitude of Z' is also found to decrease with increase in temperature and it corresponds to the negative temperature coefficient of resistance. Moreover, the magnitude of Z' exhibits a step-like behaviour in the measured frequency

range and they tend to merge at a higher frequency (≥ 10^5 Hz). This type of behaviour signifies the presence of the dielectric relaxation process in the samples. The merging of impedance spectra at higher frequencies is due to the release of space charges. The magnitude of Z' is found to decrease with increase in Ti concentration and it indicates that the substitution of Ti have large influence on its electrical properties.

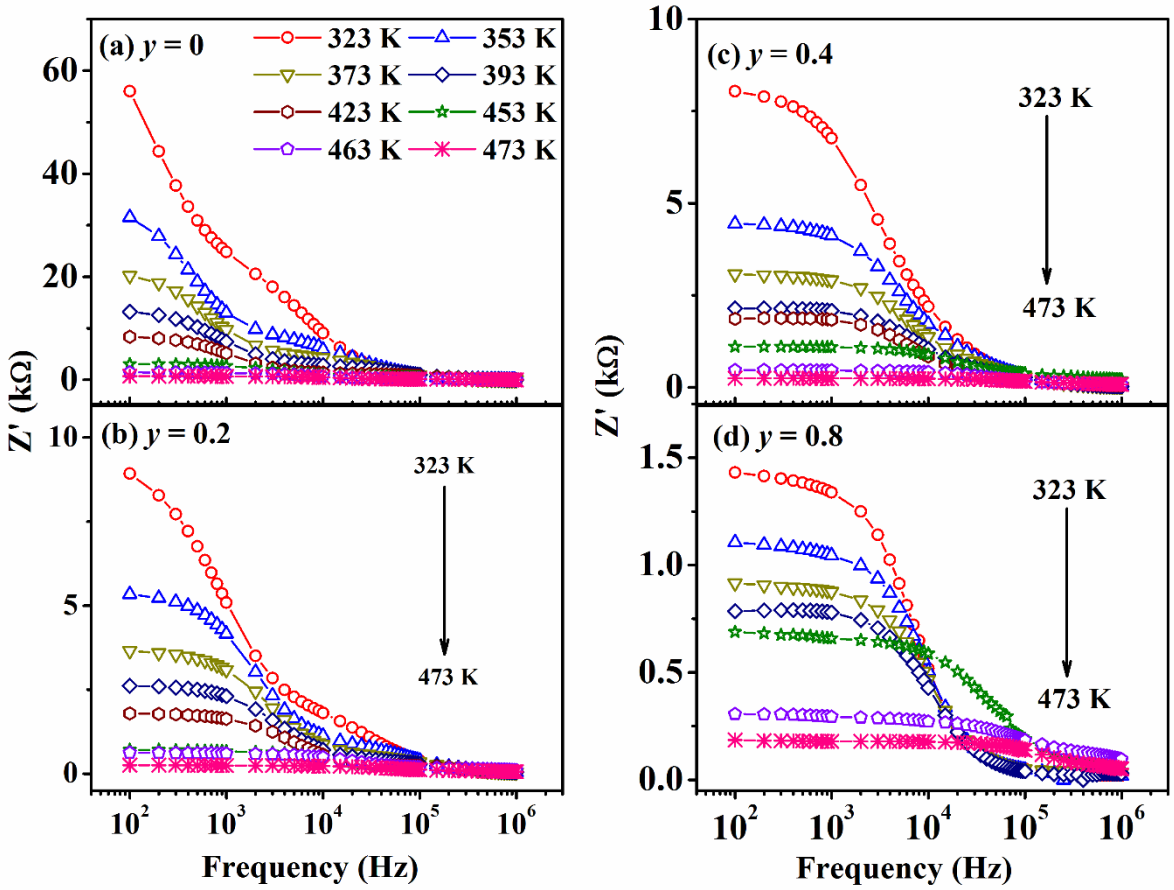

Figure 3.19: Real part of complex impedance (Z') versus frequency of Ti doped BaM hexaferrite for (a-d) y = 0, 0.2, 0.4 and 0.8 samples in the temperature range of 323 K to 473 K.

The imaginary part (Z'') of the complex impedance as a function of frequency is shown in Fig. 3.20 for $BaFe_{12-y}Ti_yO_{19}$ samples with y = 0, 0.2, 0.4 and 0.8 at different temperatures from 323 K to 473 K. The impedance spectrum observed for y = 0 sample exhibits two relaxation peaks at a particular temperature with different characteristic frequencies (f_{max}). The relaxation peak observed at higher frequency is broader than that of the low-frequency peak. However, only one relaxation peak is observed for Ti doped samples [Fig. 3.20(c-d)] except for y = 0.2 sample where a high frequency shoulder is

observed close to room temperature. The presence of relaxation peaks in the Z'' spectra demonstrate the relaxation of charge carriers towards the applied electric field. As the temperature is increased, the magnitude of relaxation peak is found to be suppressed and the peak position is shifted towards the higher frequency region. This indicates that the electrical properties are thermally activated due to the presence of space charges at grain boundaries [110, 111]. In order to understand that whether the distribution of relaxation time is temperature dependent or not, the impedance spectra were plotted by normalizing them, i.e. by plotting Z''/Z''_{max} vs $\log(f/f_{max})$ as shown in Fig. 3.21. This plot is also called the scaling behavior of impedance (Z'') spectra. The merging of loss peaks of impedance spectra into a single master curve signifies that the distribution of relaxation time is temperature independent [110]. Fig. 3.21 indicates that all the peaks merge into a single master curve for all the temperatures. Thus, it indicates that the dynamic behavior of the charges occurring at different time scales give rise to same activation energy and that the distribution of relaxation time is temperature independent.

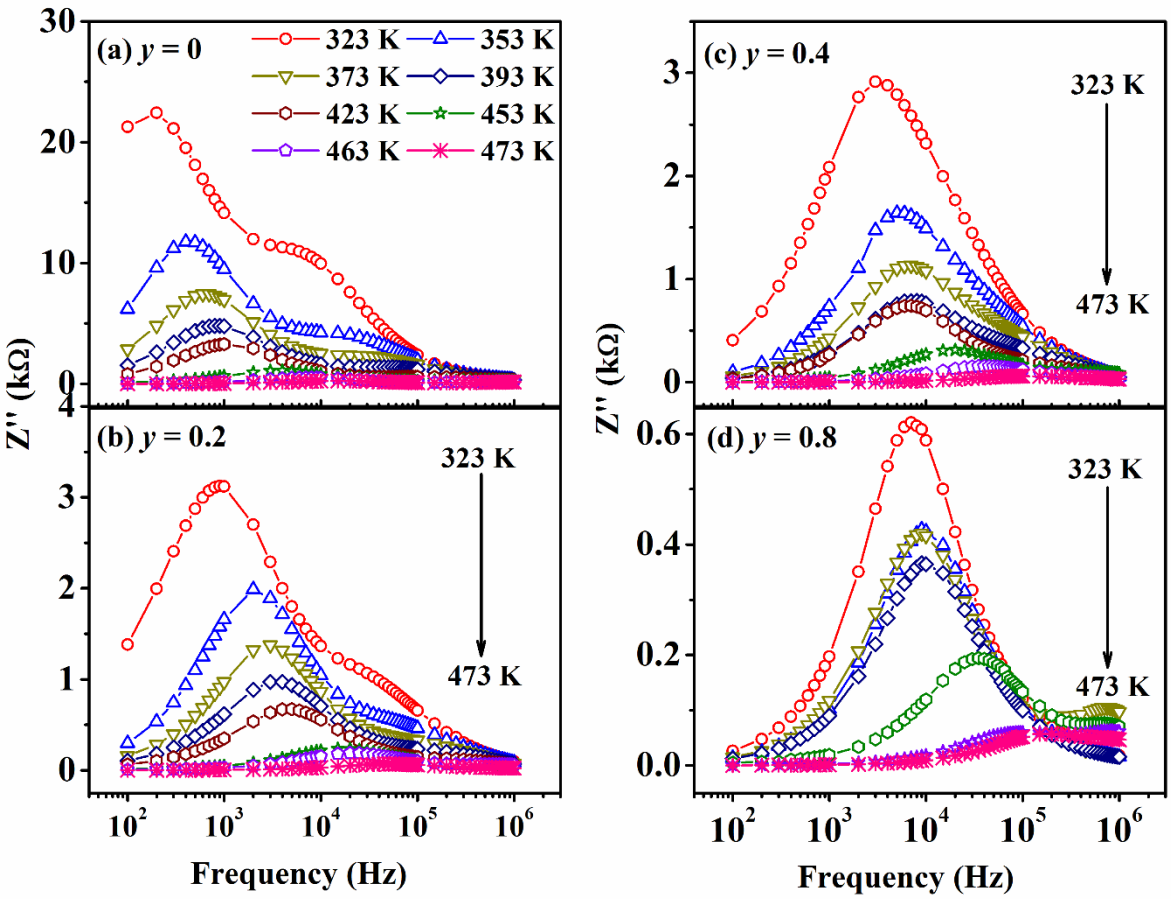

Figure 3.20: Imaginary part of complex impedance (Z'') versus frequency of Ti doped BaM hexaferrite samples for (a-d) y = 0, 0.2, 0.4 and 0.8 in the temperature range of 323 K to 473 K.

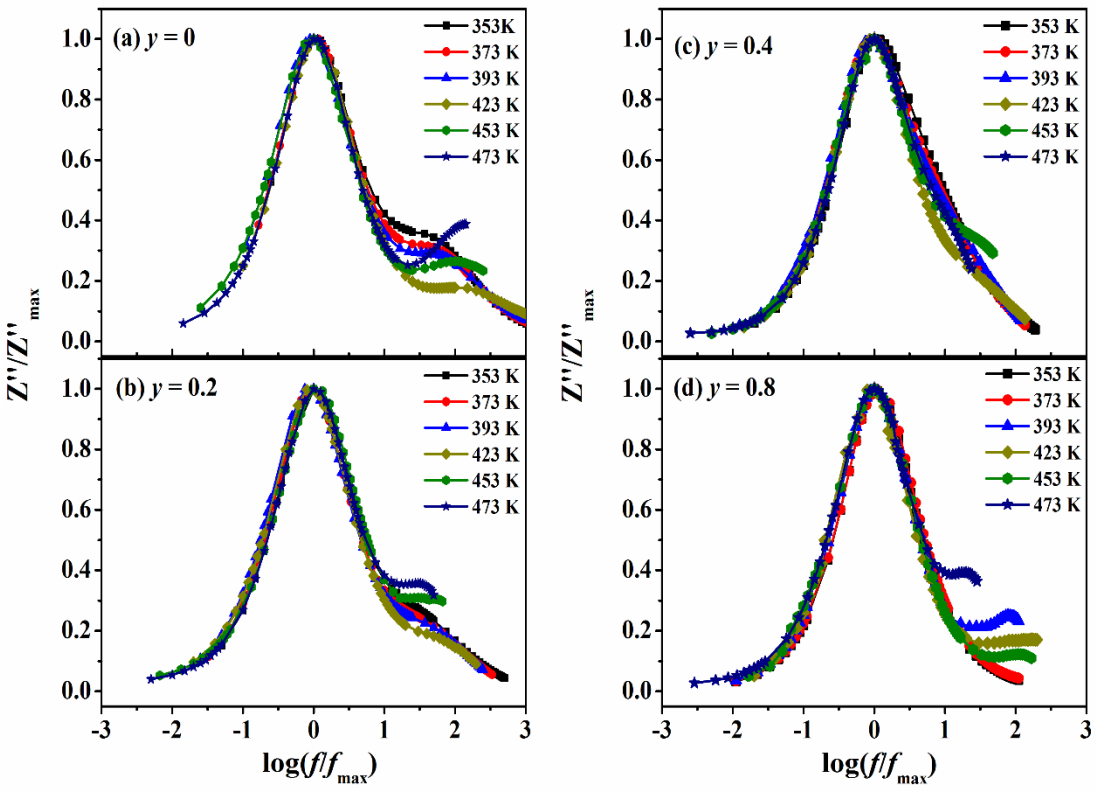

Figure 3.21: Scaling behaviour of Z'' spectra of BaM hexaferrite measured at different temperatures for (a-d) y = 0, 0.2, 0.4 and 0.8 samples respectively.

The Nyquist plots of BaM hexaferrite for y = 0, 0.2, 0.4 and 0.8 samples measured at different temperatures ranging from 323 K to 473 K are shown in Fig. 3.22(a-d). The Nyquist plots of all the samples depict depressed semicircular arc i.e. with its centre lying below the Z' axis and it signifies the deviation from the ideal Debye-type relaxation. As discussed in the earlier section 3.1.3, such deviation from the ideal Debye type behavior in impedance spectroscopy can be interpreted in terms of a constant phase element (*CPE*, denoted by *Q*). The radius of the semicircle is found to decrease with increase in temperature and it can be attributed to the decrease in resistance of the samples as the temperature is raised. For y = 0 and 0.2 samples, two distinct semicircular arcs are observed. The larger semicircular arc appearing at lower frequency (higher Z') region is attributed to the grain boundaries (GB) contributions, whereas the semicircular arc observed in the high frequency region (lower Z') is due to the contribution of grains (G). With increase in Ti

concentration (y > 0.2), the Nyquist plots exhibit a single semicircular arc at different temperatures. In order to confirm the charge carriers' contributions towards the relaxation dynamics inside the grains or across the grain boundaries, an equivalent electrical circuit was proposed. However, it is interesting to note that, the single semicircular arc is explained based on the equivalent circuit shown in Fig. 3.22(g). Here R_g and R_{gb} represent the grains and grain boundaries resistance respectively, and C_g and Q_{gb} represent the capacitance and the constant phase element associated with grains and grain boundaries respectively. Thus, it is concluded that the contributions of both grains and grain boundaries, towards the relaxation process are present in both parent and Ti doped samples.

From the Nyquist plot fitting, one can estimate the grains and grain boundaries conductivity contributions by employing the relation $\sigma_g = \frac{t}{SR_g}$ and $\sigma_{gb} = \frac{t}{SR_{gb}}$, where t represents the thickness of the sample and S is the area of the sample. The grains conductivity (σ_g) and grain boundaries (σ_{gb}) conductivity follow the Arrhenius law as [112];

$$\sigma = \sigma_0 exp(\frac{E_r}{k_B T}) \qquad (3.12)$$

Here σ_0 is the prefactor, k_B is the Boltzmann's constant and E_r is the relaxation activation energy. The activation energy due to grains (E_g) and grain boundaries (E_{gb}) were determined from the linear fit of $ln\sigma_g$ and $ln\sigma_{gb}$ versus $10^3/T$ plots as shown in Fig. 3.22(e-f). The E_g and E_{gb}values are found to vary from 0.32 – 0.14 eV and 0.40 – 0.17 eV respectively for y = 0 to 0.8 samples. The estimated activation energy values due to grains are almost comparable to the activation energy of hopping of charge carriers between Fe^{2+} and Fe^{3+} ions. Thus, the electrical conduction in the grains are mainly due to the hopping of charge carriers between Fe^{2+} and Fe^{3+} ions. Further, the substitution of Ti for Fe may increase the hopping process and results net reduction in activation energy inside the grains. In addition, the electrical conduction across the grain boundaries are due to the singly (E_r <0.7 eV) and doubly (E_r >0.7 eV) ionized oxygen vacancies. The estimated value of activation energy across the grain boundaries is attributed to the single ionized oxygen vacancies. The substitution of Ti may increase the concentration of oxygen vacancies in the material by resulting the reduction in activation energy across grain boundaries. The variation activation energies due to grains and grain boundaries contributions are tabulated in Table 3.6.

Table 3.6: Activation energy for relaxation of charge carriers across grains (E_g) and grain boundaries (E_{gb}) for various samples in $BaFe_{12-y}Ti_yO_{19}$ Series.

Samples	E_{gb} (eV)	E_g (eV)
***y* = 0**	0.40	0.32
***y* = 0.2**	0.34	0.27
***y* = 0.4**	0.26	0.24
***y* = 0.6**	0.24	0.20
***y* = 0.8**	0.17	0.14

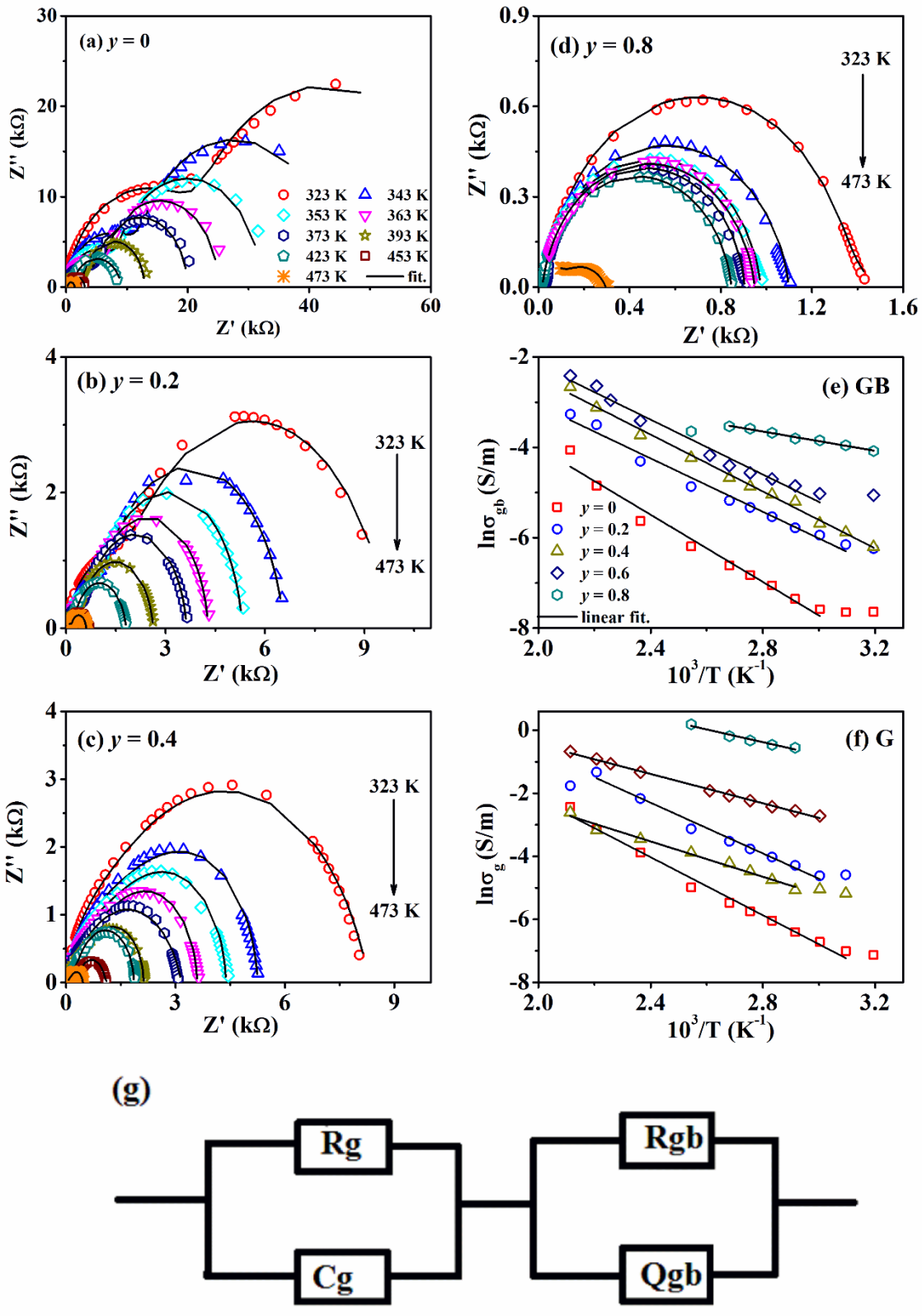

Figure 3.22: (a-d) Nyquist (*Z''* vs *Z'*) plots of Ti doped BaM hexaferrite for *y* = 0, 0.2, 0.4 and 0.8 samples in the temperature range of 323 K to 473 K, (e-f) $ln\sigma$ vs $10^3/T$ plots along with fitted (solid line) data using the Arrhenius law for both grains and grain boundaries

contributions and (g) the equivalent electrical circuit modelled for the fitting of Nyquist plots.

3.2.4 Electrical Conductivity Analysis

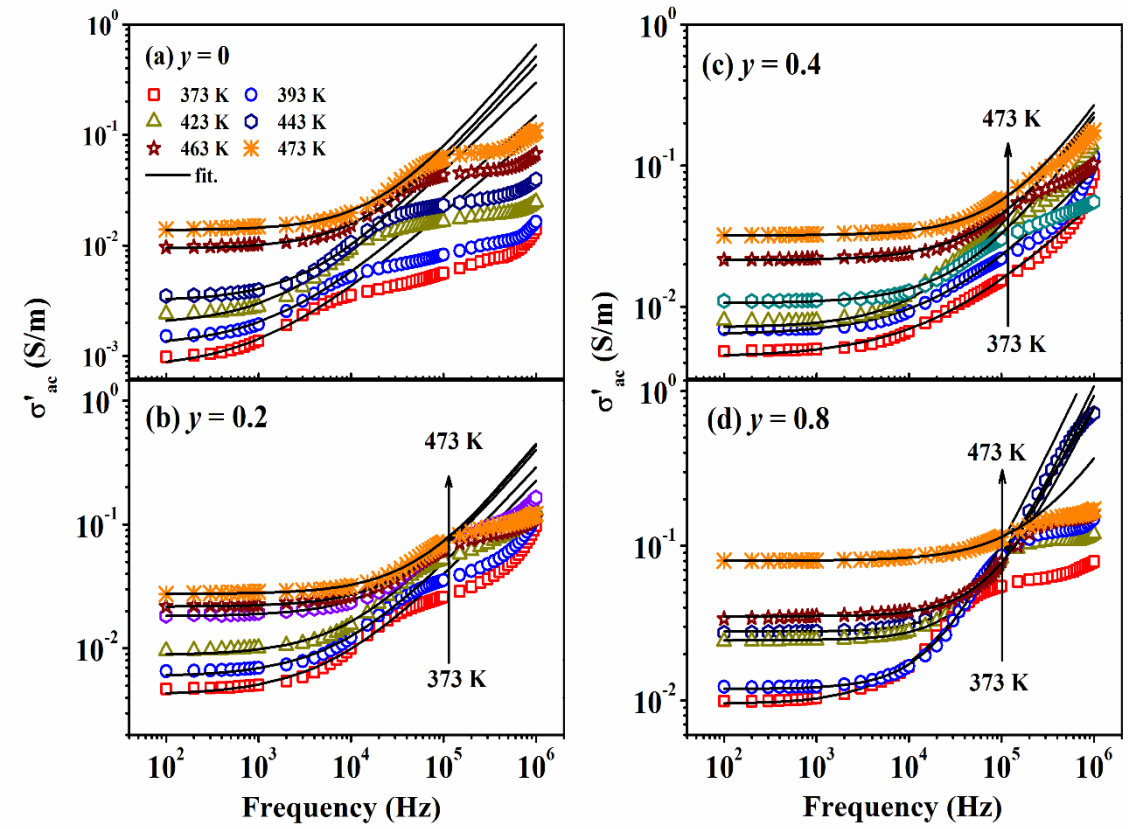

Figure 3.23: (a-d) Frequency variation of ac conductivity at different temperatures with fitted data (solid line) using equation (3.14) for BaM hexaferrite samples with y = 0, 0.2, 0.4 and 0.8.

The real part of ac conductivity (σ'_{ac}) of Ti doped BaM hexaferrites was determined at different temperatures in the frequency range of 100 Hz to 1 MHz as per the following relation as [113, 114];

$$\sigma'_{ac} = \omega\varepsilon_0\varepsilon'' \qquad (3.13)$$

where ε_0 represents the permittivity of free space, ω is the angular frequency and ε'' is the imaginary part of the permittivity determined from the measured Z' and Z'' values employing the equation (3.3). The frequency variations of σ'_{ac} of BaM hexaferrite samples at a few selected temperatures from 373 K – 473 K are shown in Fig. 3.23. In the low frequency region, a frequency independent (dc plateau) behavior i.e. the contribution of dc conductivity (σ_{dc}) is observed due to the long-range translational motion of charge carriers.

The frequency dependent behavior, i.e. increase of conductivity with frequency is observed in the high frequency region. This frequency dispersion behavior in the high frequency ($>$ 10^4 Hz) region can be ascribed to the successful hopping of charge carriers. Thus, the conductivity data were analyzed by separating them into low and high frequency parts. The real part of ac conductivity (σ'_{ac}) was analyzed by employing the Jonscher power law as (JPL) [42];

$$\sigma'_{ac} = \sigma_{dc} + A\omega^n \qquad (3.14)$$

where σ_{dc} is the frequency independent dc conductivity and $A\omega^n$ represents the frequency dependent term. The term A is a constant called pre-exponential factor and n is a frequency exponent term, which lies between 0 and 1. Fig. 3.23 demonstrates that the experimental data are well fitted to the JPL equation, where the symbols are the experimental data and the solid lines represent the fitted data. Furthermore, the underlying conduction mechanism in these samples can be understood from the n value. If the value of $n < 1$, then it corresponds to the translational motion of the charge carriers and if $n > 1$, then it corresponds to the localized motion of charge carriers due to the back and forth motion of the electrons [115, 116]. In general, when the charge carriers associated with defects move freely inside the crystal with increased effective mass, such charge carriers is known as polaron. However, the polaron may be small or large that depends upon the spatial extension. If the spatial extension is of the order of lattice constant, then it is called small polaron. Different theoretical models have been proposed by various researchers based on n values at different temperatures [117, 118]. They are the quantum mechanical tunneling (QMT) model, correlated barrier hopping (CBH) model, overlapping of large polaron tunneling (OLPT) model and non-overlapping small polaron tunneling (NSPT). In QMT model, the n is temperature independent with value close to 0.8, whereas in CBH model, the value of n decreases with increase in temperature. If the value of n decreases to a minimum and then increases with increase in temperature, then it is assigned to OLPT model. Moreover, if the value of n increases with increase in temperature then it follows NSPT model. In the present study, the value of n is found to increase with temperature i.e. in the range of $0.64 \leq n \leq 1$ as shown in Fig. 3.24(a). This suggests that the conductivity is governed by NSPT model [119].

Fig. 3.24(b) shows the plots of $ln\sigma_{dc}$ versus $10^3/T$ for all the Ti doped samples. They exhibit a linear behavior with a signature of increase in conductivity with temperature and

it signifies the semiconducting behavior of the samples. The dc conductivity data of grains and grain boundaries contributions can be analyzed by using the Arrhenius relation as [120];

$$\sigma_{dc} = \sigma_0 \exp(E_c/k_B T) \qquad (3.15)$$

where σ_0 is a constant, E_c is the activation energy of the electrical conduction and k_B is the Boltzmann's constant. The plots of $ln\sigma_{dc}$ vs $10^3/T$ exhibit a linear behavior for all the samples and are well fitted to the Arrhenius law (equation (3.15)). However, the activation energy due to grains contribution is very difficult to determine due to the limitation of the frequency range. The estimated values of conduction activation energy due to the grain boundaries contribution are found to be in the range of 0.42 – 0.22 eV (for y = 0 – 0.8). The activation energy determined from impedance spectra towards the relaxation mechanism (E_r ~ 0.40 – 0.17 eV) and the conduction spectra (E_c ~ 0.42 – 0.22 eV) due to grain boundaries contribution are almost comparable. This implies that, the same type of charge carriers govern the relaxation and conduction mechanism in the Ti doped samples. Furthermore, materials synthesized at high temperature for a long period may contain oxygen vacancies and these oxygen vacancies release conductance electrons by the ionization process resulting singly and doubly ionized oxygen vacancies. If E_c value is less than 0.7 eV then it corresponds to single ionized oxygen vacancies whereas for $E_c > 0.7$ eV, it is attributed to doubly ionized oxygen vacancies [121, 122]. However, in this case, the E_c values are found to be in good agreement with the predicted values for single ionized oxygen vacancies.

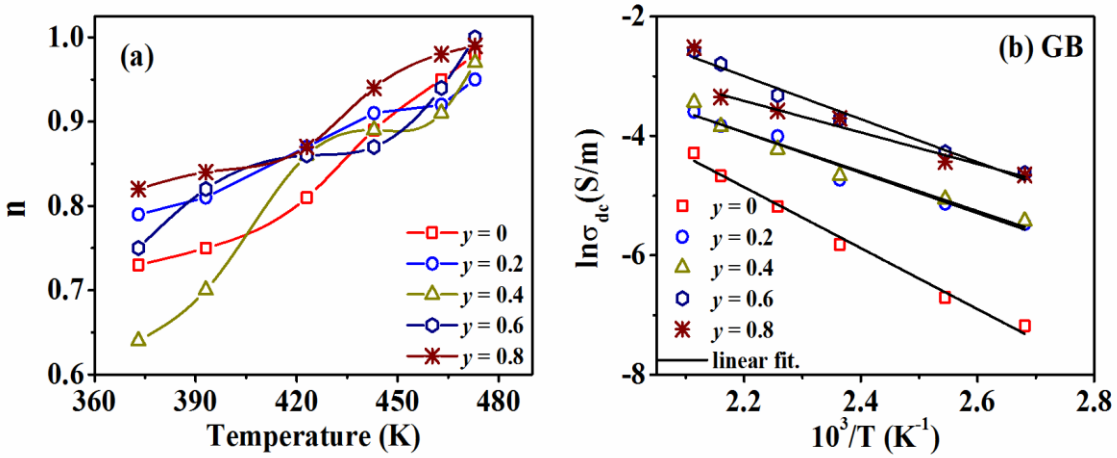

Figure 3.24:(a-b) Temperature variation of frequency exponent (n) and dc conductivity as a function of the inverse of temperature ($10^3/T$) for Ti doped BaM samples.

3.2.5 Magnetic Properties

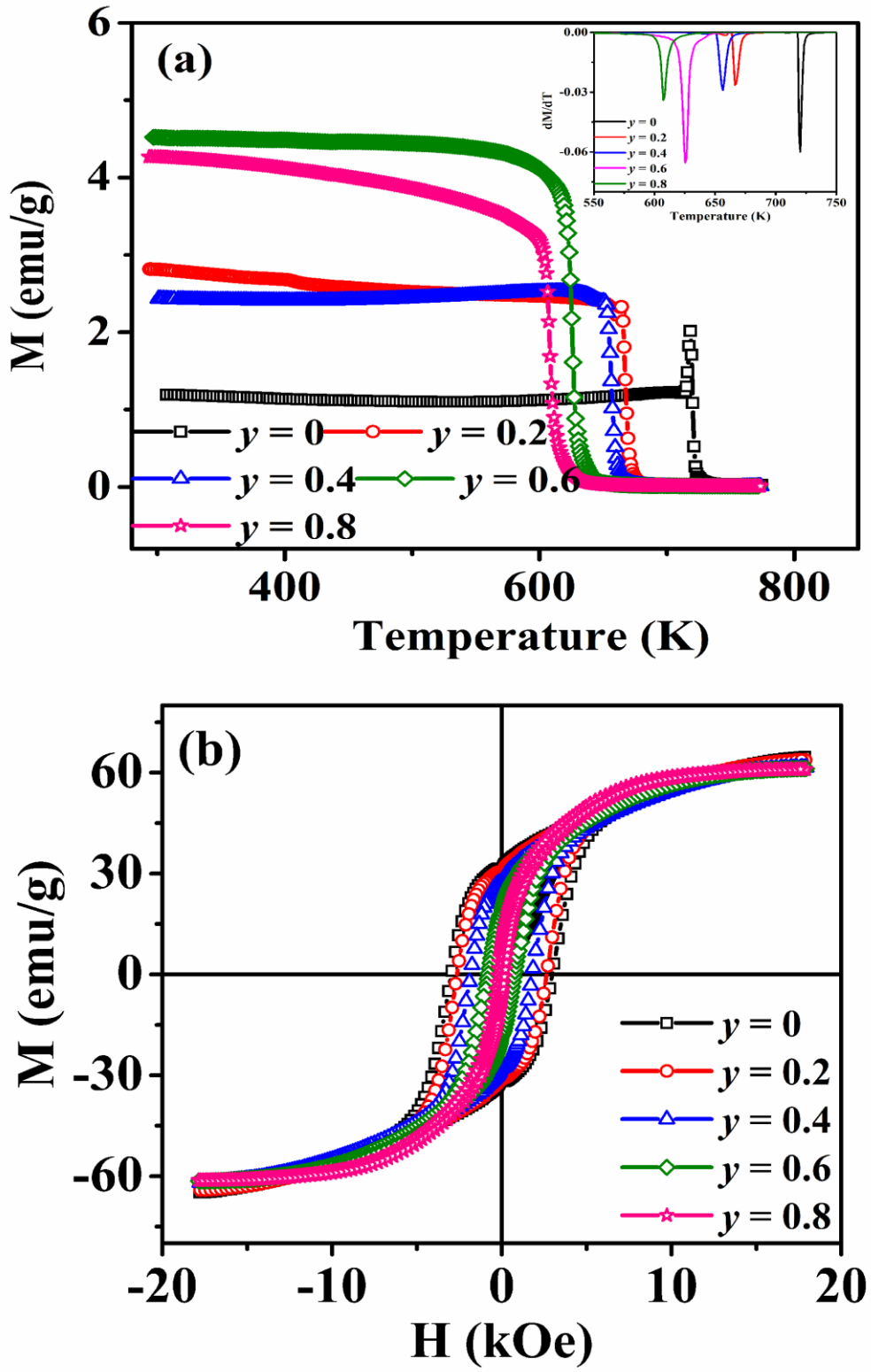

Figure 3.25: (a) Temperature variation of magnetization data from 303 K to 773 K and (b) Room temperature *M* – *H* loops of Ti doped BaM hexaferrites for $y = 0 – 0.8$.

Fig. 3.25(a) shows the magnetization versus temperature (M – T) plots of $BaFe_{12-y}Ti_yO_{19}$ samples with y = 0, 0.2, 0.4, 0.6 and 0.8. The temperature variation of magnetization measurements were performed with an applied field of 100 Oe in the temperature range of 303 K to 773 K. The ferrimagnetic transition (T_c) was determined from the minima of *dM/dT* versus temperature plots are shown in the inset of Fig. 3.25(a). For y = 0, the T_c value is around 720 K and it is comparable with the earlier reports [2, 100]. The observed T_c value is found to decrease from 720 K (for y = 0) to 608 K (for y = 0.8) with Ti substitution. The decrease in T_c value demonstrates that the nonmagnetic Ti^{4+} ions substitution weakens the inter sublattice exchange interactions in BaM hexaferrite.

Further, to investigate the influence of Ti substitution on the magnetic behavior of BaM hexaferrite, we have recorded the magnetic hysteresis (M – H) loops for all the samples at room temperature as shown in Fig. 3.25(b). It can be seen that the observed hysteresis loops are not getting saturated with the maximum applied field of 18 kOe. Thus, the law of approach to saturation (LAS) method was employed to determine the exact saturation magnetization (M_s) as well as effective magnetic anisotropy constant (K_1) values based on equation (3.8). The experimental magnetization (M) data versus the inverse square of the applied magnetic field ($1/H^2$) were plotted in the field range of 12 kOe to 18 kOe as shown in Fig. 3.26, where a straight line behavior is observed. Here the symbols denote the experimental data while the fitted data are shown as a solid line. The slope of the straight line assigned to the B value and the intercepts of the straight lines provide the M_s value. By using the equations (3.9) and (3.10), various essential magnetic parameters such as anisotropy field (H_a) and the effective anisotropy constant (K_1) were determined. The variation of M_s and K_1 values with respect to Ti concentrations are shown in the Fig. 3.26(f). The anisotropy constant K_1 follows the similar trend as that of the saturation magnetization. As the Ti concentration is increased, the M_s value is found to decrease linearly from 69.76 emu/g for y = 0 to 62.49 emu/g for y = 0.8 samples. In order to maintain the charge neutrality, the substitution of Ti^{4+} ions for Fe^{3+} ions may result in oxidation of some of the Fe^{3+} ions (high spin) into Fe^{2+} state (low spin) in 2a sites. Since the exchange interaction between Fe^{2+} – O^{2-} – $Fe^{3+}$are weaker than Fe^{3+} – O^{2-} – Fe^{3+}, thus the substitution of Ti^{4+} for Fe^{3+} gives rise to the magnetic dilution and hence smaller the saturation magnetization. Thus, the reduction in M_s values due to the nonmagnetic Ti substitution may be the signature of reduction in anisotropy constant in the doped samples. In addition to that, the substitution of nonmagnetic Ti^{4+} ions for magnetic Fe^{3+} (5 μ_B) ions give rise to the

reduction in M_s values. The coercivity (H_c) value is found to decrease with the increase in Ti concentration (Table 3.7). It is known that pure BaM hexaferrite has strong uniaxial anisotropy along *c*-axis. As the H_c value is inversely related to particle size and directly proportional to the magnetocrystalline anisotropy, the reduction in H_c with Ti concentration can be correlated to the reduction of H_a value and the increase in particle size (Fig. 3.16). All the magnetic parameters extracted from the hysteresis loops are enlisted in the Table. 3.7.

Table 3.7: Magnetic parameters (M_s, M_r, H_c and K_1) of Ti doped BaM hexaferrite samples at room temperature.

y	***M_s* (emu/g)**	***M_r* (emu/g)**	***H_c* (Oe)**	***K_1* (erg/cc)**
0	69.76	30.54	2980	5.54
0.2	68.17	28.96	2656	4.89
0.4	65.27	26.42	1836	4.18
0.6	63.61	17.80	776	3.22
0.8	62.49	7.01	209	2.46

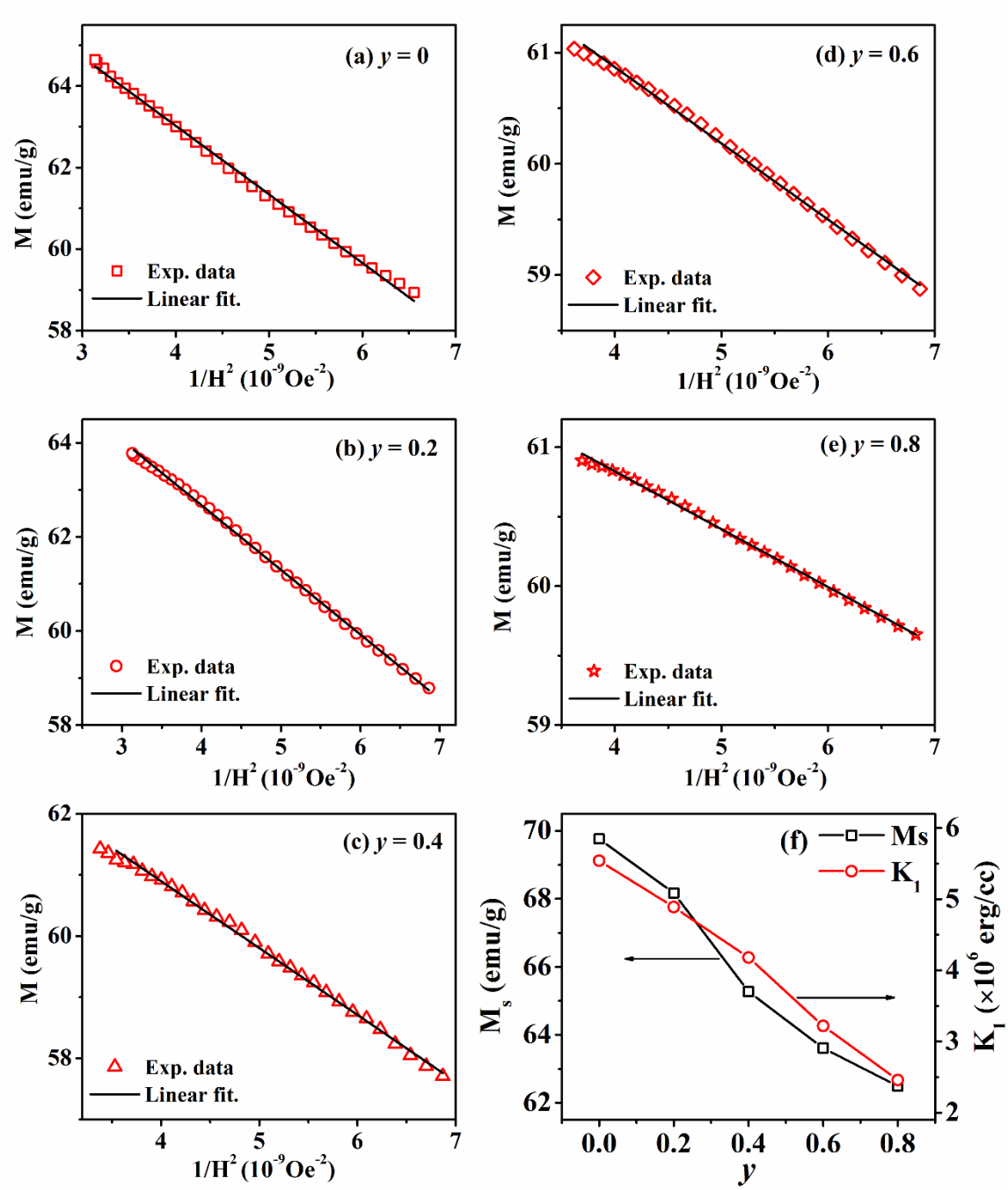

Figure 3.26: (a-e) Room temperature magnetization (M) vs $1/H^2$ plots analysed by LAS (equation (3.8)) for $BaFe_{12-y}Ti_yO_{19}$ ($0 \leq y \leq 0.8$) samples, where red symbols represent the experimental data and the solid line represents the fitted data, (f) The variation of M_s and K_1 values with Ti concentration (y).

3.2.6 Conclusions

Polycrystalline samples of $BaFe_{12-y}Ni_yO_{19}$ (y = 0 – 0.5) were successfully prepared in single phase form by employing the standard sol-gel method and their magnetic and dielectric properties were investigated in detail. The analysis of XRD patterns of these samples based on the Rietveld refinement technique reveals that the prepared samples crystallize in hexagonal structure with $P6_3/mmc$ space group. A systematic increase in lattice parameters has been noticed in BaM hexaferrite samples as the Ni concentration is increased. The microstructural analysis reveals that the average grain size value is found to be increase with increase in Ni concentration. The magnetization measurements demonstrate that the substitution of Ni at Fe site enhances the ferrimagnetic transitions (T_c) from 720 K for y = 0 to 759 K for y = 0.5 samples. The increase in T_c value suggests that the superexchange interaction among the magnetic cations is strengthened by the substitution of Ni ion. The saturation magnetization values were calculated by using the LAS model and they are found to decrease with increase in Ni concentration. Two different relaxation peaks associated with grains and grain boundaries contributions were observed in Z'' spectra and they are found to shift towards the higher frequency region with increase in temperature. The shifting of relaxation peaks towards higher frequency region with temperature signifies the thermal activation of relaxation process at grain boundaries. The Nyquist plots (Z'' vs Z') show that the grains contributions towards the dielectric relaxation is dominant for y = 0 sample at lower temperature (T = 373 K) and then the contribution of grain boundaries arises at higher temperatures (T > 373 K). However, the grains and grain boundaries contributions are clearly distinguished in Ni substituted samples. The Nyquist plots of all these samples are comprised of the different combinations of *RC* and *QR* elements, where the constant phase element *Q* is introduced to explain the deviation of observed semicircle from the ideal Debye behavior. In addition, the substitution of Ni reduces the dielectric loss tangent.

Single-phase samples of Ti substituted M-type barium hexaferrite i.e. $BaFe_{12-y}Ti_yO_{19}$ (y = 0 – 0.8) were synthesized by standard solid state route and investigated their magnetic and dielectric properties. XRD patterns of all these samples were analyzed by using hexagonal unit cell with $P6_3/mmc$ space group. The substitution of Ti ion gives rise to the expansion of the unit cell along the crystallographic *c*–axis. The microstructural study indicated that the grain size increases with the increase in Ti concentration. Temperature variation of magnetization measurements reveal that the ferrimagnetic transition (T_c)

temperature decreases from 720 K for y = 0 to 608 K for y = 0.8. The substitution of Ti^{4+} for Fe^{3+} gives rise to a reduction in superexchange interaction and the dilution of $Fe^{3+} – O^{2-} – Fe^{3+}$ networks and such process leads to a reduction in T_c. The coercivity (H_c) value is found to decrease with the increase in Ti concentration. Complex impedance spectra exhibit relaxation behavior due to grains and grain boundaries contributions. As the Ti concentration increases, the grains and grain boundaries contributions merge towards a single relaxation curve. The grains and grain boundaries contributions towards the relaxation mechanism were explained using an equivalent electrical circuit model consisting of resistance, capacitance and constant phase element. The conductivity spectra were analyzed based on Jonscher Power Law and the conduction activation energy (E_c) due to grain boundaries contribution is found to decrease with the increase in Ti doping. The activation energy values determined from the impedance spectra and the conduction spectra are comparable indicating the same type of charge carriers playing a role in the relaxation and the conduction process in Ti doped samples.

In summary, the substitution of both magnetic (Ni) and nonmagnetic (Ti) ions at Fe sites have large influence on the magnetic and dielectric properties of BaM hexaferrite. The M_s value is enhanced with substitution of Ni while it decreases with Ti substitution. However, the H_c value is decreased for both the Ni and Ti substituted samples. Well defined relaxation peaks have been observed in the Z'' spectra of both the substituted samples and this can be attributed to the grains and grain boundaries contributions towards the relaxation mechanism. This study demonstrates that the Ni and Ti substituted M-type barium hexaferrites exhibit a moderate value of saturation magnetization and a low value of coercivity, which can be useful for soft magnetic applications.

Chapter 4

$Ba(Fe_{1-x}Al_x)_{12}O_{19}$ Series

4.1 Al Substituted $BaFe_{12}O_{19}$ Series

In chapter 3, we have seen that M-type barium hexaferrite is one of the well-known series of magnetic materials that possess interesting magnetic and dielectric properties. The high uniaxial magnetic anisotropy, self-biasing nature, low eddy current loss, a narrow ferromagnetic resonance and magnetoelectric coupling make this compound a natural choice for high density magnetic recordings, permanent magnet, microwave devices, multi-state memory and magneto-optical devices [46, 47, 123-125]. As discussed in Chapters 1 and 3, there are several reports on the structural, magnetic and dielectric properties of M-type barium hexaferrite. In the earlier reports the substitution of Ba or Fe by using various elements such as Ca, Sr, Pb, La, Sc, Cr, Mn, Co, *etc*. in M-type hexaferrite has been studied in detail [44, 46-49, 51, 53, 126]. Tan *et al*., have reported that the M-type barium hexaferrite (BaM) prepared by polymer precursor method exhibits multiferrocity i.e. ferroelectricity and strong ferromagnetism [127]. Ashiq *et al*., have explained that the substitution of Al – Cr at Fe site reduces the dielectric constant, dielectric loss and the conductivity and it suggests that these materials can be suitable for applications in high density recording media [128]. Large single crystals of Al substituted M-type barium hexaferrite was prepared by carbonate flux method and it reveals that the Al substitution reduces the Curie temperature and saturation magnetization in BaM hexaferrite [129]. The magnetoelectric polarization is also observed due to Al substitution in Y-type hexaferrite [130]. Further, the Al substituted strontium hexaferrite ($SrFe_{12-x}Al_xO_{19}$) prepared by glycine-nitrate method exhibits large coercivity (17570 Oe) for $x = 4$ sample, which is very much higher than the $SrFe_{12}O_{19}$ (15072 Oe) [131]. Iqbal *et al*., [132] have reported that the substitution of Al – Ga for Fe^{3+} ions at octahedral site in M-type hexaferrite reduces the hopping of electrons. As a result, the resistivity of the material increases from 2.45×10^8 to 25.96×10^8 Ω cm and the substitution also reduces the dielectric constant and loss factor as

compared to the parent compound. Such types of materials are suitable for microwave applications [132]. Wang *et al*., [57] have demonstrated that the Al substitution leads to increase in real part of complex permittivity along with a ferromagnetic resonance in the high frequency range of 7 to 14 GHz [58]. Thus, in view of the above interesting properties of Al doped hexaferrites, the detailed study of Al substitution at Fe site in BaM hexaferrite will be quite interesting.

In the present chapter, the effect of Al substitution on crystal structure, dielectric constant and magnetic properties are systematically investigated by recording X-ray diffraction patterns, Raman spectra and FESEM micrographs and by measuring temperature and field variations of magnetization and frequency variation of dielectric constant and permeability. The systematic analysis of all these data are presented in detail.

4.1.1 Sample Preparation and Characterization

Polycrystalline samples of Al substituted M-type barium hexaferrites i.e. $Ba(Fe_{1-x}Al_x)_{12}O_{19}$ with nominal compositions of x = 0.0, 0.02, 0.04, 0.06, 0.08, 0.10 were prepared by the conventional solid state route. Stoichiometric amount of Ba_2CO_3, Fe_2O_3 and Al_2O_3, all with high purity better than 99 % were taken as starting compounds. The starting oxides/carbonates were mixed thoroughly under acetone medium using an agate mortar and pestle for 2 – 3 h. The obtained uniform mixture were calcined at 600 ℃ for 12 h. To obtain good homogeneity, the calcined powders were again ground thoroughly and then pressed into cylindrical pellets of approximately 13 mm diameter and 1.5 – 2 mm thickness at a pressure of 2.9×10^8 N/m^2 by using a hydraulic press. The final sintering was carried out at 1100 ℃ for 12 h in air followed by furnace cooling to room temperature. X-Ray diffraction patterns (XRD) of the prepared samples were recorded by using Rigaku make TTRAX III high power X-ray diffractometer by employing CuK_α (λ = 1.54056 Å) radiation. Raman spectra were recorded at room temperature by using Laser Micro Raman spectrometer (model. LabRam HR800, Jobin Yvon) in the wavenumber range of 100 – 800 cm^{-1} for an excitation wavelength of 488 nm. Recording the microstructural images and the compositional analysis of these samples were carried out by using ZEISS make field emission scanning electron microscope (FESEM, Model. ΣIGMA) equipped with an energy dispersive x-ray spectrometer (EDS) facility. Temperature and field variations of magnetization measurements were carried out by using a Lakeshore make vibrating sample magnetometer (VSM, model. 7410). The frequency dependences of dielectric permittivity

and permeability were measured at room temperature from 1 MHz to 1 GHz range by using Novocontrol make Impedance and material analyzer (model. BDS 2300). For the dielectric measurements, the electrodes were fabricated by painting silver pastes on both sides of the pellets of typical thickness 1 – 1.5 mm. Before carrying out the dielectric measurements, the pellets were dried for 2 h by using a hot air oven.

4.1.2 Structural Properties

Typical XRD patterns recorded at room temperature for $Ba(Fe_{1-x}Al_x)_{12}O_{19}$ (x = 0, 0.02, 0.04, 0.06, 0.08 and 0.10) samples are shown in Fig. 4.1. The XRD patterns of all the samples are analyzed by the Rietveld refinement technique with the help of FULLPROF program. The best refinement of these prepared samples were obtained by choosing $P6_3/mmc$ space group i.e. with hexagonal structure. Fig. 4.2 and Fig. 4.3 show the typical recorded XRD patterns for x = 0, 0.02 and 0.06, 0.10 samples along with Rietveld refined data (solid lines). The Rietveld analysis of these XRD patterns reveal that the prepared samples are found to be in single-phase form. The estimated lattice parameters for parent compound (x = 0) are found to be a = 5.892 Å and c = 23.206 Å. A systematic decreasing trend of lattice parameters (a and c) is observed with increase in Al concentration (x). The decreasing trend of lattice parameters suggest that the Al^{3+} (0.535 Å) ions having smaller ionic radius substitute for Fe^{3+} (0.645 Å) ions. The lattice parameters, reliability factors and the unit cell volume obtained from the refined data are listed in Table 4.1.

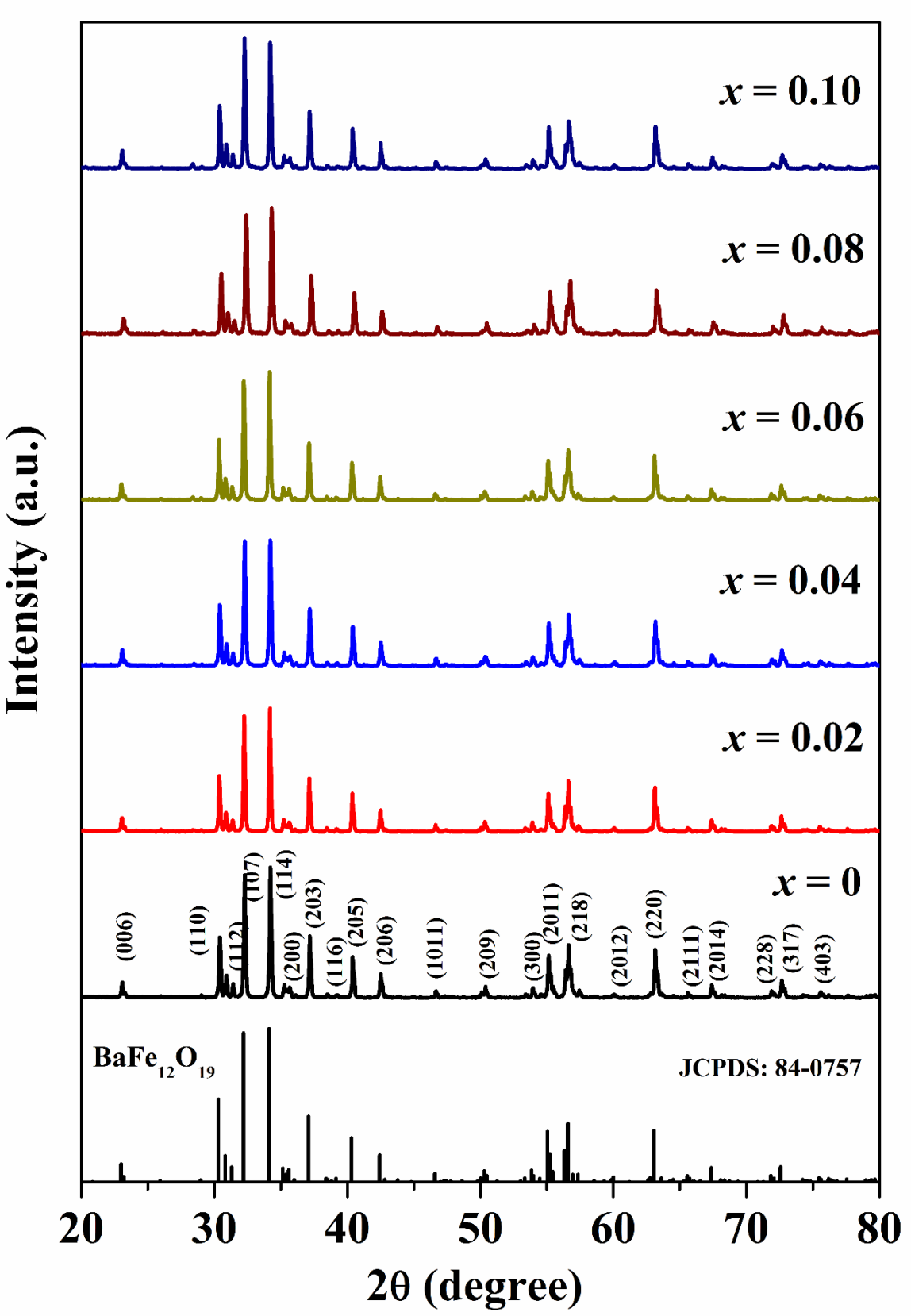

Figure 4.1: XRD patterns of Ba(Fe$_{1-x}$Al$_x$)$_{12}$O$_{19}$ samples for x = 0 – 0.10 recorded at room temperature.

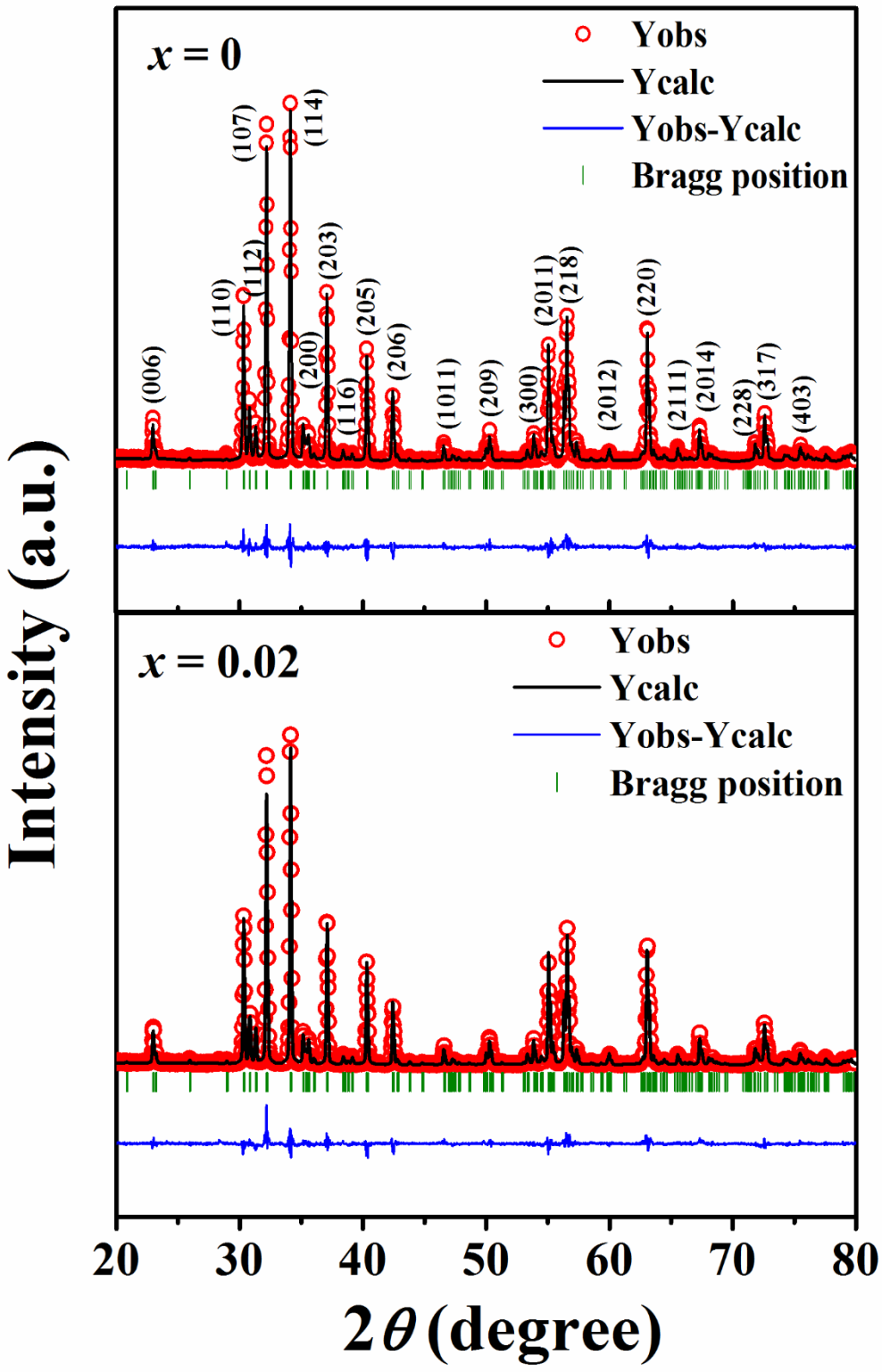

Figure 4.2: Rietveld refined XRD patterns of $Ba(Fe_{1-x}Al_x)_{12}O_{19}$ samples with x = 0 and 0.02. The red open circles represent the experimental data and the black solid lines are the fitted data. The bottom line represents the difference between experimental and refined data.

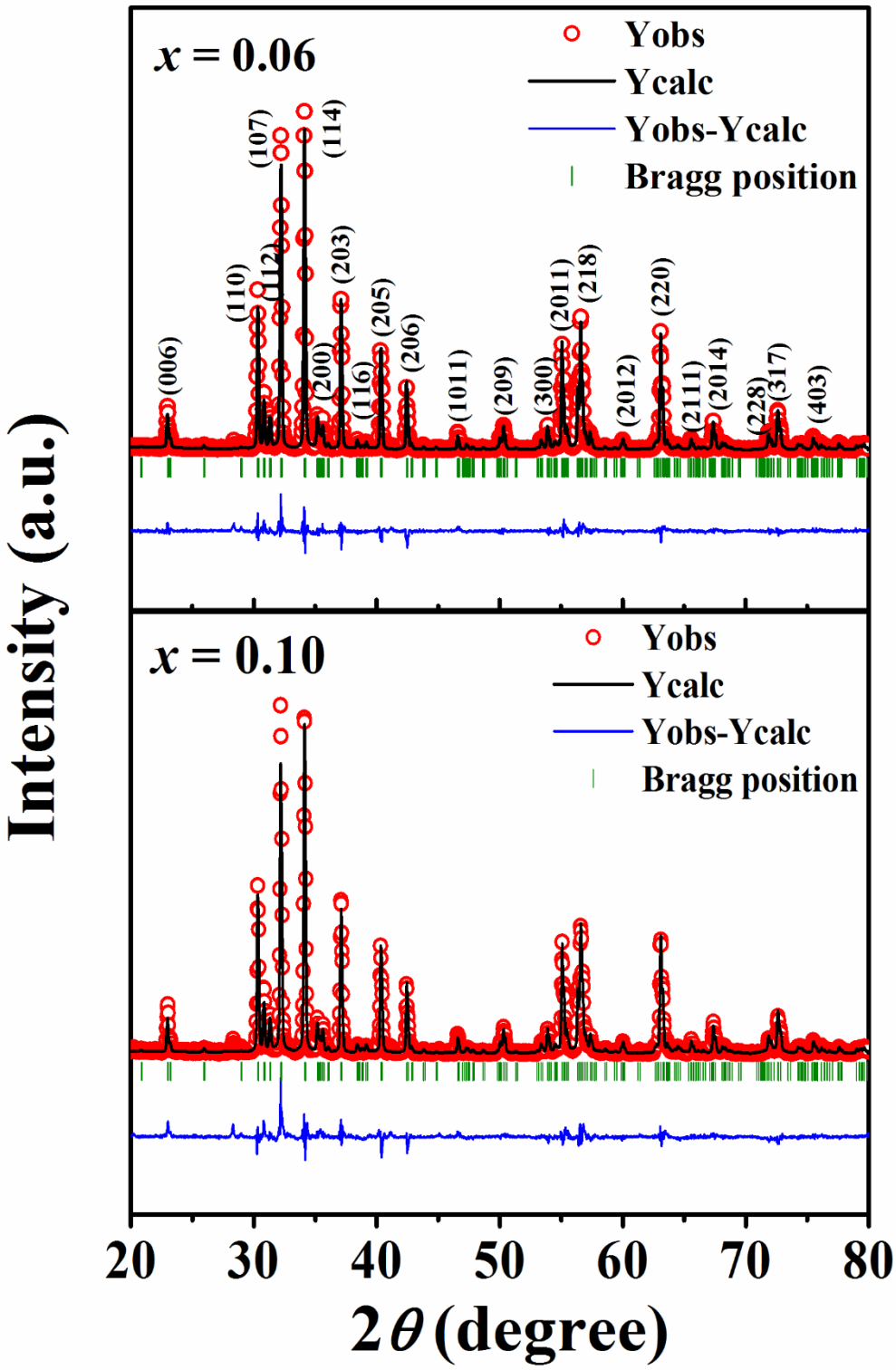

Figure 4.3: Rietveld refined XRD patterns of $Ba(Fe_{1-x}Al_x)_{12}O_{19}$ samples with x = 0.06 and 0.10. The red open circles represent the experimental data and the black solid lines are the fitted data. The bottom line represents the difference between experimental and refined data.

Table 4.1: Parameters obtained from the Rietveld refinement of XRD patterns for the samples $Ba(Fe_{1-x}Al_x)_{12}O_{19}$. R_F, R_{Bragg}, R_{exp}, R_P and χ^2 are the reliability factors.

Sample/ Parameters	***x* = 0**	***x* = 0.02**	***x* = 0.04**	***x* = 0.06**	***x* = 0.08**	***x* = 0.10**
Space group	*$P6_3/mmc$*	*$P6_3/mmc$*	*$P6_3/mmc$*	*$P6_3/mmc$*	*$P6_3/mmc$*	*$P6_3/mmc$*
***a* (Å)**	5.8920 (1)	5.8914 (2)	5.8903 (3)	5.8919 (3)	5.8914 (1)	5.8803 (2)
***c* (Å)**	23.2065 (9)	23.1976 (1)	23.1881 (5)	23.2151 (1)	23.1982 (4)	23.1872 (2)
***Volume* (Å^3)**	697.70 (4)	697.30 (6)	696.91 (7)	697.46 (6)	697.32 (8)	696.49 (5)
R_F (%)	6.33	6.82	7.36	5.82	8.52	9.84
R_{Bragg} (%)	5.23	6.74	7.60	6.19	8.12	9.64
R_P (%)	14.8	14.0	15.0	11.11	16.8	11.29
R_{exp} (%)	12.01	11.01	11.13	15.2	12.83	17.9
χ^2	3.23	3.08	3.49	3.50	3.44	4.39

In order to confirm the cationic distributions obtained from the XRD analysis and to understand the dynamic behavior of atoms at the sublattice sites of $BaFe_{12}O_{19}$, Raman spectra were studied at room temperature for all the samples. As per the XRD analysis, the $BaFe_{12}O_{19}$ (BaM) crystallizes in hexagonal structure with $P6_3/mmc$ space group. A BaM hexaferrite compound contains two formula units per unit cell. The 24 Fe^{3+} ions are distributed over five different crystallographic sites such as three octahedral (12k, 2a and $4f_2$), one tetrahedral ($4f_1$) and one trigonal bipyramidal (2b) sites respectively. As per the calculation of group theory, BaM hexaferrite containing 64 atoms per unit cell corresponds to 42 Raman active modes ($11A_{1g} + 14E_{1g} + 17E_{2g}$) [133]. Fig. 4.4 shows the Raman spectra of $Ba(Fe_{1-x}Al_x)_{12}O_{19}$ samples for x = 0 – 0.10 recorded at room temperature in the

wavenumber range of 100 – 800 cm^{-1}. It can be seen that the Al doped samples along with the parent compound exhibit 13 prominent peaks and they are consistent with the previous report [134]. The most intense peak is observed at 685 cm^{-1} for all the samples and that is associated with A_{1g} vibration of Fe – O ions at trigonal bipyramidal (2b) site. For x = 0 sample, a weak shoulder like peak is observed at the wavenumber around 719 cm^{-1} and it is associated to the A_{1g} vibration of Fe – O ions at tetrahedral sites ($4f_1$). However, with increase in Al concentration, the peak at 719 cm^{-1} disappears due to the broadening of the main peak at 685 cm^{-1}. The band observed at 614 cm^{-1} is assigned to the A_{1g} mode of vibration of Fe – O bonds at octahedral $4f_2$ site. In addition to the above peaks, there exist several distinct peaks for all the samples corresponding to the wavenumbers of 172 cm^{-1}, 182 cm^{-1}, 211 cm^{-1}, 284 cm^{-1}, 317 cm^{-1}, 336 cm^{-1}, 415 cm^{-1}, 466 cm^{-1} and 529 cm^{-1} as shown in Fig. 4.4(a). These results are comparable to the previous reports on Raman spectra in $BaFe_{12+x}O_{19+1.5x}$ samples by Zhao *et al*., [134]. Here the bands obtained at 172 cm^{-1} and 182 cm^{-1} are due to the E_{1g} vibration of whole spinel block. The bands in the region 211 cm^{-1} to 529 cm^{-1} are associated with the vibration of all Fe – O bonds in various octahedral positions such as 12k, 2a and $4f_2$ sites [133, 134]. The measured Raman spectra of Al substituted samples show that other than the broadening of various bands, no new band is observed and it confirms that the prepared samples are found to be in single-phase form. The broadening of Raman modes/peaks with increase in Al concentration is consistent with the reduction in grain size values as shown in Fig. 4.5. The line widths of some of the prominent peaks were measured as a function of Al concentration (x) and they are shown in Fig. 4.4(b). A gradual increase in bandwidth is observed, as the Al concentration is increased. The broadening of the peaks can be attributed to the structural disorder such as minor change in chemical composition, ionic radii, bond length and lattice parameters. Such distortion is possible due to the size mismatch between the host Fe^{3+} ions (0.645 Å) and the substituted Al^{3+} (0.535 Å) ions. Typical plot of fitted Raman spectra along with experimental spectrum for x = 0 sample is shown in Fig. 4.4(c).

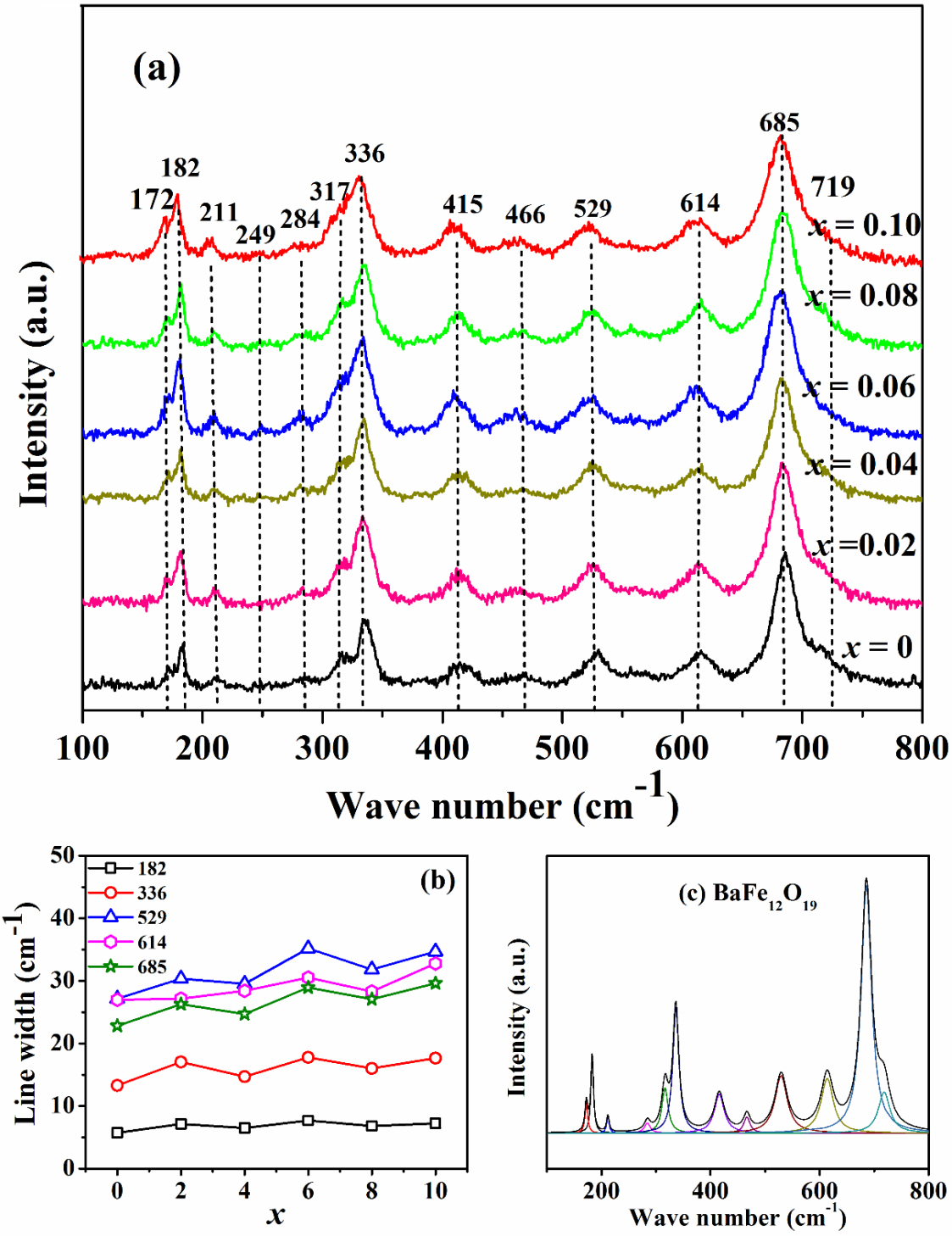

Figure 4.4: (a) Raman scattering spectra of Ba(Fe$_{1-x}$Al$_x$)$_{12}$O$_{19}$ ($0 \leq x \leq 0.10$) samples recorded at room temperature (b) Concentration (x) dependence of linewidth and (c) the fitted curve of BaFe$_{12}$O$_{19}$.

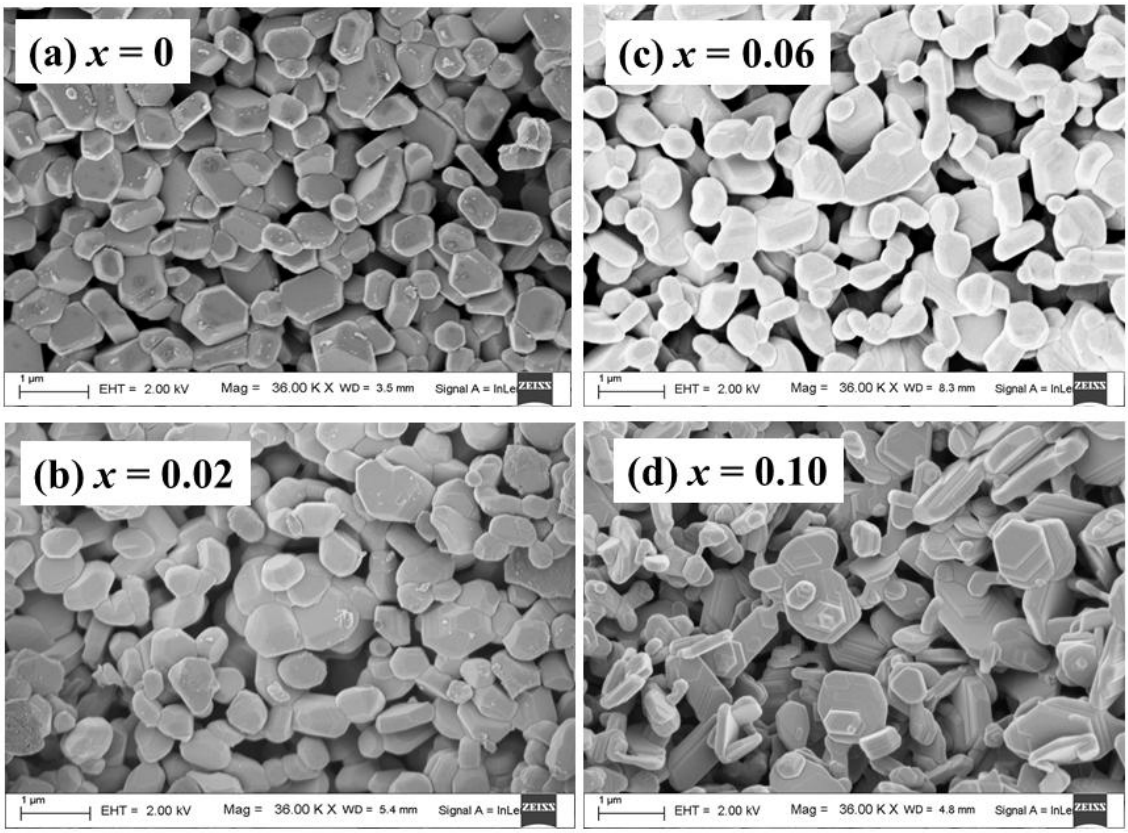

Figure 4.5: Microstructural images of $Ba(Fe_{1-x}Al_x)_{12}O_{19}$ samples with (a) $x = 0$ and (b) $x = 0.02$ (c) $x = 0.06$ and (d) $x = 0.10$.

To characterize the surface morphology of the samples, the microstructural images of all the Al substituted samples along with the parent compound ($BaFe_{12}O_{19}$) were recorded at room temperature. Fig. 4.5(a-d) show the typical FESEM micrographs of $Ba(Fe_{1-x}Al_x)_{12}O_{19}$ samples with $x = 0$, 0.02, 0.06 and 0.10. Well-defined hexagonal shaped grains are seen for $x = 0$ sample. However, irregular shaped grains are seen in Al substituted samples and that can be attributed to the possible particle agglomerations. Fig. 4.6(a-b) demonstrate that the grain sizes are distributed over a wide range for each sample. The average grain size value was obtained by fitting the log-normal distribution function given by equation (3.1) in chapter 3 to the size distribution histograms as shown in Fig. 4.6(a-b). The grain size distribution for $x = 0$ and 0.10 samples are shown in Fig. 4.6(a-b). The estimated average grain size value for $x = 0$ sample is found to be 343 nm. As the Al concentration is increased, the reduction in average grain sizes is observed down to 225 nm for $x = 0.10$ sample. In addition to that, the well defined hexagonal grains along with considerable pores have been observed in Al substituted samples and the concentration of porosity is increased with increase in Al concentration. The lattice contraction and

associated lattice strain due to the ionic size mismatch between Al^{3+} (0.535 Å) ions and host Fe^{3+} (0.645 Å) ions may hinder the growth of grains. As a result, the reduction in grain size values are observed due to Al substitution. The EDX spectra for $x = 0$ and 0.10 samples are shown in Fig. 4.6(c-d). The chemical compositions estimated from the EDX analysis are found to be comparable to the nominal starting compositions. The cationic ratios for $x = 0$, 0.02, 0.04, 0.06, 0.08 and 0.10 samples are given in Table 4.2.

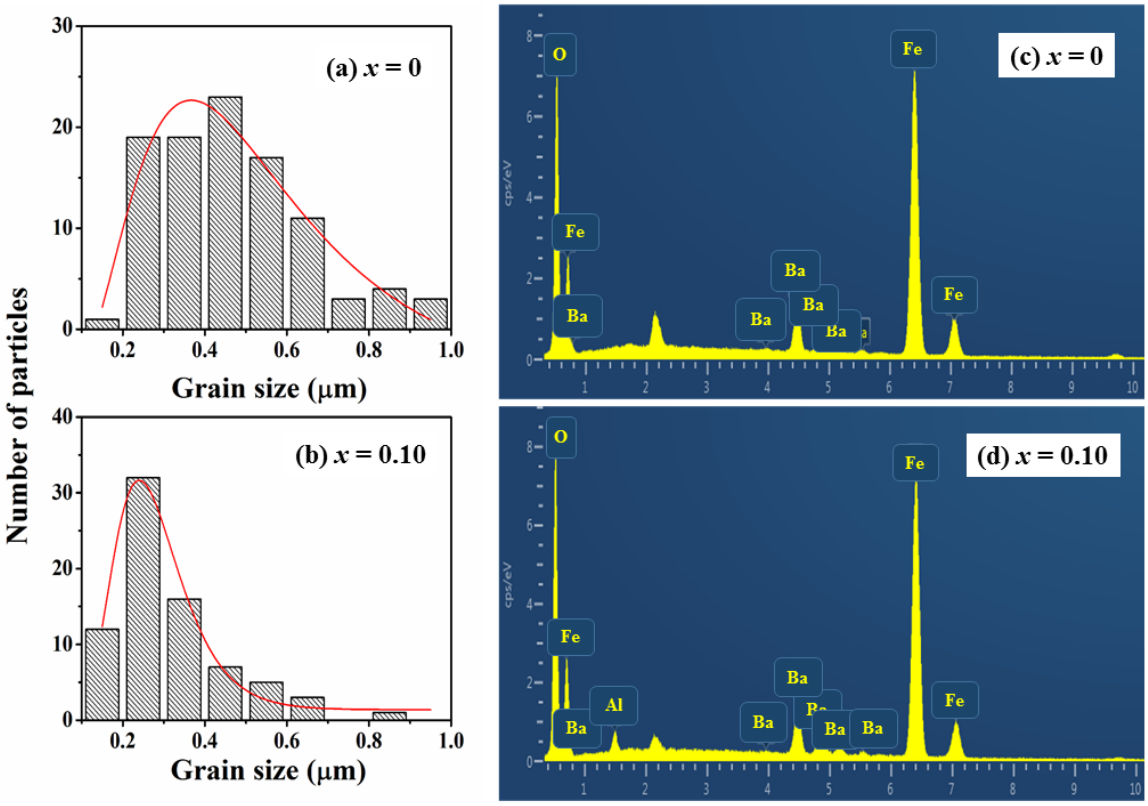

Figure 4.6: (a-d) Distribution of grain sizes along with their EDX spectra of $Ba(Fe_{1-x}Al_x)_{12}O_{19}$ samples for $x = 0$ and 0.10.

Table 4.2: The cationic ratio determined from EDX spectra for $Ba(Fe_{1-x}Al_x)_{12}O_{19}$ samples with x = 0 to 0.10.

Samples	Calculated Cationic Ratio from EDX Analysis		
	Ba	**Fe**	**Al**
***x* = 0**	1.0	11.94	0.00
***x* = 0.02**	0.98	11.76	0.21
***x* = 0.04**	1.04	11.57	0.42
***x* = 0.06**	1.04	11.29	0.69
***x* = 0.08**	1.0	11.02	0.96
***x* = 0.10**	1.04	10.86	1.10

4.1.3 Magnetic Properties

As discussed in the previous section, the magnetic Fe^{3+} ions in BaM hexaferrite are distributed over five different crystallographic sites namely three octahedral sites (12k, 2a and $4f_2$), one tetrahedral site ($4f_1$) and one trigonal bipyramidal site (2b). The Fe^{3+} ions having up spins are occupied by 12k (↑), 2a (↑) and 2b (↑) sites, while Fe^{3+} ions having spins in the opposite directions occupy the $4f_1$ (↓) and $4f_2$ (↓) sites. Further, Sözeri *et al.*, have reported that the net magnetic moment (M (T)) per formula unit of BaM hexaferrite at a particular temperature (T) can be expressed as [77];

$$M\ (T) = 6M_{12k}(T) - \ 2M_{4f1}(T) - \ 2M_{4f2}(T) + \ 1M_{2a}\ (T) + \ 1M_{2b}(T) \qquad (4.1)$$

where the magnetic moment of Fe^{3+} ion at different sublattice sites such as n = 12k, 2a, 2b, $4f_1$ and $4f_2$ are represented by M_n. Therefore, it can be expected that the partial substitution of magnetic Fe^{3+} ions by the non-magnetic Al^{3+} ions may give rise to some interesting magnetic as well as dielectric properties of BaM hexaferrite.

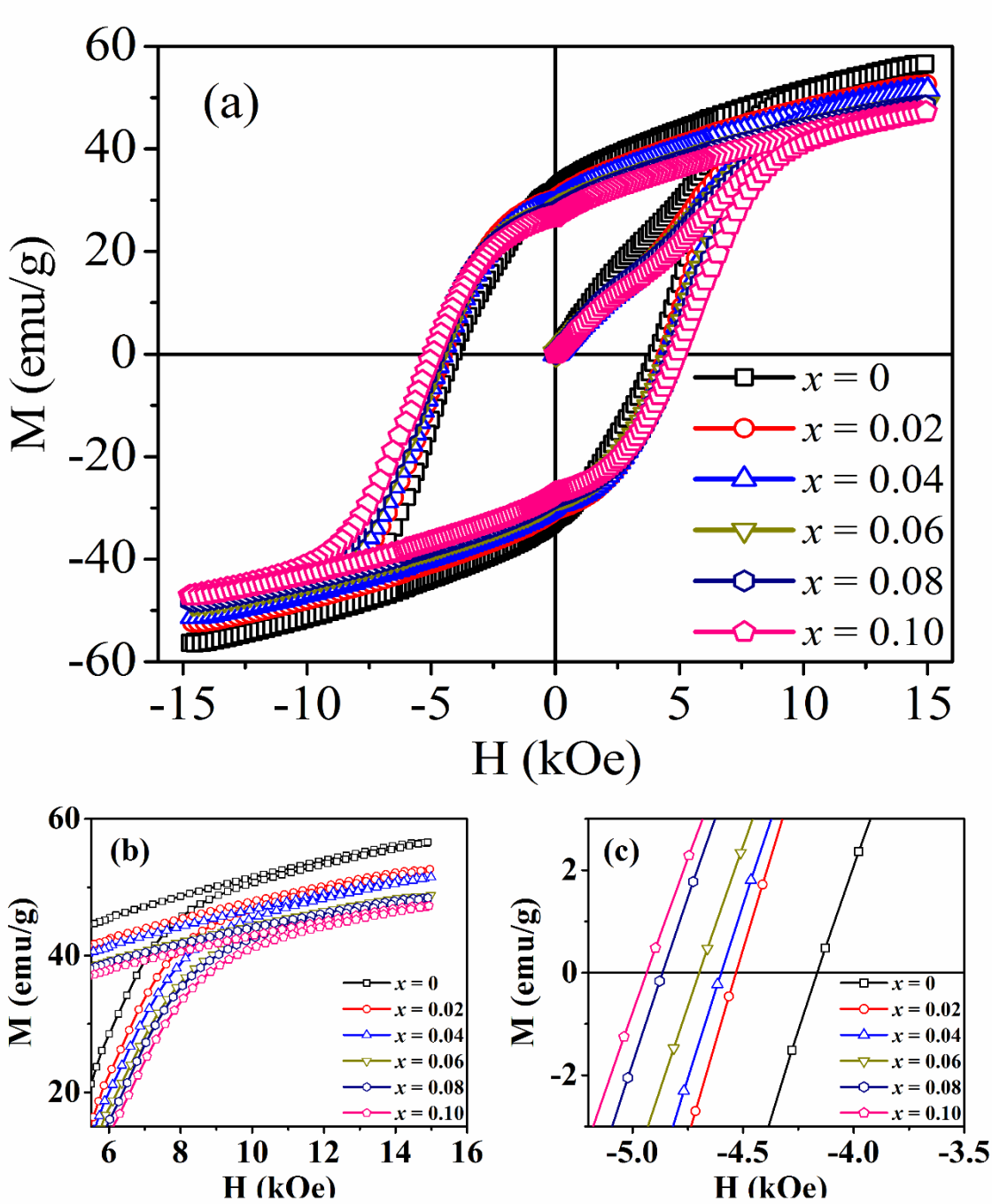

Figure 4.7: Room temperature *M* – *H* loops of Ba(Fe$_{1-x}$Al$_x$)$_{12}$O$_{19}$ samples in (a) full scale view (b) expanded view in the saturation magnetization region and (c) expanded view in the sign reversal region.

Fig. 4.7(a) shows the room temperature magnetic hysteresis (*M* – *H*) loops of Ba(Fe$_{1-x}$Al$_x$)$_{12}$O$_{19}$ samples with x = 0, 0.02, 0.04, 0.06, 0.08 and 0.10. The *M* – *H* loops of all samples show ferrimagnetic behavior. The enlarged view of *M* – *H* loops close to saturation magnetization (M_s) and coercivity (H_c) of the measured samples are shown in

Fig. 4.7 (b) and (c) respectively. It is observed that the M_s value is found to decrease with increase in Al concentration while the H_c is increased upon Al substitution. Fig. 4.7(b) reveals that, the magnetic saturation is not achieved even for a maximum applied field of 15 kOe, where the domain rotation contribution is expected to be dominant. Therefore, the value of saturation magnetizations (M_s) were estimated for all samples by using the law of approach to saturation (LAS), which is a very standard method to understand the magnetic properties of polycrystalline magnetic materials [135]. The experimental saturation magnetization (M_s) was determined by fitting the law of approach to saturation model as given by equation (3.8) in chapter 3. The initial magnetization curves were fitted to the LAS model at the high field range (approaching to saturation) and the fitted data are reproduced in the entire field range. The open symbol denotes the experimental data while the fitted data are represented by solid lines as shown in Fig. 4.8. It can be seen that the experimental M_s data of all the samples are well fitted to the LAS model. Further, it is known that the magnetic properties of a material depends upon various parameters such as method of preparation, microstructure, degree of disorder due to various cationic substitutions, *etc*. The variation of different magnetic parameters such as M_s, M_r, H_c, H_a and K_1 due to substitution of nonmagnetic Al cation is listed in Table 4.3. For $x = 0$ sample, the M_s value is found to be 51.36 emu/g. As the Al concentration is increased, the reduction in M_s value is observed down to 45.76 emu/g for $x = 0.10$. The reduction in M_s values can be attributed to the substitution of nonmagnetic Al^{3+} ions for magnetic Fe^{3+} ions. The possible occupation of Al^{3+} ions at up spin site of the Fe^{3+} ions such as 12k, 2a and 2b causes the reduction in M_s values. The remanence (M_r) magnetization i.e. the magnetization at zero applied field after reaching the saturation is found to decrease with increase in Al concentration. The decrease in density of the sample shown in the micrographs in Fig. 4.5 and/or the substitution of magnetic Fe by a nonmagnetic Al causes the reduction in M_r values. In other words, the substitution of nonmagnetic Al^{3+} for magnetic Fe^{3+} ion may weaken the superexchange interaction between $Fe^{3+} – O^{2-} – Fe^{3+}$ ions. As a result, both M_s and M_r values are found to decrease upon Al substitution. To get more understanding of the magnetic properties of a material in detail, it is essential to study the magnetic anisotropy property. From the above mentioned equation (3.8), the anisotropy field (H_a) is calculated by using the following relation as [9];

$$B = \frac{H_a^2}{15} \qquad (4.2)$$

The effective magnetic anisotropy constant (K_1) was also estimated by using the relation;

$$H_a = \frac{2K_1}{M_s} \qquad (4.3)$$

From the above two equations (4.2) and (4.3), the H_a and K_1 values were calculated exactly. The substitution of Al^{3+} ion for Fe^{3+} ion increases the K_1, and H_a values. Further, the coercivity (H_c) values of all the samples were estimated by using the following relation as;

$$H_c = (H_+ - H_-)/2 \qquad (4.4)$$

where H_+ and H_- are two magnetic field values of the ascending and descending branches of $M - H$ loop corresponding to $M = 0$. For $x = 0$ sample, the $M - H$ loop exhibits high coercivity value and this suggests the uniaxial magnetocrystalline anisotropy of BaM hexaferrite along the *c*-axis. The most interesting property of this sample is that the H_c value is enhanced with increase in Al contents. Since the coercivity is proportional to the magnetic anisotropy field, the increase in H_c values can be attributed to an increase in the anisotropy field (H_a) due to Al substitution. Further, the FESEM micrographs shown in Fig. 4.5 reveal that the porosity is increased with increase in Al substitution by decreasing the average grain sizes. As the coercivity is inversely proportional to the packing of magnetic materials or the grain sizes, such increase in porosity along with decreased grain sizes is another reason for increase in coercivity values due to Al substitution [136]. The various magnetic parameters such as M_s, H_c, H_a and K_1 determined from the LAS model are listed in Table. 4.3.

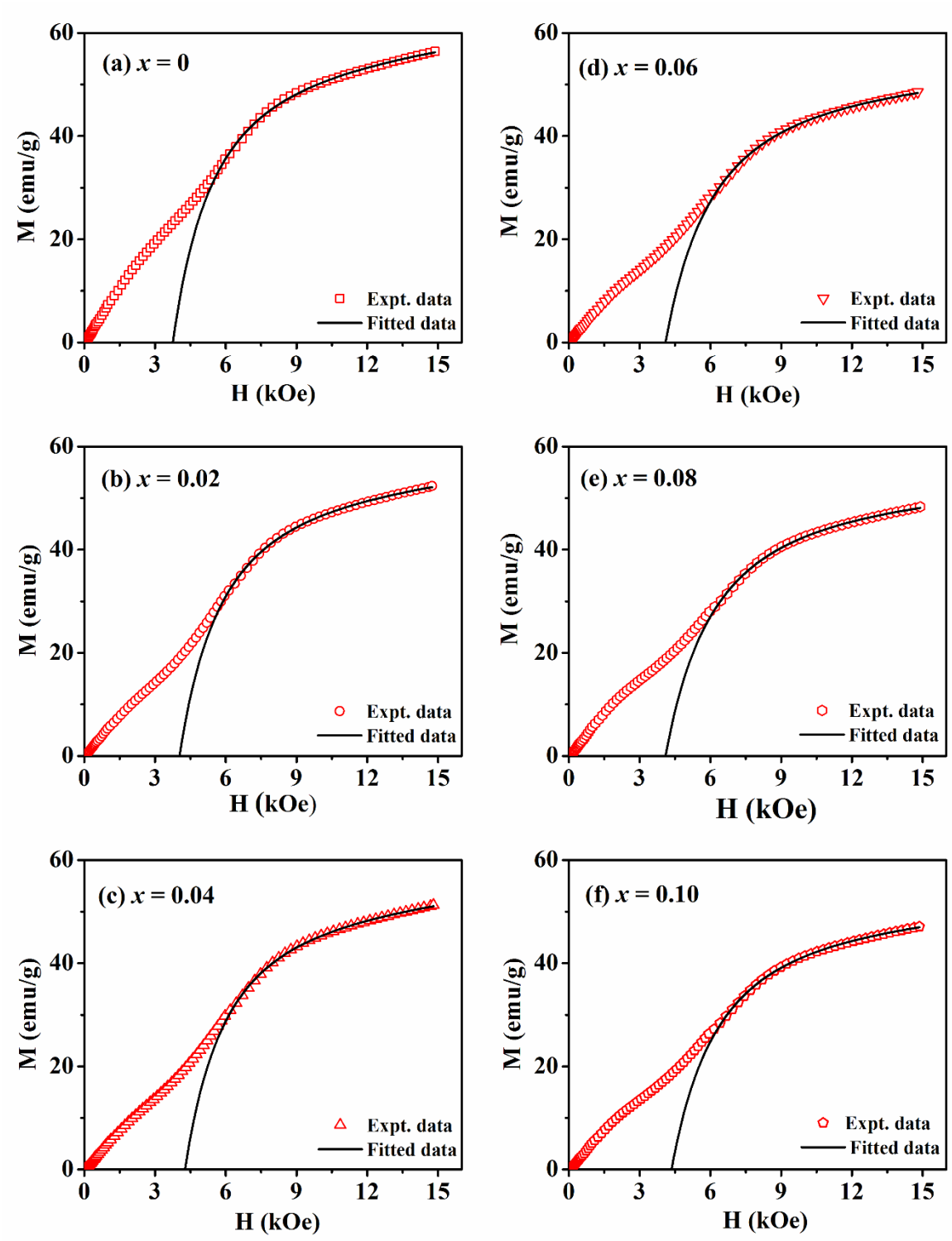

Figure 4.8: (a-f) Initial magnetization curves along with fitted data as per the law of approach to saturation model for $Ba(Fe_{1-x}Al_x)_{12}O_{19}$ samples with $x = 0 – 0.10$.

Table 4.3: Magnetic parameters (M_s, M_r, H_c, H_a and K_1) of Al doped BaM samples determined from the LAS model at room temperature.

x	M_s (emu/g)	M_r (emu/g)	H_c (Oe)	H_a (10^4 Oe)	K_1 (10^6erg/cc)
0.0	51.36	31.74	4132	1.26	0.325
0.02	49.04	30.05	4507	1.31	0.320
0.04	46.26	29.13	4588	1.40	0.323
0.06	47.80	28.45	4681	1.52	0.365
0.08	47.76	27.68	4869	1.55	0.370
0.10	45.76	26.74	4926	1.43	0.327

In order to further explore the magnetic properties, the M – H loops of BaM hexaferrite sample were recorded at different temperatures from 303 K – 673 K as shown in Fig. 4.9(a). As the temperature is increased, a systematic decrease in M_s values are observed. On the other hand, the H_c value is found to increase up to 473 K and beyond that, it decreases as it approaches the transition temperature. All the Al substituted samples exhibit similar kind of behavior as that of the parent compound (x = 0). Fig. 4.9(b) demonstrates the temperature dependence of H_c for samples of different Al concentrations, the H_c values mostly increase up to around 473 K and beyond that, it decreases. The magnetocrystalline anisotropy energy and coercivity depend upon ionic radius of substituted atoms [137]. The partial substitution of Al^{3+} ions will lead to local distortion of lattices due to ionic size mismatch with that of Fe^{3+} ions. The temperature dependence of coercivity is expected to be influenced by the temperature dependence of magnetocrystalline anisotropy energy. However, at high temperatures, the thermal fluctuations will be dominant over the energy barrier of pinning defects and that leads to sharp fall in H_c values. The temperature dependence M_s and K_1 for various concentrations of Al substituted samples along with the parent compound were estimated by fitting of magnetization data to the law of approach to saturation (LAS) model. The temperature variation of M_s and K_1 are found to decrease with increase in temperature and there are shown in Fig. 4.9 (c) and (d) respectively.

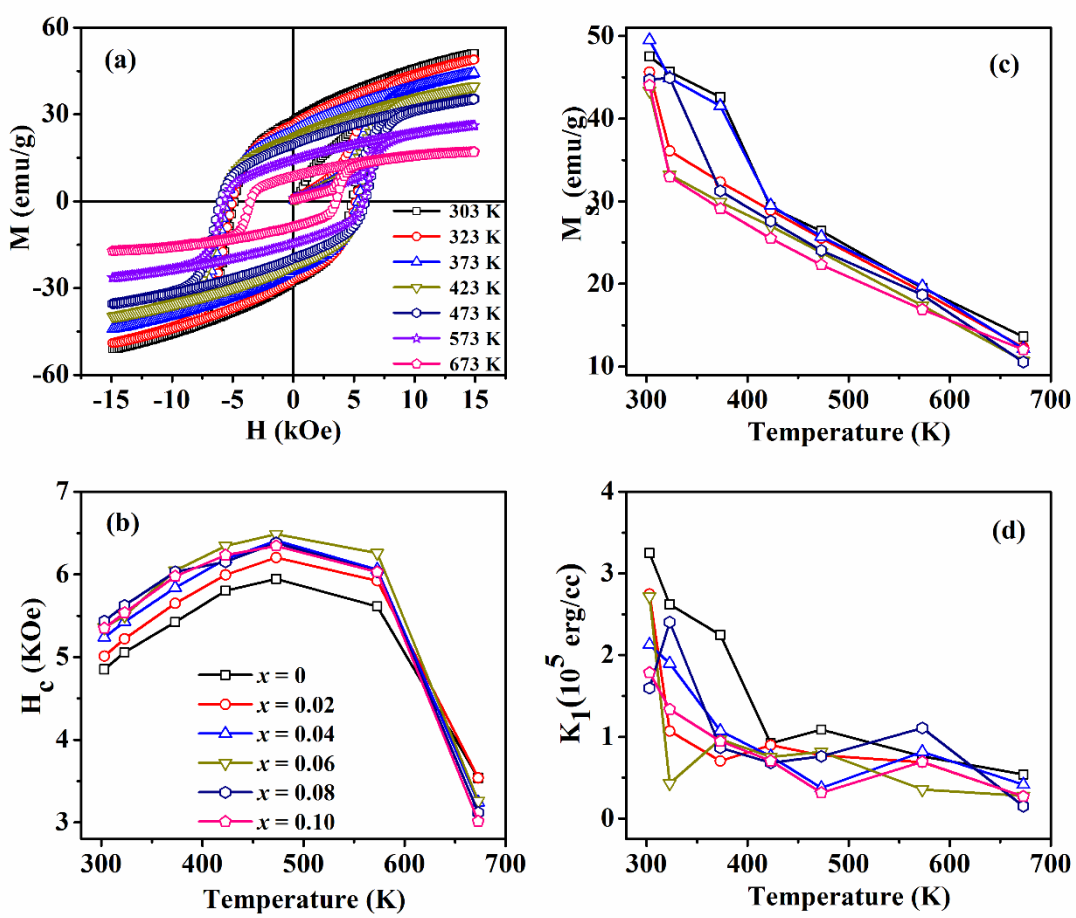

Figure 4.9: *M – H* loops of $BaFe_{12}O_{19}$ sample at different temperature (a) and the temperature dependence of (b) H_c, (c) M_s and (d) K_1 for Al substituted BaM samples.

4.1.4 Complex Permittivity and Permeability

The main objective of this section is to describe the effect of Al substitution on the dielectric permittivity and the magnetic permeability of BaM hexaferrite material. In general, the complex permittivity ($\varepsilon^* = \varepsilon' + j\varepsilon''$) and complex permeability ($\mu^* = \mu' + j\mu''$) determine the electronic and magnetic properties of a material in consequence of an applied electromagnetic field. The real parts of dielectric permittivity and magnetic permeability (ε' and μ') represent the storage capability of electric and magnetic energy respectively, whereas the complex parts of dielectric permittivity and magnetic permeability (ε'' and μ'') represent the electric and magnetic energy loss in a material. To understand the effect of Al substitution on dielectric and magnetic properties of BaM hexaferrite, the complex dielectric permittivity and magnetic permeability measurements were carried out in the frequency range of 1 MHz to 1 GHz and the obtained results are shown in Fig. 4.10. Fig. 4.10(a-b) shows the room temperature frequency variations of real

and imaginary parts of dielectric permittivity (ε' and ε'') for $Ba(Fe_{1-x}Al_x)_{12}O_{19}$ samples with x = 0, 0.02, 0.04, 0.06, 0.08 and 0.10. The plots of ε' indicate that the dielectric dispersion is large at lower frequency range and it becomes independent at higher frequency range. At low frequency, the hopping of electrons follow the applied electric field easily and give rise to large value of polarization and dielectric constant. However for higher frequencies, the hopping of electrons may not follow the applied electric field and the polarization of local charges only takes place, which in turn gives rise to low value of ε'. For a particular frequency ε' is found to decrease with increase in Al concentration. For x = 0 sample, the ε' value is found to be 189 at a characteristic frequency of 1 MHz and the ε' value is found to decrease up to 13 for x = 0.10 sample at 1 MHz frequency range. This is due to the fact that, the space charge polarization directly depends upon concentration of Fe^{2+} ions. As Al^{3+} ions have strong preference to occupy octahedral sites, so the concentration of Fe^{2+} ions on octahedral site decreases that means the hopping of charge carriers between Fe^{3+} and Fe^{2+} decreases. As a result, electric polarization decreases and consequently the dielectric constant also decrease [138, 139].

Further, the ε'' possess maximum value at low frequency region and a constant behavior is obtained at higher frequency region. The maximum value of ε'' observed at lower frequency demonstrates that, the interaction between the dipoles are more and it becomes weak with increase in frequency such that it leads to significant reduction in dielectric loss [140]. In addition, the presence of oxygen vacancies, local valence variation, porosity and grain boundary defects in ferrite materials give rise to interfacial polarization [55, 141, 142]. Since the interfacial/space charge polarization is dominant at low frequency region than the other polarization mechanisms such as electronic and ionic polarizations, thus the interfacial polarization contributes the high value of ε' and ε'' at low frequency region. However, the ε'' spectrum for x = 0 sample exhibits a peak at a characteristic frequency of 1.69 MHz range. The presence of dielectric relaxation peak can be assigned to the electron hopping between the adjacent Fe^{2+} and Fe^{3+} ions. As the Al concentration is increased, the peaks in the ε'' spectra may move towards the lower frequency (< 1 MHz) range with decreased intensity due to decrease in Fe concentration, which is not seen due to the limitation of the frequency range in the measured instrument. At a particular frequency, the dielectric loss values are found to decrease with increase in Al concentration as shown in Fig. 4.10(b).

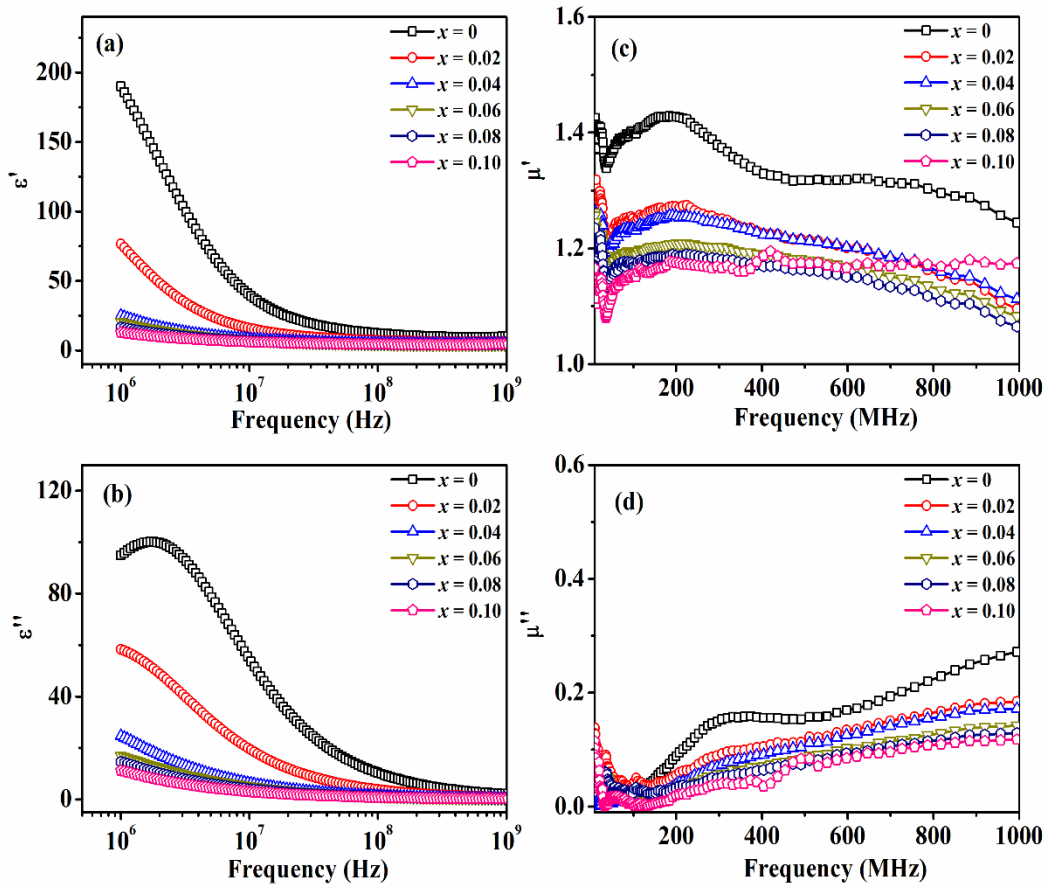

Figure 4.10: (a-d) Plots of real (ε') and imaginary (ε'') parts of dielectric permittivity of $Ba(Fe_{1-x}Al_x)_{12}O_{19}$ ($0 \leq x \leq 0.10$) samples along with real (μ') and imaginary (μ'') parts of magnetic permeability as a function of frequency.

Fig. 4.10(c) and (d) illustrates the real (μ') and imaginary (μ'') parts of complex permeability as a function of frequency for $Ba(Fe_{1-x}Al_x)_{12}O_{19}$ ($0 \leq x \leq 0.10$) samples in the frequency range of 10 MHz to 1 GHz. The permeability spectra reveal the common feature for all the samples. The real part of complex permeability is found to decrease with increase in frequency. The limited speed of spin and domain wall movement (displacement/rotation) in the sample is the main source for decrease in μ' value with frequency [143]. Further, with increase in Al concentration, the real part of permeability is found to decrease from 1.42 to 1.14 as shown in Fig. 4.10(c). Such behavior of permeability spectra can be well explained by Ohta's model [53]. According to Ohta's model, the permeability can be expressed as $\mu_i \, \alpha \, M_s^2/(K_1 + \lambda_s \sigma)$, where K_1 is the magnetocrystalline anisotropy; λs is magnetostriction factor and σ is the internal stress. From the analysis of magnetization measurement, it has been observed that the M_s values are found to decrease with increase of H_c values due to Al substitution. Thus, as per the above relation, the

observed decrease in μ' value is expected due to Al substitution. The permeability spectra of μ' also exhibits a peak around 177 MHz for all the samples. Fig. 4.10 (d) reveals that the μ'' value is slightly increasing with increase in frequency. The substitution of Al is found to reduce the magnetic loss. In general, there exist various sources such as domain wall resonance, hysteresis, eddy current effect, natural resonance and ferromagnetic resonances from which the magnetic loss is originated [144]. Since the loss due to domain wall motion occurs at low frequency region i.e. in MHz range rather than the GHz range, the observed magnetic loss in the present study could be attributed to the domain wall motion. The observation of peaks in the MHz frequency range is caused by the natural resonance mechanism. In addition, the μ'' is directly proportional to the saturation magnetization (M_s) by the following relation as; $\mu'' = \frac{M_S}{2H_a\alpha}$, where H_a is the anisotropy field and α is the extinction coefficient [144]. From the analysis of magnetization, it is found that the M_s value is reduced due to Al substitution and that may cause reduction in μ''.

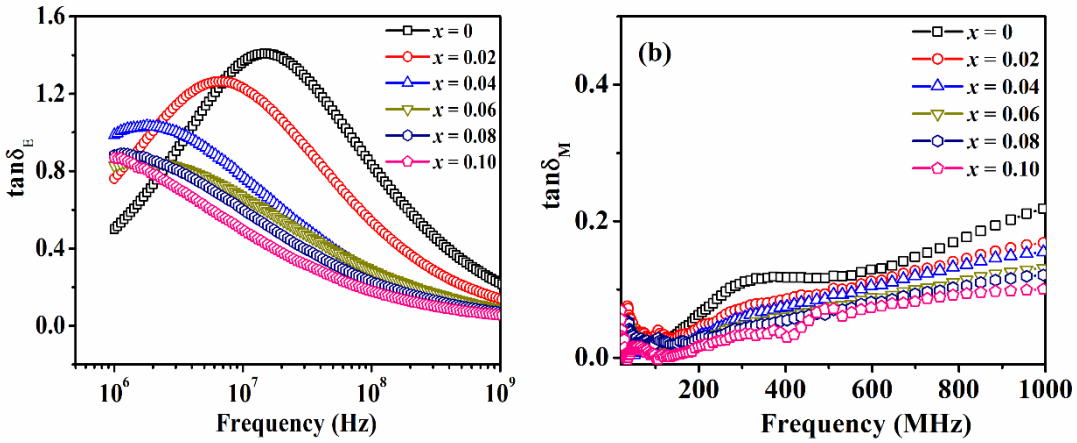

Figure 4.11: (a-b) Frequency variation of dielectric loss tangent (tanδ$_E$) and the magnetic loss tangent (tanδ$_M$) of Ba(Fe$_{1-x}$Al$_x$)$_{12}$O$_{19}$ ($0 \leq x \leq 0.10$) samples measured at room temperature.

The variation of dielectric loss tangent ($\tan\delta_E = \frac{\varepsilon''}{\varepsilon'}$) as a function of frequency for Ba(Fe$_{1-x}$Al$_x$)$_{12}$O$_{19}$ ($0 \leq x \leq 0.10$) samples are shown in Fig. 4.11(a). It is observed that the typical frequency variation of $\tan\delta_E$ is almost similar to that of ε'. Fig. 4.11(a) reveals that the $\tan\delta_E$ value is found to decrease with increase in frequency and this phenomenon is well explained by Koop's theory [145]. According to Koop's, poorly conducting grain boundaries are effective at lower frequencies and conducting grains are effective at higher frequencies. Thus at lower frequency, the resistance offered by the grain boundaries are

high. So more energy is required for the hopping of electrons between Fe^{2+} and Fe^{3+} ions, as a result energy loss is high. Whereas in the high frequency region, grains are more effective and hence small energy is required for electron hopping and it leads to small energy loss. From the above Fig. 4.11(a), it can be seen that the $\tan\delta_E$ spectra show the relaxation peaks at low frequency region. The observation of peaks in $\tan\delta_E$ spectra are due to the activation of dipoles that means the hopping frequency of localized charge carriers match with the frequency of applied ac electric field [146]. It is observed that, in the measured frequency domain, the relaxation peaks are observed for x = 0, 0.02 and 0.04 samples at a characteristic frequency of 14.6 MHz, 6.84 MHz and 1.34 MHz range respectively. This implies that the relaxation peaks are shifted towards the lower frequency region with Al substitutions. The relaxation peaks are not seen for x = 0.06 – 0.10 samples due to the limitation of frequency range. With increase in Al concentration, the $\tan\delta_E$ values are getting supressed. The suppression of $\tan\delta_E$ spectra demonstrates that the substitution of Al supresses the dc conduction of BaM hexaferrite.

Further, in order to understand the dissipation of magnetic energy of a system, the magnetic loss tangent ($\tan\delta_M = \frac{\mu''}{\mu'}$) measurements were carried out for $Ba(Fe_{1-x}Al_x)_{12}O_{19}$ ($0 \leq x \leq 0.10$) samples at room temperature in the frequency range of 10 MHz to 1 GHz as shown in Fig. 4.11(b). For x = 0 sample, a peak is observed at a characteristic frequency of around 320 MHz. The substitution of Al at Fe site is found to suppress the peak intensity and it shifts towards to lower frequency range. Such type of mechanism of $\tan\delta_M$ could be attributed to the domain wall motion and domain rotation [29, 109, 147, 148]. Besides that, the magnetic loss is found to increase with increase in frequency for all the samples. However, at a particular frequency, the substitution of Al reduces the magnetic loss. In the earlier reports on M-type hexaferrite, some of the authors have shown that the domain wall motion is dominant at low frequency region (< 2GHz) and domain rotation at higher frequencies [148]. The observed low value of magnetic loss ($< 2\%$) and high permeability at higher frequencies especially for Al doped samples highlight the importance of these samples for potential applications towards microwave absorber [50, 149].

4.1.5 Conclusions

Polycrystalline samples of $Ba(Fe_{1-x}Al_x)_{12}O_{19}$ ($0 \leq x \leq 0.10$) were successfully prepared by standard solid state reaction method. Phase purity of the synthesized samples are confirmed from the XRD patterns and they crystallize in hexagonal symmetry with

$P6_3/mmc$ space group. The analysis of x-ray diffraction patterns based on the Rietveld refinement technique reveals that the lattice parameters *a* and *c* are found to decrease with increase in Al concentration. Raman spectra were studied to investigate the lattice vibration characteristics of all samples and that confirms the single-phase nature of all the samples. The effect of Al substitutions on the microstructure, dielectric and magnetic properties of M-type hexaferrites were systematically investigated. The room temperature magnetization measurement reveals that the saturation magnetization (M_s) is found to decrease from 51.36 emu/g for $x = 0$ to 45.76 emu/g for $x = 0.10$. However, the coercivity (H_c) value is found to increase upon Al substitution. Therefore, the high values of coercivity of these magnetic materials are suitable for applications in permanent magnets and microwave devices. Further, to understand the effect of temperature on the magnetic properties of Al doped BaM hexaferrite, the $M - H$ loops were measured at selected temperatures varying from 303 K to 673 K. It reveals that the M_s value is decreased with increase in Al concentration. However, the H_c value is increased up to around 500 K and then decreases due to the dominant property of thermal fluctuation over the magnetocrystalline anisotropy. Further, the variations of relative complex dielectric permittivity and permeability were systematically analyzed at room temperature. The substitution of Al at Fe site is found to suppress the dielectric permittivity and the permeability values.

Chapter 5

$Ba_2(Co_{1-x}Zn_x)_2Fe_{12}O_{22}$ Series

5.1 Zn Substituted $Ba_2Co_2Fe_{12}O_{22}$ Series

As discussed in the previous chapters 3 and 4, like M-type hexaferrite, Y-type hexaferrite is another important class of hexaferrite that possesses interesting magnetic and dielectric properties. In recent years, Y-type hexaferrite is one of the prominent material that draws the research attention due to their potential applications in radio frequency (RF) and microwave devices, multilayer chip inductors, electromagnetic-wave absorbers, high frequency antennas, *etc.* [2, 71, 150-154]. The noncollinear magnetic structure of Y-type hexaferrites ($Ba_2Me_2Fe_{12}O_{22}$) make these materials suitable for study of various interesting magnetic properties such as magnetoelectric effect and the electric polarization induced by an external magnetic field [60, 61, 155]. Knizek *et al*., have reported that the relative fractions of Fe and Zn in the tetrahedral sublattice of spinel block induces the electrical conductivity in $(Ba,Sr)Zn_2Fe_{12}O_{22}$ hexaferrite [156]. It exhibits insulating behavior, when the tetrahedral sublattice is completely occupied by Zn and to the metallic state when the site is completely filled with Fe ions. The magnetic and dielectric parameters such as saturation magnetization, magnetocrystalline anisotropy, permittivity, impedance spectra and permeability *etc*., can be effectively modified by various cationic substitutions for Fe^{3+}, Ba^{2+} or Co^{2+} sites in Co_2Y hexaferrite [152, 157]. Stergiou *et al*., have reported that the permeability and permittivity of Y-type hexaferrite is enhanced due to Ni substitution [158]. The magnetic and dielectric properties can be tuned by the substitution of Ni in Co_2Y hexaferrite such that it can be used for microwave absorbance [158]. The partial substitution of nonmagnetic Zn^{2+} ion in Co_2Y hexaferrite induces tunable magnetoelectric behavior [59] and similar magnetoelectric behavior is also obtained in a few other Y-type hexaferrites [159, 160]. The relatively low resonance width at microwave frequencies is also observed in the Zn based Y-type hexaferrites [66, 152, 161, 162].

In view of the interesting properties of Y-type hexaferrites upon Zn substitution and the lack of detailed study on structural, dielectric and magnetic properties of these modified compounds, we have taken up the detailed study on $Ba_2(Co_{1-x}Zn_x)_2Fe_{12}O_{22}$ by varying the Zn concentration, i.e. for x = 0, 0.1, 0.3, 0.5, 0.75 and 1.0 via solid state route. The structural, magnetic and dielectric properties of these Zn substituted compounds are systematically investigated in this chapter.

5.1.1 Sample Preparation and Characterization

Polycrystalline samples of $Ba_2(Co_{1-x}Zn_x)_2Fe_{12}O_{22}$ with x = 0, 0.1, 0.3, 0.5, 0.75 and 1.0 were synthesized by the standard solid state reaction route. Stoichiometric ratio of high purity (> 99.9%) $BaCO_3$, Fe_2O_3, ZnO, and Co_3O_4 powders were mixed and ground together under acetone medium for 2 h. The uniform mixture of the above oxides/carbonates was calcined at 600 ℃ and 800 ℃ for 12 h each. To obtain good homogeneity, the calcined powders were ground and pressed into cylindrical pellets of diameter ~13 mm using a hydraulic press followed by the final sintering at 1150 ℃ for 12 h in air. The structural, microstructural, dielectric and magnetic properties are studied using the experimental techniques discussed in chapter 2.

5.1.2 Structural Properties

Fig. 5.1 shows the XRD patterns of $Ba_2(Co_{1-x}Zn_x)_2Fe_{12}O_{22}$ (BCZFO) samples with different compositions ($0 \leq x \leq 1.0$) recorded at room temperature. The XRD patterns of all these samples were analyzed by the Rietveld refinement technique based on R-3m space group with rhombohedral structure. The analysis of XRD patterns endorsed the formation of well defined Y-type barium hexaferrite ($Ba_2Co_2Fe_{12}O_{22}$) for all Zn concentrations. Typical XRD patterns for x = 0, 0.3, 0.5 and 1.0 samples along with their Rietveld refined data are shown in Fig. 5.2 and Fig. 5.3 respectively. The lattice parameters determined from the Rietveld refinement for the parent compound (x = 0) are found to be a = 5.856 Å and c = 43.477 Å and they are found to increase with increase in Zn concentration up to a = 5.878 Å and c = 43.598 Å for x = 1.0 sample. The systematic increase in lattice parameters due to the substitution of Zn at Co site can be attributed to the difference in their ionic radii. Further, the preferential site occupation of Zn^{2+} ions at the tetrahedral site for which some of the Fe^{3+} ions transferred from the tetrahedral sites to the octahedral sites (r = 0.49 Å and 0.645 Å for Fe ions at tetrahedral and octahedral sites respectively) is also another reason for the increase in lattice parameters. The lattice parameters, unit cell volume and the

reliability factors determined from the analysis based on Rietveld refinement are tabulated in Table 5.1.

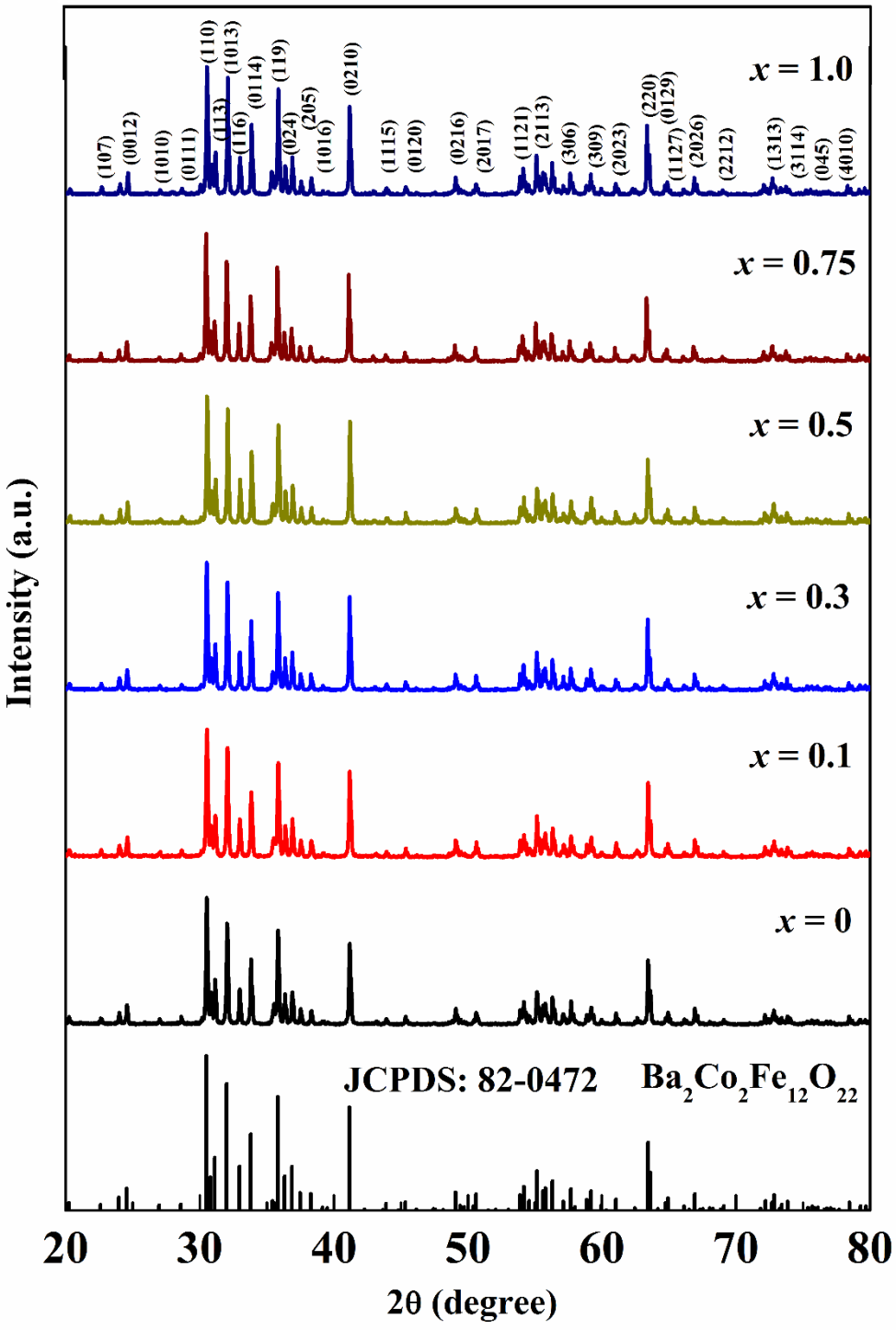

Figure 5.1: XRD patterns of BCZFO samples for $x = 0 – 1.0$ measured at room temperature.

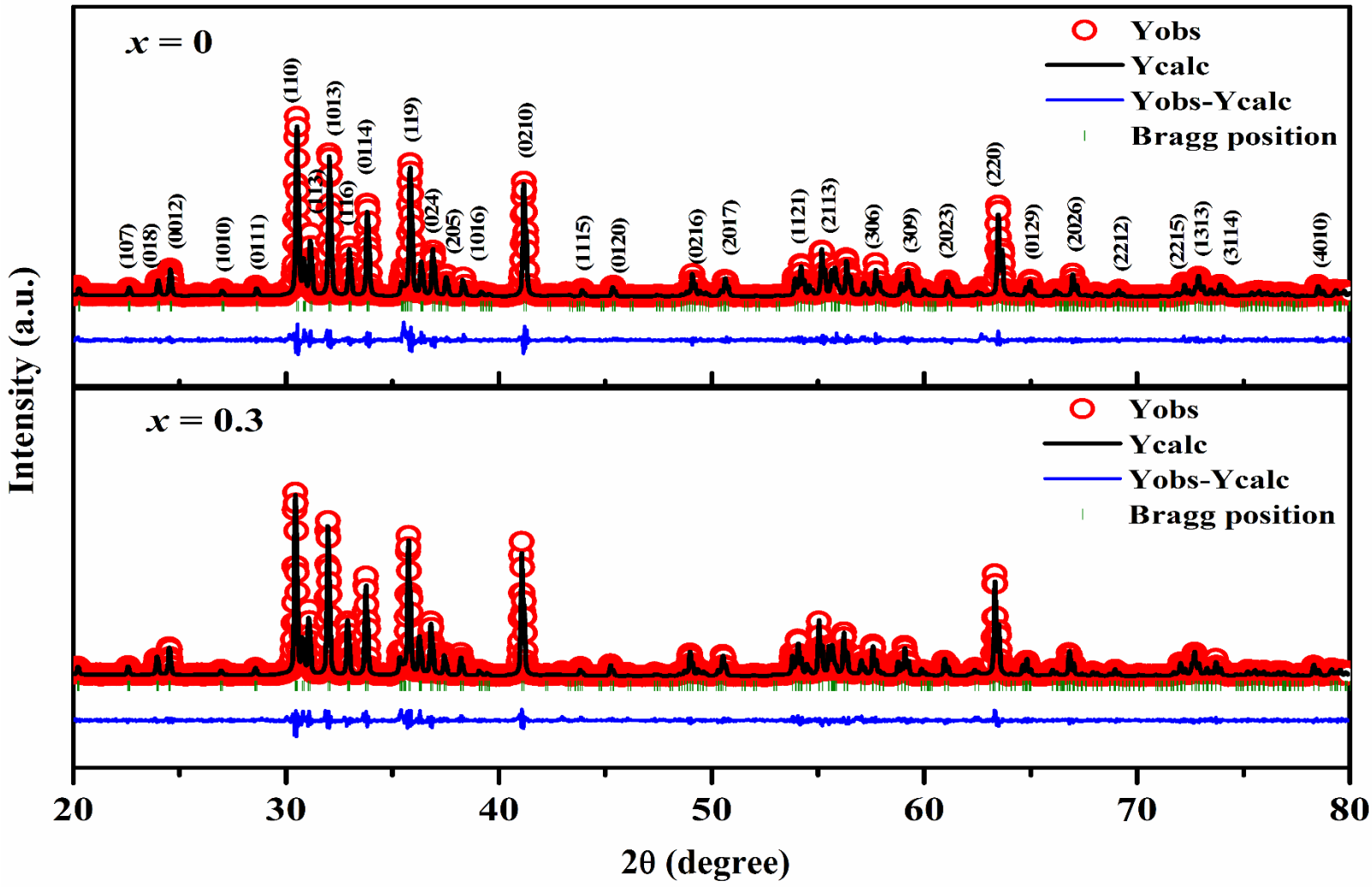

Figure 5.2: Rietveld refined XRD patterns of BCZFO samples with x = 0 and 0.3. The red open circles represent the experimental data and the black solid lines are the fitted data. The bottom line represents the difference between experimental and refined data.

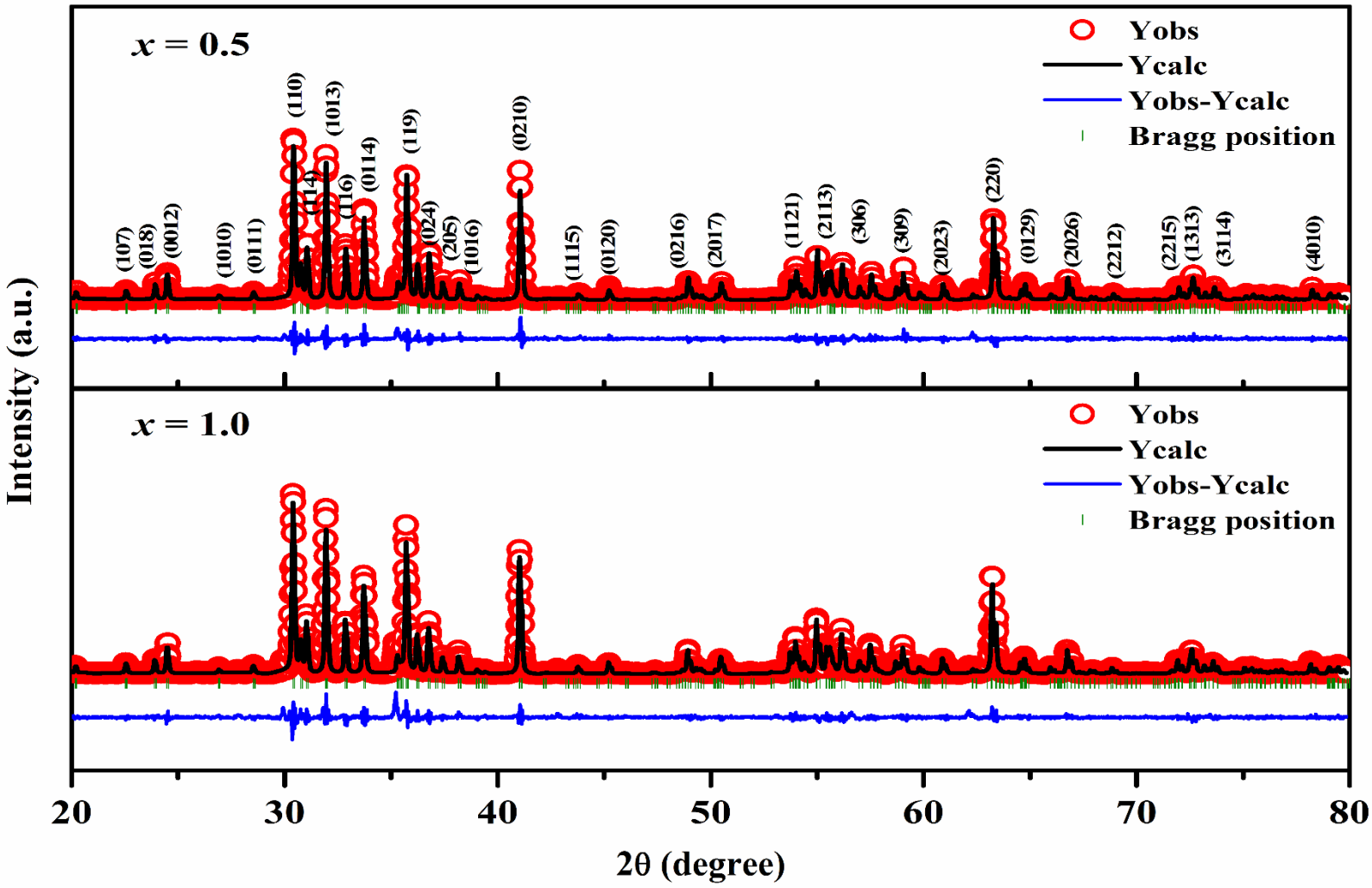

Figure 5.3: The XRD patterns of BCZFO samples along with Rietveld refined data for x = 0.5 and 1.0. The red open circles represent the experimental data and the black solid lines are the fitted data. The bottom line represents the difference between experimental and refined data.

Table 5.1: Parameters determined from the Rietveld analysis of $Ba_2(Co_{1-x}Zn_x)_2Fe_{12}O_{22}$ (x = 0 – 1.0).

Sample/ Parameters	x **= 0**	x **= 0.1**	x **= 0.3**	x **= 0.5**	x **= 0.75**	x **= 1.0**
Space group	*R-3m*	*R-3m*	*R-3m*	*R-3m*	*R-3m*	*R-3m*
***a* (Å)**	5.8568 (7)	5.8644 (6)	5.8700 (5)	5.8728 (1)	5.8738 (0)	5.8783 (7)
***c* (Å)**	43.4778 (8)	43.5285 (8)	43.5610 (1)	43.5877 (2)	43.5796 (1)	43.5981 (3)
***Volume* (Å^3)**	1291.60 (0)	1296.45 (5)	1299.88 (1)	1301.95 (5)	1302.11 (7)	1304.70 (7)
R_F **(%)**	5.08	5.00	5.19	5.58	5.13	5.47
R_{Bragg} **(%)**	5.42	5.27	5.30	5.99	5.40	6.44
R_P **(%)**	17.00	15.9	15.9	18.4	15.7	17.9
R_{exp} **(%)**	11.34	11.34	11.28	11.31	10.59	11.32
χ^2	3.95	3.63	3.65	4.48	4.21	4.65

Typical FESEM micrographs of BCZFO samples with x = 0, 0.3, 0.5 and 1.0 are shown in Fig. 5.4(a-d). The grain sizes of the samples were calculated using ImageJ software. The microstructural images of all these samples constitute the mixture of smaller and larger hexagonal platelets like structure. The observed grain sizes are found to be distributed in over a wide range with random orientations as shown in the right column of Fig. 5.4. The average grain size of each sample was estimated by fitting the data using the log-normal distribution function [163];

$$f(d, \mu, \sigma) = \frac{1}{d\sigma\sqrt{2\pi}} \exp \frac{-(lnd - \mu)^2}{2\sigma^2} \qquad (5.1)$$

where d is the cross-sectional length of the particle, σ is the standard deviation and μ represents the logarithmic mean. The average grain size for $x = 0$ sample is found to be 1.9 µm with a standard deviation of 0.4 µm. The average grain size values are found to lie in the range of 1.5 µm – 2 µm for various samples in this series. Fig. 5.5 depicts the EDX spectra for $x = 0$, 0.3, 0.5 and 1.0 samples. The cationic ratios Ba:Co:Zn:Fe obtained from the analysis of EDX spectra for all these samples are given in Table 5.2 and they are comparable with the nominal starting compositions.

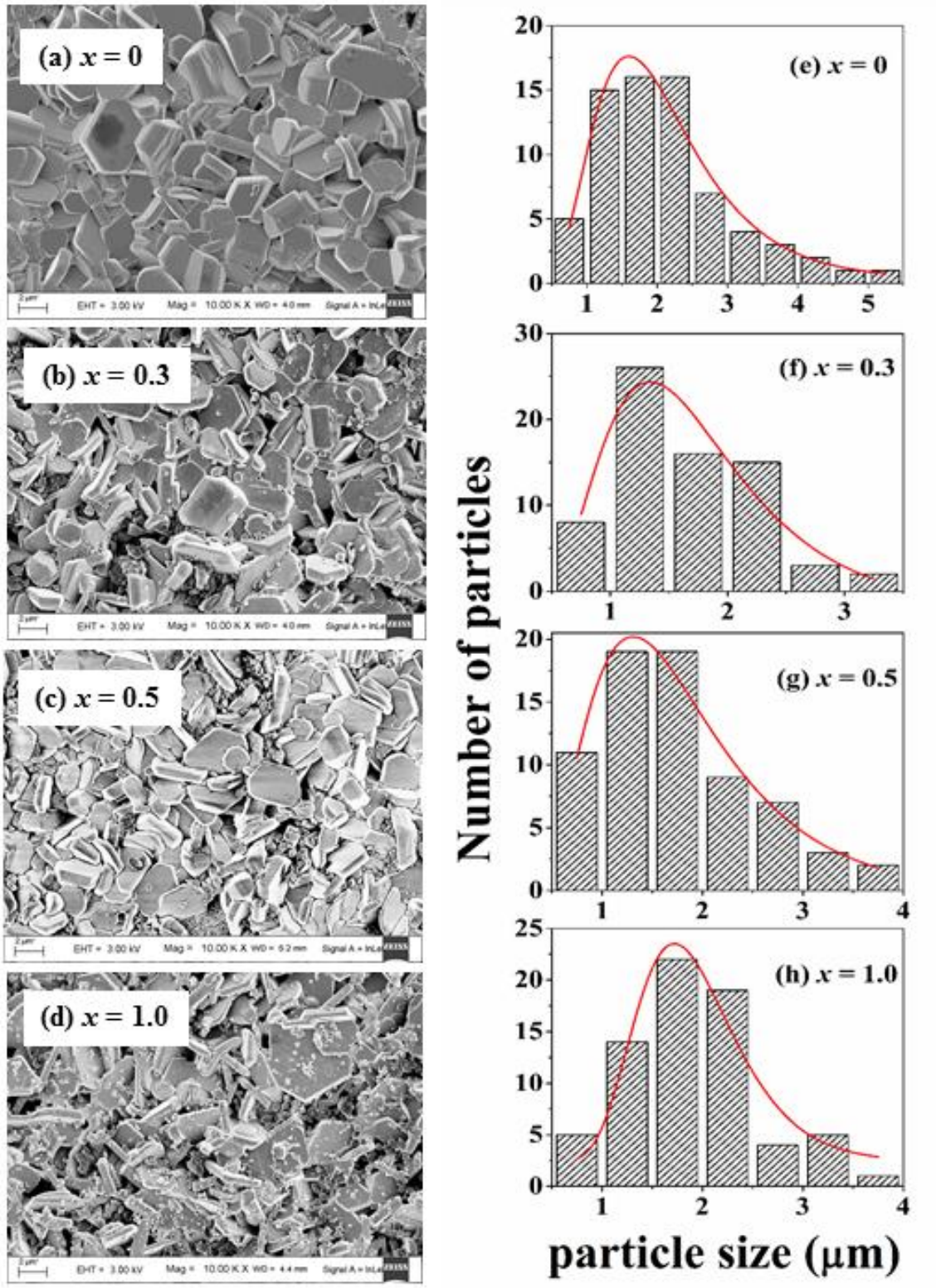

Figure 5.4: FESEM micrographs of BCZFO samples for (a) x = 0 (b) x = 0.3 (c) x = 0.5 and (d) x = 1.0 along with their corresponding particle size distributions (e-h).

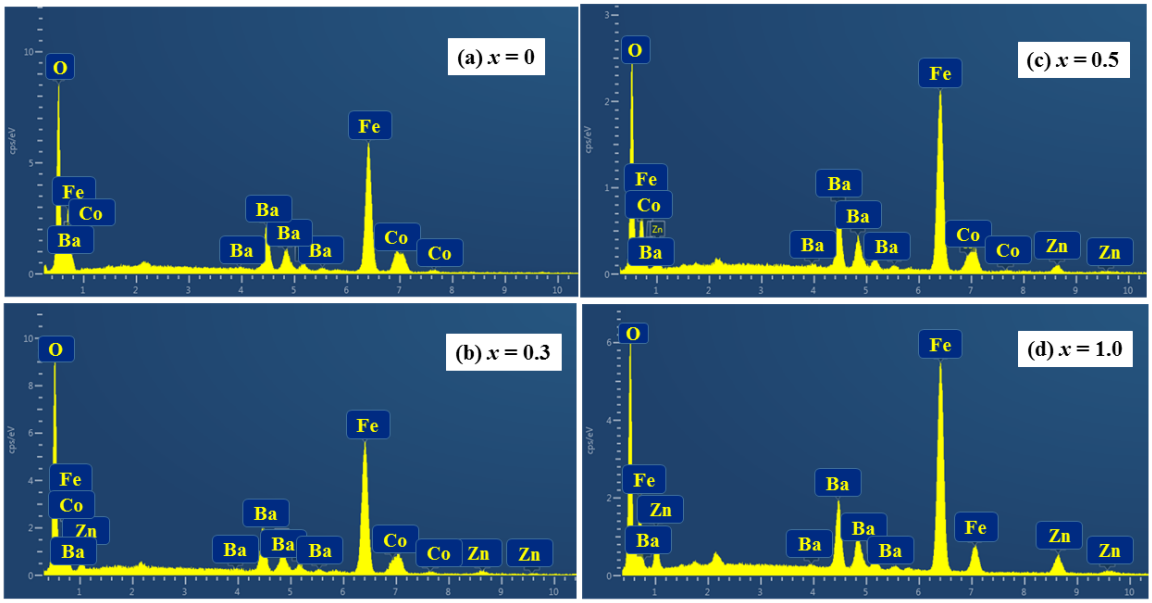

Figure 5.5: (a-d) EDX spectra of BCZFO samples with x = 0, 0.3, 0.5 and 1.0.

Table 5.2: The cationic ratio determined from the analysis of EDX spectra for BCZFO samples with x = 0 to 1.0.

Samples	Calculated Cationic Ratio from EDX Analysis			
	Ba	**Co**	**Zn**	**Fe**
***x* = 0**	2.00	1.79	0.00	11.01
***x* = 0.1**	2.00	1.80	0.20	11.15
***x* = 0.3**	2.20	1.39	0.61	12.03
***x* = 0.5**	2.00	1.02	0.98	11.10
***x* = 0.75**	2.08	0.53	1.47	11.80
***x* = 1.0**	2.00	0.00	1.92	11.21

5.1.3 Complex Impedance Spectroscopy Analysis

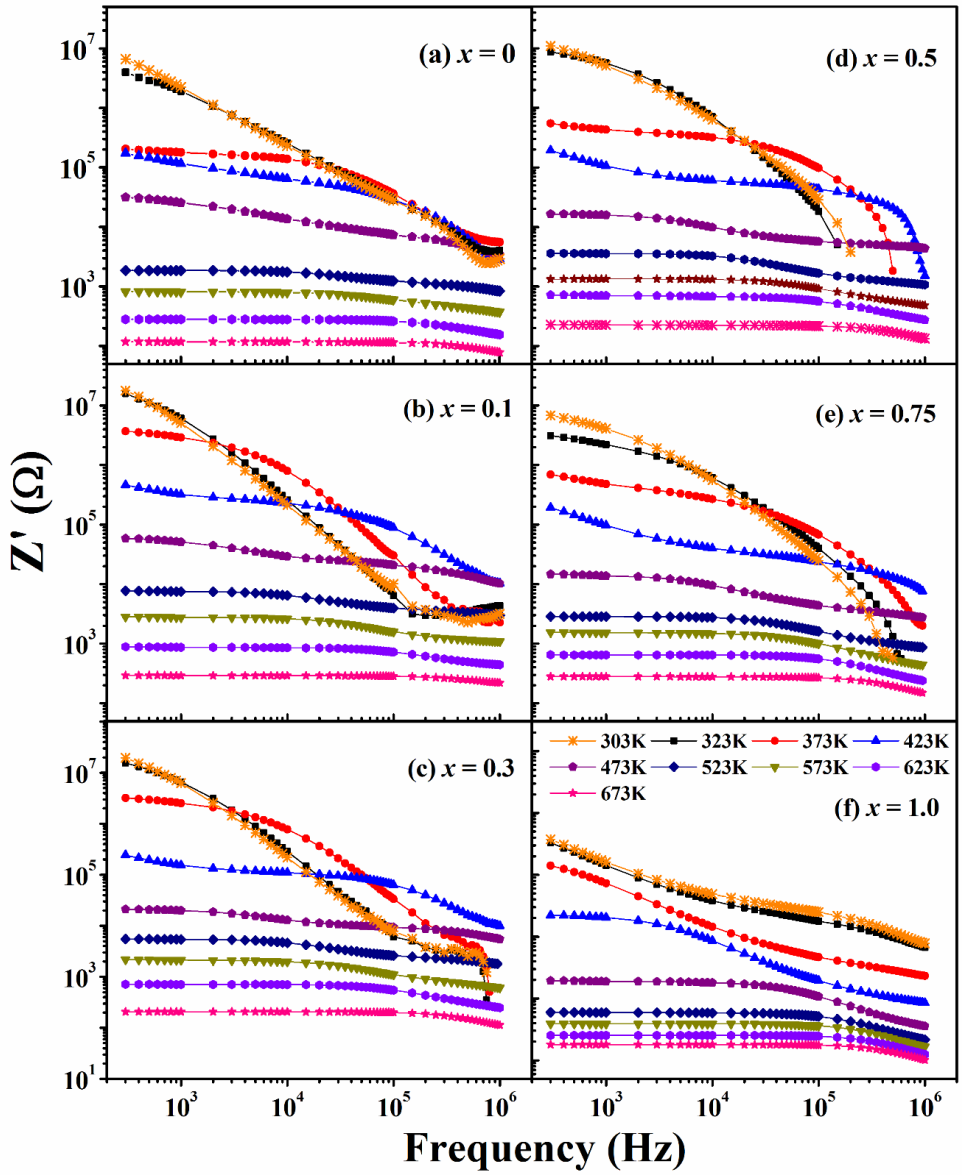

Figure 5.6: Real part of complex impedance (Z') as a function of frequency for BCZFO samples with (a-f) x = 0 – 1.0 at different temperatures ranging from 303 K to 673 K.

Complex impedance spectroscopy is one of the convenient and powerful techniques to understand the electrical transport properties of polycrystalline materials over a wide range of frequency and temperature. It is well known that the motion of charge carriers at the intragrain, intergrain regions and material electrode interfaces contribute to the impedance behavior in a material. There are several ways of charge carriers movement such as long-range/short-range displacement, dipole reorientation and via the formation of space charges, *etc*. All these motions of charge carriers give rise to the frequency response of Z'

spectra. Fig. 5.6 shows the real part (Z') of the complex impedance spectra for $Ba_2(Co_{1-x}Zn_x)_2Fe_{12}O_{22}$ ($0 \leq x \leq 1.0$) samples measured at different temperatures in the frequency range of 100 Hz to 1 MHz. At a particular temperature, the Z' values are found to decrease with increase in frequency and tend to merge with each other at higher frequencies. This kind of behavior can be attributed to the release of space charge polarization. Furthermore, for a particular concentration, the Z' value is also found to decrease with increase in temperature and it suggests that the temperature coefficient of resistance is basically negative [95]. The effect of Zn substitution at Co site is observed in terms of reduction in the Z' value.

The frequency dependence of imaginary part (Z'') of the complex impedance spectra for BCZFO samples with x = 0, 0.1, 0.3, 0.5, 0.75 and 1.0 measured at different temperatures from 373 K to 673 K are shown in Fig. 5.7. A relaxation peak is observed in the impedance spectrum of x = 0 sample at a characteristic frequency of f_{max} = 30 kHz for measurements carried out at 373 K. Similar relaxation behavior is observed from the measurements carried out in other samples as denoted by region (I) in Fig. 5.7. This relaxation dynamics can be ascribed to the relaxation of charge carriers towards applied ac electric field inside the grains. Suppression of relaxation peak (Z''_{max}) and its shifting towards the higher frequency are observed with increase in temperature. This reveals that the relaxation is due to thermally activated charge carriers. As the temperature is increased, a shoulder like secondary peak starts appearing in the low frequency regions denoted by region (II) as shown in Fig. 5.7. This secondary peak could be ascribed to the relaxation across the grain boundaries. As the temperature is increased, the secondary relaxation peak gets suppressed with shifting towards the higher frequency range. With further increase in temperature, the secondary peak moves out of the measured frequency range. Similar relaxation peaks due to grains and grain boundaries contributions are observed for all the Zn doped samples. In addition to that, the magnitude of relaxation peak of Z'' gets suppressed and shifted towards higher frequency range as the Zn concentration is increased. Furthermore, in order to understand the distribution of relaxation phenomena with respect to temperature, the impedance spectra (Z'') were plotted in scaled coordinates i.e. (Z''/Z''_{max}) versus log (f/f_{max}) plots as shown in Fig. 5.7(g-h). They clearly show that the relaxation loss peaks are merged into a single master curve. This signifies that the distribution of relaxation phenomena is temperature independent [110].

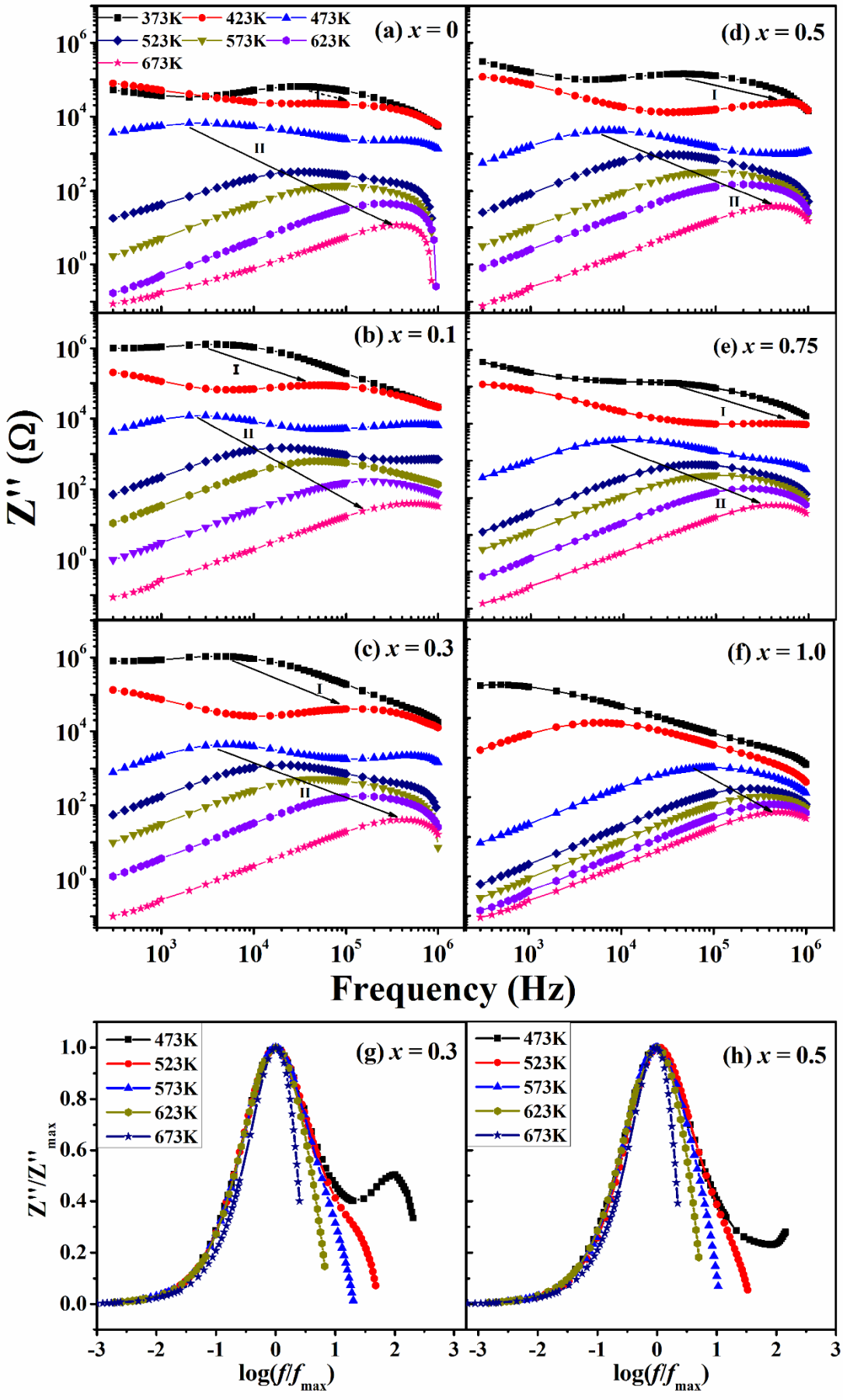

Figure 5.7: Imaginary part (Z'') of complex impedance as a function of frequency for BCZFO samples with (a-f) x = 0 – 1.0 at different temperatures ranging from 373 K to 673 K. Normalized impedance spectra (g-h) with respect to its maximum value (Z''_{max}) for x = 0.3 and 0.5 samples.

5.1.4 Complex Dielectric Permittivity Analysis

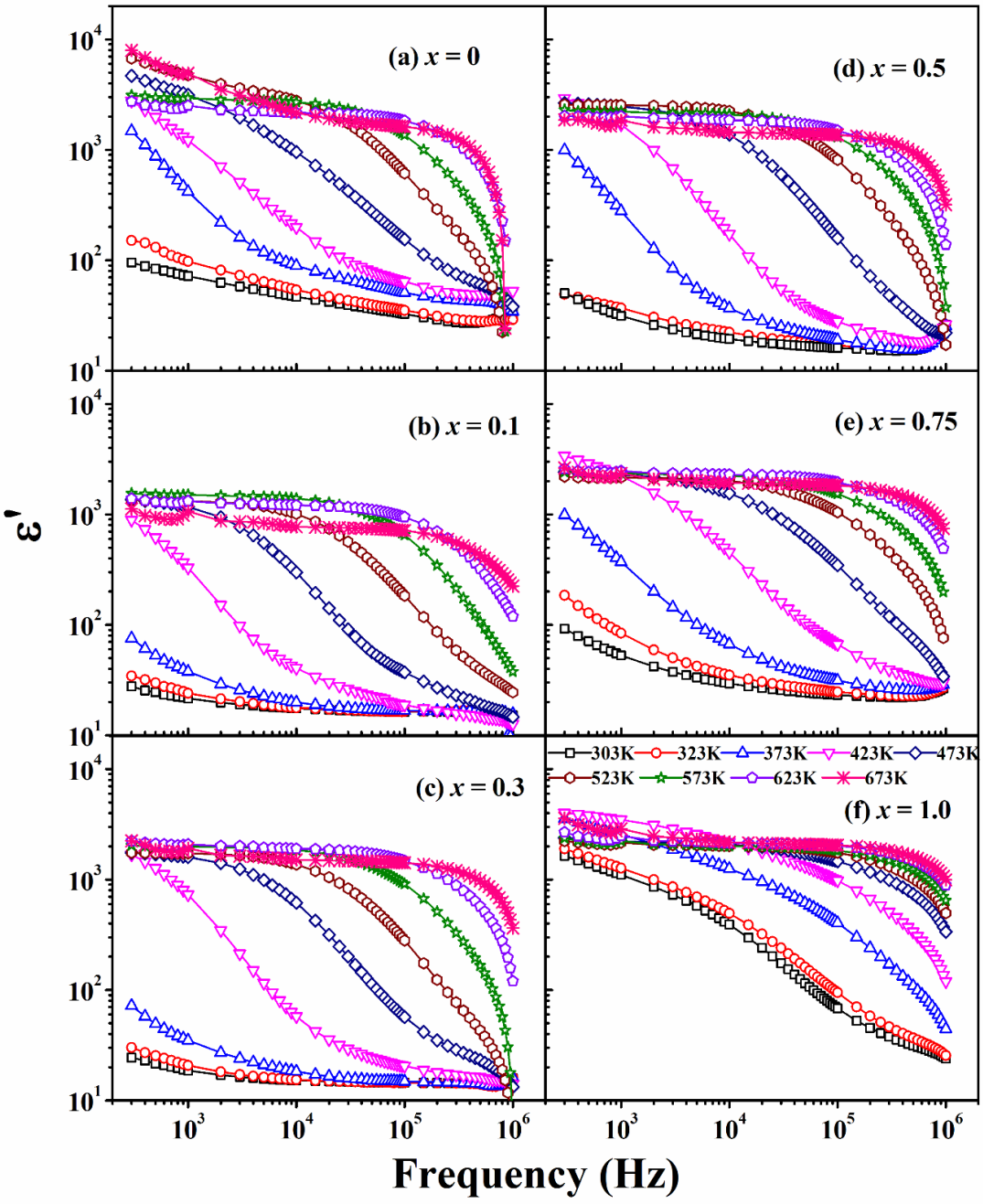

Figure 5.8: Real part of complex dielectric permittivity (ε') as a function of frequency in log-log scale at different temperatures from 303 K to 673 K for BCZFO samples with (a-f) x = 0 – 1.0.

In order to understand the dielectric properties of the materials, the complex dielectric permittivity (ε^*) were measured at different temperatures from 303 K to 673 K. The real (ε') and imaginary (ε'') parts of the complex permittivity of BCZFO were calculated from the complex impedance by employing the following relation as [95, 164];

$$\varepsilon^* = \varepsilon' - j\varepsilon'' \tag{5.2}$$

where

$$\varepsilon' = \frac{-Z''}{\omega C_0 (Z'^2 + Z''^2)} \tag{5.3}$$

$$\varepsilon'' = \frac{Z'}{\omega C_0 (Z'^2 + Z''^2)} \tag{5.4}$$

where ω is the angular frequency, C_0 is the geometrical capacitance of the sample, Z' and Z'' represent the real and imaginary parts of the complex impedance. Fig. 5.8 shows the frequency dependence of ε' of BCZFO samples with x = 0 – 0.10 in the log-log scale at some selected temperatures in the frequency range of 10^2 – 10^6 Hz. The concept of this frequency dependent dielectric constant of ferrite samples can be well understood based on different polarization mechanisms. The frequency dispersion of ε' of x = 0 sample can be classified into two temperature regions; the high temperature region for $T \geq 573$ K and the low temperature region for $T \leq 523$ K. In the high temperature region i.e. near or above the ferrimagnetic T_c, a plateau like behavior has been observed as shown in ε' vs f plot followed by the decrease in its value at higher frequency. This is the typical dielectric relaxation behavior in most of the dielectric materials, where at higher frequency, the dipoles cannot follow the oscillation behavior of electric field and it results in sharp fall in ε' value. Further, it is known that, the impediment of charges at physical barriers such as grain boundaries, electrode – material interfaces *etc*., give rise to space charge (interfacial) polarization in the material. In such cases, when an electric field is applied, the charges pile up at the grain boundaries and behaves like dipoles. These dipoles produce large polarization in a material known as space charge polarization. At low temperature and low frequency region, the ε' exhibits maximum value and then falls quite sharply with increase in frequency. The increased value of ε' in the low frequency region is assigned to the space charge polarization mechanism. Similar behavior is also observed in other samples. Since the frequency range of response for such type of polarization falls within the range of 10^{-3} Hz to kHz range, the ε' exhibits maximum value in the low frequency region. In addition, the density of charges contributing to space charge polarization may increase with increase in temperature. As a result, the maximum value of ε' is obtained at low frequency and high

temperatures. The observed plateau like behavior at higher temperatures can be attributed to the complete polarization of electric dipoles at low frequency of applied electric field. As the frequency is increased, the dipoles lag behind the applied electric field by contributing no net polarization and hence the sharp decrease in ε' is observed. Moreover, the dielectric constant is found to decrease as the temperature is reduced and this can be attributed to the lack of conductivity contribution due to the magnetic ordering of Fe^{3+} and Co^{2+} ions. No appreciable variation in the magnitude of ε' is observed with increase in Zn concentration.

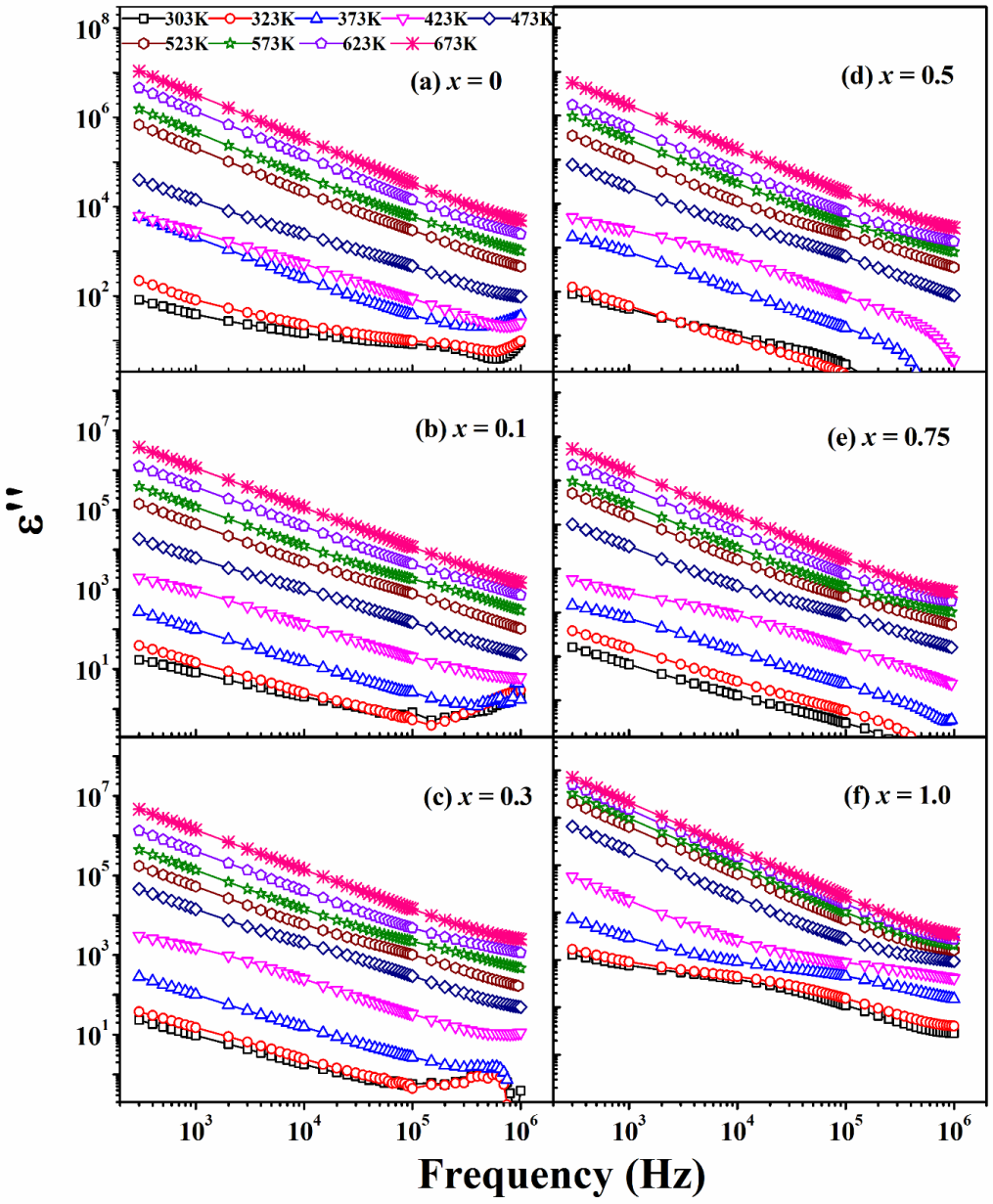

Figure 5.9: Imaginary part of complex dielectric permittivity (ε'') as a function of frequency in log-log scale at different temperatures ranging from 303 K to 673 K for BCZFO samples with (a-f) x = 0 – 1.0.

Fig. 5.9 depicts the frequency variations of ε'' spectra measured at different temperatures for BCZFO samples. The ε'' is found to decrease with increase in frequency. From the log-log plots of ε'' vs frequency, the slope of the curve in the lower frequency region was estimated at a few selected temperatures and is found to be nearly equal to –1 according to the Universal Dielectric Response (UDR), i.e. $\varepsilon' \alpha\ \omega^{s-1}$ and $\varepsilon'' \alpha\ \omega^{s-1}$ ($s < 1$) [95, 165]. Such power law dependence of ε'' on ω reveals the presence of conductivity

contribution towards the dielectric response. The observed large values of ε'' at higher temperatures are the signature of increase in conductivity due to thermally activated charge carriers. Fig. 5.9 shows that the dielectric loss ε'' decreases with increase in Zn concentration up to x = 0.5. With further increase in Zn concentration, there is a slight increase in dielectric loss.

5.1.5 Electrical Conductivity Analysis

The real part of ac conductivity (σ'_{ac}) was determined by using the following relation as [95];

$$\sigma'_{ac}(\omega) = \omega\varepsilon_0\varepsilon'' = \omega\varepsilon_0\varepsilon' tan\delta \qquad (5.5)$$

where ω is the angular frequency of ac signal applied to the sample, ε' and ε'' are the real and imaginary parts of complex dielectric permittivity and ε_0 is the permittivity of free space (8.854×10^{-12} F/m). The salient features of this frequency dispersion behavior of σ'_{ac} is that it provides the detailed understanding of migration of charge carriers, particularly their interaction with other defects inside the materials. Fig. 5.10 shows the frequency variation of σ'_{ac} for BCZFO samples with x = 0 – 1.0 at different temperatures from 303 K to 673 K. As the temperature is increased, the conductivity of the samples is also increased and it signifies the thermally assisted hopping of charge carriers (oxygen vacancy). Similar to the increasing trend of both real and imaginary parts of permittivity (ε' and ε'') as shown in Figs. (5.8) and (5.9), the conductivity spectra as shown in Fig. 5.10, also exhibit increasing trend with temperature. It signifies that there must be a strong correlation between dielectric polarization and conduction mechanism in hexaferrites. With increase in temperature, the number of charge carriers and hence their space charge polarization increases, which in turn leads to increase in dielectric permittivity.

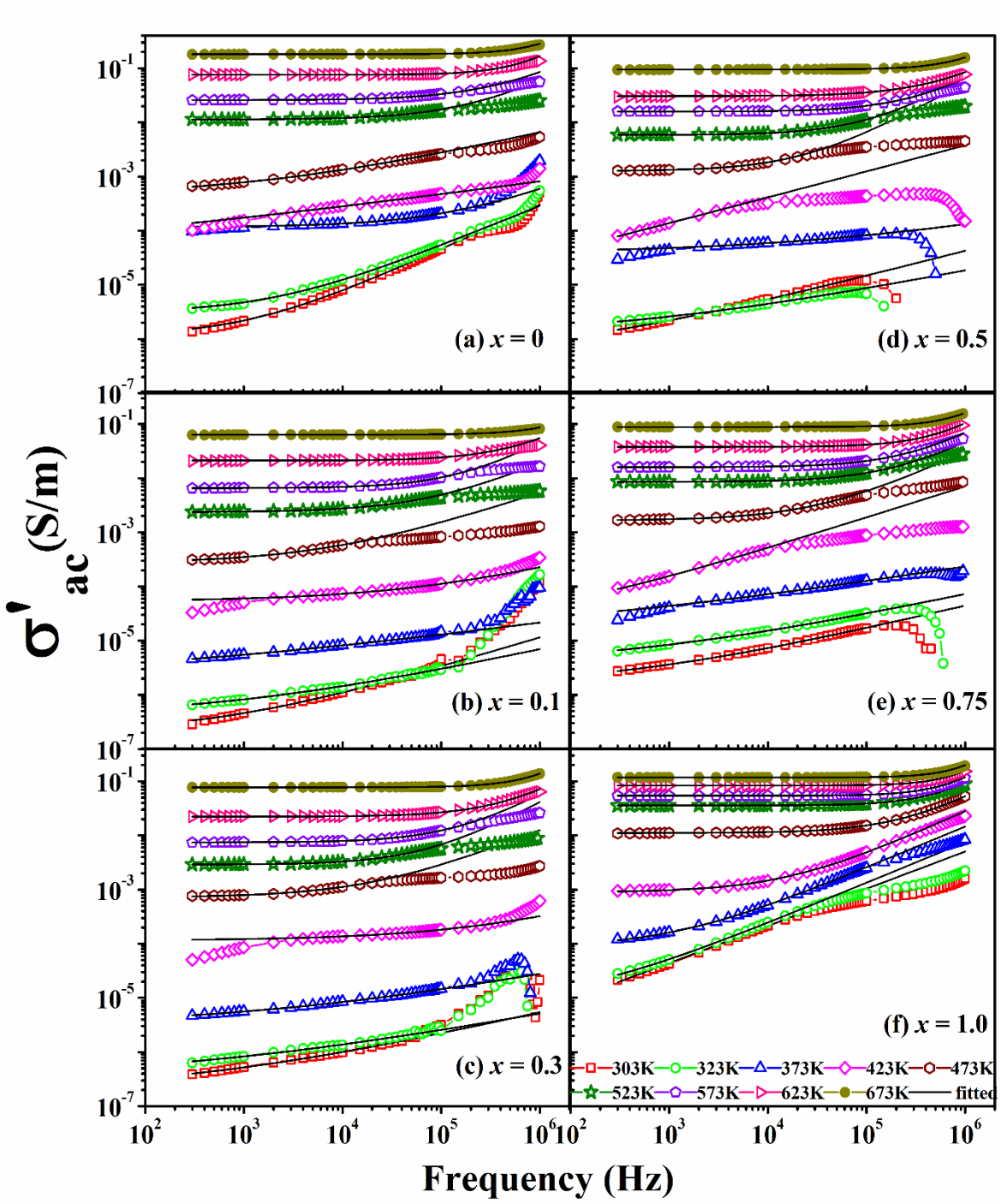

Figure 5.10: Real part of conductivity (σ'_{ac}) as a function of angular frequency at different temperatures from 303 K to 673 K with fitted data (solid line) of BCZFO samples for (a-f) x = 0 – 1.0.

In addition, at a particular temperature, the conductivity curve consists of two parts; (*a*) dc plateau region (dc conductivity) i.e. independent of frequency at lower frequency region and (*b*) the frequency dependent region at higher frequency. The frequency independent behavior at lower frequency is due to the drift of charge carriers ascribed to

successful hopping of charge carriers to neighborhood vacant sites. At higher frequency, σ_{ac} is found increase with increase in frequency due to increase in successful to unsuccessful hopping. This frequency dispersion behavior can be understood by Funke's jump relaxation model (JRM) [165]. According to JRM, at higher frequency, there is a possibility of two types of relaxation process such as (i) the unsuccessful hopping i.e. the jumping ion may jump back to its initial position and (ii) successful hopping i.e. when the jumping ions stay in the new site and the neighborhood ions become relaxed with respect to jumping ion position. This successful to unsuccessful hopping ratio is generally responsible for the dispersive conductivity at higher frequency region. The frequency dispersion behavior of σ'_{ac} could be analyzed by using Jonscher Universal Power Law (JPL) [42];

$$\sigma'_{ac}(\omega) = \sigma_0 + A\omega^n \qquad (5.6)$$

Here $\sigma'_{ac}(\omega)$ is the real part of ac conductivity and σ_0 is the frequency independent dc conductivity. The term $A\omega^n$ represents the frequency dependence term and characterizes all the dispersion phenomena, where A is a constant and n is the frequency exponent.

The intrinsic properties of ferrite materials are characterized by the factors A and n. The value of n predicts the conduction mechanism as well as the degree of interaction of mobile charge carriers with the lattice around them and its temperature dependence could give the opportunity to understand the underlying conduction mechanism. In addition, the value of n determines the details of charge carriers movement such as translational or localized. According to JPL, the n value lies between 0 and 1 i.e. $0 \leq n \leq 1$. When $n < 1$, it is attributed to the short-range hopping by translational motion of charge carriers, whereas $n > 1$ corresponds to the localized or reorientation hopping of electrons between two charge defects [166]. The present study shows that the value of n lies within the range of $0.41 \leq n < 1.7$. In order to get the clear understanding on the conduction mechanism at different temperatures, different theoretical models have been proposed based on the n values. These theoretical models are the quantum mechanical tunneling (QMT), correlated barrier hopping of electrons (CBH), small polaron tunneling model (SPT) and overlapping large polaron tunneling model (OLPT) [117, 118]. According to QMT model, the typical value of $n \sim 0.8$ and it is independent of the temperature. If the value of n decreases continuously with increase in temperature, it is known as CBH model. The SPT model predicts the increasing tendency of n with increase in temperature. As per the OLPT model,

the value of *n* decreases with increase in temperature to a minimum value and then increases for further increase in temperature. The temperature dependence of *n* for all the samples are shown in Fig. 5.11(a). It can be seen that *n* decreases up to certain temperature and then increases with further increase in temperature. For $x = 0$ sample, *n* value decreases up to 423 K and then increases and is attributed to OLPT model. Similarly other samples up to $x = 0.75$ follow the OLPT model, but when Co is completely replaced by Zn i.e. for ZnY ferrite, the value of *n* is found to increase with increase in temperature. Thus the most probable conduction mechanism for $x = 1.0$ sample is attributed to small polaron tunneling mechanism.

The dc conductivity variation as a function of $10^3/T$ is shown in Fig. 5.11(b) and it is found to exhibit a linear behavior. The linear behavior of σ_{dc} with respect to inverse temperature is fitted to the Arrhenius law [167];

$$\sigma_{dc} = \sigma_0 \exp\left(\frac{-E_g}{k_B T}\right) \tag{5.7}$$

where σ_{dc} is the dc conductivity, σ_0 is the pre-exponential factor, E_g is the activation energy related to conduction process, k_B is the Boltzmann constant and T is the temperature. The activation energy value was subsequently estimated from the linear fit of the plots shown in Fig. 5.11(b) and is found to be 0.84 eV for $x = 0$ sample. The activation energy values are found to decrease from 0.84 eV for $x = 0$ to 0.53 eV for $x = 1.0$. Since these samples are sintered at high temperature that possibly leads to volatilization of Zn. In addition to that there is a possibility of oxygen vacancy and hence the reduction of some of Fe^{3+} ions into Fe^{2+} state facilitating the electron hopping [168]. This leads to decrease in activation energy with Zn substitution. Further, the ionization of oxygen vacancies (V_0) is responsible for the creation of conduction electrons and can be expressed as [121];

$$V_0 \leftrightarrow V^{\cdot}_0 + e^- \tag{5.8}$$

$$V^{\cdot}_0 \leftrightarrow V^{\cdot\cdot}_0 + e^- \tag{5.9}$$

where V_0, $V^{\cdot}_0$ and $V^{\cdot\cdot}_0$ represent the neutral, single and doubly ionized oxygen vacancies respectively. At higher temperatures, the oxygen vacancies ($V^{\cdot}_0$ and $V^{\cdot\cdot}_0$) are the major mobile ionic defects observed in ferrite materials. Depending upon the nature of the materials, these $V^{\cdot}_0$ and $V^{\cdot\cdot}_0$ are activated at different temperatures range. The energy values associated with first and the second ionization of oxygen vacancies are $E_g < 0.7$ eV

and $E_g \approx 1.4$ eV respectively [169]. Here the activation energy is found to be in the range of 0.84 – 0.53 eV for $x = 0$ to 1.0 samples and this can be attributed to predominantly single ion oxygen vacancy induced hopping of charge carriers. Similarly, the Zn substitution up to $x = 1.2$ in $Ba_2Ni_{2-x}Zn_xFe_{12}O_{22}$, $Ba_2Mg_2Fe_{12}O_{22}$ and $(Ba,Sr)_3Co_2Fe_{24}O_{41}$, the oxygen vacancies are responsible for the variation in E_g in Y-type and Z-type hexaferrites [98, 170, 171].

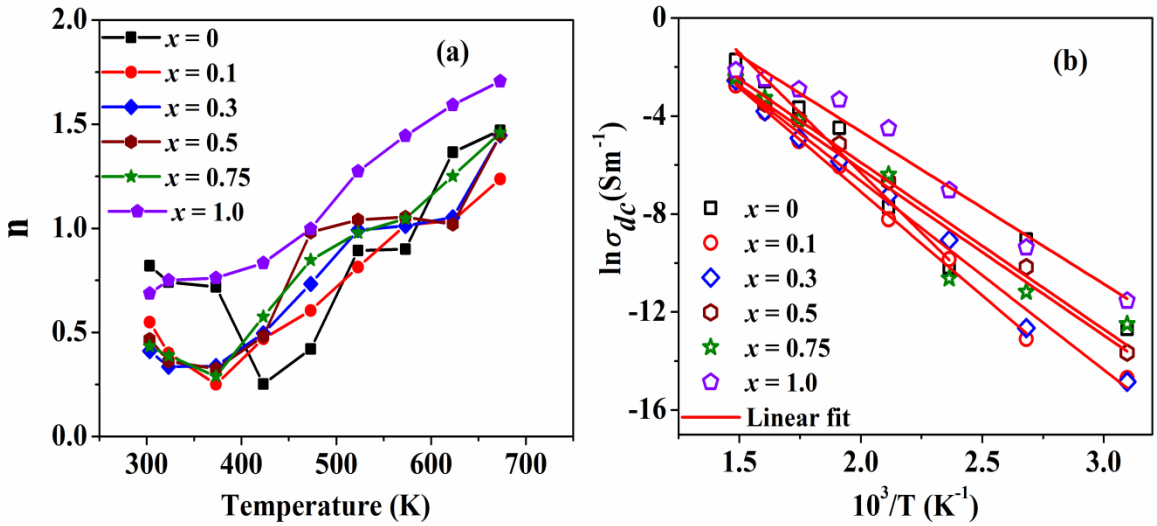

Figure 5.11: (a) Temperature variation of frequency exponent (n) and (b) dc conductivity variation with inverse of temperature ($10^3/T$) for polycrystalline BCZFO ($x = 0 – 1.0$) samples.

5.1.6 Magnetic Properties

Temperature dependence of dc magnetization ($M – T$) measurements were carried out for BCZFO samples with $x = 0 – 1.0$. Fig. 5.12(a) shows the zero field cooled (ZFC) $M – T$ plots for all these samples under an applied field of 100 Oe. For $x = 0$ sample, a clear ferrimagnetic transition is observed around 600 K and it is found to decrease with increase in Zn concentration. In addition, other than these ferrimagnetic transitions, a sharp fall in magnetization is observed at low temperatures below $T < 250$ K and is attributed to helimagnetic to ferrimagnetic orderings due to spin reorientations [11, 172]. The transition temperature values corresponding to the ferrimagnetic transition (T_c) and the spin reorientation (T_s) were determined from the plots of $|dM/dT|$ versus temperature. Fig. 5.12(b) depicts these transition temperatures (T_c and T_s) as a function of Zn concentrations (x). Both T_c and T_s values are found to decrease systematically with increase in Zn concentration. For $x = 0$ sample, the T_c value is found to be 600 K and it decreases to 380

K for x = 1.0. Similarly the T_s value is found to decrease from 225 K for x = 0 to around 60 K for x = 0.75 sample. The decrease in T_c values can be explained in terms of weakening of superexchange interactions among the magnetic sublattices as a result of substitution of Co by nonmagnetic Zn ion. Since the spin reorientation transition strongly depends upon the magnetic anisotropy, the decrease in T_s value is due to decrease in anisotropy values due to Zn substitution. Since Co has strong magnetic anisotropy and Zn has no anisotropy, the disappearance of T_s for x = 1.0 i.e. $Ba_2Zn_2Fe_{12}O_{22}$ (Zn_2Y) sample can be anticipated to the decrease in magnetic anisotropy due to the complete replacement of Co^{2+} ions by Zn^{2+} ions.

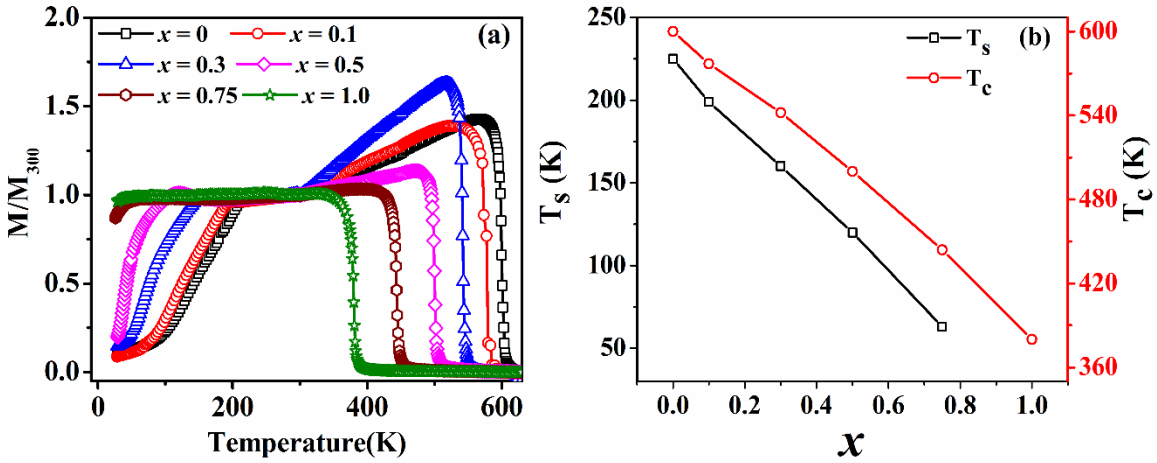

Figure 5.12: (a) Temperature dependence of magnetization (M) normalized to measured magnetization at 300 K (M_{300}) for BCZFO (x = 0 – 1.0) samples in zero field cooled mode from 30 K to 630 K and (b) spin reorientation transition temperatures (T_s) and the ferrimagnetic transition temperature (T_c) as a function of Zn concentrations (x).

Fig. 5.13(a) shows the magnetic hysteresis (M – H) loops of BCZFO samples for x = 0 – 1.0. Typical soft ferrimagnetic like behavior has been observed for both parent and Zn substituted samples. It is known that the domain wall movement of the polycrystalline materials in high field region becomes relatively unimportant; however, the magnetization changes occur primarily by the domain rotations. The experimental magnetization (M) data as a function of magnetic field (H) can be analyzed based on the law of approach to saturation model (LAS). The LAS model can be fitted in two ways namely; (i) intercept method that have been discussed in chapter 3 and (ii) the direct method. Both these fittings provide almost the same result. The LAS model mostly describes the dependence of

magnetization on the applied magnetic field, where the rotation process of magnetic domains against the anisotropy occurs. The LAS model can be expressed as [135, 173];

$$M\ (H) = M_s\left(1 - \frac{A}{H} - \frac{B}{H^2}\right) + \chi H \qquad (5.10)$$

where M_s is the saturation magnetization and H represents the applied magnetic field. χ is the high field susceptibility and A, B are constants. The term $\frac{A}{H}$ corresponds to structural defects and non-magnetic inclusions, whereas the term $\frac{B}{H^2}$ arises due to uniform magnetocrystalline anisotropy and the term χH is called forced magnetization. As discussed in the previous chapters and some of the earlier reports, the 2nd (A/H) and 4th (χH) terms in equation (5.10) have been neglected [106]. However, for these Zn substituted samples, the best fitting of LAS has been obtained without neglecting the 2nd and 4th terms in equation (5.10). The experimental magnetization data were fitted to equation (5.10) by taking M_s, A, B and C as free parameters of the fit. The fitted data are shown as solid lines in Fig. 5.13(b), which closely follows the experimental data.

Fig. 5.13(c) shows the estimated M_s values along with H_c values determined from the $M - H$ loops as a function of Zn concentration (x). The H_c value is found to decrease from 149.4 Oe for x = 0 to 49.7 Oe for x = 1.0. However, the systematic increase in M_s value is observed with increase in Zn concentration up to x = 0.5 and beyond that it decreases. In other words, the M_s values are efficiently tailored with the substitution of Co^{2+} ion by nonmagnetic Zn^{2+} ion. It is well known that in Y-type hexaferrites, Fe and Me ions are distributed over six different crystallographic sites: four octahedral sites ($3a_{vi}$, $3b_{vi}$, $6c_{vi}$ and $18h_{vi}$) and two tetrahedral sites ($6c_{iv}$ and $6c_{iv*}$). Among the six crystallographic sites, the cations in $3a_{vi}(\uparrow)$, $3b_{vi}(\uparrow)$ and $18h_{vi}(\uparrow)$ are in the spin up state while those in $6c_{vi}(\downarrow)$, $6c_{iv}(\downarrow)$ and $6c_{iv*}(\downarrow)$ are in the spin down state. Therefore, the preferential site occupation of doped metal ions and their distribution over tetrahedral and octahedral sites are expected to give rise to interesting magnetic properties. For x = 0 sample, the M_s value is found to be 5.85 μ_B/f.u. and it increases up to 8.43 μ_B/f.u. for x = 0.5 sample at room temperature (Fig. 5.13(c)). This enhancement in M_s values can be attributed to the substitution of nonmagnetic Zn^{2+} ions having strong preference to occupy at the tetrahedral sites ($6c_{iv}(\downarrow)$ and $6c_{iv}*(\downarrow)$) corresponding to Co^{2+} ions and as a result, the net magnetic moment increases with Zn concentration. In other words, the substitution of Zn does not change the spin directions, but it reduces the magnetic moment of the sublattice sites ($6c_{iv}(\downarrow)$ and $6c_{iv}*(\downarrow)$)

by resulting the increase in net magnetic moment. Furthermore, the magnetocrystalline anisotropy for hexagonal symmetry, which plays a major role in the magnetic properties of BCZFO samples can be estimated from the constant B in equation (5.10) by using the following expression [173];

$$B = \frac{4K_1}{15{M_s}^2} \tag{5.11}$$

where M_s is the saturation magnetization and K_1 is the magnetocrystalline anisotropy constant. The anisotropy constant value is found to decrease from 9.7×10^4 erg/cm^3 for x = 0 to 6.7×10^4 erg/cm^3 for x = 1.0. In ferrites, the magnetocrystalline anisotropy arises due to the presence of strong spin – orbit coupling at the crystal lattice. The relatively large value of K_1 observed for x = 0 sample is mainly due to the presence of strong anisotropy associated with Co^{2+} ions at octahedral sites. The orbital degeneracy of Co^{2+} ions at the octahedral site is not generally affected and hence the orbital magnetic moment is not quenched [174]. Therefore, there is a signature of strong spin – orbit coupling in Co^{2+} ions and it leads to strong magnetic anisotropy in Co_2Y ferrites. With increase in Zn concentration at the Co site, the spin – orbit coupling will be reduced and as a result, the anisotropy constant is found to decrease with Zn substitution.

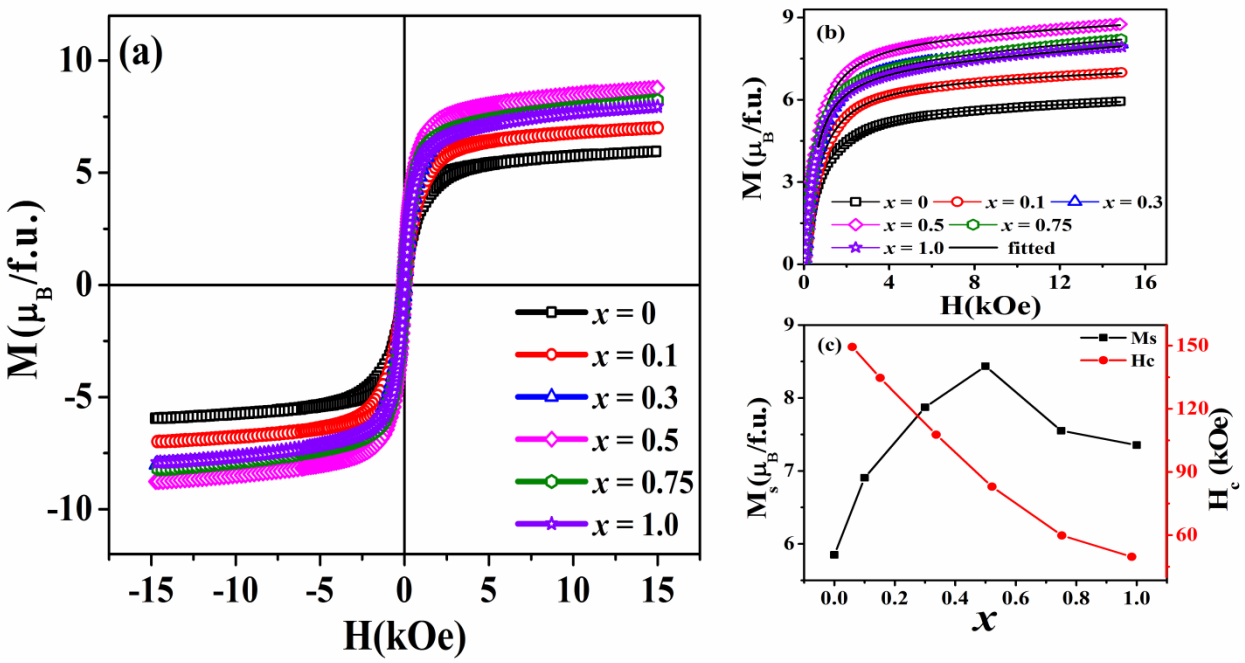

Figure 5.13: (a) Room temperature M – H curves of BCZFO samples for x = 0 to 1.0 (b) Initial magnetization curves of BCZFO samples along with fit to the law of approach to saturation at room temperature and (c) M_s and H_c as a function of Zn concentrations.

In order to get more understanding on the magnetic properties of these samples, the *M* – *H* loops were recorded at 30 K for *x* = 0, 0.1, 0.3, 0.5, 0.75 and 1.0 samples as shown in Fig. 5.14. The area under the loop is found to decrease gradually with increase in Zn concentration and correspondingly H_c also decreases from 338 Oe for *x* = 0 to 24 Oe for *x* = 1.0 as shown in Fig. 5.15. This can be easily understood in terms of gradual decrease in planar magnetic anisotropy due to the substitution of nonmagnetic Zn ion at Co site. The decrease in magnetic planar anisotropy due to Zn substitution will make the magnetic domain rotation easier and as a result, the H_c value decreases with Zn substitution. To obtain the experimental M_s values, the initial magnetization curves recorded at 30 K were also fitted to the law of approach to saturation (equation (5.10)). Fig. 5.15 depicts the experimental M_s values obtained at 30 K and it is found to increase with increase in Zn concentration (*x*). Such increase in M_s values with increase in *x* can be understood due to the preferential site occupation of Zn^{2+} ions at tetrahedral sites ($6c_{iv}(\downarrow)$ and $6c_{iv}{}^*(\downarrow)$) of BCZFO samples. Thus, Zn substitution dilutes the down spin magnetic moment and hence the overall magnetization increases.

The site occupation factors for Co (p_{Co}), Zn (p_{Zn}) and Fe (p_{Fe}) ions for different compositions of *x* can be calculated by using the relations, $p_{Co} = (1 - x)\, p^0_{Co}$, $p_{Zn} = x\, p^0_{Zn}$ and $p_{Fe} = 1 - (p_{Co} + p_{Zn})$ respectively [175]. Here p^0_{Co} represents the site occupation factor of Co in Co_2Y and p^0_{Zn} is the site occupation factor of Zn in Zn_2Y hexaferrites. The distribution of cations such as Co in Co_2Y and Zn in Zn_2Y are in accordance with the report of Collomb *et al*., [175, 176]. At a particular temperature, the net magnetization *M* in terms of Bohr magneton (μ_B) per unit cell can be calculated by using the following empirical relation as [177];

$$M(T) = [3N_{Co}(up) + 5N_{Fe}(up)] - [3N_{Co}(down) + 5N_{Fe}(down)] \qquad (5.12)$$

where *N* represents the number of ions in each crystallographic site per unit cell and is given by $N = n^*p$, where *n* signifies the number of equivalent positions of the crystallographic sites in the unit cell and *p* is the corresponding occupation factor. The multiplication factors 3 and 5 in equation (5.12) correspond to the magnetic moment of Co^{2+} and Fe^{3+} ions respectively in the unit of μ_B. The theoretical M_s values were calculated by using the above empirical relation (5.12) and compared with that of experimental data measured values at 30 K and room temperature (300 K). By considering the number of formula units (*Z* = 3) per unit cell, the M_s value is estimated per formula unit (f.u.). For *x*

= 0 sample, the estimated M_s value is found to be 8.14 μ_B/f.u. and is comparable to the experimental M_s value of 8.31 μ_B/f.u. obtained from the analysis using the law of approach to saturation (equation (5.10)). These measured and the theoretically estimated M_s values are shown in Fig. 5.15 and they are found to increase with increase in Zn concentration. The theoretically estimated M_s values up to x = 0.3 closely follow the experimental data. However for $x \geq 0.3$, even though the experimental M_s value increases with x, it deviates from the linear theoretical data. Here, no longer the experimental M_s value increases linearly with x. Such deviation of M_s values can be attributed to some of the substituted Zn^{2+} ions occupying the spin up states such as $3a_{vi}$, $3b_{vi}$ and $18h_{vi}$. Bai *et al.*, have reported that the $Ba_2Me_2Fe_{12}O_{22}$ (Me = Zn, Co, Cu) samples at 77 K exhibit the linear increase of M_s values, as the concentration of Zn doping is increased [161]. However in our case, the measured M_s value at room temperature is found to increase up to x = 0.5 and then decreases beyond that as shown in Fig. 5.13(c). This behavior of BCZFO samples can be attributed to the considerable decrease in Curie temperature of higher Zn concentration materials, whose T_c values are not far away from room temperature. This leads to the considerable thermal agitation induced reduction in M_s value at room temperature.

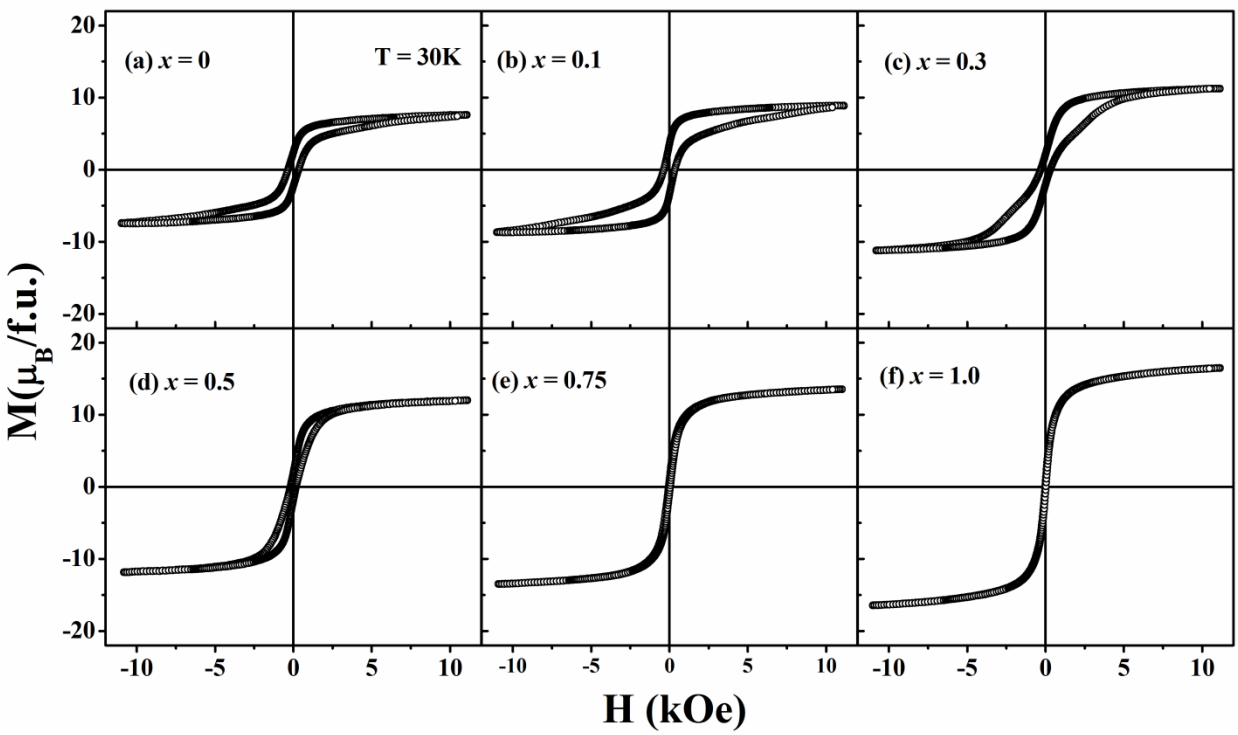

Figure 5.14: *M – H* loops of BCZFO samples measured at 30 K for (a-f) x = 0, 0.1, 0.3, 0.5, 0.75 and 1.0.

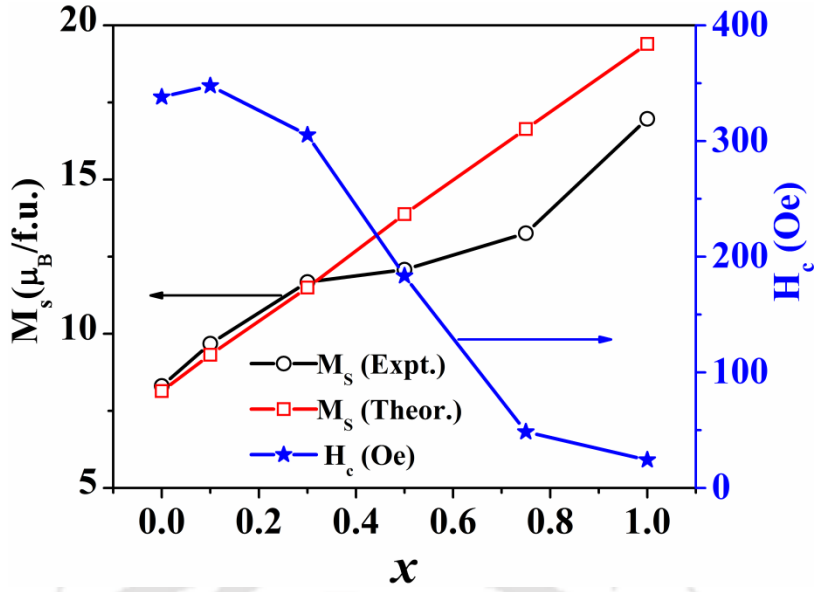

Figure 5.15: M_s and H_c as a function of Zn concentrations (x) at 30 K.

5.1.7 Magnetic Permeability Analysis

Magnetic permeability is one of the important parameter that offers the dynamic magnetic properties of the material. In general, the real and imaginary parts of the complex permeability (μ^*) demonstrate the storage capability of magnetic energy and associated magnetic loss in the material. Fig. 5.16(a-b) displays the frequency dependence of real (μ') and imaginary parts (μ'') of complex permeability of BCZFO samples measured at room temperature. The μ' remains almost independent of frequency except for x = 1.0 sample. An increasing trend of μ'' is noticed in the semi-logarithmic scale near 1 GHz except for x = 1.0 sample. However, a strong dispersion behavior is observed for x = 1.0 sample with a gradual decrease in μ' and a broad peak at μ'' in the frequency range of 10^7 – 10^8 Hz. The μ' value is found to be 1.92 for x = 0 sample and is comparable to that reported in literature [158]. Generally, the magnetization dynamics in ferrites behave differently in the low and high frequency regions. In the lower frequency region (< 2 GHz), domain wall resonance is predominant, while the resonance due to spin rotational component occurs at higher frequencies [126, 148]. In the present work, we have seen that μ' value increases with increase in Zn substitution. This enhancement in μ' value is basically due to the reduction in domain wall stiffness caused by the decrease in magnetocrystalline anisotropy with Zn substitution. Furthermore, the permeability of BCZFO can also be explained by Ohta's model [126];

$$\mu = M_s^2 + K_1 \lambda s \qquad (5.13)$$

where M_s is the saturation magnetization, K_1 is the magnetocrystalline anisotropy constant, λ is the magnetostriction factor and s is the internal stress. According to this model both M_s and K_1 play the vital role to determine the permeability of the BCZFO samples. Therefore, the substitution of Zn^{2+} for Co^{2+} is expected to yield the highest permeability for x = 0.5 sample due to its large saturation magnetization at room temperature. The μ'' value is found to be close to zero with a small rise in its value at higher frequency. However, the frequency dependence of μ'' for x = 1.0 sample shows a peak like behavior around 65 MHz. To further understand the origin of the peak, a Cole – Cole plot (μ'' vs μ') for x = 1.0 sample is shown in Fig. 5.16(c) where a clear semicircular arc is seen in the frequency region of (10^7 – 10^8) Hz. This suggests that magnetic relaxation plays a major role in the above frequency region for x = 1.0 sample and this can be attributed to the domain wall motion [178]. The peak observed in the μ' vs f plot of x = 1.0 sample in the frequency range of (10^8 – 10^9 Hz) can be attributed to resonance peak and it is clearly seen compared to other samples due to the shift in the resonance peak towards lower frequency with the increase in Zn concentration. Thus, it can be concluded that BCZFO for x = 0.5 shows high permeability and low magnetic loss and can be suitable for RF and antenna device applications in ultra-high frequency (UHF) band [126, 149].

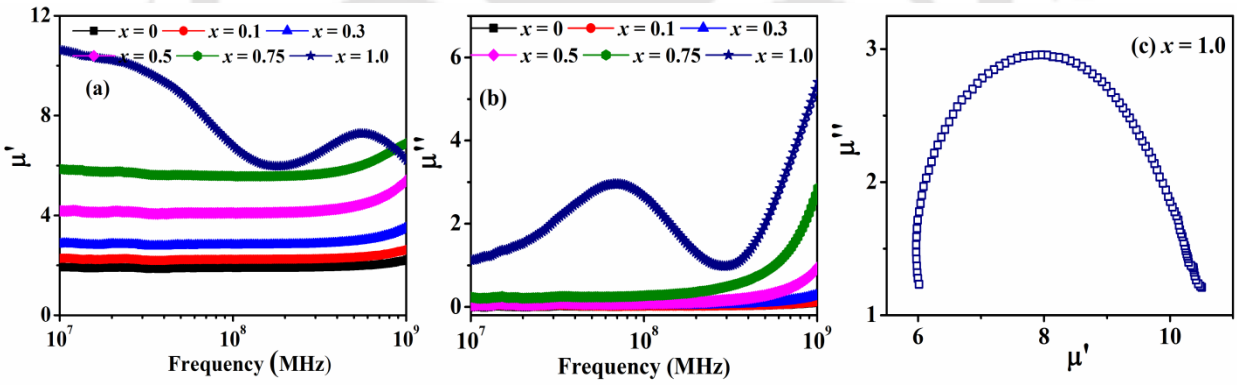

Figure 5.16: (a-b) Real and Imaginary parts of complex permeability spectra of BCZFO for x = 0 to 1.0 along with (c) Cole – Cole plot of x = 1.0 sample.

5.1.8 Conclusions

In this chapter, the effect of Zn substitution on structural, dielectric and magnetic properties of Y-type hexaferrite i.e. $Ba_2(Co_{1-x}Zn_x)_2Fe_{12}O_{22}$ ($0 \leq x \leq 1$) were investigated in detail. Single-phase polycrystalline samples of $Ba_2(Co_{1-x}Zn_x)_2Fe_{12}O_{22}$ were successfully prepared by standard solid state reaction method. The Rietveld refinement analysis of these

XRD patterns were carried out by choosing R-3m space group with rhombohedral structure and it confirms the phase purity of the samples with Zn substitution. The frequency variation of impedance and dielectric constants were studied at different temperatures. At low frequency, the maximum value of dielectric constant is obtained and this can be attributed to the interfacial polarization mechanisms. As the temperature is increased, the conductivity is also increased due to the thermal activation of charge carriers across the grains and grain boundaries. The frequency dispersion behavior of conductivity spectra were analyzed based on the JPL. It is found that the experimental data are well fitted with JPL. From the analysis of conductivity spectra by JPL, the frequency exponent signifies that the electrical conductivity of Zn doped samples up to $x = 0.75$ follows the overlapping of large polaron tunneling model and $x = 1.0$ sample follows the small polaron tunneling model.

Temperature variation of magnetization measurements show ferrimagnetic nature of $Ba_2Co_2Fe_{12}O_{22}$ with $T_c = 600$ K along with the spin reorientation transition (T_s) below room temperature around $T_s = 225$ K. The systematic decrease in both T_c and T_s values are obtained, as the Zn concentration is increased. Such systematic decrease in T_c and T_s values with increase in x indicates the weakening of superexchange interaction and the decrease in magnetic planar anisotropy. The magnetic hysteresis loops were recorded at room temperature and 30 K for all the samples. The experimental M_s values were calculated by using LAS and it is found to increase with increase in Zn concentration up to $x = 0.5$. While the H_c value is found to decrease with increase in Zn concentration. In addition, the experimentally measured and the theoretically estimated M_s values obtained from the law of approach to saturation at 30 K are almost comparable with each other. The complex magnetic permeability studies reveal that the real part of complex permeability is found to increase with increase in Zn concentration with low magnetic loss. However, the $x = 1.0$ sample exhibits a relaxation peak in the permeability spectra. The analysis of permeability spectra indicates that the $x = 0.5$ sample exhibits high permeability value with low magnetic loss and can be suitable for various microwave and antenna applications.

Chapter 6

$Ba_2(Co_{1-x}Mg_x)_2Fe_{12}O_{22}$ Series

6.1 Mg Substituted $Ba_2Co_2Fe_{12}O_{22}$ Series

In chapter 5, we have seen that the substitution of Zn at Co site in $Ba_2Co_2Fe_{12}O_{22}$ has largely influenced its magnetic and dielectric properties. Since Zn^{2+} ion occupies the tetrahedral sites of the cations having spin down states, the net magnetic moment of Co_2Y hexaferrites is enhanced. Both the ferrimagnetic transition (T_c) and spin reorientation transition (T_s) temperatures are decreased with increase in Zn concentration. The magnetic permeability analysis, which is useful for the study of microwave absorption applications reveal that the real part of permeability is enhanced due to Zn substitution with low magnetic loss. The relaxation dynamics in the impedance spectra for both parent and Zn substituted samples are due to the contributions of both grains and grain boundaries. The analysis of conductivity reveals that the conduction process in the Zn substituted samples follow the small polaron tunneling model.

In the present chapter, the effect of Mg substitution on the structural, magnetic and dielectric properties of Y-type hexaferites are going to be discussed in detail. Some of the Y-type barium hexaferrites, such as $Ba_2Mg_2Fe_{12}O_{22}$, $Ba_{0.5}Sr_{1.5}Zn_2Fe_{12}O_{22}$, $Ba_{0.5}Sr_{1.5}Co_2Fe_{12}O_{22}$ are found to exhibit magnetoelectric coupling at low temperatures for low magnetic fields [60, 179, 180]. The partial substitution of non-magnetic Al^{3+} ion in $Ba_2Co_2Fe_{12}O_{22}$ (Co_2Y) hexaferrite gives rise to magnetoelectricity at room temperature [159]. Costa *et al.*, have shown that Co_2Y hexaferrite exhibits excellent dielectric, impedance and conductivity behavior at different temperatures, which are important properties for microwave applications [181]. The substitution of Ni^{2+} and Mg^{2+} ions have large influence on the microstructure and magnetic properties of Co_2Y hexaferrite [70]. Zhang *et al.*, have reported that the substitution of Mg for Zn in $Ba_{0.5}Sr_{1.5}Zn_2Fe_{12}O_{22}$ stabilizes the magnetic field induced ferroelectric phase at zero magnetic field and these can be potential candidate for application in magnetoelectric devices [182]. The cationic

distribution of non-magnetic Mg^{2+} ions at Co^{2+} site in other hexaferrites is found to exhibit excellent magnetic, dielectric and electrical properties with an ability to tune the planar anisotropy [183, 184]. The substitution of Mg^{2+} ions at Co^{2+} site in W-type hexaferrite gives rise to better magnetization values and they are found to be suitable for microwave absorption and electromagnetic interference attenuations [183]. Several interesting results are observed in Mg substituted hexaferrites. Therefore, it would be interesting to carry out the research on such substitution of Mg at Co site in $Ba_2Co_2Fe_{12}O_{22}$. The investigation of magnetic and dielectric properties of Mg substituted $Ba_2Co_2Fe_{12}O_{22}$ would be quite interesting to study. We have systematically investigated the effect of Mg substitution on structural, magnetic and dielectric properties of Co_2Y hexaferrte in this chapter.

6.1.1 Sample Preparation and Characterization

Bulk polycrystalline samples of $Ba_2(Co_{1-x}Mg_x)_2Fe_{12}O_{22}$ ($0 \leq x \leq 0.5$) were prepared by using the standard solid state reaction technique. Stoichiometric molar ratio of high purity (> 99%) $BaCO_3$, Fe_2O_3, MgO, and Co_3O_4 powders were taken as starting compounds. The molar ratios of these compounds were weighed and ground together in acetone medium for 3 h using agate mortar and pestle. The samples were presintered at 600 ℃ and 800 ℃ for 12 h with intermediate grinding. The presintered powders were pressed into cylindrical pellets of diameter ~13 mm using a hydraulic press with a pressure of 2.9 $\times$ 10^8 N/m^2 and the final annealing was carried out at 1150 ℃ for 12 h in air medium. Structural, microstructural, magnetic and dielectric properties were studied using the facilities described in chapter 2.

6.1.2 Structural Properties

The XRD patterns of $Ba_2(Co_{1-x}Mg_x)_2Fe_{12}O_{22}$ (x = 0 – 0.5) samples recorded at room temperature are shown in Fig. 6.1. These XRD patterns were analyzed by Rietveld refinement technique based on R-3m space group. As per the Rietveld refinement, all the observed peaks are accounted within the R-3m space group and it confirms that the prepared materials are in single-phase form with rhombohedral structure. Similar refining was carried out for all other samples in this series. Typical XRD patterns along with their Rietveld refined data for x = 0, 0.1, 0.3 and 0.5 samples are shown in Fig. 6.2 and Fig. 6.3 respectively. The determined lattice parameters in hexagonal coordinates are found to be a = 5.862 Å and c = 43.512 Å for x = 0. The lattice parameter a is almost constant and c is found to decrease systematically with increase in Mg concentration and they are

comparable to those of earlier work [157, 182]. The unit cell volume determined from the above analysis is found to decrease with increase in Mg concentration. The decrease in lattice parameter *c* and the unit cell volume with respect to Mg concentration can be attributed to the substitution of smaller Mg^{2+} (0.72Å) ions at Co^{2+} (0.745Å) site [149, 185]. The lattice parameters, reliability factors and the unit cell volume determined from the above analysis for all these samples are given in Table 6.1.

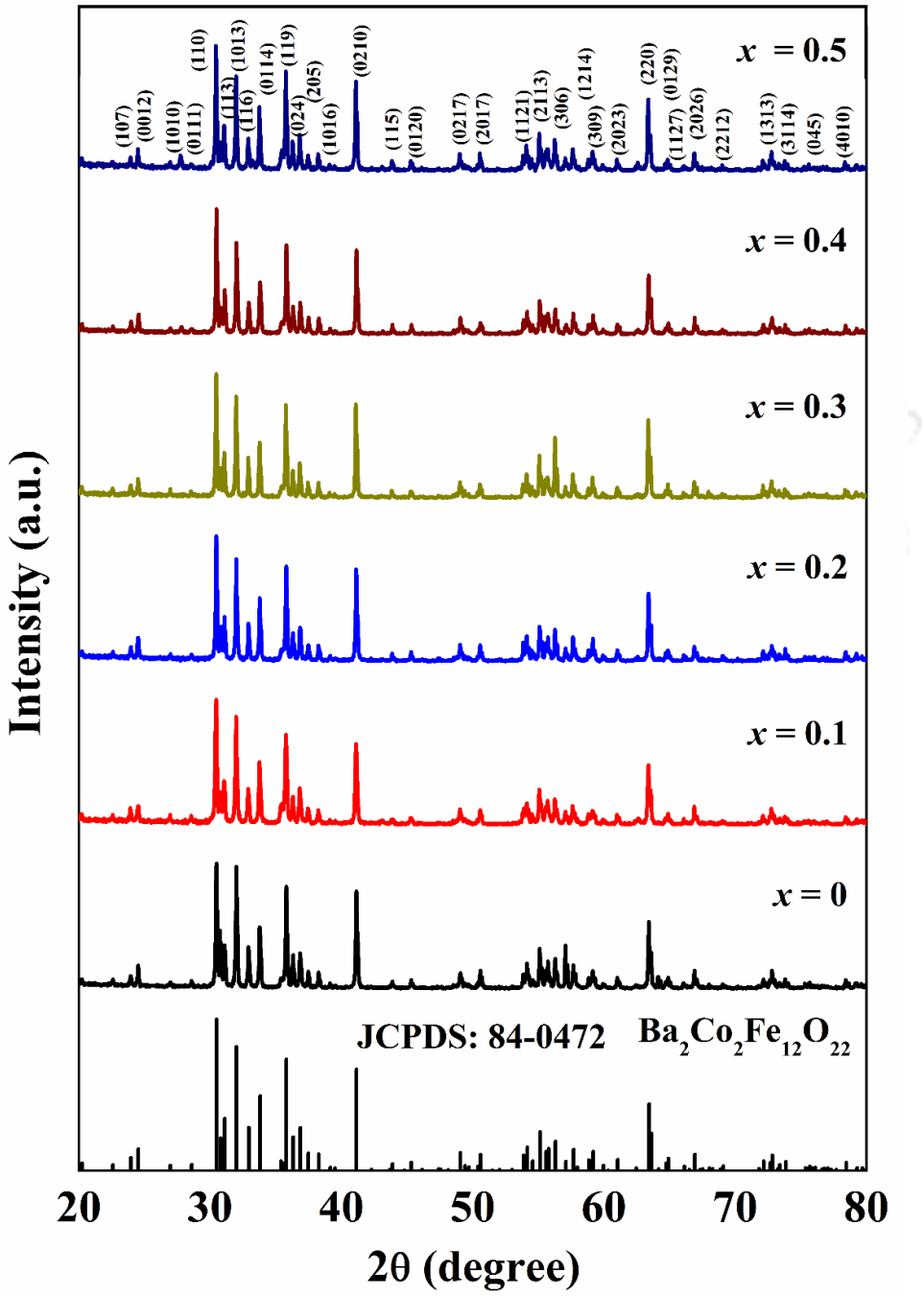

Figure 6.1: XRD patterns of $Ba_2(Co_{1-x}Mg_x)_2Fe_{12}O_{22}$ samples for $x = 0 – 0.5$

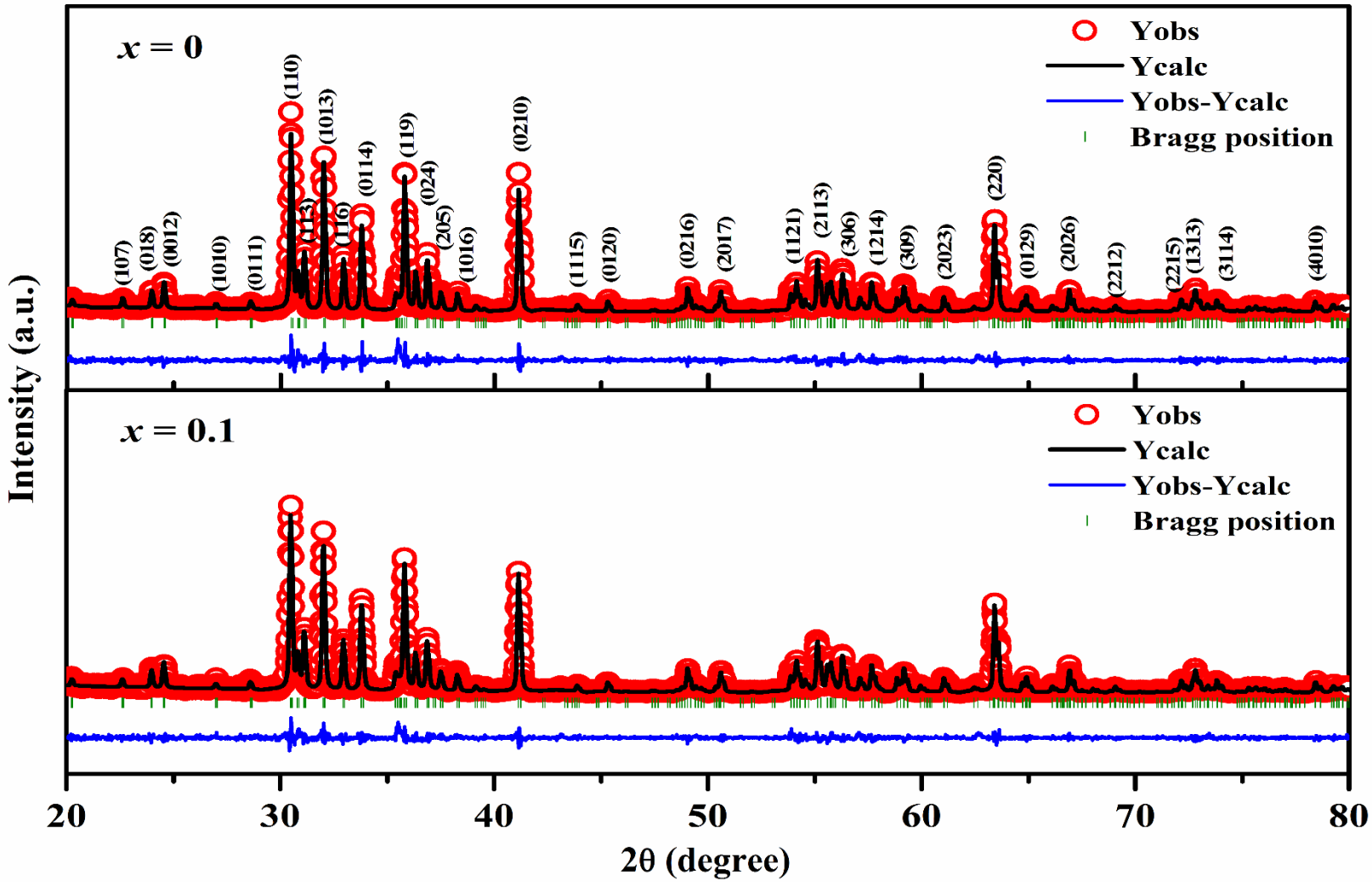

Figure 6.2: XRD patterns (circles) of $Ba_2(Co_{1-x}Mg_x)_2Fe_{12}O_{22}$ samples for x = 0 and 0.1 along with Rietveld refined data (solid line). The dashed lines (blue) represent the difference between experimental and refined data. The (green) vertical lines show the allowed Bragg's positions.

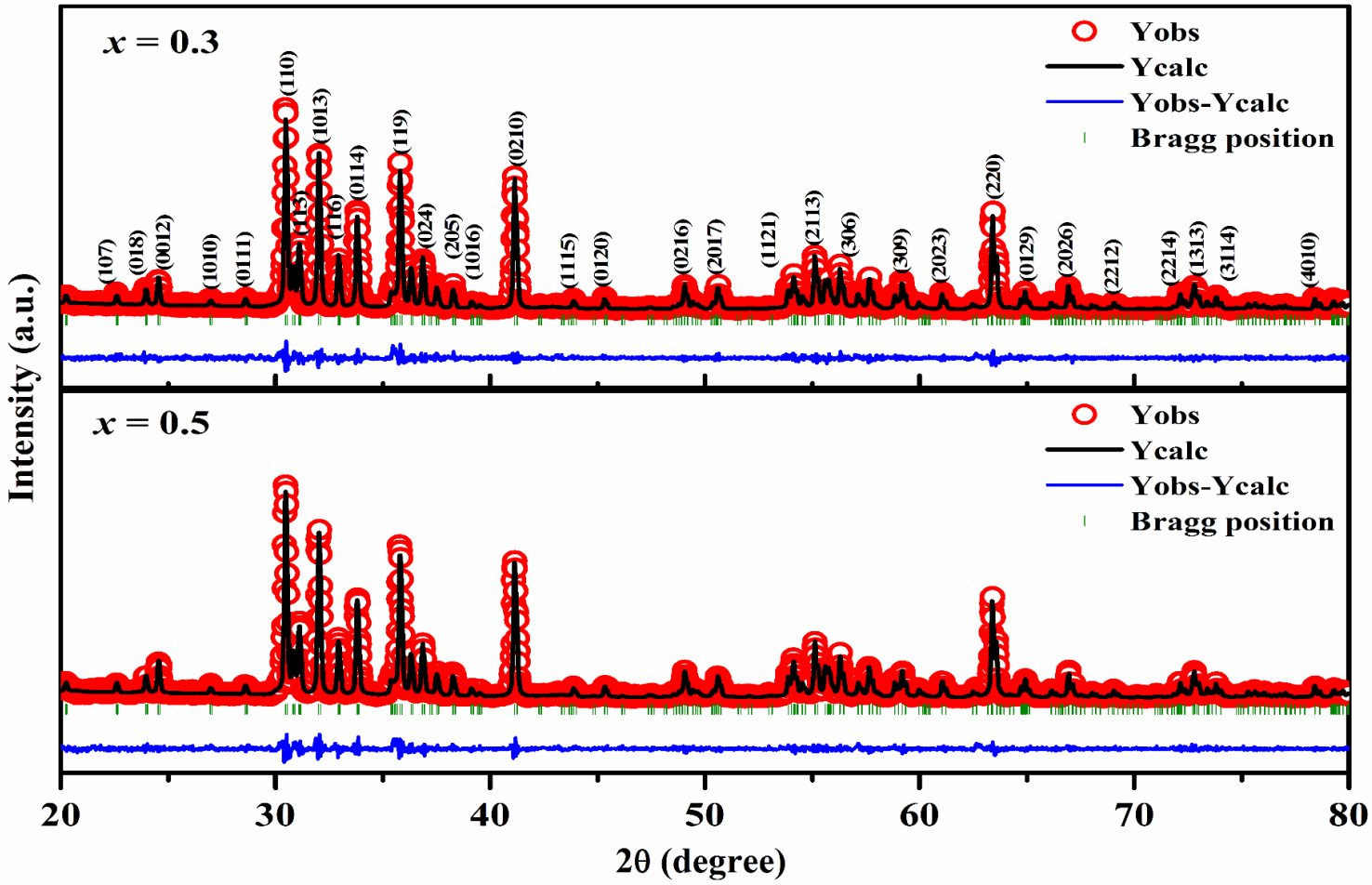

Figure 6.3: XRD patterns (circles) of $Ba_2(Co_{1-x}Mg_x)_2Fe_{12}O_{22}$ samples for x = 0.3 and 0.5 along with Rietveld refined data (solid line). The dashed lines (blue) represent the difference between experimental and refined data. The (green) vertical lines show the allowed Bragg's positions.

Table 6.1: Parameters obtained from the Rietveld analysis of XRD patterns for the samples $Ba_2(Co_{1-x}Mg_x)_2Fe_{12}O_{22}$ (x = 0 – 0.5). R_F, R_{Bragg}, R_{exp}, R_P, χ^2 are the reliability factors.

Sample/ Parameters	***x* = 0**	***x* = 0.1**	***x* = 0.2**	***x* = 0.3**	***x* = 0.4**	***x* = 0.5**
Space group	*R-3m*	*R-3m*	*R-3m*	*R-3m*	*R-3m*	*R-3m*
***a* (Å)**	5.8626 (1)	5.8619 (1)	5.8629 (1)	5.8627 (1)	5.8625 (1)	5.8634 (1)
***c* (Å)**	43.5127 (3)	43.5020 (4)	43.5005 (3)	43.4918 (3)	43.4817 (2)	43.4794 (2)
***Volume* (Å^3)**	1295.20 (5)	1294.54 (6)	1294.97 (5)	1294.62 (5)	1294.22 (5)	1294.55 (5)
R_F (%)	5.24	4.74	5.07	4.90	4.66	4.27
R_{Bragg} (%)	5.59	5.24	5.62	4.99	4.78	4.33
R_P (%)	18.2	17.9	17.9	17.1	16.7	16.4
R_{exp} (%)	12.08	12.53	12.21	12.17	11.42	11.41
χ^2	3.73	3.27	3.43	3.23	3.52	3.39

The microstructural images of all the samples were recorded by using field emission scanning electron microscope (FESEM) and their typical images for x = 0, 0.1, 0.3 and 0.5 samples are shown in Fig. 6.4(a-d). All the samples show hexagonal platelet like morphology. From Fig. 6.4(a-d) it can be seen that the grains are distributed in random orientations. The porosity in the samples is found to decrease with increase in Mg concentration. The average grain sizes of all the samples were estimated by using ImageJ software and they are found to be in the range of 1.5 µm to 2.2 µm. To determine the chemical composition in the samples, the EDX spectra were recorded for all the samples and these spectra for x = 0.1 and 0.5 samples are shown in Fig. 6.4(e-f). The typical cationic ratios of Ba:Co:Mg:Fe for x = 0, 0.1, 0.3 and 0.5 samples are found to be 2.00:1.81:0:11.10,

2.00:1.80:0.19:11.09, 2.00:1.41:0.59:11 and 2.04:0.96:0.96:11.68 respectively and they are comparable to the nominal starting compositions.

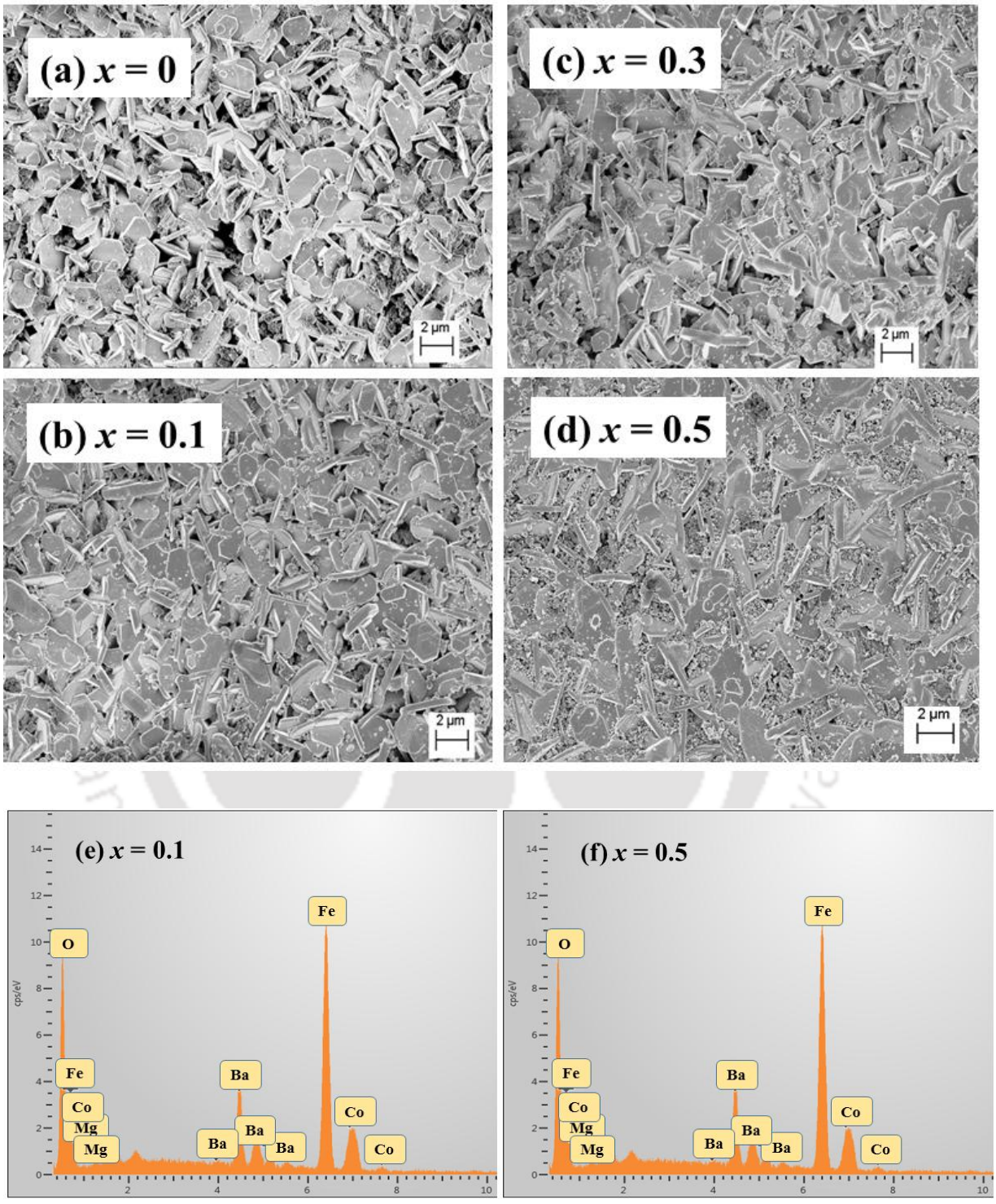

Figure 6.4: FESEM micrographs of $Ba_2(Co_{1-x}Mg_x)_2Fe_{12}O_{22}$ samples for (a-d) x = 0, 0.1, 0.3 and 0.5 along with EDX spectra for (e-f) x = 0.1 and 0.5 samples.

6.1.3 Complex Impedance Spectroscopy Analysis

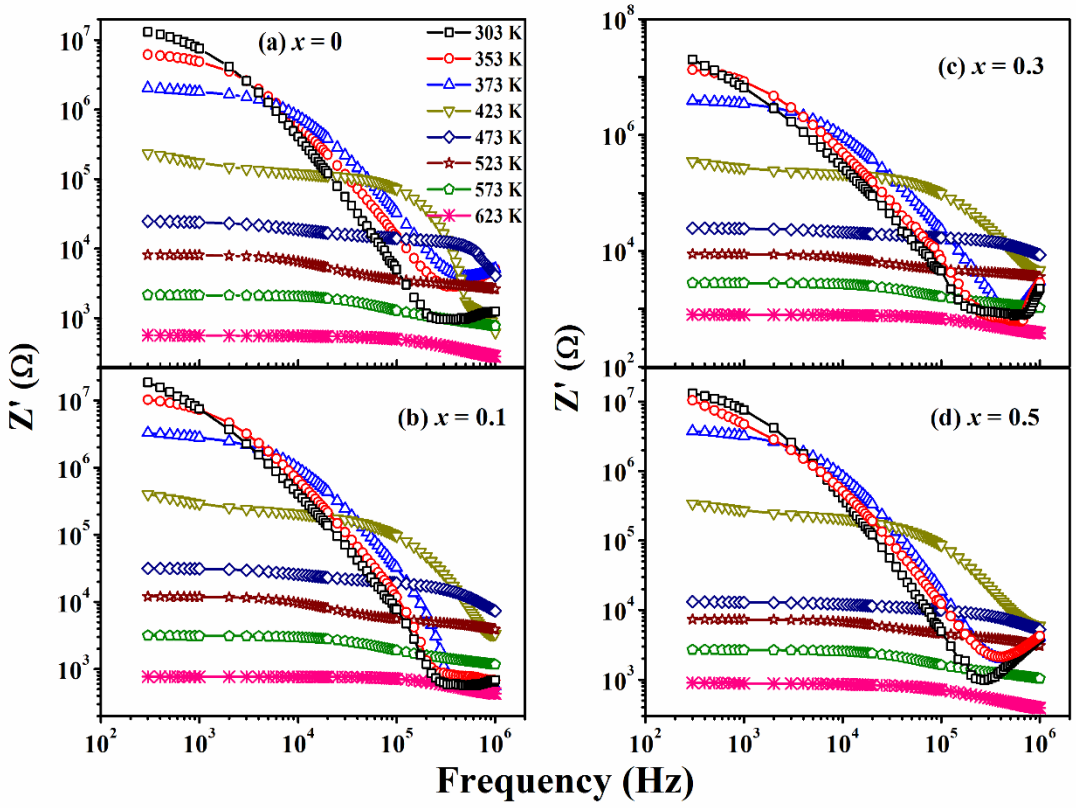

Figure 6.5: Real part (Z') of complex impedance as a function of frequency for $Ba_2(Co_{1-x}Mg_x)_2Fe_{12}O_{22}$ samples with (a-d) x = 0, 0.1, 0.3 and 0.5 measured at different temperatures.

As discussed in earlier chapters that the Impedance spectroscopy is one of the important techniques used to understand the dielectric properties and the relaxation dynamics of dielectric materials. Fig. 6.5 shows the frequency variation of real part (Z') of the impedance of $Ba_2(Co_{1-x}Mg_x)_2Fe_{12}O_{22}$ samples with x = 0, 0.1, 0.3 and 0.5 measured at different temperatures from 303 K to 623 K. At a particular temperature, the value of Z' decreases with increase in frequency with the formation of plateau like region. The impedance mechanism in a dielectric material arises due to the movement of charge carriers at intragrain, intergrain regions and the material – electrode interface. Thus, the charge carriers' movement are of different types such as long/short range displacement, dipole reorientation and via the formation of space charges. All these types of charge carriers' movement provides the frequency dependence of Z' in the material. The formation of plateau like behavior and the sharp decrease in Z' value with increase in frequency indicates the presence of relaxation behavior in the samples. It can be seen that, for x = 0 sample, the Z' value is found to decrease with increase in temperature from 303 K to 623 K. Similar

behavior is observed for all the Mg doped samples. This signifies that the material possesses the negative temperature coefficient of resistance. Further, a slight increase in the magnitude of Z' value is noticed with increase in Mg concentration.

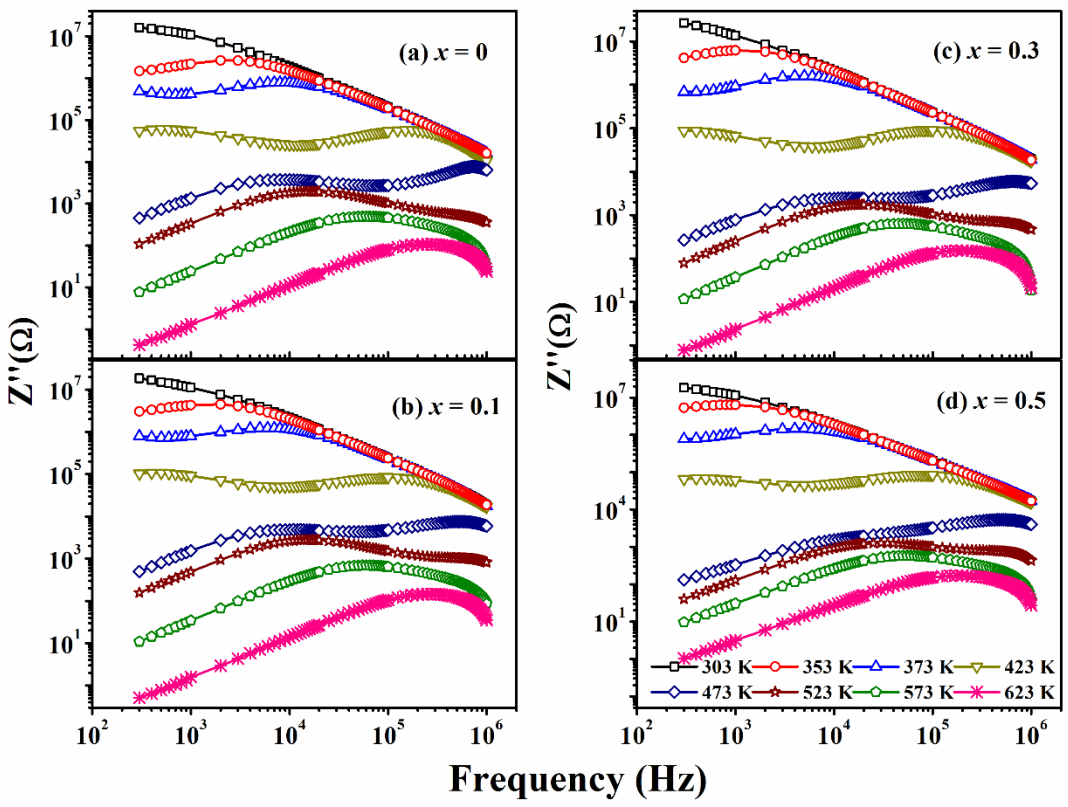

Figure 6.6: Imaginary part (Z'') of complex impedance for $Ba_2(Co_{1-x}Mg_x)_2Fe_{12}O_{22}$ samples with (a-d) x = 0, 0.1, 0.3 and 0.5 measured at different temperatures.

Fig. 6.6 shows the frequency variation of imaginary (Z'') part of the complex impedance for x = 0, 0.1, 0.3 and 0.5 samples measured at different temperatures from 303 K to 623 K. It reveals that, the impedance spectra of all the samples tend to merge together at higher frequencies ($f > 10^5$ Hz) for $T \leq 423$ K and this can be attributed to the possible release of space charges at the grain boundaries [186]. The impedance spectra recorded at different temperatures for various concentrations of Mg show relaxation peak at a characteristic frequency f_{max}, which matches the relaxation time of charge carriers towards the applied electric field. At a given temperature of T = 353 K, the relaxation peak is observed for x = 0 sample with a characteristic frequency of f_{max} = 2 kHz. As the temperature is increased, the relaxation peak is found to shift towards higher frequency along with decrease in the magnitude of Z'' spectra due to the thermal activation of relaxation process and then move out of the measured frequency range. In addition to that,

a secondary relaxation peak is noticed in the low frequency region at higher temperature, especially for $T \geq 423$ K. For $x = 0$ sample, the secondary relaxation peak is observed at $f_{max} = 5$ kHz for $T = 423$ K. As the Mg concentration is increased, the secondary peak is found to be suppressed and broadened. The secondary peaks observed in the low frequency region can be attributed to the relaxation of charge carriers in the long-range region, i.e. across the grain boundaries. Such behavior is expected at higher temperature due to the thermal activation of charge carriers. On the other hand, the primary peaks observed even at relatively low temperatures can be attributed to relaxation within the short-range scale, i.e. within the grains. The contributions of grains and grain boundaries towards the relaxation dynamics have been observed for all the Mg doped samples. The shifting of relaxation peaks towards higher frequency with increase in temperature can be easily understood based on the Arrhenius law.

Furthermore, to understand the dielectric relaxation and the nature of charge carriers responsible for the relaxation dynamics in thermally activated process, we have analyzed the temperature dependence of relaxation frequency by using the Arrhenius law [98];

$$f = f_0 \exp[-\frac{E_a^z}{k_B T}] \qquad (6.1)$$

where f_0 is the prefactor, k_B is the Boltzmann constant (8.617×10^{-5} eV/K) and E_a^z is the activation energy of relaxation. The plots of $\ln f_{max}$ versus temperature (T) corresponding to the contributions from grains and grain boundaries are shown in Fig. 6.7, where they all exhibit a linear behavior. The fitting of these data using the Arrhenius law (equation 6.1) by taking f_0 and E_a^z as the free parameters of the fit is shown as solid line. The E_a^z values corresponding to relaxation of charges within the grains are found to vary from 0.71 – 0.82 eV for $x = 0 – 0.5$. The corresponding E_a^z values across the grain boundaries are found to be in the range of 0.63 – 0.81 eV for $x = 0 – 0.5$ samples.

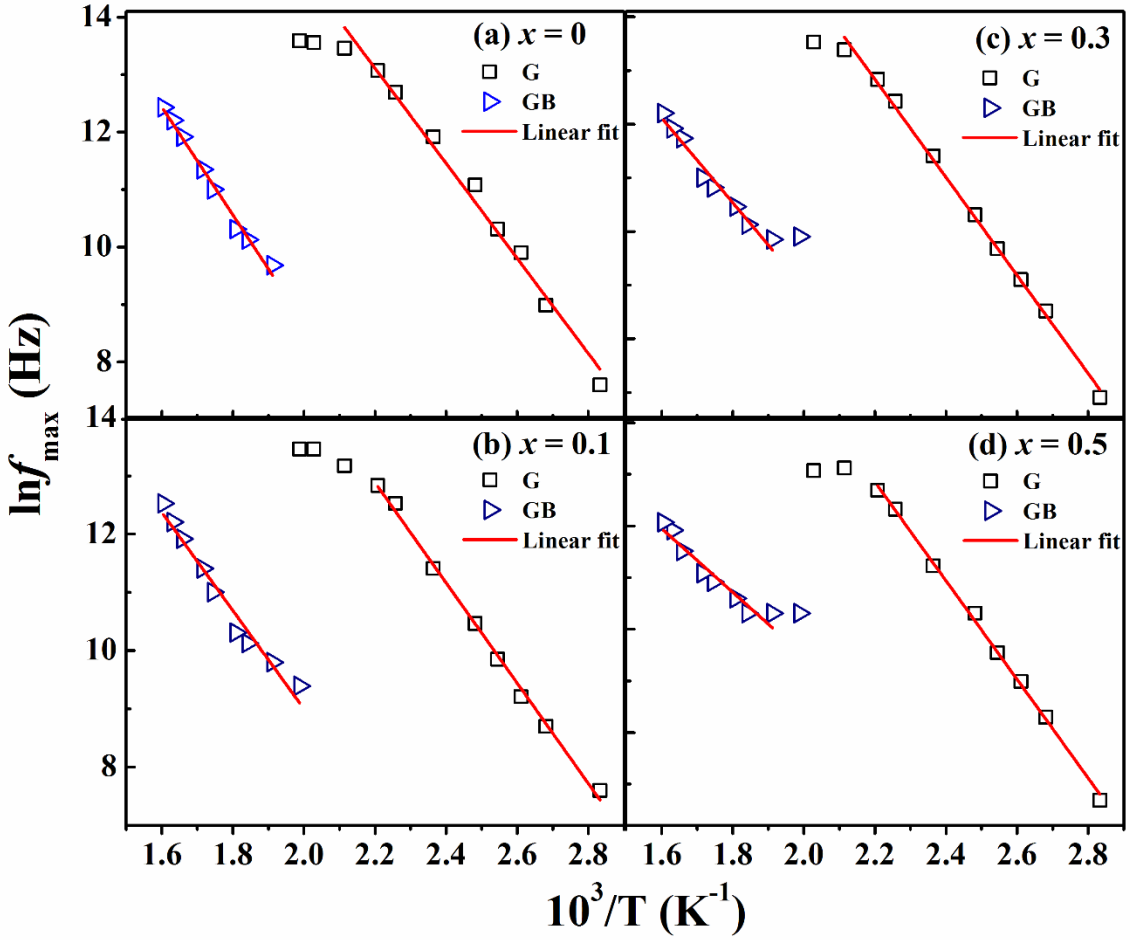

Figure 6.7: Temperature dependence of relaxation frequency for (a) x = 0, (b) x = 0.1, (c) x = 0.3 and (d) x = 0.5 samples corresponding to both grains and grain boundaries contributions along with fitted data (solid line) using Arrhenius law.

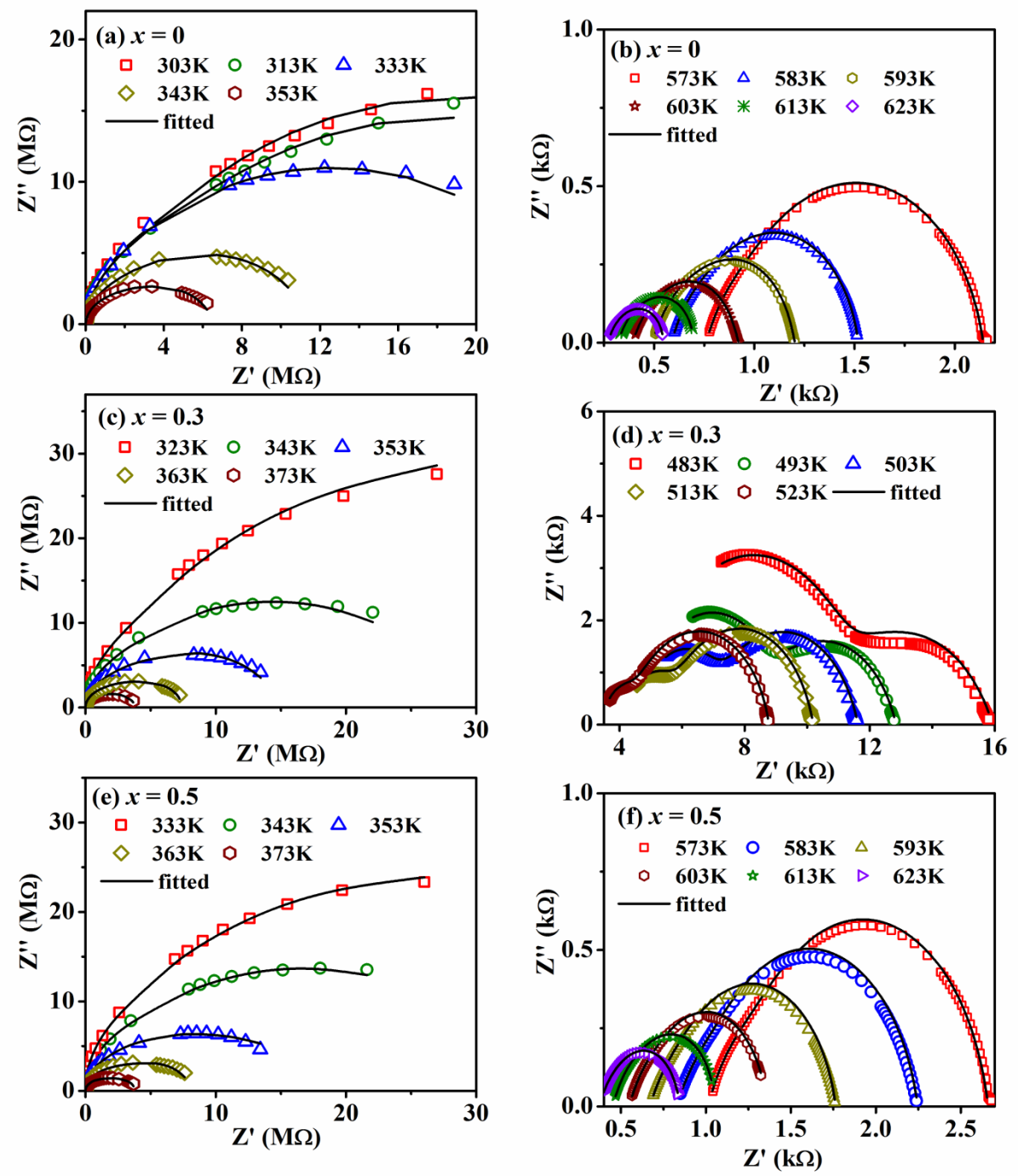

Figure 6.8: Nyquist plots (*Z''* vs *Z'*) of complex impedance spectra of *x* = 0, 0.3 and 0.5 samples in the low temperature (a, c, e) and in the high temperature (b, d, f) regions respectively. The solid lines represent the fitted data.

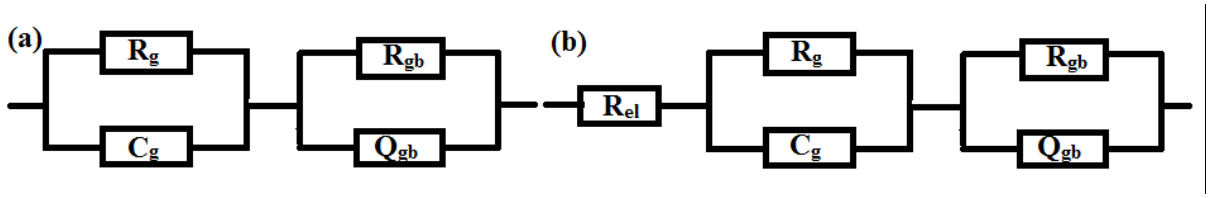

Figure 6.9: Equivalent circuits used for the fitting of Nyquist plots (Z'' vs Z') of $Ba_2(Co_{1-x}Mg_x)_2Fe_{12}O_{22}$ samples in the low temperature (a) and in the high temperature (b) regions respectively.

The typical Nyquist plots (Z'' vs Z') of $Ba_2(Co_{1-x}Mg_x)_2Fe_{12}O_{22}$ samples with x = 0, 0.3 and 0.5 in the temperature range of 303 K to 623 K are shown in Fig. 6.8. A semicircular arc appears in the lower temperatures region ($T \leq$ 373 K) for all the samples. In polycrystalline materials, the relaxation peaks in the impedance spectra are basically due to the contributions from both grains and grain boundaries. For an ideal Debye type behavior, the center of the semicircle in the Nyquist plot should lie on the Z' axis. In this case, an asymmetric and depressed semicircles are observed in the Nyquist plots. However, such depression of semicircle signifies the statistical distribution of relaxation time. In addition, if there exists more than one relaxation process and the mean relaxation time differs by two orders of magnitude, then the distortion occurs in the Nyquist plot [187]. Such mechanism in the Nyquist plot arises due to the presence of non-uniformity in the microstructures and the electromagnetic diffusions in intragrain/intergrain regions. In such case, the effect of grains and grain boundaries in the semicircles can be modeled by considering an electrical equivalent circuit as shown in Fig. 6.9, where the parallel combination of *RC* due to grains are connected in series with that of grain boundaries. From Fig. 6.8, it can be seen that the centre of the asymmetric semicircle lies below the Z' axis. It reveals that the relaxation dynamics deviate from the ideal Debye type relaxation. Any deviation from the ideal Debye type relaxation in the impedance spectra can be modeled by using a constant phase element (*CPE*) denoted by *Q*. The *CPE* in the impedance spectra can be defined as $Z^*_{CPE} = \frac{1}{A}(j\omega)^{-s}$, where *A* is a constant and *s* represents the relaxation time distribution function ($0 \leq s \leq 1$). Fig. 6.8(a) depicts a semicircular arc for x = 0 sample at 303 K. The distorted nature of semicircle reveals the presence of constant phase element in its equivalent circuit. As the temperature is increased, the arc bends towards the Z' axis with decreased diameter and it forms a complete semicircle at around 573 K. It suggests that the conductivity of the samples is enhanced with increase in temperature [188]. Although, Fig. 6.8(a) shows a single semicircle in the temperature range of 303 K to 353

K, but both grains and grain boundaries contribute towards the relaxation dynamics and that can be confirmed from the fitting of Nyquist plots based on an equivalent circuit as shown in Fig. 6.9(a). In this case, an equivalent circuit comprising of two parallel R_gC_g and $R_{gb}Q_{gb}$ elements connected in series explains the Nyquist plots. As the temperature is increased ($T \geq 573$ K) for $x = 0$ sample, the electrode contribution arises in the relaxation process. Therefore, the Nyquist plots in the high temperature region ($T \geq 573$ K) could be modeled to an equivalent circuit of parallel R_gC_g and $R_{gb}Q_{gb}$ elements connected in series with electrode resistance R_{el} as shown in Fig. 6.9(b). Here R_g and R_{gb} represent the resistance of grains and grain boundaries respectively, whereas C_g and Q_{gb} represent the capacitance and the constant phase element associated with the grains and grain boundaries respectively. As the Mg concentration is increased, two semicircular arcs are clearly distinguished in the intermediate temperature range of 483 K – 523 K as shown in Fig. 6.8(d). The presence of two semicircular arcs in the intermediate temperature range reveals that the electrical response is composed of two relaxation process with different characteristic frequencies due to contributions from both grains and grain boundaries at higher (lower Z') and lower (higher Z') frequency regions. These depressed semicircles gradually shifts towards lower Z' value up to 523 K and beyond that, they disappear. The Nyquist plots of all other samples follow the similar behavior.

6.1.4 Electric Modulus Analysis

The frequency dependence of real part **(M')** of electric modulus of $Ba_2(Co_{1-x}Mg_x)_2Fe_{12}O_{22}$ samples for $x = 0$, 0.1, 0.3 and 0.5 measured at different temperatures from 353 K to 423 K are shown in Fig. 6.10. It can be seen that, at low frequency region, the M' spectra have very low value i.e. approaching to zero and it indicates that the contribution of the electrode polarization towards M' is negligible [189, 190]. As the frequency is increased, a continuous increase in M' is noticed by yielding the dispersion behavior. For all the samples, the M' spectrum attains the maximum asymptotic value at a particular frequency (f_{max}) and then starts decreasing for all the temperatures. This indicates that the short-range movement of charge carriers is a conduction process. In addition, since the relaxation processes are spread over a particular frequency range, therefore the M'spectra starts decreasing at higher frequency.

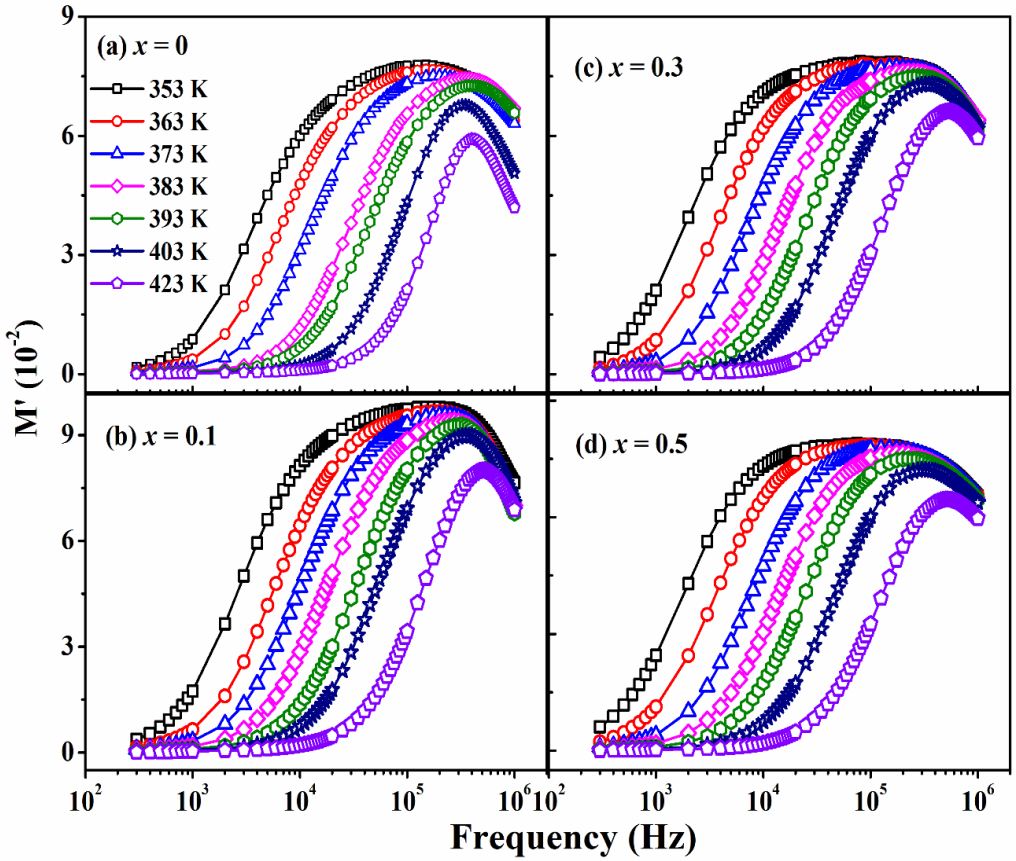

Figure 6.10: Real part (M') of electric modulus as a function of frequency for $Ba_2(Co_{1-x}Mg_x)_2Fe_{12}O_{22}$ samples for (a) x = 0, (b) x = 0.1, (c) x = 0.3 and (d) x = 0.5 measured at different temperatures.

The complex electric modulus of a material can be defined as;

$$M^* = M' + jM'' = 1/\varepsilon^* \qquad (6.2)$$

The real (M') and imaginary (M'') parts of the complex modulus can be expressed as;

$$M' = \frac{\varepsilon'}{\varepsilon'^2 + \varepsilon''^2} \qquad (6.3)$$

$$M'' = \frac{\varepsilon''}{\varepsilon'^2 + \varepsilon''^2} \qquad (6.4)$$

where ε' and ε'' represent the real and imaginary parts of the complex permittivity values determined by using the equations (1.22) and (1.23) respectively. The study of complex electric modulus is one of the important tool that provides the relevant information on electrical response of the low capacitive region such as grains, which cannot be determined in detail from the impedance formalism. In addition, the electrode polarization phenomena is also suppressed by the modulus formalism. The variation of imaginary part of modulus

(M'') spectra with frequency at different temperatures for $Ba_2(Co_{1-x}Mg_x)_2Fe_{12}O_{22}$ samples with x = 0, 0.1, 0.3 and 0.5 are shown in Fig. 6.11. The electrical modulus spectra exhibit peak due to relaxation of charge carriers at a characteristic frequency (f_{max}) for all the samples. The peak is found to shift towards the higher frequency with increase in temperature due to thermal activation of charge carriers. Further, the observation of peaks in the M'' vs frequency plot defines the motion of charge carriers at different frequency ranges. The frequency range below the peak maximum in M''spectra determine the range in which the charge carriers are mobile over long distances. The frequency range above the peak maximum (higher frequency), the charge carriers are confined within the potential well with mobility over the short-range distances. The region, where the peak occurs is the signature of the transition from long-range order to short-range mobility of charges with increase in frequency. The formation of peaks in the M''spectra signify the presence of the conduction relaxation process in the sample [189].

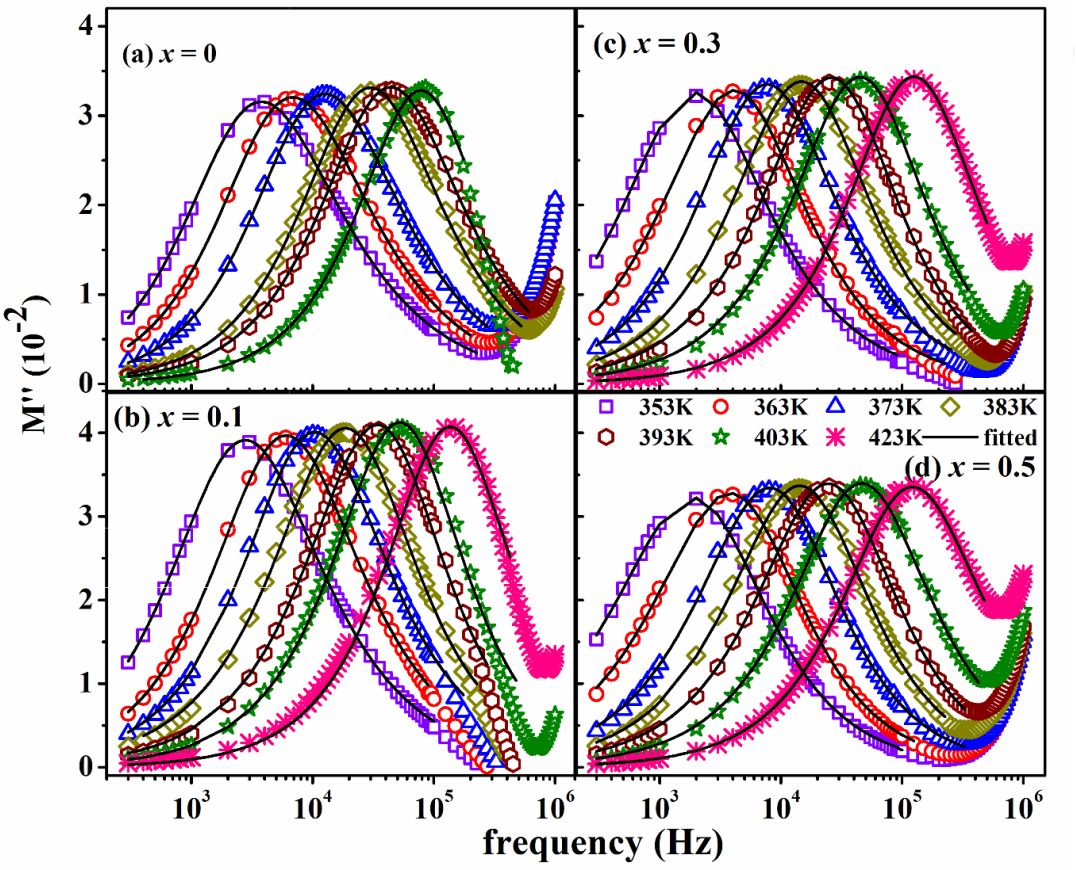

Figure 6.11: Imaginary part (M'') of electric modulus as a function of frequency for $Ba_2(Co_{1-x}Mg_x)_2Fe_{12}O_{22}$ samples for (a) x = 0, (b) x = 0.1, (c) x = 0.3 and (d) x = 0.5 along with fitted (solid line) data using equation (6.2) at different temperatures.

The analysis of M''spectra were carried out by fitting the general four-parameter expression (equation (1.29)) for susceptibility and that can be reproduced as [41];

$$M''(\omega) = \frac{M''_{max}}{\left(\frac{1-|p-q|}{p+q}\right)\left(q\left(\frac{\omega}{\omega_{max}}\right)^{-p} + p\left(\frac{\omega}{\omega_{max}}\right)^{q}\right) + |p-q|} \qquad (6.5)$$

where M''_{max} represents the imaginary part of complex modulus and ω_{max} is the corresponding peak angular frequency. Here p and q are the stretching parameters ($0 \leq p \leq 1$), ($0 \leq q \leq 1$) at low and high frequency regions respectively. The M''data were fitted to Bergman's 4-parameter general expression i.e. equation (6.5) and the fitted data are shown as solid lines in Fig. 6.11. In this case, p and q are the shape parameters at low and high frequency regions respectively. For $p = q = 1$, the relaxation process corresponds to the ideal Debye type behavior with no interaction among the relaxation species. Moreover, the shape of M''spectra are determined from the interaction strength among the relaxation species. Therefore, the knowledge of shape parameters p and q would lead to qualitative information about the interaction among the dipoles. The value of p is found to vary from 0.85 to 1 and that of q is in the range 0.73 to 1 for increase in temperature from 353 K to 423 K. The small increase in q value signifies that the relaxing species are being separated with increase in temperature.

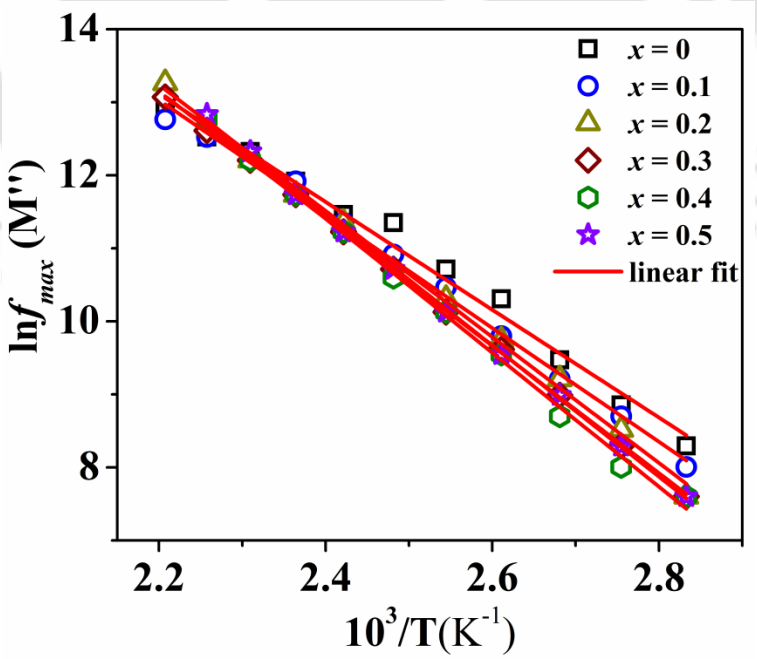

Figure 6.12: Temperature dependence of relaxation frequency obtained from modulus spectra for x = 0, 0.1, 0.3 and 0.5 samples along with fitted data using Arrhenius relation.

Furthermore, the magnitudes of M''spectra for different samples are found to be comparable and a small shifting of M''spectra towards the lower frequency is noticed with Mg substitution. With increase in temperature, the modulus spectra are shifted towards the higher frequency side. The peak position in the modulus spectra also provides the relaxation frequency and they can be analyzed based on Arrhenius relation;

$$f = f_0 \exp[-\frac{E_a^M}{k_B T}] \quad (6.6)$$

where f_0 is the prefactor, k_B is the Boltzmann constant and E_a^M is the activation energy due to relaxation. From the analysis of the above modulus spectra in terms of Arrhenius law, the activation energy (E_a^M) values were estimated by plotting lnf_{max} vs $10^3/T$ and carrying out the linear fit data as shown in Fig. 6.12. The estimated E_a^M values are found to vary from 0.64 eV for x = 0 to 0.77 eV for x = 0.5. The E_a^M values are found to increase with increase in Mg concentration. It is well known that the activation energies E_a^z and E_a^M corresponding to Z'' and M'' spectra represent the localized (i.e. dielectric relaxation) and non-localized conductivity (i.e. long-range conductivity) respectively. In our case, we have seen that the estimated E_a^z and E_a^M values are almost comparable with each other and it suggests that the relaxation and conduction process is governed by the same type of charge carriers [181].

6.1.5 Electrical Conductivity Analysis

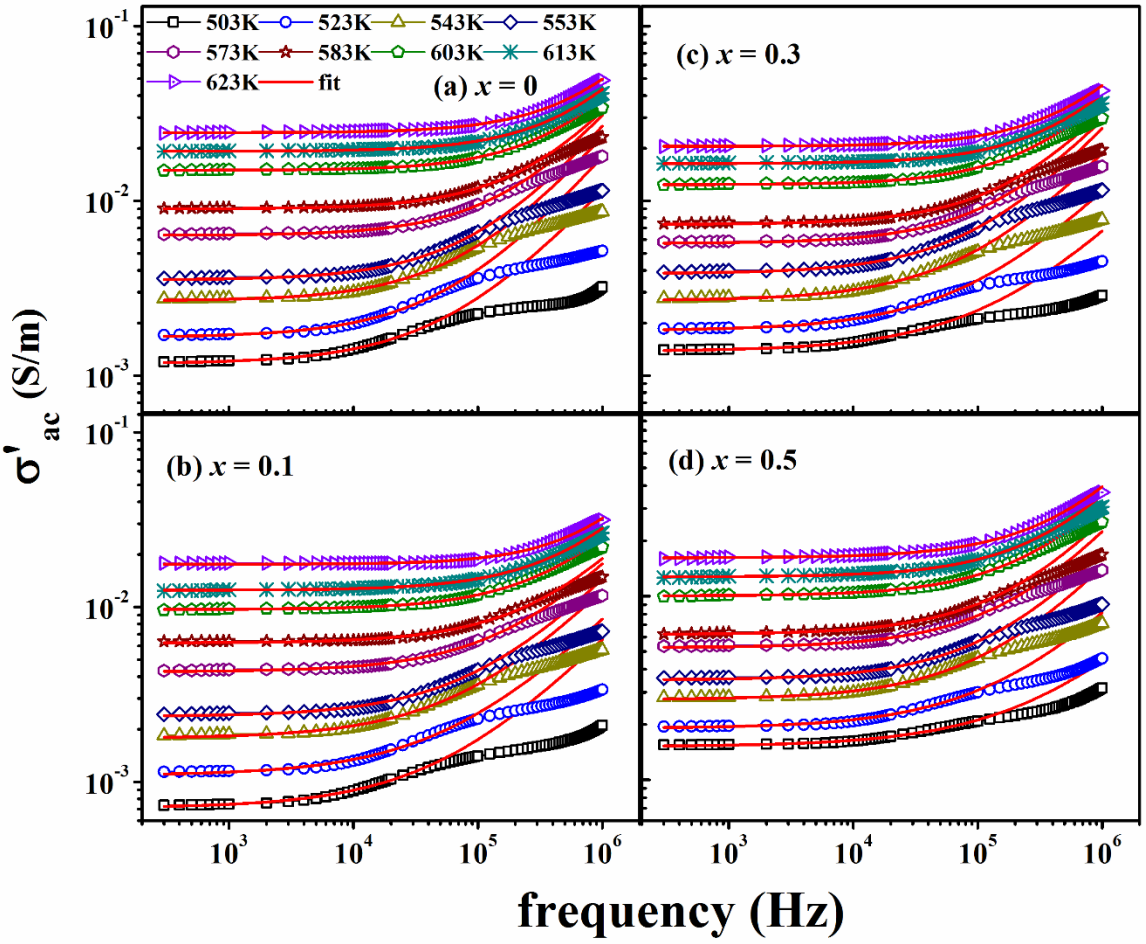

Figure 6.13: (a-d) Frequency variation of ac conductivity at different temperatures along with fitted data (solid line) using equation (6.7) for $Ba_2(Co_{1-x}Mg_x)_2Fe_{12}O_{22}$ samples with x = 0, 0.1, 0.3 and 0.5.

Further, to understand the electrical conductivity of Mg doped Y-type barium hexaferrite, the ac conductivity data were extracted from the experimental $\varepsilon''(= \frac{Z'}{\omega C_0(Z'^2+Z''^2)})$ values by using the relation [95];

$$\sigma'_{ac}(\omega) = \omega\, \varepsilon_0\, \varepsilon'' \qquad (6.7)$$

where ω represents the angular frequency of ac applied field, ε_0 is the permittivity of free space. The frequency dependence of σ'_{ac} of $Ba_2(Co_{1-x}Mg_x)_2Fe_{12}O_{22}$ samples with x = 0, 0.1, 0.3 and 0.5 at different temperatures are shown in Fig. 6.13. From the Fig. 6.13, it can be seen that the ac conductivity is found to increase with increase in temperature and it suggests the negative temperature coefficient of resistance behavior. The magnitude of ac

conductivity is found to decrease with increase in Mg concentration. Furthermore, the ac conductivity plot at a particular temperature is characterized by two different regions; one is the frequency independent plateau in the low frequency region attributed to dc conductivity due to the long-range translational motion of the charge carriers. The other one in the high frequency region, where the conductivity increases with frequency due to increase in hopping of charge carriers. In the low temperature region, the relaxation and conduction process are due to electron hopping between Fe^{2+} and Fe^{3+} ions and the hole transfer between Co^{2+} and Co^{3+} ions. Whereas at higher temperature, it is mainly due to the oxygen vacancies. The frequency dispersion of ac conductivity at different temperatures can be easily understood from the mechanism of the jump relaxation model (JRM) [165]. According to JRM, two competing relaxation process takes place at higher frequency region such as (i) the unsuccessful hopping, where the jumping of ions jump back to its initial position and (ii) the successful hopping ,where the jumping ions will stay in the new site and the neighborhood ion become relaxed with respect to the jumping ions position. Thus, the enhancement in successful to unsuccessful hopping ratio will give rise to dispersive region in the conductivity spectra at higher frequency region. This characteristic feature of the conductivity spectra can be understood as per Jonscher Power Law (JPL) [191];

$$\sigma'_{ac} = \sigma_0 + A\omega^n \qquad (6.8)$$

where σ_0 is the frequency independent dc conductivity that corresponds to plateau region in the low frequency region. The term $A\omega^n$ characterizes the dispersion phenomena, where A is a constant and n is the frequency exponent term that depends on temperature and the material's intrinsic properties. The parameter n explains the degree of interaction of mobile charges with the lattice around them and its temperature dependence mechanism describes the underlying conduction mechanism. The value of n basically provides the information about the nature of charge carriers is either translational or localized. If the value of n is between $0 \leq n \leq 1$ then it signifies the short-range hopping due to translational motion of charge carriers. The value of n will be greater than 1, if there is a localized or reorientational hopping of electrons between two charge defects [166]. The conductivity data of all these samples were fitted to Jonscher Power Law and the corresponding fitted data are shown as solid lines in Fig. 6.13 for typical values of x = 0, 0.1, 0.3, and 0.5 samples. Fig. 6.13 reveals that the fitted data closely follow the experimental data. From the analysis of the above

conductivity spectra, the values of frequency exponent *n* estimated for all the samples at different temperatures are shown in Fig. 6.14. It can be seen that, the frequency exponent *n* is found to increase with increase in temperature and highlights that the conduction process is controlled by small polaron tunneling model [117].

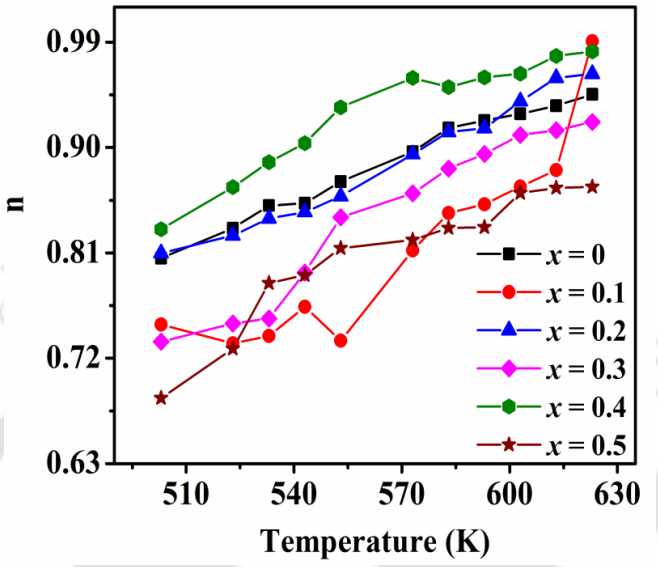

Figure 6.14: Temperature variation of frequency exponent *n* for $Ba_2(Co_{1-x}Mg_x)_2Fe_{12}O_{22}$ samples with $x = 0 – 0.5$.

6.1.6 Magnetic Properties

Magnetization as a function of temperature were measured for $Ba_2(Co_{1-x}Mg_x)_2Fe_{12}O_{22}$ samples under zero field cooled (ZFC) mode for an applied magnetic field of 100 Oe. The magnetization versus temperature ($M – T$) plots for different concentrations of Mg in Co_2Y hexaferrite are shown in Fig. 6.15(a). It is noticed that all samples exhibit two magnetic transitions i.e. ferrimagnetic transition (T_c) at high temperature followed by the helimagnetic transition (T_s) at low temperature. Such type of transitions have been observed in the previous reports on Zn, Ni and Sr substituted Y-type hexaferrites [11, 65, 149]. Both T_c and T_s values were determined from the inflection points, i.e. corresponding to valley and peak positions of dM/dT vs T plots. For $x = 0$ sample, the T_c and T_s values are found to be 613 K and 225 K respectively. The systematic decrease in both T_c and T_s values are observed with increase in Mg concentrations and it reaches to $T_c = 581$ K and $T_s = 182$ K respectively for $x = 0.5$ sample. In general, the T_c value of ferrite materials depend upon the thermal stability of the spin alignments and the spin alignments strongly depends upon the superexchange interaction between metal ions at two magnetic sublattices. Therefore,

the occupation of non-magnetic Mg^{2+} ions at the octahedral sites of magnetic Co^{2+} ions may give rise to the weakening of superexchange interaction among these magnetic cations and results in decrease in T_c values. Further, since the Co^{2+} ion have stronger anisotropy than that of Mg^{2+} ion, the decrease in T_s value can be explained based on decrease in magnetic anisotropy. In addition, to get some more information regarding the magnetic interactions at low temperatures, the magnetization measurements were carried out in both zero field cooled (ZFC) and field cooled (FC) mode at 100 Oe for x = 0 and 0.5 samples in the temperature range of 30 K to 300 K as shown in Fig. 6.15(b-c). It can be seen that, below the helimagnetic spin-reorientation transition temperature (T_s), a large irreversibility is seen between ZFC and FC curves. Such irreversibility is expected for $T < T_s$ [9]. The variations of T_c and T_s values with respect to Mg concentrations in Co_2Y hexaferrite are given in Table 6.2.

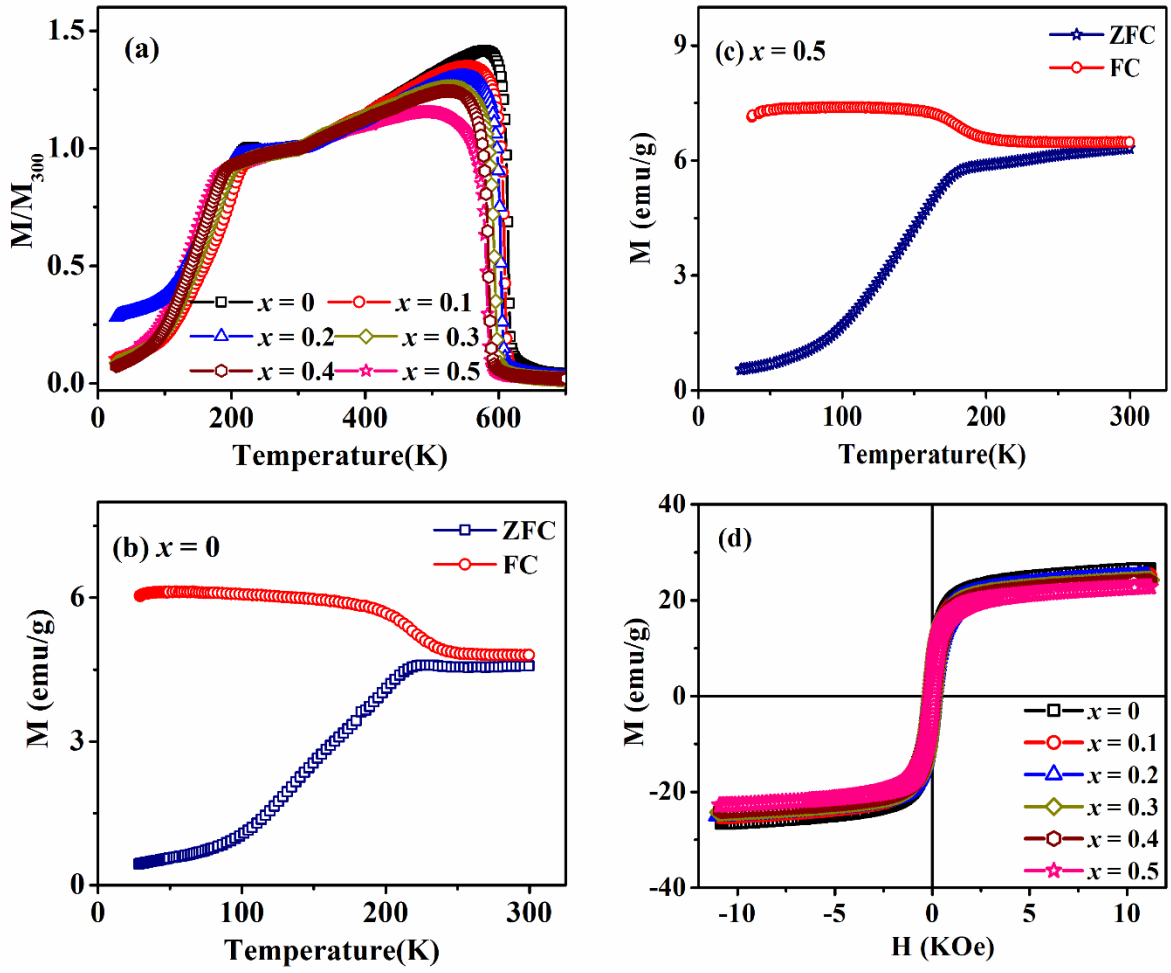

Figure 6.15: (a) Temperature variation of magnetization (M) normalized to magnetization measured at 300 K (M_{300}) for $Ba_2(Co_{1-x}Mg_x)_2Fe_{12}O_{22}$, (b-c) Both *ZFC* and *FC*

magnetization measured from 30 K to 300 K for x = 0 and 0.5 samples (d) Magnetic hysteresis loops measured at room temperature for x = 0 – 0.5.

In order to further understand the magnetic properties of $Ba_2(Co_{1-x}Mg_x)_2Fe_{12}O_{22}$ in detail, the magnetic hysteresis loop measurements were carried out at room temperature for x = 0 – 0.5 samples as shown in Fig. 6.15(d). The M – H loops of all these samples show the soft ferrimagnetic nature. Since the saturation magnetization (M_s), coercivity (H_c), remanence (M_r) and magnetocrystalline anisotropy (K_1) are the important magnetic parameters to define the magnetic properties of a material, therefore all these magnetic parameters were determined from the M – H loops. The law of approach to saturation (LAS) model is one of the important phenomena that was employed for the analysis of M – H loops. The modified LAS model as described in equation (6.9) was used for the analysis [192];

$$M = M_s\left(1 - \frac{B}{H^2}\right) \tag{6.9}$$

By employing the above equation (6.9), the initial magnetization curves were fitted for all the samples. The experimental magnetization (M) data were plotted against the inverse square of applied magnetic field ($1/H^2$) and a straight line is obtained in the field range of 8 kOe to 10 kOe as shown in Fig. 6.16. The symbols denote the experimental data while the fitted data are shown as solid lines. The slope of the straight line gives rise to M_s values while the intercept provides the B value. Since magnetic anisotropy is one of the important parameter for magnetic materials, this can be determined from the B value. Thus, the experimental saturation magnetization (M_s) and the constant B values were estimated by fitting to the modified LAS model. Further, the anisotropy field (H_a) can be calculated by using the relation [9];

$$B = \frac{H_a^2}{15} \tag{6.10}$$

The effective magnetic anisotropy constant (K_1) is also calculated by using the following relation:

$$H_a = \frac{2K_1}{M_s} \tag{6.11}$$

By using equations (6.10) and (6.11), the H_a and K_1 values were calculated. A systematic decrease in magnetic parameters such as anisotropy constant K_1, M_s and H_c values have been observed due to Mg substitutions. It is known that the Fe and Me ions in Y-type

hexaferrites are distributed over six different crystallographic sites: four octahedral sites ($3a_{vi}$, $3b_{vi}$, $6c_{vi}$ and $18h_{vi}$) and two tetrahedral sites ($6c_{iv}$ and $6c_{iv*}$). Among the six crystallographic sites, the cations in $3a_{vi}(\uparrow)$, $3b_{vi}(\uparrow)$ and $18h_{vi}(\uparrow)$ are in the spin up state while those in $6c_{vi}(\downarrow)$, $6c_{iv}(\downarrow)$ and $6c_{iv*}(\downarrow)$ are in the spin down state. Therefore, the occupation of metal ions and their distribution over different tetrahedral and octahedral sites lead to change in magnetic properties of the materials. The magnetization measurements reveal that both the saturation magnetization (M_s), magnetic anisotropy constant (K_1) and the coercivity (H_c) values are found to decrease marginally with increase in Mg^{2+} ion concentrations. For $x = 0$ sample, the saturation magnetization value is found to be 26.6 emu/g and it decreases to 22.7 emu/g for $x = 0.5$ sample. The substitution of non-magnetic Mg^{2+} ions at the magnetic Co^{2+} ions having magnetic moment 3.88 μ_B per ion could be the major reason for the reduction in M_s values [70]. Moreover, the coercivity (H_c) value of the samples were calculated by using the relation;

$$H_c = (H_+ - H_-)/2 \qquad (6.12)$$

where H_+ and H_- are two magnetic field values of the ascending and descending branch of $M - H$ loop corresponding to $M_s = 0$. The H_c value for the parent compound i.e. $x = 0$ sample is found to be 129.4 Oe and it decreases to 77.4 Oe due to Mg substitution for $x = 0.5$. Since the Co^{2+} ions have large magnetic anisotropy than that of Mg^{2+} ions, the substitution of Co^{2+} by Mg^{2+} ion causes the reduction in magnetocrystalline anisotropy constant and that leads to the decrease in coercivity. The magnetic parameters such as M_s, H_c, H_a and K_1 estimated from the fitted data are tabulated in Table. 6.2.

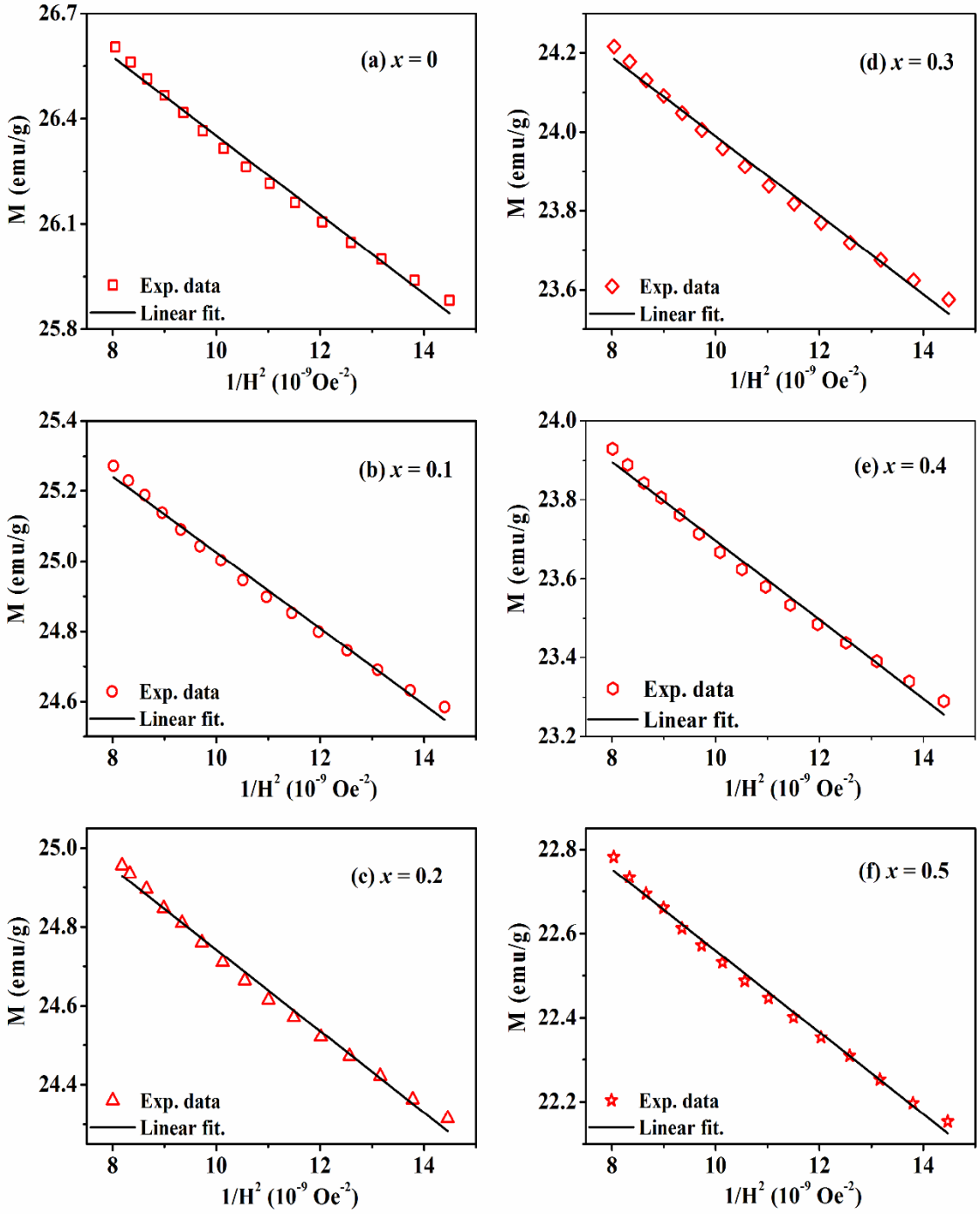

Figure 6.16: Room temperature magnetization (M) vs $1/H^2$ plots analysed by LAS (equation (6.9)) for $Ba_2(Co_{1-x}Mg_x)_2Fe_{12}O_{22}$ samples with x = 0, 0.1, 0.2, 0.3, 0.4 and 0.5. Here the red symbols represent the experimental data and the solid line represents the fitted data.

Table 6.2: Various magnetic parameters M_s, H_c, H_a, K_1 along with T_c and T_s values for different concentrations of Mg in Co_2Y hexaferrtite.

x	T_s (K)	T_c (K)	M_s (emu/g)	H_c (Oe)	H_a (10^4 Oe)	K_1 (10^6 erg/cc)
0.0	225	613	26.6	129.4	4.11	0.55
0.1	218	609	26.1	123.6	4.03	0.52
0.2	209	603	25.7	106.9	3.93	0.50
0.3	200	593	24.9	95.5	3.88	0.48
0.4	192	585	24.6	91.7	3.87	0.47
0.5	182	581	22.7	77.4	3.81	0.43

6.1.7 Conclusions

Polycrystalline samples of $Ba_2(Co_{1-x}Mg_x)_2Fe_{12}O_{22}$ ($0 \leq x \leq 0.5$) were prepared in single-phase form by solid state reaction method and they are found to be crystallized into rhombohedral structure with R-3m space group. A systematic decrease in lattice constant *c* is obtained with increase in Mg concentration. The impedance spectra (Z'') reveals that the well-defined relaxation peaks are observed at different characteristic frequencies and they are governed by grains and grain boundaries contributions. The appearance of relaxation peaks due to grains and grain boundaries contributions are confirmed from Nyquist plots by fitting to different electrical equivalent circuits. The asymmetric and depressed semicircular arc observed in the Nyquist plots demonstrate the non-Debye like dielectric relaxation inside grains and across the grain boundaries. The activation energy estimated from relaxation peaks of impedance, modulus spectra are almost comparable, and it signifies that the same type of charge carriers govern both dielectric relaxation and the conduction process. As per the analysis of ac conductivity data, the conduction process in Mg doped Co_2Y hexaferrte is attributed to the small polaron model. The $M - H$ measurements recorded at room temperature reveals that both M_s and H_c values are found to decrease with increase in Mg concentration. The temperature dependence of magnetization plots show two magnetic transition temperatures corresponding

ferrimagnetic (T_c) and helimagnetic spin-reorientation (T_s) transitions. The reduction of both T_c and T_s values have been observed due to the Mg substitutions. The decrease in T_c value signifies the weakening of superexchange interaction while the decrease in T_s value is attributed to the decrease in magnetic planar anisotropy of the samples.

Chapter 7

Conclusions

The overall summary of conclusions obtained from the analysis of structural, dielectric and magnetic properties of (Ni, Ti and Al) substituted M-type and (Zn and Mg) substituted Y-type hexaferrites are presented.

Single-phase samples of $BaFe_{12-y}Ni_yO_{19}$ ($0 \leq y \leq 0.5$) have been successfully prepared by using standard sol-gel route and they are found to be crystallized in hexagonal structure with $P6_3/mmc$ space group. The substitution of Ni at Fe site leads to the systematic increase in lattice parameters and such increase in lattice parameters can be understood due to the larger ionic radius of Ni^{2+} ion than that of Fe^{3+} ion. The analysis of microstructure based on FESEM micrographs of all the samples demonstrate the well defined hexagonal shaped grains and the average grain size value increases with increase in Ni concentration. Similarly, the Ti substituted barium hexaferrite i.e. $BaFe_{12-y}Ti_yO_{19}$ ($0 \leq y \leq 0.8$) samples were also successfully prepared in single-phase form by solid state reaction method. The analysis of XRD patterns were performed by the Rietveld refinement technique based on $P6_3/mmc$ space group with hexagonal symmetry. The lattice parameter *a* is almost constant and *c* is found to increase with increase in Ti concentration. The increase in lattice parameter can be ascribed to the substitution of smaller Fe^{3+} ion by larger Ti^{4+} ion.

The variation of Z'' spectra as a function of frequency for $BaFe_{12-y}Ni_yO_{19}$ ($0 \leq y \leq 0.5$) samples measured at different temperatures show two different relaxation peaks. These two relaxation peaks are assigned to the grains and grain boundaries contributions. As the temperature is increased, these two peaks are found to shift towards higher frequency range and it is ascribed to the thermal activation of charge carriers. The Nyquist (Z'' vs Z') plots of all the samples demonstrate two depressed semicircles with their centre lying below the Z' axis. The asymmetric and depressed semicircles in the Nyquist plot signifies the deviation from ideal Debye behavior. The Nyquist plots of all these samples are modeled to equivalent electrical circuit that is basically a series connection of two parallel circuits

attributing to grains and grain boundaries components respectively. The Nyquist plots reveal that at low temperature around T = 373 K, grains contributions are dominant for y = 0 sample and it is explained based on the electrical circuit, where capacitance (C_g), resistance (R_g) and a constant phase element (Q_g) due to grains contributions are connected in parallel to each other. As the temperature increases i.e. for $T >$ 373 K, the grain boundaries contributions take place. However, the grains and grain boundaries contributions are clearly distinguished in Ni substituted samples. In such cases, the grains and grain boundaries contributions are modeled by the series combination of two parallel circuits consisting of resistor and a constant phase element. The frequency dispersions of ε' and ε'' were analyzed based on the Havriliak – Negami (HN) equation by considering the electrical conductivity contribution towards the dielectric response. It is noticed that the experimental data is well fitted with the HN equation. The loss tangent is found to reduce with increase in Ni concentration. Further, the temperature dependence of magnetization measurements carried out at different temperature reveals the ferrimagnetic transitions (T_c). The transition temperature T_c is found to increase from 720 K for y = 0 to 759 K for y = 0.5 sample and this implies that the superexchange interaction among the magnetic cations is strengthened due to Ni substitution. To understand the magnetic properties in detail, the M – H loops of all the samples were measured at room temperature and various important magnetic parameters such as M_s, H_c, K_1 *etc*. values were determined by employing the law of approach to saturation (LAS) model. The M_s, H_c, K_1 values are found to decrease with increase in Ni substitution.

Like Ni substituted BaM hexaferrite, the Ti substituted BaM hexaferrite i.e. $BaFe_{12-y}Ti_yO_{19}$ ($0 \leq y \leq 0.8$) samples exhibit ferrimagnetic transitions for all the samples. Substitution of Ti at Fe site reduces the T_c values from 720 K for y = 0 to 608 K for y = 0.8. The reduction in T_c values due to Ti substitution can be ascribed to the replacement of magnetic Fe^{3+} ion by non-magnetic Ti^{4+} ion. As a result, the superexchange interaction in $Fe^{3+} – O^{2-} – Fe^{3+}$ networks are weakened and that leads to the reduction in T_c values. The moderate decrease in M_s value is observed due to Ti substitution with large decrease in H_c values. The H_c value for y = 0 sample is found to be 2980 Oe and it decreases to 209 Oe for y = 0.8 sample. Thus, moderate value of M_s with low value of H_c due to Ni and Ti substitution can be useful for applications in soft magnetic ferrites. The frequency dependence of Z' data possesses a step-like behaviour. At a particular frequency, the Z' value decreases with increase in temperature and this can be attributed to the negative

temperature coefficient of resistance. Moreover, the magnitude of Z' also decreases with Ni substitution and it indicates that the Ti substitution has large influence on its electrical properties. In addition, the Z'' spectra demonstrate two relaxation peaks due to grains and grain boundaries contributions and they are merged together due to Ti substitutions. The Nyquist plots of impedance spectra show the grains and grain boundaries contributions towards the relaxation process and this can understood by considering an electrical equivalent circuit consisting of resistor, capacitor and constant phase element. The ac conductivity data as a function of frequency at different temperatures were analyzed by Jonscher's power law. The conduction activation energy across the grain boundaries are found to decrease from 0.42 – 0.22 eV for y = 0 – 0.8 samples. The relaxation activation energy determined from the impedance spectra and the conduction activation energy are almost comparable and it suggests that the same type of charge carriers mediate both the process.

Polycrystalline samples of $Ba(Fe_{1-x}Al_x)_{12}O_{19}$ (x = 0 – 0.10) were synthesized by solid state reaction method. The XRD patterns of all the samples recorded at room temperature were Rietveld refined by choosing $P6_3/mmc$ space group with hexagonal structure. The analysis of these XRD patterns suggest that the prepared samples are found to be in single-phase form. The lattice parameters a and c are found to decrease with increase in Al concentration and it can be understood in terms of smaller ionic radius of Al^{3+} ion than that of Fe^{3+} ion. No secondary peak rather than the broadening of peak is observed in the Raman spectra. It confirms the single-phase nature of the samples and the broadening of peaks due to Al substitution is ascribed to the ionic size mismatch between Al^{3+} and Fe^{3+} ions. Substitution of Al gives rise to decrease in average grain size value from 343 nm for x = 0 to 225 nm for x = 0.10 sample. The substitution of Al at Fe site reduces the M_s values from 51.36 emu/g for x = 0 to 45.76 emu/g for x = 0.10 sample. However, the H_c value is enhanced due to Al substitution from 4132 Oe for x = 0 to 4926 Oe for x = 0.10. In order to understand the effect of temperature on magnetic properties, the measurement of $M – H$ loops were carried out at different temperatures from 303 K to 673 K. The M_s value is decreased with increase in temperature, but the H_c value is increased up to 473 K and then starts decreasing with further increase in temperature. The complex permittivity and permeability measurements were carried out at room temperature for all the samples. The ε' value decreases with increase in frequency and this is the normal behavior of dielectric materials. At a particular frequency, the ε' value along with the ε''

value is reduced due to Al substitution. The μ' is found to decrease from 1.42 for x = 0 to 1.14 for x = 0.10. Further, the μ'' is also reduced upon Al substitution and it follows the increasing trend with increase in frequency. The dielectric loss tangent demonstrates the relaxation peaks at low frequency region, which arises due to the matching of hopping frequency of charge carriers with that of the frequency of applied field. As the Al concentration is increased, the relaxation peaks are found to shift towards the lower frequency range and then move out of the measured frequency range. Further, the magnetic loss tangent is also reduced upon Al substitution. Thus, the high value of permeability at higher frequency with low magnetic loss due to Al substitution could be suitable for microwave absorber applications.

Similar to M-type hexaferrite, the Zn substituted Y-type barium hexaferrite i.e. $Ba_2(Co_{1-x}Zn_x)_2Fe_{12}O_{22}$ (x = 0 – 1.0) were prepared in single-phase form by using standard solid state reaction route. The Rietveld refinement of the XRD patterns recorded at room temperature was carried out based on R-3m space group with rhombohedral structure. The refined data of these XRD patterns demonstrate that the prepared samples exhibit the single-phase nature. The lattice parameters are found to increase with increase in Zn concentration and it can be explained in terms of difference in their ionic radius as well as the preferential site occupation of Zn ion at the tetrahedral site. The FESEM micrographs of all the samples reveal the mixture of smaller and larger size hexagonal shaped grains and the average grain size values for these samples are in the range of 1.5 – 2.0 µm.

The frequency variations of dielectric permittivity and impedance spectra were measured at different temperatures. The ε' spectra exhibit maximum value at low frequency region and it decreases with increase in frequency. The maximum value of ε' at low frequency is attributed to the interfacial polarization mechanism. However, the substitution of Zn slightly reduces the ε'' value. The Z'' spectra measured as a function of frequency at different temperatures exhibit two relaxation peaks due to grains and grain boundaries contributions. The relaxation peaks shift towards the higher frequency with increase in temperature. The normalized component of the impedance spectra i.e. Z''_{max}/Z'' vs f_{max}/f reveal that the relaxation peaks are merged into a single master curve and it indicates that the relaxation phenomena occurring in these spectra are temperature independent. The frequency dispersion of conductivity data were analyzed by Jonscher Power Law (JPL). Analysis of conductivity spectra for x = 0 – 0.75 follows the overlapping of large polaron tunneling (OLPT) model and the x = 1.0 sample follows the small polaron tunneling (SPT)

model. Both spin reorientation transition (T_s) and the ferrimagnetic transition (T_c) have been observed from the magnetization versus temperature measurements for all the samples. Substitution of Zn at Co site reduces the ferrimagnetic and spin reorientation transition temperatures for all the samples. Such reduction in T_s value indicates that the substitution of Zn reduces the magnetic anisotropy and the reduction in T_c value is due to the weakening of superexchange interaction among the magnetic cations in Y-type hexaferrite. Analysis of complex magnetic permeability reveals that the real part (μ') of permeability is enhanced due to Zn substitution while it reduces the magnetic loss (μ'').

The polycrystalline samples of Mg substituted Y-type barium hexaferrite i.e. $Ba_2(Co_{1-x}Mg_x)_2Fe_{12}O_{22}$ (x = 0 – 0.5) were prepared by solid state reaction method. The XRD patterns of all the samples were Rietveld refined by choosing R-3m space group with rhombohedral symmetry. Analysis of refined data reveals that the prepared samples are found to be in single-phase form and the lattice parameters are found to decrease with increase in Mg concentration. The decrease in lattice parameters due to Mg substitution can be explained in terms of substitution of Mg^{2+} ions having smaller ionic radius compared to that of host Co^{2+} ion. The FESEM micrographs show the average grain sizes of all the samples are in the range of 1.5 – 2.2 µm.

Further, at a particular concentration, the magnitude of the real part of Z' is found to decrease with increase in temperature and it suggests that the material possesses negative temperature coefficient of resistance. The frequency variations of Z'' show the relaxation peaks due to grains and grain boundaries contributions. The peak observed in lower frequency is due to grain boundaries contributions and the peak observed at higher frequency is due to grains. The activation energy (E_a^z) values corresponding to grains and grain boundaries are found to be in the range of 0.71 – 0.82 eV and 0.63 – 0.81 eV respectively. The Nyquist plots of these samples were modeled by considering two equivalent electrical circuits connected in series combination. Each individual circuits refer to grains and grain boundaries, where the capacitor, resistor and a constant phase element are connected in parallel to each other. The frequency dependence of M'' exhibits relaxation peaks for all the samples measured at different temperatures. The activation energy estimated from the Z'' and M'' spectra are almost comparable and it signifies that the relaxation and conduction process is governed by the same type of charge carriers. The frequency dispersion of conductivity data were analyzed based on Jonsche Power Law (JPL) and it suggests that the experimental data are well fitted to JPL. The frequency

exponent '*n*' values estimated from the JPL is found to be in the range of 0 to 1. The variation of *n* with respect to temperature suggests that the Mg substituted Y-type barium hexaferrite follows the small polaron tunneling (SPT) conduction mechanism. Further, the room temperature magnetization hysteresis ($M - H$) loops were recorded for all the samples. The substitution of Mg reduces the M_s and H_c values. The reduction in M_s value is due to the substitution of nonmagnetic Mg^{2+} ion by the magnetic Co^{2+} ion and the decrease in H_c value is due to the decrease in magnetic anisotropy. The magnetization versus temperature ($M - T$) plots of $Ba_2(Co_{1-x}Mg_x)_2Fe_{12}O_{22}$ ($x = 0 - 0.5$) samples exhibit helimagnetic spin reorientation transition (T_s) and ferrimagnetic transition (T_c) for all the samples. The T_c and T_s values are found to decrease upon Mg substitution. The decrease in T_s value is ascribed to the reduction in magnetic anisotropy while the reduction in T_c value is explained in terms of weakening of superexchange interaction among the magnetic cations.

Future Scope of Studies

The future scope of studies in this area is listed below.

- The multiferroic properties of these prepared M- and Y- type hexaferrites can be explored by studying the magnetoelectric/magnetodielectric properties.
- The co-substitution of suitable transition elements along with Ti can be useful for investigating the magnetoelectric properties of BaM hexaferrite.
- The materials can be studied for microwave absorption.
- Preparation of $BaFe_{12-x}M_xO_{19}$ (M = Ti, Ni or Al) in thin film forms and the effect of cationic substitutions on the magnetoelectric coupling can be further studied.
- M*ö*ssbauer spectroscopy can be studied for the prepared samples of M- and Y-type hexaferrites to get clear understanding of the site preference of each of the cationic distributions.
- Study of dielectric properties at low temperatures for both Zn and Mg substituted will be useful to get more correlation between magnetic and dielectric properties, especially near spin reorientation transition temperatures.
- The electric polarization as a function of magnetic field at different temperatures can be measured for both Mg and Zn substituted Y-type hexaferrite to understand the magnetism induced ferroelectricity.

- Study of Neutron powder diffraction at different temperatures under zero field cooled condition will lead to get better insight into the magnetic structure and the origin of magnetic properties of Zn and Mg substituted $Ba_2Co_2Fe_{12}O_{22}$ samples. Especially the magnetic structure can be easily understood at low temperatures, where the spin reorientation transition occurs.

References

[1] J. Smit, H. Wijn, Ferrites, Philips technical library, Eindhoven, The Netherlands, 278 (1959).

[2] R.C. Pullar, Hexagonal ferrites: A review of the synthesis, properties and applications of hexaferrite ceramics, Progress in Materials Science, 57 (2012) 1191-1334.

[3] V.V. Soman, V.M. Nanoti, D.K. Kulkarni, Dielectric and magnetic properties of Mg–Ti substituted barium hexaferrite, Ceramics International, 39 (2013) 5713-5723.

[4] C.-W. Nan, M. Bichurin, S. Dong, D. Viehland, G. Srinivasan, Multiferroic magnetoelectric composites: Historical perspective, status, and future directions, Journal of Applied Physics, 103 (2008) 1.

[5] L.W. Martin, S.P. Crane, Y.H. Chu, M.B. Holcomb, M. Gajek, M. Huijben, C.H. Yang, N. Balke, R. Ramesh, Multiferroics and magnetoelectrics: thin films and nanostructures, Journal of Physics: Condensed Matter, 20 (2008) 434220.

[6] W. Prellier, M.P. Singh, P. Murugavel, The single-phase multiferroic oxides: from bulk to thin film, Journal of Physics: Condensed Matter, 17 (2005) R803-R832.

[7] J. Wang, J.B. Neaton, H. Zheng, V. Nagarajan, S.B. Ogale, B. Liu, D. Viehland, V. Vaithyanathan, D.G. Schlom, U.V. Waghmare, N.A. Spaldin, K.M. Rabe, M. Wuttig, R. Ramesh, Epitaxial BiFeO3 Multiferroic Thin Film Heterostructures, Science, 299 (2003) 1719-1722.

[8] T. Kimura, T. Goto, H. Shintani, K. Ishizaka, T.-h. Arima, Y. Tokura, Magnetic control of ferroelectric polarization, nature, 426 (2003) 55.

[9] A. Alsmadi, I. Bsoul, S. Mahmood, G. Alnawashi, K. Prokeš, K. Siemensmeyer, B. Klemke, H. Nakotte, Magnetic study of M-type doped barium hexaferrite nanocrystalline particles, Journal of Applied Physics, 114 (2013) 243910.

[10] T. Kimura, Magnetoelectric hexaferrites, Annu. Rev. Condens. Matter Phys., 3 (2012) 93-110.

[11] J.T. Lim, C.S. Kim, Investigation of Magnetic Properties of Zn Doped Y-Type Barium Ferrite, IEEE Transactions on Magnetics, 49 (2013) 4192-4195.

[12] A. Deriu, F. Licci, S. Rinaldi, T. Besagni, Y-type hexagonal ferrites containing zinc, copper and cadmium: Magnetic properties and cation distribution, Journal of Magnetism and Magnetic Materials, 22 (1981) 257-262.

[13] B.D. Cullity, C.D. Graham, Introduction to magnetic materials, John Wiley & Sons, 2011.

[14] S. Blundell, Magnetism in Condensed Matter, OUP Oxford, 2001.

[15] H. Kramers, L'interaction entre les atomes magnétogènes dans un cristal paramagnétique, Physica, 1 (1934) 182-192.

[16] J.B. Goodenough, Theory of the role of covalence in the perovskite-type manganites [La, M (II)] Mn O 3, Physical Review, 100 (1955) 564.

[17] J.B. Goodenough, A.L. Loeb, Theory of ionic ordering, crystal distortion, and magnetic exchange due to covalent forces in spinels, Physical Review, 98 (1955) 391.

[18] M.A. Ruderman, C. Kittel, Indirect exchange coupling of nuclear magnetic moments by conduction electrons, Physical Review, 96 (1954) 99.

[19] T. Kasuya, Electrical resistance of ferromagnetic metals, Progress of Theoretical Physics, 16 (1956) 58-63.

[20] K. Yoshida, Magnetic properties of Cu-Al alloys, Phys. Rev, 106 (1957) 893.

[21] C. Zener, Interaction between the d-shells in the transition metals. II. Ferromagnetic compounds of manganese with perovskite structure, Physical Review, 82 (1951) 403.

[22] C. Zener, Interaction between the d shells in the transition metals, Physical Review, 81 (1951) 440.

[23] P. Anderson, Hasegawa, Phys. Rev, 100 (1955) 675.

[24] I. Dzyaloshinsky, A thermodynamic theory of "weak" ferromagnetism of antiferromagnetics, Journal of Physics and Chemistry of Solids, 4 (1958) 241-255.

[25] T. Moriya, Anisotropic superexchange interaction and weak ferromagnetism, Physical Review, 120 (1960) 91.

[26] A.H. Morrish, The physical principles of magnetism, The Physical Principles of Magnetism, by Allan H. Morrish, pp. 696. ISBN 0-7803-6029-X. Wiley-VCH, January 2001., (2001) 696.

[27] C. Kittel, P. McEuen, P. McEuen, Introduction to solid state physics, Wiley New York, 1976.

[28] N.A. Spaldin, Magnetic materials: fundamentals and applications, Cambridge University Press, 2010.

[29] Q. Xia, H. Su, G. Shen, T. Pan, T. Zhang, H. Zhang, X. Tang, Investigation of low loss Z-type hexaferrites for antenna applications, Journal of Applied Physics, 111 (2012) 063921.

[30] J. Lee, Y.-K. Hong, W. Lee, G.S. Abo, J. Park, N. Neveu, W.-M. Seong, S.-H. Park, W.-K. Ahn, Soft M-type hexaferrite for very high frequency miniature antenna applications, Journal of Applied Physics, 111 (2012) 07A520.

[31] J.R. Macdonald, E. Barsoukov, Impedance spectroscopy: theory, experiment, and applications, History, 1 (2005) 1-13.

[32] S. Havriliak, S. Negami, A complex plane representation of dielectric and mechanical relaxation processes in some polymers, Polymer, 8 (1967) 161-210.

[33] A. Boersma, J. Van Turnhout, M. Wübbenhorst, Dielectric characterization of a thermotropic liquid crystalline copolyesteramide: 1. Relaxation peak assignment, Macromolecules, 31 (1998) 7453-7460.

[34] N.G. McCrum, B.E. Read, G. Williams, Anelastic and dielectric effects in polymeric solids, (1967).

[35] H. Wagner, R. Richert, Thermally stimulated modulus relaxation in polymers: method and interpretation, Polymer, 38 (1997) 5801-5806.

[36] D.K. Pradhan, R. Choudhary, C. Rinaldi, R. Katiyar, Effect of Mn substitution on electrical and magnetic properties of Bi 0.9 La 0.1 FeO 3, Journal of Applied Physics, 106 (2009) 024102.

[37] C. Moynihan, Decay function for the electric field relaxation in vitreous ionic conductors, Phys. Chem. Glasses, 14 (1973) 122-125.

[38] P. Macedo, The role of ionic diffusion in polarisation in vitreous ionic conductors, Phys. Chem. Glasses, 13 (1972) 171-179.

[39] R. Kohlrausch, Poggendorff's Ann, Phys, 91 (1854) 179.

[40] G. Williams, D.C. Watts, Non-symmetrical dielectric relaxation behaviour arising from a simple empirical decay function, Transactions of the Faraday society, 66 (1970) 80-85.

[41] R. Bergman, General susceptibility functions for relaxations in disordered systems, Journal of Applied Physics, 88 (2000) 1356-1365.

[42] K.J. Andrew, Dielectric relaxation in solids, Journal of Physics D: Applied Physics, 32 (1999) R57.

[43] R.M. Almeida, W. Paraguassu, D.S. Pires, R.R. Correa, C.W. de Araujo Paschoal, Impedance spectroscopy analysis of BaFe12O19 M-type hexaferrite obtained by ceramic method, Ceramics International, 35 (2009) 2443-2447.

[44] Ashima, S. Sanghi, A. Agarwal, Reetu, N. Ahlawat, Monica, Structure refinement and dielectric relaxation of M-type Ba, Sr, Ba-Sr, and Ba-Pb hexaferrites, Journal of Applied Physics, 112 (2012) 014110.

[45] Y. Liu, M.G. Drew, Y. Liu, J. Wang, M. Zhang, Preparation, characterization and magnetic properties of the doped barium hexaferrites BaFe12−2xCox/2Znx/2SnxO19, x= 0.0–2.0, Journal of Magnetism and Magnetic Materials, 322 (2010) 814-818.

[46] S. Verma, P. Sharma, O.P. Pandey, A. Paesano, A.-C. Sun, Structure and Magnetic Properties of Ba1-xLaxFe12O19 Prepared by Ba1-xLaxFe2O4, IEEE Transactions on Magnetics, 50 (2014) 1-4.

[47] M.N. Ashiq, R.B. Qureshi, M.A. Malana, M.F. Ehsan, Synthesis, structural, magnetic and dielectric properties of zirconium copper doped M-type calcium strontium hexaferrites, Journal of Alloys and Compounds, 617 (2014) 437-443.

[48] S.-P. Shen, Y.-S. Chai, J.-Z. Cong, P.-J. Sun, J. Lu, L.-Q. Yan, S.-G. Wang, Y. Sun, Magnetic-ion-induced displacive electric polarization in FeO5 bipyramidal units of (Ba,Sr)Fe12O19 hexaferrites, Physical Review B, 90 (2014) 180404.

[49] P. Sharma, R.A. Rocha, S.N. Medeiros, B. Hallouche, A. Paesano, Structural and magnetic studies on mechanosynthesized BaFe12−xMnxO19, Journal of Magnetism and Magnetic Materials, 316 (2007) 29-33.

[50] K.K. Mallick, P. Shepherd, R.J. Green, Magnetic properties of cobalt substituted M-type barium hexaferrite prepared by co-precipitation, Journal of Magnetism and Magnetic Materials, 312 (2007) 418-429.

[51] S. Ounnunkad, P. Winotai, Properties of Cr-substituted M-type barium ferrites prepared by nitrate–citrate gel-autocombustion process, Journal of Magnetism and Magnetic Materials, 301 (2006) 292-300.

[52] Z. Li, L. Chen, C. Ong, Studies of static and high-frequency magnetic properties for M-type ferrite BaFe12−2xCoxZrxO19, Journal of applied physics, 92 (2002) 3902-3907.

[53] P. Kuruva, P.R. Matli, B. Mohammad, S. Reddigari, S. Katlakunta, Effect of Ni–Zr codoping on dielectric and magnetic properties of SrFe12O19 via sol–gel route, Journal of Magnetism and Magnetic Materials, 382 (2015) 172-178.

[54] M. Zhang, Z. Zi, Q. Liu, X. Zhu, C. Liang, Y. Sun, J. Dai, Solvothermal synthesis and magnetic properties of BaFe12−2x(NiTi)xO19 nanoparticles, Journal of Magnetism and Magnetic Materials, 369 (2014) 23-26.

[55] Z. Haijun, L. Zhichao, M. Chenliang, Y. Xi, Z. Liangying, W. Mingzhong, Preparation and microwave properties of Co- and Ti-doped barium ferrite by citrate sol–gel process, Materials Chemistry and Physics, 80 (2003) 129-134.

[56] Y. Guan, Y. Lin, L. Zou, Q. Miao, M. Zeng, Z. Liu, X. Gao, J. Liu, The effects of Co-Ti co-doping on the magnetic, electrical, and magnetodielectric behaviors of M-type barium hexaferrites, AIP Advances, 3 (2013) 122115.

[57] S. Wang, J. Ding, Y. Shi, Y.J. Chen, High coercivity in mechanically alloyed BaFe10Al2O19, Journal of Magnetism and Magnetic Materials, 219 (2000) 206-212.

[58] J. Qiu, Q. Zhang, M. Gu, H. Shen, Effect of aluminum substitution on microwave absorption properties of barium hexaferrite, Journal of Applied Physics, 98 (2005) 103905.

[59] F. Wang, T. Zou, L.-Q. Yan, Y. Liu, Y. Sun, Low magnetic field reversal of electric polarization in a Y-type hexaferrite, Applied Physics Letters, 100 (2012) 122901.

[60] T. Kimura, G. Lawes, A. Ramirez, Electric polarization rotation in a hexaferrite with long-wavelength magnetic structures, Physical review letters, 94 (2005) 137201.

[61] S. Ishiwata, Y. Taguchi, H. Murakawa, Y. Onose, Y. Tokura, Low-magnetic-field control of electric polarization vector in a helimagnet, Science, 319 (2008) 1643-1646.

[62] S. Ishiwata, Y. Taguchi, Y. Tokunaga, H. Murakawa, Y. Onose, Y. Tokura, Electric polarization induced by transverse magnetic field in the anisotropy-controlled conical helimagnet Ba2(Mg1−xZnx)2Fe12O22, Physical Review B, 79 (2009) 180408.

[63] I.A. Sergienko, E. Dagotto, Role of the Dzyaloshinskii-Moriya interaction in multiferroic perovskites, Physical Review B, 73 (2006) 094434.

[64] H. Katsura, N. Nagaosa, A.V. Balatsky, Spin current and magnetoelectric effect in noncollinear magnets, Physical review letters, 95 (2005) 057205.

[65] K.L. Cho, C.S. Kim, Magnetic Properties of Sr Substituted Y-Type Hexaferrite, IEEE Transactions on Magnetics, 49 (2013) 4291-4294.

[66] Z. Haijun, Y. Xi, Z. Liangying, The preparation and microwave properties of Ba2ZnzCo2− zFe12O22 hexaferrites, Journal of the European Ceramic Society, 22 (2002) 835-840.

[67] M. El Hiti, A.A. El Ata, Semiconductivity in Ba2Ni2− xZnxFe12O22 Y-type hexaferrites, Journal of Magnetism and Magnetic Materials, 195 (1999) 667-678.

[68] Y. Bai, J. Zhou, Z. Gui, L. Li, Magnetic properties of Cu, Zn-modified Co2Y hexaferrites, Journal of magnetism and magnetic materials, 246 (2002) 140-144.

[69] I. Ali, M. Islam, M.N. Ashiq, H.M. Khan, M.A. Iqbal, M. Najam-Ul-Haq, Effect of Eu–Ni substitution on electrical and dielectric properties of Co–Sr–Y-type hexagonal ferrite, Materials research bulletin, 49 (2014) 338-344.

[70] Y.A. Farzin, O. Mirzaee, A. Ghasemi, Influence of Mg and Ni substitution on structural, microstructural and magnetic properties of Sr2Co2−xMgx/2Nix/2Fe12O22 (Co2Y) hexaferrite, Journal of Magnetism and Magnetic Materials, 371 (2014) 14-19.

[71] A. Elahi, M. Ahmad, I. Ali, M. Rana, Preparation and properties of sol–gel synthesized Mg-substituted Ni2Y hexagonal ferrites, Ceramics International, 39 (2013) 983-990.

[72] M. Hee Won, C. Sung Kim, Effect of Ni substitution on Y-type barium ferrite, Journal of Applied Physics, 113 (2013) 17D906.

[73] R.A. Young, The rietveld method, International union of crystallography, 1993.

[74] R. Kumar, Atomic and Molecular Physics, Campus Book International, 2009.

[75] S. Foner, Versatile and sensitive vibrating-sample magnetometer, Review of Scientific Instruments, 30 (1959) 548-557.

[76] M. Küpferling, R. Grössinger, M.W. Pieper, G. Wiesinger, H. Michor, C. Ritter, F. Kubel, Structural phase transition and magnetic anisotropy of La-substituted M-type Sr hexaferrite, Physical Review B, 73 (2006) 144408.

[77] H. Sözeri, H. Deligöz, H. Kavas, A. Baykal, Magnetic, dielectric and microwave properties of M–Ti substituted barium hexaferrites (M=Mn2+, Co2+, Cu2+, Ni2+, Zn2+), Ceramics International, 40 (2014) 8645-8657.

[78] S. Trukhanov, A. Trukhanov, V. Kostishyn, L. Panina, A.V. Trukhanov, V. Turchenko, D. Tishkevich, E. Trukhanova, O. Yakovenko, L.Y. Matzui, Investigation into the structural features and microwave absorption of doped barium hexaferrites, Dalton Transactions, 46 (2017) 9010-9021.

[79] S.V. Trukhanov, A.V. Trukhanov, V.A. Turchenko, A.V. Trukhanov, E.L. Trukhanova, D.I. Tishkevich, V.M. Ivanov, T.I. Zubar, M. Salem, V.G. Kostishyn, L.V. Panina, D.A. Vinnik, S.A. Gudkova, Polarization origin and iron positions in indium doped barium hexaferrites, Ceramics International, 44 (2018) 290-300.

[80] S.V. Trukhanov, A.V. Trukhanov, V.G. Kostishin, L.V. Panina, I.S. Kazakevich, V.A. Turchenko, V.V. Kochervinskii, Coexistence of spontaneous polarization and magnetization in substituted M-type hexaferrites BaFe12–xAlxO19 ($x \leqslant 1.2$) at room temperature, JETP Letters, 103 (2016) 100-105.

[81] M.N. Ashiq, M.J. Iqbal, M. Najam-ul-Haq, P.H. Gomez, A.M. Qureshi, Synthesis, magnetic and dielectric properties of Er–Ni doped Sr-hexaferrite nanomaterials for applications in High density recording media and microwave devices, Journal of magnetism and magnetic materials, 324 (2012) 15-19.

[82] M. Awawdeh, I. Bsoul, S.H. Mahmood, Magnetic properties and Mössbauer spectroscopy on Ga, Al, and Cr substituted hexaferrites, Journal of Alloys and Compounds, 585 (2014) 465-473.

[83] I. Bsoul, S.H. Mahmood, Magnetic and structural properties of BaFe12−xGaxO19 nanoparticles, Journal of Alloys and Compounds, 489 (2010) 110-114.

[84] D. Chen, Y. Liu, Y. Li, K. Yang, H. Zhang, Microstructure and magnetic properties of Al-doped barium ferrite with sodium citrate as chelate agent, Journal of Magnetism and Magnetic Materials, 337-338 (2013) 65-69.

[85] X. Zhang, Y. Duan, H. Guan, S. Liu, B. Wen, Effect of doping MnO2 on magnetic properties for M-type barium ferrite, Journal of Magnetism and Magnetic Materials, 311 (2007) 507-511.

[86] S. Singhal, A.N. Garg, K. Chandra, Evolution of the magnetic properties during the thermal treatment of nanosize BaMFe11O19 (M=Fe, Co, Ni and Al) obtained through aerosol route, Journal of Magnetism and Magnetic Materials, 285 (2005) 193-198.

[87] W. Zhang, Y. Bai, X. Han, L. Wang, X. Lu, L. Qiao, Magnetic properties of Co–Ti substituted barium hexaferrite, Journal of Alloys and Compounds, 546 (2013) 234-238.

[88] K.M. Batoo, S. Kumar, C.G. Lee, Alimuddin, Study of dielectric and ac impedance properties of Ti doped Mn ferrites, Current Applied Physics, 9 (2009) 1397-1406.

[89] A. Baniasadi, A. Ghasemi, A. Nemati, M. Azami Ghadikolaei, E. Paimozd, Effect of Ti–Zn substitution on structural, magnetic and microwave absorption characteristics of strontium hexaferrite, Journal of Alloys and Compounds, 583 (2014) 325-328.

[90] V. Ketsko, E. Beresnev, M. Kop'Eva, L. Elesina, A. Baranchikov, A. Stognii, A. Trukhanov, N. Kuznetsov, Specifics of pyrohydrolytic and solid-phase syntheses of solid solutions in the (MgGa2O4)x(MgFe2O4)1−x system, Russian Journal of Inorganic Chemistry, 55 (2010) 427-429.

[91] G. Nipan, V. Ketsko, A. Stognij, A. Trukhanov, T. Kol'tsova, M. Kop'eva, L. Elesina, N. Kuznetsov, Properties of Mg(Fe1−xGax)2O4+δ solid solutions in stable and metastable states, Inorganic materials, 46 (2010) 429-433.

[92] J. Rodríguez-Carvajal, Recent advances in magnetic structure determination by neutron powder diffraction, Physica B: Condensed Matter, 192 (1993) 55-69.

[93] J. Barman, S. Ravi, Magnetization reversal and tunable exchange bias behavior in Mn-substituted NiCr 2 O 4, Journal of Materials Science, 53 (2018) 7187-7198.

[94] S. Trukhanov, A. Trukhanov, H. Szymczak, C. Botez, A. Adair, Magnetotransport properties and mechanism of the A-site ordering in the Nd–Ba optimal-doped manganites, Journal of Low Temperature Physics, 149 (2007) 185-199.

[95] S. Pattanayak, B.N. Parida, P.R. Das, R.N.P. Choudhary, Impedance spectroscopy of Gd-doped BiFeO3 multiferroics, Applied Physics A, 112 (2013) 387-395.

[96] S.V. Trukhanov, A.V. Trukhanov, V.G. Kostishyn, L.V. Panina, A.V. Trukhanov, V.A. Turchenko, D.I. Tishkevich, E.L. Trukhanova, V.V. Oleynik, O.S. Yakovenko, L.Y. Matzui, D.A. Vinnik, Magnetic, dielectric and microwave properties of the BaFe12-xGaxO19 ($x \leq 1.2$) solid solutions at room temperature, Journal of Magnetism and Magnetic Materials, 442 (2017) 300-310.

[97] P. Thongbai, S. Tangwancharoen, T. Yamwong, S. Maensiri, Dielectric relaxation and dielectric response mechanism in (Li, Ti)-doped NiO ceramics, Journal of Physics: Condensed Matter, 20 (2008) 395227.

[98] A.M. Abo El Ata, S.M. Attia, Dielectric dispersion of Y-type hexaferrites at low frequencies, Journal of Magnetism and Magnetic Materials, 257 (2003) 165-174.

[99] M.J. Iqbal, S. Farooq, Impact of Pr–Ni substitution on the electrical and magnetic properties of chemically derived nanosized strontium–barium hexaferrites, Journal of Alloys and Compounds, 505 (2010) 560-567.

[100] P. Wartewig, M. Krause, P. Esquinazi, S. Rösler, R. Sonntag, Magnetic properties of Zn-and Ti-substituted barium hexaferrite, Journal of magnetism and magnetic materials, 192 (1999) 83-99.

[101] S. Trukhanov, L. Lobanovski, M. Bushinsky, V. Khomchenko, N. Pushkarev, I. Troyanchuk, A. Maignan, D. Flahaut, H. Szymczak, R. Szymczak, Influence of oxygen vacancies on the magnetic and electrical properties of La1-xSrxMnO3-x/2 manganites, The European Physical Journal B-Condensed Matter and Complex Systems, 42 (2004) 51-61.

[102] V. Turchenko, A. Trukhanov, S. Trukhanov, I. Bobrikov, A.M. Balagurov, Features of crystal and magnetic structures of solid solutions BaFe12-xDxO19 (D= Al3+, In3+; x= 0.1) in a wide temperature range, The European Physical Journal Plus, 131 (2016) 82.

[103] S. Trukhanov, A. Trukhanov, V. Turchenko, V. Kostishin, L. Panina, I. Kazakevich, A. Balagurov, Magnetic Ordering in BaFe11.9In0.1O19 Hexaferrite, Journal of Low Temperature Physics, 186 (2017) 44-62.

[104] A. Trukhanov, L. Panina, S. Trukhanov, V. Turchenko, M. Salem, Evolution of structure and physical properties in Al-substituted Ba-hexaferrites, Chinese Physics B, 25 (2015) 016102.

[105] A.V. Trukhanov, S.V. Trukhanov, L.V. Panina, V.G. Kostishyn, I.S. Kazakevich, A.V. Trukhanov, E.L. Trukhanova, V.O. Natarov, V.A. Turchenko, M.M. Salem, A.M. Balagurov, Evolution of structure and magnetic properties for BaFe11.9Al0.1O19 hexaferrite in a wide temperature range, Journal of Magnetism and Magnetic Materials, 426 (2017) 487-496.

[106] R. Grössinger, A critical examination of the law of approach to saturation. I. Fit procedure, physica status solidi (a), 66 (1981) 665-674.

[107] A. Baykal, I. Auwal, S. Güner, H. Sözeri, Magnetic and optical properties of Zn2+ ion substituted barium hexaferrites, Journal of Magnetism and Magnetic Materials, 430 (2017) 29-35.

[108] S.Y. An, I.-B. Shim, C.S. Kim, Mössbauer and magnetic properties of Co–Ti substituted barium hexaferrite nanoparticles, Journal of Applied Physics, 91 (2002) 8465-8467.

[109] X. Tang, Y. Yang, K. Hu, Structure and electromagnetic behavior of BaFe12−2x(Ni0.8Ti0.7)xO19−0.8x in the 2–12GHz frequency range, Journal of Alloys and Compounds, 477 (2009) 488-492.

[110] R. Tang, C. Jiang, J. Jian, Y. Liang, X. Zhang, H. Wang, H. Yang, Impedance spectroscopy and scaling behaviors of Sr3Co2Fe24O41 hexaferrite, Applied Physics Letters, 106 (2015) 022902.

[111] J. Liu, C.-G. Duan, W.-G. Yin, W.-N. Mei, R.W. Smith, J.R. Hardy, Large dielectric constant and Maxwell-Wagner relaxation in Bi2⁄3Cu3Ti4O12, Physical review B, 70 (2004) 144106.

[112] L. Zhuo, F. Huiqing, Relaxation behaviour induced by oxygen vacancies of barium strontium titanate at high temperatures, Journal of Physics D: Applied Physics, 42 (2009) 075415.

[113] B. Unal, Z. Durmus, H. Kavas, A. Baykal, M.S. Toprak, Synthesis, conductivity and dielectric characterization of salicylic acid–Fe3O4 nanocomposite, Materials Chemistry and Physics, 123 (2010) 184-190.

[114] P. Behera, S. Ravi, Impedance spectroscopy and magnetic properties of Mg doped Y-type barium hexaferrite, Journal of Materials Science: Materials in Electronics, 29 (2018) 20206-20215.

[115] S. Kumari, N. Ortega, A. Kumar, S.P. Pavunny, J.W. Hubbard, C. Rinaldi, G. Srinivasan, J.F. Scott, R.S. Katiyar, Dielectric anomalies due to grain boundary conduction in chemically substituted BiFeO3, Journal of Applied Physics, 117 (2015) 114102.

[116] B.T. Phan, N. Kim, J. Lee, Ac Conductivity of Cr-doped SrTiO3 Thin Films, J. Korean Phys. Soc, 54 (2009) 873.

[117] R. Gangopadhyay, A. De, S. Das, Transport properties of polypyrrole–ferric oxide conducting nanocomposites, Journal of Applied Physics, 87 (2000) 2363-2371.

[118] S. Nasri, M. Megdiche, M. Gargouri, DC conductivity and study of AC electrical conduction mechanisms by non-overlapping small polaron tunneling model in LiFeP2O7 ceramic, Ceramics International, 42 (2016) 943-951.

[119] N. Ortega, A. Kumar, P. Bhattacharya, S. Majumder, R. Katiyar, Impedance spectroscopy of multiferroic Pb Zr x Ti 1− x O 3⁄Co Fe 2 O 4 layered thin films, Physical Review B, 77 (2008) 014111.

[120] M. El-Saadawy, DC conductivity for hexaferrites of the Zn2−xCuxBa1Fe16O27 system, Journal of Magnetism and Magnetic Materials, 219 (2000) 69-72.

[121] J. Wu, J. Wang, Ferroelectric and impedance behavior of La-and Ti-codoped BiFeO3 thin films, Journal of the American Ceramic Society, 93 (2010) 2795-2803.

[122] G. Li, Z. Chen, X. Sun, L. Liu, L. Fang, B. Elouadi, Electrical properties of AC3B4O12-type perovskite ceramics with different cation vacancies, Materials Research Bulletin, 65 (2015) 260-265.

[123] Y. Tokunaga, Y. Kaneko, D. Okuyama, S. Ishiwata, T. Arima, S. Wakimoto, K. Kakurai, Y. Taguchi, Y. Tokura, Multiferroic M-type hexaferrites with a room-temperature conical state and magnetically controllable spin helicity, Physical review letters, 105 (2010) 257201.

[124] K. Ahn, B. Ryu, D. Korolev, Y. Jae Kang, Substantial enhancement in intrinsic coercivity on M-type strontium hexaferrite through the increase in magneto-crystalline

anisotropy by co-doping of group-V and alkali elements, Applied Physics Letters, 103 (2013) 242417.

[125] S. Ram, H. Krishnan, K. Rai, K. Narayan, Magnetic and electrical properties of Bi2O3 modified BaFe12O19 hexagonal ferrite, Japanese Journal of Applied Physics, 28 (1989) 604.

[126] K.L. Cho, C.H. Rhee, C.S. Kim, The crystal structure and magnetic properties of Ba2−xSrxCo2Fe12O22, Journal of Applied Physics, 115 (2014) 17A523.

[127] G. Tan, X. Chen, Structure and multiferroic properties of barium hexaferrite ceramics, Journal of Magnetism and Magnetic Materials, 327 (2013) 87-90.

[128] M.N. Ashiq, M. Javed Iqbal, I. Hussain Gul, Effect of Al–Cr doping on the structural, magnetic and dielectric properties of strontium hexaferrite nanomaterials, Journal of Magnetism and Magnetic Materials, 323 (2011) 259-263.

[129] D.A. Vinnik, D.A. Zherebtsov, L.S. Mashkovtseva, S. Nemrava, M. Bischoff, N.S. Perov, A.S. Semisalova, I.V. Krivtsov, L.I. Isaenko, G.G. Mikhailov, R. Niewa, Growth, structural and magnetic characterization of Al-substituted barium hexaferrite single crystals, Journal of Alloys and Compounds, 615 (2014) 1043-1046.

[130] H. Chang, H.B. Lee, Y.-S. Song, J.-H. Chung, S. Kim, I. Oh, M. Reehuis, J. Schefer, Al doping effect on magnetic phase transitions of magnetoelectric hexaferrite Ba0.7Sr1.3Zn2(Fe1−xAlx)12 O22, Physical Review B, 85 (2012) 064402.

[131] H.Z. Wang, B. Yao, Y. Xu, Q. He, G.H. Wen, S.W. Long, J. Fan, G.D. Li, L. Shan, B. Liu, L.N. Jiang, L.L. Gao, Improvement of the coercivity of strontium hexaferrite induced by substitution of Al3+ ions for Fe3+ ions, Journal of Alloys and Compounds, 537 (2012) 43-49.

[132] M.J. Iqbal, M.N. Ashiq, P. Hernandez-Gomez, J.M. Munoz, Synthesis, physical, magnetic and electrical properties of Al–Ga substituted co-precipitated nanocrystalline strontium hexaferrite, Journal of Magnetism and Magnetic Materials, 320 (2008) 881-886.

[133] J. Kreisel, G. Lucazeau, H. Vincent, Raman Spectra and Vibrational Analysis of BaFe12O19Hexagonal Ferrite, Journal of Solid State Chemistry, 137 (1998) 127-137.

[134] W.Y. Zhao, P. Wei, X.Y. Wu, W. Wang, Q.J. Zhang, Lattice vibration characterization and magnetic properties of M-type barium hexaferrite with excessive iron, Journal of Applied Physics, 103 (2008) 063902.

[135] M. Ahmad, Q. Ali, I. Ali, I. Ahmad, M. Azhar Khan, M.N. Akhtar, G. Murtaza, M.U. Rana, Effects of Sr-substitution on the structural and magnetic behavior of Ba-based Y-type hexagonal ferrites, Journal of Alloys and Compounds, 580 (2013) 23-28.

[136] I. Ali, M. Ahmad, M. Islam, M. Awan, Substitution effects of La 3+ ions on the structural and magnetic properties of Co 2 Y hexaferrites synthesized by sol–gel autocombustion method, Journal of sol-gel science and technology, 68 (2013) 141-149.

[137] S. Utsumi, D. Yoshiba, N. Momozawa, Superexchange interactions of (Ba1− xSrx) 2Zn2Fe12O22 system studied by neutron diffraction, Journal of the Physical Society of Japan, 76 (2007) 034704-034704.

[138] N. Rezlescu, E. Rezlescu, Abnormal dielectric behaviour of copper containing ferrites, Solid State Communications, 14 (1974) 69-72.

[139] A.A. El Ata, M. El Nimr, D. El Kony, A. Al-Hammadi, Dielectric and magnetic permeability behavior of BaCo2− xNixFe16O27 W-type hexaferrites, Journal of magnetism and magnetic materials, 204 (1999) 36-44.

[140] I. Afandiyeva, I. Dökme, Ş. Altındal, M. Bülbül, A. Tataroğlu, Frequency and voltage effects on the dielectric properties and electrical conductivity of Al–TiW–Pd2Si/n-Si structures, Microelectronic Engineering, 85 (2008) 247-252.

[141] B. Want, B.H. Bhat, B.Z. Ahmad, Effect of lanthanum substitution on dielectric relaxation, impedance response, conducting and magnetic properties of strontium hexaferrite, Journal of Alloys and Compounds, 627 (2015) 78-84.

[142] C.A. Stergiou, I. Manolakis, T.V. Yioultsis, G. Litsardakis, Dielectric and magnetic properties of new rare-earth substituted Ba-hexaferrites in the 2–18GHz frequency range, Journal of Magnetism and Magnetic Materials, 322 (2010) 1532-1535.

[143] P. Meng, K. Xiong, K. Ju, S. Li, G. Xu, Wideband and enhanced microwave absorption performance of doped barium ferrite, Journal of Magnetism and Magnetic Materials, 385 (2015) 407-411.

[144] P. Shen, J. Luo, Y. Zuo, Z. Yan, K. Zhang, Effect of La-Ni substitution on structural, magnetic and microwave absorption properties of barium ferrite, Ceramics International, 43 (2017) 4846-4851.

[145] C. Koops, On the dispersion of resistivity and dielectric constant of some semiconductors at audiofrequencies, Physical Review, 83 (1951) 121.

[146] L. John Berchmans, R. Kalai Selvan, P.N. Selva Kumar, C.O. Augustin, Structural and electrical properties of Ni1−xMgxFe2O4 synthesized by citrate gel process, Journal of Magnetism and Magnetic Materials, 279 (2004) 103-110.

[147] P. Meng, K. Xiong, L. Wang, S. Li, Y. Cheng, G. Xu, Tunable complex permeability and enhanced microwave absorption properties of BaNixCo1−xTiFe10O19, Journal of Alloys and Compounds, 628 (2015) 75-80.

[148] Z. Zhang, X. Liu, X. Wang, Y. Wu, R. Li, Effect of Nd–Co substitution on magnetic and microwave absorption properties of SrFe12O19 hexaferrites, Journal of Alloys and Compounds, 525 (2012) 114-119.

[149] M.H. Won, C.S. Kim, Magnetic properties of Ni substituted Y-type barium ferrite, Journal of Applied Physics, 115 (2014) 17A509.

[150] A.V. Nazarov, C.E. Patton, Effect of large magnetocrystalline anisotropy on the spin wave linewidth in Zn–Y hexagonal ferrite, Journal of Applied Physics, 93 (2003) 9195-9201.

[151] A.L. Geiler, J. Wang, J.S. Gao, S.D. Yoon, Y. Chen, V.G. Harris, C. Vittoria, Low Bias Field Hexagonal Y-Type Ferrite Phase Shifters at K_U-Band, IEEE Transactions on Magnetics, 45 (2009) 4179-4182.

[152] J. Jalli, Y.-K. Hong, S. Bae, J.-J. Lee, G.S. Abo, J.-H. Park, B.-C. Choi, T. Mewes, S.-G. Kim, S.-H. Gee, I.-T. Nam, T. Tanaka, Magnetic and microwave properties of ferrimagnetic Zr-substituted Ba2Zn2Fe12O22 (Zn-Y) single crystals, Journal of Applied Physics, 109 (2011) 07A509.

[153] Y. Bai, F. Xu, L. Qiao, J. Zhou, Effect of Mn doping on physical properties of Y-type hexagonal ferrite, Journal of Alloys and Compounds, 473 (2009) 505-508.

[154] M. Matsumoto, Y. Miyata, A gigahertz-range electromagnetic wave absorber with wide bandwidth made of hexagonal ferrite, Journal of Applied Physics, 79 (1996) 5486-5488.

[155] S.-W. Cheong, M. Mostovoy, Multiferroics: a magnetic twist for ferroelectricity, Nature materials, 6 (2007) 13.

[156] K. Knížek, P. Novák, M. Küpferling, Electronic structure and conductivity of ferroelectric hexaferrite: Ab initio calculations, Physical Review B, 73 (2006) 153103.

[157] M. Ahmad, Q. Ali, I. Ali, I. Ahmad, M. Azhar Khan, M.N. Akhtar, G. Murtaza, M.U. Rana, Effects of Sr-substitution on the structural and magnetic behavior of Ba-based Y-type hexagonal ferrites, Journal of Alloys and Compounds, 580 (2013) 23-28.

[158] C.A. Stergiou, G. Litsardakis, Y-type hexagonal ferrites for microwave absorber and antenna applications, Journal of Magnetism and Magnetic Materials, 405 (2016) 54-61.

[159] M.X. Wu, W.J. Zhong, X.S. Gao, L.J. Liu, Z.W. Liu, Analysis of the alternating current conductivity and magnetic behaviors for the polycrystalline Y-type Ba0.5Sr1.5Co2(Fe1-xAlx)12O22 hexaferrites, Journal of Applied Physics, 116 (2014) 224103.

[160] S. Hirose, K. Haruki, A. Ando, T. Kimura, Mutual control of magnetization and electrical polarization by electric and magnetic fields at room temperature in Y-type BaSrCo2−xZnxFe11AlO22 ceramics, Applied Physics Letters, 104 (2014) 022907.

[161] Y. Bai, J. Zhou, Z. Gui, Z. Yue, L. Li, Complex Y-type hexagonal ferrites: an ideal material for high-frequency chip magnetic components, Journal of Magnetism and Magnetic Materials, 264 (2003) 44-49.

[162] S. Kamba, V. Goian, M. Savinov, E. Buixaderas, D. Nuzhnyy, M. Maryško, M. Kempa, V. Bovtun, J. Hlinka, K. Knížek, P. Vaněk, P. Novák, J. Buršík, Y. Hiraoka, T. Kimura, K. Kouřil, H. Štěpánková, Dielectric, magnetic, and lattice dynamics properties of Y-type hexaferrite Ba0.5Sr1.5Zn2Fe12O22: Comparison of ceramics and single crystals, Journal of Applied Physics, 107 (2010) 104109.

[163] J. Barman, S. Ravi, Study of magnetic compensation behavior in Mn(Cr1−xFex)2O4, Journal of Magnetism and Magnetic Materials, 437 (2017) 42-50.

[164] A. Srivastava, A. Garg, F.D. Morrison, Impedance spectroscopy studies on polycrystalline BiFeO3 thin films on Pt/Si substrates, Journal of Applied Physics, 105 (2009) 054103.

[165] B. Deka, S. Ravi, A. Perumal, D. Pamu, Effect of Mn doping on magnetic and dielectric properties of YFeO3, Ceramics International, 43 (2017) 1323-1334.

[166] S. Khadhraoui, A. Triki, S. Hcini, S. Zemni, M. Oumezzine, Variable-range-hopping conduction and dielectric relaxation in Pr0.6Sr0.4Mn0.6Ti0.4O3±δ perovskite, Journal of Magnetism and Magnetic Materials, 371 (2014) 69-76.

[167] S. Elliott, Frequency-dependent conductivity in ionically and electronically conducting amorphous solids, Solid State Ionics, 70 (1994) 27-40.

[168] C. Prakash, J.S. Baijal, Dielectric behaviour of tetravalent titanium-substituted Ni-Zn ferrites, Journal of the Less Common Metals, 107 (1985) 51-57.

[169] J. Wu, J. Wang, Ferroelectric and Impedance Behavior of La- and Ti-Codoped BiFeO3 Thin Films, Journal of the American Ceramic Society, 93 (2010) 2795-2803.

[170] M. Wu, L. Liu, X. Gao, Z. Liu, Electric and magnetic properties of Y-type Ba2Mg2Fe12O22 hexaferrites with various Co doping, Journal of Materials Science: Materials in Electronics, 27 (2016) 10516-10524.

[171] C.L. Li, S. Huang, X.H. Chen, T.Y. Yan, Q.S. Fu, R. Zhang, C.M. Zhu, S.L. Yuan, Colossal dielectric response and relaxation properties in Co2Z-type hexaferrites, Ceramics International, 43 (2017) 12435-12441.

[172] J.T. Lim, C.M. Kim, B.W. Lee, C.S. Kim, Investigation of magnetic properties of non-magnetic ion (Al, Ga, In) doped Ba2Mg0.5Co1.5Fe12O22, Journal of Applied Physics, 111 (2012) 07A518.

[173] Z. Yang, C.S. Wang, X.H. Li, H.X. Zeng, (Zn, Ni, Ti) substituted barium ferrite particles with improved temperature coefficient of coercivity, Materials Science and Engineering: B, 90 (2002) 142-145.

[174] L. Kumar, P. Kumar, M. Kar, Cation distribution by Rietveld technique and magnetocrystalline anisotropy of Zn substituted nanocrystalline cobalt ferrite, Journal of Alloys and Compounds, 551 (2013) 72-81.

[175] A. Collomb, J. Muller, J.C. Guitel, J.M. Desvignes, Crystal structure and zinc location in the BaZnFe6O11 Y-type hexagonal ferrite, Journal of Magnetism and Magnetic Materials, 78 (1989) 77-84.

[176] A. Collomb, M.H. Farhat, J. Joubert, Cobalt location in the Y-type hexagonal ferrite: BaCoFe6O11, Materials Research Bulletin, 24 (1989) 453-458.

[177] S.G. Lee, S.J. Kwon, Saturation magnetizations and Curie temperatures of Co□Zn Y-type ferrites, Journal of Magnetism and Magnetic Materials, 153 (1996) 279-284.

[178] J. Füzerová, J. Füzer, P. Kollár, R. Bureš, M. Fáberová, Complex permeability and core loss of soft magnetic Fe-based nanocrystalline powder cores, Journal of Magnetism and Magnetic Materials, 345 (2013) 77-81.

[179] G. Wang, S. Cao, Y. Cao, S. Hu, X. Wang, Z. Feng, B. Kang, Y. Chai, J. Zhang, W. Ren, Magnetic field controllable electric polarization in Y-type hexaferrite Ba0.5Sr1.5Co2Fe12O22, Journal of Applied Physics, 118 (2015) 094102.

[180] K. Taniguchi, N. Abe, S. Ohtani, H. Umetsu, T.-h. Arima, Ferroelectric polarization reversal by a magnetic field in multiferroic Y-type hexaferrite Ba2Mg2Fe12O22, Applied physics express, 1 (2008) 031301.

[181] M. Costa, G.P. Junior, A. Sombra, Dielectric and impedance properties' studies of the of lead doped (PbO)-Co2Y type hexaferrite (Ba2Co2Fe12O22 (Co2Y)), Materials Chemistry and Physics, 123 (2010) 35-39.

[182] M. Zhang, J. Dai, L. Yin, X. Kong, Q. Liu, Z. Zi, Y. Sun, Mg doping effect on the magnetic properties of Y-type hexaferrite Ba0.5Sr1.5Zn2−xMgxFe12O22, Journal of Alloys and Compounds, 689 (2016) 75-80.

[183] R.A. Khan, S. Mizukami, A.M. Khan, B. Ismail, A.R. Khan, T. Miyazaki, Static and dynamic magnetic characteristics of Mg substituted Ba–Co2 W-type hexaferrites, Journal of Alloys and Compounds, 637 (2015) 197-202.

[184] R.A. Khan, S. Mir, A.M. Khan, B. Ismail, A.R. Khan, Doping magnesium ion to tune electrical and dielectric properties of BaCo2 hexaferrites, Ceramics International, 40 (2014) 11205-11211.

[185] R.D. Shannon, Revised effective ionic radii and systematic studies of interatomic distances in halides and chalcogenides, Acta crystallographica section A: crystal physics, diffraction, theoretical and general crystallography, 32 (1976) 751-767.

[186] R. Tang, C. Jiang, W. Qian, J. Jian, X. Zhang, H. Wang, H. Yang, Dielectric relaxation, resonance and scaling behaviors in Sr(3)Co(2)Fe(24)O(41) hexaferrite, Scientific Reports, 5 (2015) 13645.

[187] E. Barsoukov, J.R. Macdonald, Impedance spectroscopy: theory, experiment, and applications, John Wiley & Sons, 2018.

[188] Y.J. Wong, J. Hassan, M. Hashim, Dielectric properties, impedance analysis and modulus behavior of CaTiO3 ceramic prepared by solid state reaction, Journal of Alloys and Compounds, 571 (2013) 138-144.

[189] B.V.R. Chowdari, R. Gopalakrishnan, ac conductivity analysis of glassy silver iodomolybdate system, Solid State Ionics, 23 (1987) 225-233.

[190] K.P. Padmasree, D.K. Kanchan, A.R. Kulkarni, Impedance and Modulus studies of the solid electrolyte system 20CdI2–80[xAg2O–y(0.7V2O5–0.3B2O3)], where 1≤x/y≤3, Solid State Ionics, 177 (2006) 475-482.

[191] A.K. Jonscher, The 'universal'dielectric response, nature, 267 (1977) 673-679.

[192] S. Kumar, S. Supriya, R. Pandey, L.K. Pradhan, R.K. Singh, M. Kar, Effect of lattice strain on structural and magnetic properties of Ca substituted barium hexaferrite, Journal of Magnetism and Magnetic Materials, 458 (2018) 30-38.

Publications/Communications in International Journals

1. **Pratap Behera** and S. Ravi, "*Influence of Al substitution on Structural, Dielectric and Magnetic properties of M-type Barium Hexaferrite* ", **Journal of Super Conductivity and Novel Magnetism**, **30** (2017) 1453-1461.
2. **Pratap Behera** and S. Ravi, "*Magnetic and Dielectric Spectroscopic Studies in Zn doped Y-type Barium Hexaferrite*", **Journal of Alloys and Compounds**, **767** (2018) 712-723.
3. **Pratap Behera** and S. Ravi, "*Impedance Spectroscopy and Magnetic properties of Mg doped Y-type Barium Hexaferrite*", **Journal of Materials Science: Materials in Electronics**, **29** (2018) 20206-20215.
4. **Pratap Behera** and S. Ravi, "*Effect of Ni doping on Structural, Magnetic and Dielectric properties of M-type Barium Hexaferrite*", **Journal of Solid State Sciences**, **89** (2019) 139-149.
5. **Pratap Behera** and S. Ravi, "*Influence of Ti substitution on Structural, Magnetic and Dielectric properties of M-type Barium Hexaferrite*", **Journal of Electronic Materials**, **48** (2019) 5062-5074.

Papers Presented in International and National Conferences

1. **Pratap Behera** and S. Ravi, "*Effect of Al substitution on Structural and Magnetic properties of M-type Barium Hexaferrite*", **International Conference on Material Science and Technology (ICMST 2016), ST Thomas College, Palai, Kerala, India.**
2. **Pratap Behera** and S. Ravi, "*Effect of Zn doping on Structural and Magnetic properties of* $Ba_2(Co_{1-x}Zn_x)_2Fe_{12}O_{22}$ *Hexaferrite*", **International Conference on Magnetic Materials and applications (ICMAGMA 2017), Leonia Resort, Hyderabad, India.**
3. **Pratap Behera** and S. Ravi, "*Investigation on Crystal Structure and Magnetic properties of Mg doped Y-type Barium Hexaferrite*", **International Conference on Material Science (ICMS 2017), Tripura Central University, Agartala, India.**
4. **Pratap Behera** and S. Ravi, "*Magnetic and Dielectric Characterization of Zn doped Y-type Barium Hexaferrite*", **International Conference on Sophisticated Instruments in Modern Research (ICSMR 2017), IIT Guwahati, Assam, India**.
5. **Pratap Behera** and S. Ravi, "*Structural, Dielectric and Magnetic studies of Zn doped Y-type Hexaferrite*", **National Conference on Condensed Matter Days (CMDAYS 2017), Tezpur Central University, Assam, India**.
6. **Pratap Behera** and S. Ravi, "*Magnetic and Dielectric properties of Ni and Zn substituted Y-type Barium Hexaferrite*", **International Conference on Magnetic Materials and Applications (ICMAGMA 2019), NISER, Bhubaneswar, India**.

Workshops Attended

1. National Workshop on **Advanced Probing Techniques in Transmission Electron Microscope (APTEM 2016).**
2. IUCR Workshop on **X-Ray Diffraction Systems and Related Applications (2014).**